SOLIDIFICATION OF Al-4.5wt%Cu

IN THE PRESENCE OF SiC FIBERS

by

Andreas Mortensen

Ingénieur Civil des Mines de Paris, 1980

SUBMITTED TO THE DEPARTMENT OF MATERIALS SCIENCE AND ENGINEERING
IN PARTIAL FULFILLMENT OF THE REQUIREMENTS FOR THE DEGREE OF

DOCTOR OF PHILOSOPHY

at the

MASSACHUSETTS INSTITUTE OF TECHNOLOGY
June 1986

Signature of author _____
Department of Materials Science and Engineering
May 2 , 1986

Certified by _____
Merton C. Flemings
Thesis Supervisor

Certified by _____
James A. Cornie
Thesis Supervisor

Accepted by _____
Bernhardt J. Wuensch
Chairman, Department Comittee on
Graduate Students

SOLIDIFICATION OF Al-4.5wt%Cu

IN THE PRESENCE OF SiC FIBERS

by

ANDREAS MORTENSEN

Submitted to the Department of Materials Science and Engineering on May 2 , 1986
in partial fulfillment of the requirements for
the degree of Doctor of Philosophy in Materials Engineering

ABSTRACT

The solidification of metal alloys in the presence of a high volume fraction of parallel reinforcing fibers is studied using a model system of silicon carbide fibers in an Al-4.5 wt% Cu matrix.
Pressure cast samples were melted and solidified at steady state using a Bridgman furnace. Temperature gradients (100 to 30 °C/cm) and growth rates (25 to 200 μm/s) cover dendritic growth at and beyond the dendritic/cellular transition.
Growth of the solidifying metal matrix takes place dendritically, with dendrite tips growing at approximately the same undercooling in the composite as in a usual casting. Dendrites grow so as to avoid the fibers, with the result that the fiber/metal interface tends to comprise the second phase Al_2Cu.
The kinetics of secondary dendrite arm coarsening are affected by the presence of the fibers. An important and original finding of this work is that the usual $t^{1/3}$ coarsening relation between dendrite arm spacing and solidification time is violated when the dendrite arm spacing approaches the interfiber spacing. The fibers inhibit secondary dendrite arm coarsening by ripening beyond a certain dendrite arm spacing, and accelerate secondary dendrite arm coalescence. At sufficiently long solidification times, the dendritic structure is eliminated. Secondary dendrite arm coalescence is modelled with a simplified dendrite geometry to calculate the time for full coalescence of secondary dendrite arms and conditions that yield non dendritic microstructures in metal matrix composites. Results of the model are in agreement with microstructural observations.
The amount of microsegregation is significantly reduced at low cooling rates because the scale of the matrix microstructure is restricted by the fibers. The influence of ripening on the supression of microsegregation is calculated with a simple and general modification of the Scheil equation derived herein. A finite-difference computer model is then used to predict the effect of solid state diffusion on concentration profiles in the solid during solidification

assuming full coalescence of the dendritic structure due to the fibers. Comparison between data collected by electron probe microanalysis on the samples and calculations from the model is good.
Engineering applications of this work include the possibility of modifying the matrix microstructure with new solidification processing approaches for metal matrix composites. In particular, the matrix can be cast directly into the solutionized state.

Thesis Supervisor: Dr. Merton C. Flemings
Title: Toyota Professor of Materials Engineering
Thesis Supervisor: Dr. J.A.Cornie
Title: Principal Research Associate

TABLE OF CONTENTS

EXPERIMENTAL RESULTS

THEORY

DISCUSSION

LIST OF ILLUSTRATIONS AND FIGURES

LIST OF TABLES

Page

ACKNOWLEDGMENTS

The author wishes to express his sincere appreciation to everyone who extended aid during the course of this investigation and especially to acknowledge the following:

Professor Merton C. Flemings for his guidance, support, advice, open-mindedness and patience throughout the five years the author spent in his research group.

Dr. James A. Cornie for introducing the author to the field of metal matrix composites and for his support, guidance and enthousiasm during the course of this thesis.

Dr. Yuh Shiohara and Professor Theodoulos Kattamis for many enlightening discussions. Permission from Dr. Shiohara to use his computer program for calculating dendrite tip radii is also gratefully acknowledged.

Ms. Maria Wehrle-Due, Mr. Joseph Adario, Ms. Brenda Chin, Ms. Kei Yamamoto and Mr. Larry Masur for help with the experimental work.

Cherie and my Parents for putting up with it all.

INTRODUCTION

These past fifteen years have witnessed the emergence on an industrial scale of a new class of materials : Metal Matrix Composites (MMC). Most of these consist of the combination by artificial means of two materials. One of these is the reinforcing material, a fine scale material that displays a set of particularly desirable properties (high strength, stiffness, etc). The other, the matrix, bonds the reinforcing particles or fibers together and is metallic.

The decreasing cost and exceptional mechanical properties of presently available reinforcing fibers or whiskers make such materials both attractive and affordable. In particular, if a light metal matrix is used, outstanding strength to weight properties can be achieved. This makes composite materials particularly attractive to industries such as the aerospace or automotive industries where a smaller weight for an equal strength is synonymous with considerable energy savings. As metal matrices are both stronger and more resistant to elevated temperatures or corrosion than resin matrices, metal matrix composites stand out as exceptionally promising. This has warranted a considerable effort in their fabrication technology.

A number of methods have been devised to combine metal and reinforcement. Some are solid-state (powder metallurgy, diffusion bonding, deformation processing), some involve molten metal

(pressure casting, compocasting, liquid-phase diffusion bonding, infiltration of precoated fibers). Most are intricate, time consuming, or delicate. Cost is therefore a concern, and these materials are generally expensive.

Compared with most fabrication processes for metal matrix composites, casting stands out as one of the simplest and most economical for large scale production. Here, liquid metal is driven between the fibers by capillary or external forces, and solidified. It is apparent in the most recent literature on cast metal matrix composites that the presence of the fibers can affect the microstructure the metal displays [5,7,14,19,20,24,31, 33,34,38,39,53,64,66-68,192]. Since this in turn exerts a considerable influence on the properties of the finished material, a sounder knowledge of the fundamentals of solidification in metal matrix composites would be of considerable engineering importance.

The purpose of this thesis is to help further our basic understanding of the changes imparted on the solidification of a metal alloy by a high volume fraction of reinforcing fibers. The first half of the literature survey reviews the solidification processing of metal matrix composites with particular emphasis on the fibers and matrix used herein. A broad review of dendritic solidification theory forms the second part of the literature survey. Experimental methods and results are given in the two following chapters. Theoretical derivations are given in the subsequent chapter and the appendices. The discussion then

compares results from both experiments and calculations and highlights the consequences from an engineering standpoint of the findings in this thesis.

REVIEW OF LITERATURE

I - Solidification Processing of Metal Matrix Composites.

a - The process.

With the advent of reinforcements that react less violently with molten aluminum than the early boron fibers [1] it is now often a viable process to cast metal matrix composites. The liquid metal flows easily and can be made to surround all fibers completely and in a short time. Compared to previous methods, the process is rapid and simple. Most often, however, the infiltration process is not spontaneous and some energy is required to force the metal between the fibers.

Practical methods of casting metal matrix composites vary. The following are the most representative processes:

1- Squeeze-casting.

This is a variant of a pre-existing process employing pressure to enhance casting quality [16,17]. The basic principle is to "forge" a liquid metal which thus solidifies rapidly under considerable amounts of pressure. For metal matrix composites, a preheated fiber preform is inserted in the die, liquid metal is poured and a punch is lowered to apply pressure [2,3,5,6,8,10,14,18-20,192,197]. Advantages include simplicity, speed of operation and high pressures that can feed shrinkage

while the part is solidifying. One limitation is the narrow range of shapes that can be cast.

2- Other pressure casting processes.

These processes allow more intricate shapes to be cast. Liquid metal is forced into a preheated fiber preform often by means of a pressurised gas [21-23]. Fukunaga et al. successfully produced fiber reinforced parts using a die casting machine [15]. Various parameters, as well as means to reduce microporosity, were investigated. High pressures, short infiltration paths and columnar solidification toward the gate produced void-free castings. Both squeeze-casting and these processes are termed pressure casting in what follows.

3- Gravity or vacuum casting along conventional routes has been used for systems where the metal wets the fibers [24-26].

4- Incorporation into an agitated melt [7] or semi-solid slurry ("compocasting") [27-29] of loose particles or fibers. These processes are generally used for low volume densities of reinforcement.

5- Infiltration of fiber tows passed through a bath of molten metal [30-34]. Often the fibers are coated to promote wetting. Further consolidation of the composite wires is necessary.

6-"Liquid phase diffusion bonding" or "liquid phase hot-pressing", where fibers and metal are intimately mixed or layered in the solid state, and the whole assembly is heated, often under pressure, to melt at least part of the metal [35-42].

Several publications dealing with the fundamentals of the

infiltration process have been published. The main parameters of interest are the pressures and temperatures necessary to achieve complete infiltration.

The pressure difference at the liquid metal front due to capillary effects has been evaluated using various assumptions. The equations given in the literature [2,3,4,5,6] all are different versions of Kelvin's equation :

$$p = \frac{2\,\sigma_{LA}\cos\theta}{r}$$

where θ = wetting angle of the liquid metal on the fiber in the infiltration atmosphere,

r = radius of curvature at the molten metal front.

Different assumptions lead to various forms of r as a function of fiber volume fraction and diameter. Often, $\theta = 180^0$ is assumed for simplicity.

It should be noted that such an equation makes sense only if θ exists, i.e. if $(\sigma_{LF} - \sigma_{FA}) \in [-\sigma_{LA}, +\sigma_{LA}]$. It also is dependent on the assumed fiber distribution. A simple and general equation is derived in Appendix C using a somewhat different approach. Also, a more complete analysis was given by Rohatgi and coworkers [7] for the incorporation of particles into a melt.

Friction forces due to the viscosity of the liquid metal impede the progress of the metal through the narrow interfiber channels. An additional amount of pressure must thus be applied,

this term being dependent on the rate of infiltration.

Frictional forces have been modelled (i) with the Washburn equation for wetting systems where the metal is driven by capillary forces into the fiber bundle [4], and (ii) with the Blake-Kozeny equation [5,6,8] or another modification of D'Arcy's law [9] using the Hagen-Poiseuille equation [10,8] for a plane infiltration front in systems where the metal is forced into a non wetting fiber bundle. For a circular front, another more complex equation was used [2,3]. Using D'Arcy's law is permissible because the channels between the fibers are fine enough for the metal flow to remain in the laminar regime at normal velocities of infiltration [2,5,6,10].

Comparison with experimentally measured permeabilities was good, provided a correction was made for temperature effects to be discussed below, and the factor in the Blake-Kozeny equation was about 32 [8,10].

The temperature of the fibers and that of the metal also are important parameters for casting metal matrix composites. Some authors have addressed the problem for pure metal matrices [2,8,10,11,12,13]. Both their experimental and modelling work have shown that the most crucial of the two is the fiber temperature. Temperatures below the melting point of the metal are permissible though only insofar as they allow only a limited amount of the metal to solidify. Beyond that point, enough metal solidifies to "choke" the advancing liquid and infiltration cannot proceed. Thus, Nagata and Matsuda [11,12,13] measured a

"critical preheating temperature" below which particles could not be infiltrated by a given pure metal. This temperature was independent in particular of metal superheat. The volume fraction of solid formed was obtained by a simple heat balance equation, and a critical volume fraction of solid formed was deduced. Fukunaga and Goda [2,8,10] postulated that a solid layer initially forms around the fibers. Their calculations assumed instant heat transfer between the fibers and the metal (a reasonable assumption given the dimensions at hand) and the solidification onto the fibers of a metal layer thick enough to bring the fibers to the melting point of the metal through evolution of latent heat. This modifies the effective fiber diameter and volume fraction, and thus the permeability coefficient given by the Blake-Kozeny equation. Correlation with their experiments was, as reported above, good.

Fukunaga and Goda also assumed that infiltration ceases when the infiltration velocity reaches a value low enough for the fibers ahead of the infiltration front to extract enough heat to solidify the metal. This assumption correlated well with their measured infiltration lengths [10]. This also explains the observation [12] that metal superheat has no influence on the infiltration length since the metal at the infiltration front is rapidly brought to its freezing point by the cold fibers.

These models are also in agreement with the following observations:(i) magnesium alloys with a low latent heat of fusion are more difficult to cast into a cold fiber bundle than aluminum alloys [14],and (ii) casting under conditions that

preclude the formation of the solidified layer in Al/SiC composites led to degraded mechanical properties of both the composite and leached fibers [8]. This is thought to be due to a reduced reactivity of the fibers with the solid aluminum layer formed around the fibers under adequate casting conditions. The solid layer thus protects the fibers, which indeed had an improved appearance when examined in the SEM after leaching the matrix from infiltrated specimens.

One last aspect of the process complicates its modelling : the fiber preform can be compressed under high infiltration pressures [5,6,15]. The volume fraction of the fibers can thus vary during the process.

b - Fibers and interfacial reactions.

The amount of interfacial reaction between the fibers and the matrix will depend both on the chemical nature of the species at hand and the processing cycle to which they have been subjected, i.e. temperatures and contact times. Only aluminum/carbon and aluminum/silicon carbide composites are discussed inasmuch as they have some relevance to this thesis.

The fiber utilized in this thesis was manufacturered by AVCO, Specialty Materials Division, Lowell, Massachusetts. It has a complex microstructure, shown schematically in figure 1. It is composed of several layers, described from the fiber center to its surface:

1 - a carbon wire that serves as a substrate for depositing subsequent layers,

2 - a thin layer of pyrolitic graphite,

3 - two layers of silicon carbide that form the bulk of the fiber. These are composed of fine crystals of predominantly beta SiC with close packed {111} planes parallel to the fiber surface. The two layers differ by their grain size [43] and their carbon content [44]. Free carbon has been observed at the grain boundaries of both the inner and outer SiC layers [44].

4 - the SCS coating, itself comprised of several layers is described in detail elsewhere [43,45]. The silicon content gradually drops to zero. A zone of pure carbon is found in the central portion of the coating. This carbon rich layer enhances the mechanical properties of the fiber [46], presumably through healing of surface defects of the fibers [43,46]. As the pure carbon is neither wet nor stable with molten aluminum [47], the silicon content is raised again at the surface to protect the fiber and promote wetting during infiltration.

The reactivity of carbon fibers to molten aluminum has been the subject of several recent studies. It has been shown that above about 500 ^{0}C, carbon and aluminum react to form aluminum carbide Al_4C_3 . This product first forms on the surface of the fiber, then grows into the matrix and somewhat into the fiber as large hexagonal plates [1,34,48-55,77]. When the reaction reaches this phase, the fiber strength is degraded [49-51,56,77], with concommitant loss of strength in the longitudinal direction of

the composite. A slight amount of reaction at the interface was, however, reported to increase the transverse strength of the composite [55]. As Al_4C_3 is hygroscopic, its presence also affects the wet corrosion resistance of the composite [55]. In spite of their inter-reactivity, wetting of carbon by aluminum is poor below 1000 ^{0}C [34,56-58].

The effect of alloying additions to the aluminum matrix has been investigated, both as regards to wettability [56,57] and fiber reactivity [48,49,52,53,192]. A common - but not general [51] - observation is that the presence of some silicon reduces the amount of reaction at the interface and hence fiber degradation [48,53,56].

Aluminum oxide, in addition to TiB_2, was also found on various graphite fiber reinforced aluminum matrix composites fabricated by the Ti-B coating-infiltration technique. Matrices were alloys 201 and 6061. This oxide was also found on fibers coated by ion vapor deposition of Al-4%Mg. The origin of the oxide layer was not determined [75-76]. A similar observation was made on uncoated graphite fiber squeeze cast composites with various aluminum base matrices. Both oxides and excess carbon were found on the matrix side of the interface [192]. This oxide was believed to be present due to oxygen adsorbed on the fiber surface prior to infiltration.

For SiC fibers, similar studies have been conducted and results indicate that SiC is not wet by aluminum or its alloys below 900-1000 ^{0} C [59,60]. Most interfacial studies on SiC fibers

in aluminum have been done with "Nicalon" fibers which are amorphous or fine grained silicon carbide fibers manufactured by Nippon Carbon [45]. The reaction that is expected to take place at the interface from a thermodynamic point of view is [59,61]:

$$3\ SiC + 4\ Al \quad --- \quad Al_4C_3 + 3\ (\ Si\ )$$

provided the activity of silicon is somewhat less than one [61]. This reaction occurs in practice [61-65] and ensuing fiber degradation was reported [62,64] for exposures to molten aluminum above about 700 ^{0}C. The presence of silicon in the matrix was found to decrease the amount of reaction taking place on individually coated fibers [62]. It was also found [63] using differential thermal analysis that on reheating reacted fibers, the reaction proceeded at a much slower rate. This was attributed to both the limited supply of free carbon in the fiber [45] and the presence of SiO_2 at the surface due to oxidation. Also, in contradiction with Kohara [62], these researchers measured a decrease in fiber and composite strength with increasing Si and Mg contents [63]. Some diffusion of Al into the SiC fiber was also claimed to occur on whiskers by Arsenault and Pande [193].

The behavior of the SCS-2 fiber is intermediate between that of SiC and carbon fibers. In the absence of the final silicon enhancement at the outer layer of the fiber, rapid formation of Al_4C_3 was noted [43], similar to that observed with carbon fibers. The silicon rich outer layer inhibits the reaction, and

the fibers can withstand about one hour in contact with molten aluminum at 700 ^{0}C without significant interfacial reaction taking place [45,66]. Longer exposure times or higher temperatures allow the underlying carbon to react and form Al_4C_3 through crack formation in the silicon rich outer layer [45].

c - Matrix Microstructure

Porosity is the first and most critical microstructural feature present in the matrix. Voids have been repeatedly noted and proven to be deleterious to the properties of cast metal matrix composites [23,31-34,36,38]. Assuming the infiltration process is properly performed, the main source of porosity is the shrinkage most metals experience during solidification. A high volume fraction of reinforcement may impede the flow of interdendritic liquid, and will preclude bulk movement of the metal in the semi solid state. Feeding porosity is therefore expected to be a somewhat more difficult problem to solve for metal matrix composites. Few authors have addressed the problem [15].

On the subject of the matrix microstructure proper, published research is relatively scarce. In what follows, observations made in various studies are given by alloy system.

Aluminum-silicon alloys are frequently used because of their good fluidity and compatibility with various fibers. That the

second phase is readily visible on unetched polished micrographs increases as well the number of photographs available in the literature. In all cases, the large eutectic regions in hypoeutectic alloys were found surrounding the fibers [5,20,34,38,53,64]. Silicon plates tend to nucleate on several reinforcements (carbon, SiO_2 and Al_4O_3 particles) for low volume fraction composites [5,7,67,68] and the eutectic is thus somewhat modified. It was also observed in hypereutectic alloys that the primary phase grew from the fibers into the interfiber spaces [7,34].

Aluminum-magnesium alloys, which are more difficult to etch, were reported to display a fine grain size with Saffil alumina fibers [5]. However, it is not clear from the micrographs that the different growth elements are not within the same grain. The second phase was predominantly on the fibers. In other studies, the second phase is again located on the fiber surfaces and along boundaries that run between the fibers [19,20,53].

Aluminum-lithium alloys used with Du Pont's "Fiber FP" alumina fibers displayed " surprisingly small amounts of LiAl intermetallic phases present in the matrix " [24]. This was attributed to the interfacial reaction. The interpretation is reasonable with 60 vol.% fibers since the interfacial reaction layer was shown to be about 0.5 to 1 micron thick, and consists of $LiAl_5O_8$ [69].

Cobalt base superalloys cited in reference [25] show small dendrites barely perturbed by the comparatively large fibers.

Commercial aluminum alloys 6061, 220 and Al-13%Si displayed

very large grain sizes and coarse continuous grain boundary networks of brittle second phase [33]. In reference [31] the eutectic regions are seen to coincide with the fiber location. However, these fibers were coated and the alloy composition is therefore complex. Similar observations were made by Harrigan [70] who showed that the solute content in 6061/carbon fiber composites increased close to the fibers.

Copper-8 wt% tin polluted by a TiB_2 coating on carbon fibers displayed unperturbed dendrites in larger interfiber regions of infiltrated tows [31].

Titanium-copper alloys were infiltrated into carbon fiber bundles [39]. A heavy reaction layer resulted, but the matrix clearly displays the eutectoid regions in the center of interfiber spaces. This corresponded during solidification to the primary titanium-rich phase which is clearly seen to have avoided the copper-rejecting interface during growth.

Aluminum-copper alloy composites have been shown to have a similar structure, with the primary phase in the interfiber regions and the eutectic precipitated onto the fibers or between individual dendrite arms [5,14,20,38,53,66,192]. Appropriate etching and microprobe scans displayed equiconcentrates parallel to the fiber surfaces with the concentration minimum in the center of the interfiber regions. Fukunaga et al. [14] also observed that increasing the pressure during squeeze casting reduced the amount of eutectic present. They explained the structures they observed with a solidification mechanism whereby the alpha phase first nucleates and grows on the cold fibers, the

copper rich liquid thus being rejected in the center of interfiber regions. To explain the above mentioned microstructural features, they postulate that a film of liquid seeps between the fibers and the primary phase due to shrinkage of the latter toward the end of solidification. They interpret the role of pressure with rapid solidification effects due to enhanced contact of the metal on the cold fibers. As copper-rich liquid may have been exuded out of the reinforced regions during solidification under high pressures, their interpretation is speculative at best.

Magnesium-aluminum alloys with SiC fibers display similar features: the eutectic is at the fiber-matrix interface and along "bridges" between the fibers [14].

Commercial magnesium ZE41 has been used to infiltrate "Fiber FP" alumina fibers. Microstructures are given in reference [71]. The matrix displays large grains but, as the alloy was not replenished in zirconium before infiltrating the fibers, the cause for that observation is not clear.

Al-9Si-4Cu was used to infiltrate carbon fiber bundles. The fibers are surrounded by Al_2Cu as in Al-Cu alloys [34]. This was the last to solidify [72], contrary to the text of reference [34].

Aluminum-nickel alloys formed by assimilation into the matrix of a nickel coating was seen to display primary Al_3Ni dendrites [7] or platelets [34] growing from the graphite reinforcements.

In conclusion, three types of microstructures are encountered:

1- a fine network of dendrites when the latter are much smaller than the fibers,

2- dendrites nucleating on the fibers and growing into the interfiber spaces (hypereutectic Al-Si alloys, Al_3Ni), or

3- a primary phase that avoided the fibers during growth. Any second phase is found on the fibers or between primary arms. This represents the majority of cases.

After it is cast, the composite must cool down to room temperature. As the thermal expansion coefficient of the metal is usually higher than that of the fiber, tensile stresses can build up in the matrix. This may influence the microstructure of the matrix. In particular, the dislocation density was found to be increased [73]. This increase in defect density was shown to be responsible for an increase in the ageing response of 6061 alloys with B_4C or SiC fibers [74].

The mechanical properties of the matrix have a considerable influence on those of the composite, especially in the off-axis direction(s) . The need for good control of the matrix structure is therefore obvious. The nature and properties of the interface are also of paramount importance in determining the quality of the composite. Both depend to a large extent on the matrix alloy and its processing. Studies concerning the fabrication, the evaluation, the interfaces and the mechanical properties of metal matrix composites abound. Few, however, address the solidification of the alloy and even fewer do so in depth. Of the

many problems in this field that need to be solved, this thesis tries to address in a more systematic and quantitative way the problem of the solidification of a metal in a tight fiber bundle.

The next section of this literature survey therefore reviews broadly the solidification of Al-4.5 wt% Cu.

II - Solidification of Al-4.5wt%Cu .

a - General.

The aluminum rich end of the Al-Cu phase diagram displays a eutectic between the aluminum-rich alpha phase and the intermetallic theta phase, Al_2Cu. Shown in figure 2 is the phase diagram as it appears in most current references [78,79].

Copper is one of the most important alloying elements of aluminum and forms the basis of the 200 series casting alloys and 2000 series wrought alloys, using the current Aluminum Association terminology [78,80]. These alloys usually display good mechanical properties and are heat-treatable. They often serve in fact as a textbook example illustrating the principles and mechanisms of precipitation hardening (reference [80] has a copiously illustrated section on the matter).

After an ingot or a part is cast, the microstructure is usually dendritic and displays both concentration gradients (coring) and some eutectic. The dendritic structure of Al-4.5wt%Cu castings has been the subject of a considerable effort in the past, notably with the work of T.Bower [81,82] at MIT. His work has shown that the dendrite arms grow along the ⟨100⟩ direction as is usual with cubic crystals and coalesce at higher volume fractions solid to form plates. A terminology was defined, calling primary arms those growing first from which secondary arms form. The same logic is used to define tertiary arms, etc, as well as primary, secondary, etc, plates in the

later stages of solidification. This terminology, now usual, is adopted here.

In the final stages of solidification, the eutectic is formed and is found between the dendrite plates and grains of the alloy. As the alloy shrinks during solidification and in particular during formation of the eutectic, voids are often found in the same areas. The scale of the dendritic structure is defined by the dendrite arm spacing which, in itself, is determined by the cooling rate as shall be seen later. Because diffusion is sluggish in the solid phase, the central core of each dendrite arm remains solute-poor and solidification does not follow thermodynamic equilibrium conditions. As the eutectic phase and the outer portions of the dendrite arms are approached, the copper content increases. These concentration gradients and the amount of off-equilibrium eutectic phase determine the quantitative amount of microsegregation, which will be described later in more detail (Figure 8 illustrates these observations).

Two types of dendritic structures are encountered in alloys of this type:

1 - Equiaxed dendrites. These grow concurrently in all three directions. They can initiate from an isolated nucleation event or from a small piece of alpha phase from another region of the casting. These structures form where the metal solidifies in the absence of any significant temperature gradients. In order to remove the latent heat liberated at the interface, the liquid must be at a temperature slightly below the equilibrium interface

temperature. Thus, equiaxed dendrites grow into an undercooled liquid and both solute and enthalpy diffusion into the liquid must be taken into account when modelling the process [16,83-85].

2 - Columnar dendrites. These dendrites grow in one direction, determined by the existence of a temperature gradient. Primary arms progress into the liquid region from the cold region where they first formed. Since they grow fastest in the <100> direction, crowding out of the slowest dendrites ensures that all primary arms are oriented more or less parallel to the temperature gradient, G. Heat is transported backwards through the solid phase. Therefore, only solute is rejected into the liquid.

An ingot can display up to three zones from surface to center [16, 83-85] :

1 - the chill zone, formed of equiaxed dendrites disposed in a thin layer along the surface of the casting,

2 - the columnar zone,

3 - the equiaxed zone.

If an ingot is solidified slowly under conditions aproaching Newtonian cooling, it will be totally equiaxed. A heavily chilled ingot, on the other hand, may be entirely columnar, with the exception of the thin chill zone. Alloys poured with very little superheat display a large fine grained equiaxed region close to the chill, independent of any fluid flow [86]. The addition of an active heterogeneous nucleation catalyst will yield a fine grained equiaxed structure [83,85]. The formation and extent of the equiaxed zone, however, is not determined solely by the

ability of the metal to nucleate ahead of any growing dendrites. It has been proven that fluid flow in the solidifying casting plays an important role in determining the existence and extent of equiaxed zones. This was convincingly shown for the chill zone [87,88]. Fluctuations in temperature induced by turbulent fluid flow have been shown to melt off dendrite arms [89,90]. These, and nuclei formed at the chill wall, can be transported by convection currents in the liquid to grow elsewhere and form an equiaxed zone [83,85,86,91-93,189,190]. Convection induced heat transfer can also aid in achieving the low thermal gradients necessary for equiaxed dendrite formation. A last process, the showering with dendrites formed at the free top surface of an ingot requires movement of crystallites through the liquid phase [86,94]. The introduction of mechanical barriers or of a magnetic field hindering these transport phenomena within the liquid phase results in a significant enhancement of columnar zone formation [86,91,92,94,190].

It is thus apparent that, in the presence of a high volume fraction of reinforcement, one of several cases may be encountered :

1 - The fiber surface acts as a heterogeneous nucleation site for the solidifying metal. In this case, fine grained equiaxed structures are to be expected.

2 - The fibers do not act as heterogeneous nucleation sites for the solid. No nucleation enhancement occurs. As the fibers preclude most any fluid flow, growth of the solid should be columnar whenever a thermal gradient is present. Otherwise, an

equiaxed structure with a larger grain size is to be expected since convection induced grain multiplication should be non existant for all practical purposes. However, if the fibers are initially at a low temperature, intense nucleation may occur in the metal and result in unique structures.

Columnar dendrites are investigated in this work mainly because of the great degree of precision attainable in controlling the solidification parameters with the steady state solidification technique. Usually, as an ingot solidifies, the chilling effect decays as the solidification front progresses away from the chill. The thermal gradient becomes shallower and, as the mold heats up, the growth rate decreases. In steady state solidification, both the growth rate R and the temperature gradient G are kept constant as the solidification front progresses into the sample. This is achieved in practice by pulling a rod of metal contained in a long crucible at a constant rate (R) through a fixed temperature gradient (G). The latter is obtained by bringing a heat source and a quenching tank appropriately close together. The resulting apparatus is termed a Bridgman furnace and has been used by now in a large number of investigations. In-situ composites, plane front and cellular solidification as well as dendrite growth have been studied in this fashion. Modelling is facilitated because the process is steady-state, evacuation of heat is through the solid, and the temperature profile is known. Also, by suddenly varying the growth rate, phenomena such as the break-down of a planar front

or readjustments in the primary dendrite arm spacing can be investigated. By rapidly pulling the whole sample through the quenching tank, growing structures can be quenched-in and studied at all stages of the solidification process. Technical aspects of the method are reviewed in more detail in the "EXPERIMENTAL" section.

In what follows, G and R are treated as two independent parameters, which define the solidification conditions. Their product GxR is the cooling rate, of more practical use in engineering work.

b - Solidification at the dendrite tip .

For any thermal gradient G, there is a range of velocities where a plane front is unstable and cells or dendrites form. Outside this range, plane front solidification obtains.

That at low velocities a plane front is stable, and breaks down at a certain value of G/R was first explained by the constitutional supercooling criterion [83,84,95,96]. The reason invoked is that above a certain front velocity, rejection of solute is impossible without the creation of a zone of undercooled liquid metal solution. The criterion is simple and its agreement with experimental observations is excellent [83,84]. A more complete treatment of plane front stability was initiated by Mullins and Sekerka's morphological stability analysis [83,84,97-102]. Here, the stabilizing influence of surface tension and a more complete analysis of heat transfer are

included. The result of both analyses are given in figure 3 (from references [103-104]) for Al-4.5 wt%Cu. Both very high and very low growth velocities lead to a stable plane front. Several more complete and complex analyses have evolved since then. The most recent study the stablility of non planar interfaces with the intent of modelling cellular fronts [101,105].

Inside the region of plane front instability, either of two growth morphologies may be encountered. At low growth rates, regular cells are obtained. As the velocity increases, these degenerate progressively into dendrites as (i) side branches appear and (ii) the growth direction starts to deviate from a direction parallel to the thermal gradient and follow the <100> directions of the growing crystal. Modelling the growth of cells or dendrites is a highly complex task as this is a free boundary problem where both the shape and the diffusion fields must be derived. Nearly all solutions to the problem have concentrated on the tip region of cells or "needle" dendrites so as to render the problem free of the time dependent aspect of secondary dendrite arm formation.

From the diffusion point of view, the problem of a growing dendrite tip giving off solute in a fixed temperature gradient is similar to that of the tip of a pure substance growing into a supercooled melt. The equations are similar, with the difference that the diffusion coefficient is assumed to be zero in the solid phase for solute transport. Principal models are:

1 - the hemispherical cap [84,95,106-108], assumed to be an isoconcentrate growing at steady state.

2 - the paraboloidal isoconcentrate with a circular (Ivantsov solution) [84,109,131,195] or an elliptical cross-section [110]. This is a shape preserving solution but it contains a contradiction in that at small tip radii, the undercooling due to surface tension renders the isoconcentrate assumption invalid [111,112].

3 - the "corrected Ivantsov" solution, where the temperature/concentration of the Ivantsov paraboloid is adjusted to that of its tip [101,102,113,114].

4 - the Temkin approach, solving the heat flux condition at the tip of a non isothermal paraboloid of revolution [112,115-119].

5 - the Nash-Glicksman approach, truly a free boundary approach deriving the shape of the needle (but with the maximum growth rate assumption built-in) [120,205].

6 - numerical techniques, free-boundary approaches as well [121-123].

A solution to the diffusion problem does not unequivocally describe the growth conditions of a dendrite tip. Another criterion is needed to select the operating point of a dendrite needle. To that effect, such assumptions as a maximum growth rate for a given undercooling [107,112,115,117,120] and minimum entropy production [119] have been used. It has recently been shown that stability considerations at the tip must be taken into account and provide a criterion for selection of the operating point [84,101,108,122,124-132,134,195]. This criterion appropriately describes data in pure [127,129,130] and binary

organic model systems [133-135]. Further, the tip radius was shown to be scaled by a constant factor to other dimensional characteristics of the dendrite. In particular, the initial dendrite arm spacing is about twice the tip radius [125,129,130,132-137].

For the case at hand, namely the constrained growth of Al-4.5wt%Cu dendrites, recent publications make use of the marginal stability criterion [84,108,128,131,132,195]. A plot of the radius of curvature from the more complete Trivedi analysis [128,134] is given in figure 4 using system parameters as given in Appendix B. The picture emerging at present from theoretical and experimental work is as follows :

1 - within experimental error, the composition and undercooling at the dendrite tips are quite accurately predicted by theory [82,83,107,132,138],

2 - the cellular-dendritic transition is well predicted by theory [132],

3 - if the measurements of Miyata et al. are correct, theory is less accurate in predicting the dendrite tip radius [132]. This discrepancy may, however, be due to an improper choice of the system parameters (see Appendix B).

It should be stressed that these models treat the problem of an isolated dendrite tip. In directional solidification, primary dendrite arms, each capped by a dendrite tip, grow close to one another. The boundary conditions would thus be more accurately described by a non flux condition at $r = \lambda_1/2$, λ_1 being the primary dendrite arm spacing. To date, only computer models have

tackled the problem [122,123].

For the primary dendrite arm spacing, no clear description has evolved so far. In reference [139], an empirical expression is given, together with qualitative arguments, that agrees with data published at the time. Other authors [84,108,140,141] have assumed the primary dendrite arm spacing was dictated by conditions at the tip, using various assumptions as to the overall shape of the cell or dendrite. From studies of the breakdown of a planar interface in an organic alloy and a modification of Hunt's analysis, Trivedi and coworkers [133,134,136] gave a relationship [140] that fits their data in that alloy.

In the present thesis, dendrites are grown unidirectionally inside narrow interfiber "tubes". This is equivalent to artificially reducing the primary dendrite arm spacing. The question addressed here is to what extent does the presence of these fibers affect the tip radius, undercooling and composition.

As seen on the plot in figure 4, at a growth rate R = 0.0001 m/s, an isolated dendrite would adopt a tip radius around ten microns. This is the distance from the center of the interstice to the fiber-matrix interface in the narrow triangular fiber interstices investigated in this work. Some interaction should thus be expected between the fibers and the dendrite tips in a metal matrix composite. One article is of special relevance to this problem.

In reference [123] cited above, McCartney and Hunt calculated

the tip curvature, undercooling and composition for cells in an Al-Si-Mg alloy. A computer model was used, and the gradient, the velocity and the primary dendrite arm spacing were treated as parameters. Essentially, the problem they treated is that of cellular growth inside a tube of fixed diameter. The authors found that :

1 - There is a maximum in the arm diameter beyond which no stable solution exists. As the velocity is increased, no stable cells can exist since this maximum diameter decreases to zero.

2 - As the diameter is decreased, the tip composition and undercooling decrease to a minimum and then increase again, both varying within a very narrow range.

3 - As the diameter is decreased, the tip radius decreases significantly.

Both constants and parameters were close to the values relevant for the alloy and experiments in this thesis. It is therefore appropriate to expect that :

1 - The tip undercooling and composition should hardly be affected by the fibers.

2 - The tip radius should be reduced.

3 - The fibers should tend to stabilize cellular structures within the dendritic/cellular transition region.

4 - At high growth rates, no matter how narrow the interfiber spaces, cellular structures should be unstable and dendrites should be observed.

The only experimental confirmation of these calculations was found in the work of Somboonsuk et al. who noted that the

composition and undercooling at the tip of succinonitrile-acetone dendrites were very slightly raised by narrowing the gap between the two glass slides within which they were constrained to grow [133]. Both radii of curvature at the tip were not measured, however. The reported variations in tip undercooling and composition are consistent with McCartney and Hunt's results in that they are quite small.

c - Dendrite coarsening

The intricate geometry of dendrites generated by instabilities in the initial phases of their growth is thermodynamically unstable due to the high amount of excess liquid-solid surface energy present. There is therefore a driving force for the liquid/solid surface area to decrease and hence for the scale of the microstructure to increase during solidification. The kinetics of the phenomenon are dictated by the rate of solute diffusion in the liquid phase. The process is therefore relatively rapid. The resulting increase on the scale of the microstructure is termed microstructural coarsening in what follows.

In dendritic microstructures, coarsening results in a secondary dendrite arm spacing that increases with time. Flemings and coworkers [83,142] thus showed in a synthesis of their own and earlier experiments, that over about seven orders of magnitude in the total solidification time t_f the final secondary dendrite arm spacing λ_{2_f} in both equiaxed and columnar dendrites is

described by

$$\lambda_{2_f} = 7.5,10^{-6} \; t_f^{0.39} \qquad \text{(S.I. units)}$$

In a subsequent publication, Kattamis, Flemings and coworkers [83,143,144] performed experiments and calculations to show that in metallic alloys dendrite arm coarsening processes are driven by surface tension and that the kinetics of coarsening are fairly independent of the detailed geometry at hand. Several detailed mechanisms can account for the phenomenon in a quantitative manner. These mechanisms involve the melting back of smaller dendrite arms with concomitant growth of larger and thus more stable dendrite arms. These mechanisms are similar to the Ostwald ripening of precipitates. The word ripening is thus used herein to name this particular class of coarsening mechanisms.

Following the initial work of Kattamis et al., authors [145,146] have discussed the mechanisms first given by Kattamis et al. An interesting observation was made in several articles [147-150] on both organic systems and Al-Cu alloys. It was noted that at higher volume fractions solid, a coarsening mechanism different from ripening also operates. Here, the liquid space between dendrite arms fills in or dendrite arms "coalesce" into what can be counted as one arm. Young and Kirkwood derived an expression for the critical time of this mechanism [149]. This class of microstructural coarsening mechanisms is termed coalescence in what follows. Both ripening and coalescence processes are driven by a reduction in surface energy through solute diffusion in the liquid. The essential difference is that

in coalescence, at higher volume fractions solid, negative radii of curvature are involved in the process.

For coarsening by ripening, the parallel with Ostwald ripening comes to mind and this prompted the work of Voorhees and Glicksman [151-153] who extended the approach of the classical Lifschitz-Schlyozov-Wagner (LSW) analysis [154-157] to solid spherical particle volume fractions up to 50 % . Their results indicated a strong influence of the volume fraction solid on the ripening kinetics. However, the basic results of the LSW analysis persist i.e. (i) the curvature distribution curve reaches a constant shape, and (ii) the average particle size increases linearly with $t^{1/3}$:

$$\bar{R}^3 - \bar{R}_0^3 = K\,t \qquad (1)$$

where $\bar{R}_0$ = average radius at t=0

$\bar{R}$ = average radius at t.

Their calculations correlate well with thermal measurements on adiabatic succinonitrile dendrites [153] and the ripening of liquid phase sintered structures [151].

Coarsening by coalescence has been studied both experimentally [206-208] and theoretically [209-212] for liquid phase sintered structures. It is shown that the kinetics of coarsening by coalescence are similar to those of coarsening by ripening and the basic characteristics of the LSW analysis persist. This is reasonable in view of the many similarities between the two processes.

Most theoretical work on dendrite coarsening treats the case of a liquid-solid mixture held at a constant temperature i.e isothermal coarsening. In a solidifying dendrite network, the liquid composition and the volume fraction solid increase with time. The only serious attempt at solving this complicated problem that was found in the literature is by Whistler and Kattamis for simplified dendrite arms [158] and for spherical grains [194]. They successfully correlated their calculations with experimental measurements on Al-4.5wt%Cu [158] and Mg-6%Zn-Zr [194]. Two closely related attempts [84,217] have been made recently at deriving the $t^{1/3}$ law and its constant using ripening models of the type originally proposed by Kattamis and Flemings [143]. The change in the liquid concentration was incorporated to model coarsening during solidification. Both models are based on unjustified geometrical assumptions. Agreement with experiment is strongly dependent on the value attributed to the (surface energy related) Gibbs Thomson coefficient. It should also be noted that, contrary to ripening, coalescence can be aided by the solidification process since matter can preferentially deposit so as to fill in the trough separating dendrite arms.

A different dendrite arm remelting phenomenon of interest in unidirectional solidification under steep gradients is that of temperature gradient zone melting (TGZM), the migration of secondary arms up the thermal gradient due to differences in temperature across the liquid pools between arms [159,160].

Experimental work on Aluminum-copper alloys relating to the case of steady state directional solidification is quite abundant [148-150,161-163,196]. A brief synthesis of conclusions from these studies is :

1 - In the dendritic regime, the secondary dendrite arm spacing is given by approximately the same law as a function of coarsening time for all gradients and growth rates until coarsening by coalescence becomes predominant. The exponent n in

$$\lambda_2 = B\ t^n \qquad (2)$$

is somewhat smaller than 0.39. According to Young and Kirkwood [149] who performed the most extensive investigation,

$$\lambda_2 = 16.1 \times 10^{-6}\ t^{0.31} \qquad \text{in meters}$$

with t in seconds.

2 - Toward the end of solidification, coalescence predominates.

3 - In the cellular-dendritic region, the secondary dendrite arm spacing no longer follows the simple relationship found in the dendritic regime. Possible reasons include (i) an increased importance of coalescence [148], (ii) a large initial λ_{2_0}, as can be seen from figure 4 since $\lambda_{2_0} = 2r_{tip}$. This means that in equation (1) , $\bar{R}_0$ is no longer negligible and equation (2) must be modified accordingly :

$$\lambda_2^3 = K\ t + \lambda_{2_0}^3$$

Measuring secondary dendrite arm spacings is not trivial, and results vary with methods. In particular, when coalescence

becomes important, the degree of arbitrariness becomes considerable (so much so that Young and Kirkwood [149] simply decided not to make any measurements in that area of their samples). This probably explains most of the scatter in the measurements reported in the literature.

The articles cited above also report measurements of the primary arm spacing in cells and dendrites. Here, G and R seem to play independent roles and can not be lumped into a single parameter GxR. That the dependence on solidification parameters should be different makes good sense in view of the fact that primary arms do not coarsen (exception made for some coalescence in cellular structures [148]).

d - Microsegregation.

The diffusion coefficient in the solid phase is low enough to allow for significant deviations from thermodynamic equilibrium (lever rule) during dendritic solidification. So much so that the opposite extreme assumption of no solid state diffusion describes quite well the majority of solidification microstructures. Solidification then proceeds according to the "Scheil equation" [83]:

$$C_L = C_0 f_L^{k-1}$$

This equation is independent of all solidification variables, phase diagram excepted.

The amount of microsegregation is most often measured with either of two variables : (i) the volume or weight fraction of eutectic formed or (ii) the minimum solute concentration present in the primary phase. For Al-4.5 wt%Cu, equilibrium solidification yields no eutectic and a minimum of 4.5 wt%Cu. The Scheil equation gives 0.0903 weight fraction eutectic and 0.77 wt%Cu respectively.

Two processes allow for a reduction in the amount of microsegregation. First and most obviously, the solid state diffusion coefficient is not zero and some back-diffusion does occur. Second, solute poor regions remelt during ripening and redeposit elsewhere as a solid richer in copper.

Diffusion in the solid phase allows the incorporation of additional solute at the solidification front and reduces concentration gradients within the solid phase during and after solidification. The solute distribution profiles are thus necessarily geometry and cooling rate dependent. The first article to seriously address this problem was the work of Brody and Flemings [83,164,168]. An approximate but simple analytical model was given as well as a more exact finite difference computer model.

The analytical model is strictly valid only for systems that experience a limited amount of diffusion since it otherwise overestimates the amount of solute incorporated at the interface. Based solely on mathematical manipulation, Clyne and Fisher later proposed a modified version of this equation to obtain the

equilibrium lever rule at high values of the diffusion coefficient [165]. Solari and Biloni also modified the Brody-Flemings analytical model to account for undercooling at the tip using Burden and Hunt's model [166]. At low growth rates, their expression is a combination of both Brody-Flemings models for tip undercooling and solid state diffusion. (At high growth rates their expression is invalid since the assumed solute gradient is in error [107,167]).

To obtain the solute distribution within the solid, and in particular the minimum solute concentration, numerical methods are necessary. The Brody-Flemings model solved the problem for cases where only the cooling rate is known by assuming a linear or parabolic thickening law for the dendrite arms. Other authors later published slightly perfected versions of this model [169].

The dendrite arm thickening law need not be assumed if the relationship between time and temperature (and hence concentration in the liquid) is known. The problem is then fully specified and can be solved rigorously. Being a solidification problem, however, it is not simple and one resorts again to computer models in which both the solid front and the solute profile are calculated. Kirkwood and Evans solved this problem for the case of an alloy cooling at a constant rate of heat removal [170]. It was further assumed that the solid diffusion coefficient was constant. They showed that for this cooling situation (i) Brody and Flemings' model came close to theirs if a parabolic growth rate was assumed and (ii) that the main reason for the discrepancy between Brody et al.'s calculated and

measured results [82] was too low a diffusion coefficient. This model has been perfected since to take the temperature dependence of the diffusion coefficient into account [171].

The influence of coarsening on microsegregation is less well understood. A first attempt was made by Basaran in which solute was unfortunately not conserved [172]. The work of Ogilvy and Kirkwood [171] adequately addresses the problem in a modification of their numerical diffusion model allowing for an expanding planar dendrite arm. Their model indicates a strong effect of coarsening on microsegregation.

Another remelting mechanism TGZM, was also shown to have an effect on microsegregation since it was able to generate assymetric concentration profiles in secondary dendrite arms of directionally solidified Fe-Cr-C alloys [173]. Since the secondary arms may remelt completely during the solidification process due to this mechanism, the effect may be drastic under some circumstances (steep gradients and low growth rates) [159,160].

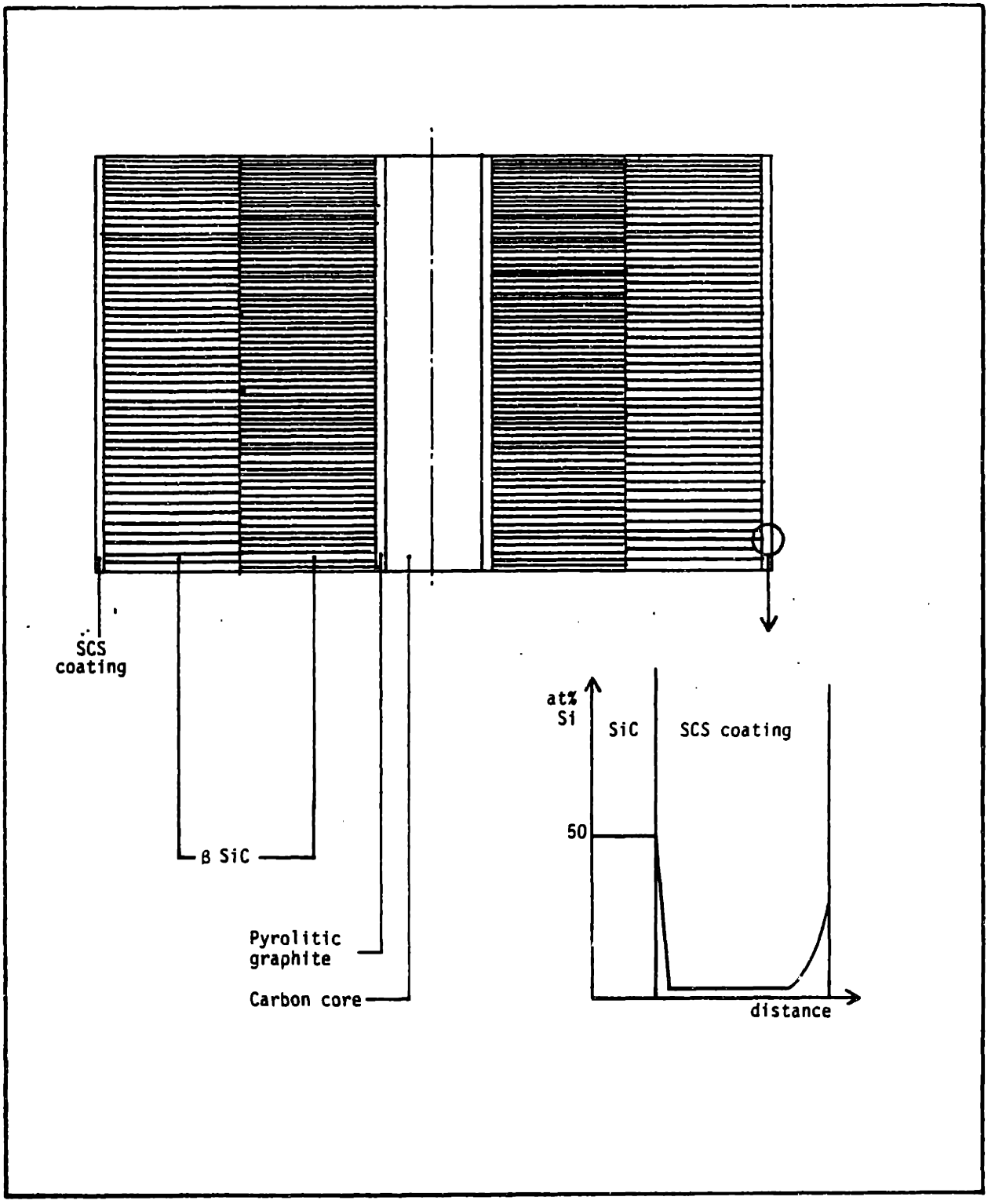

Figure 1. Schematic section of the SCS-2 silicon carbide fiber. The fiber diameter is 140 microns.

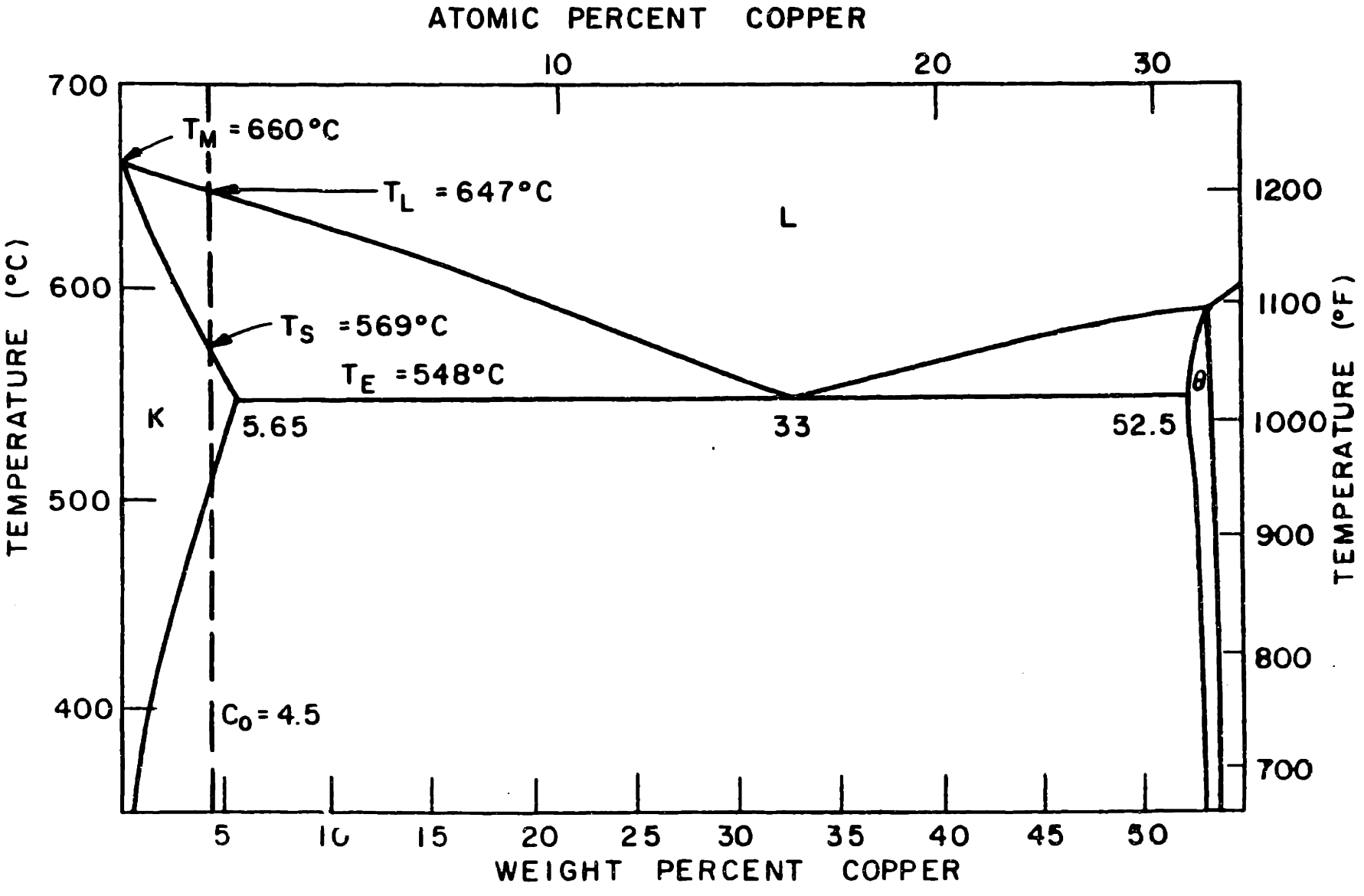

Figure 2. Phase diagram of the aluminum-copper system, showing the alloy used in this thesis, 4.5 per cent copper (A.S.M. Metals Handbook, 1948 edition).

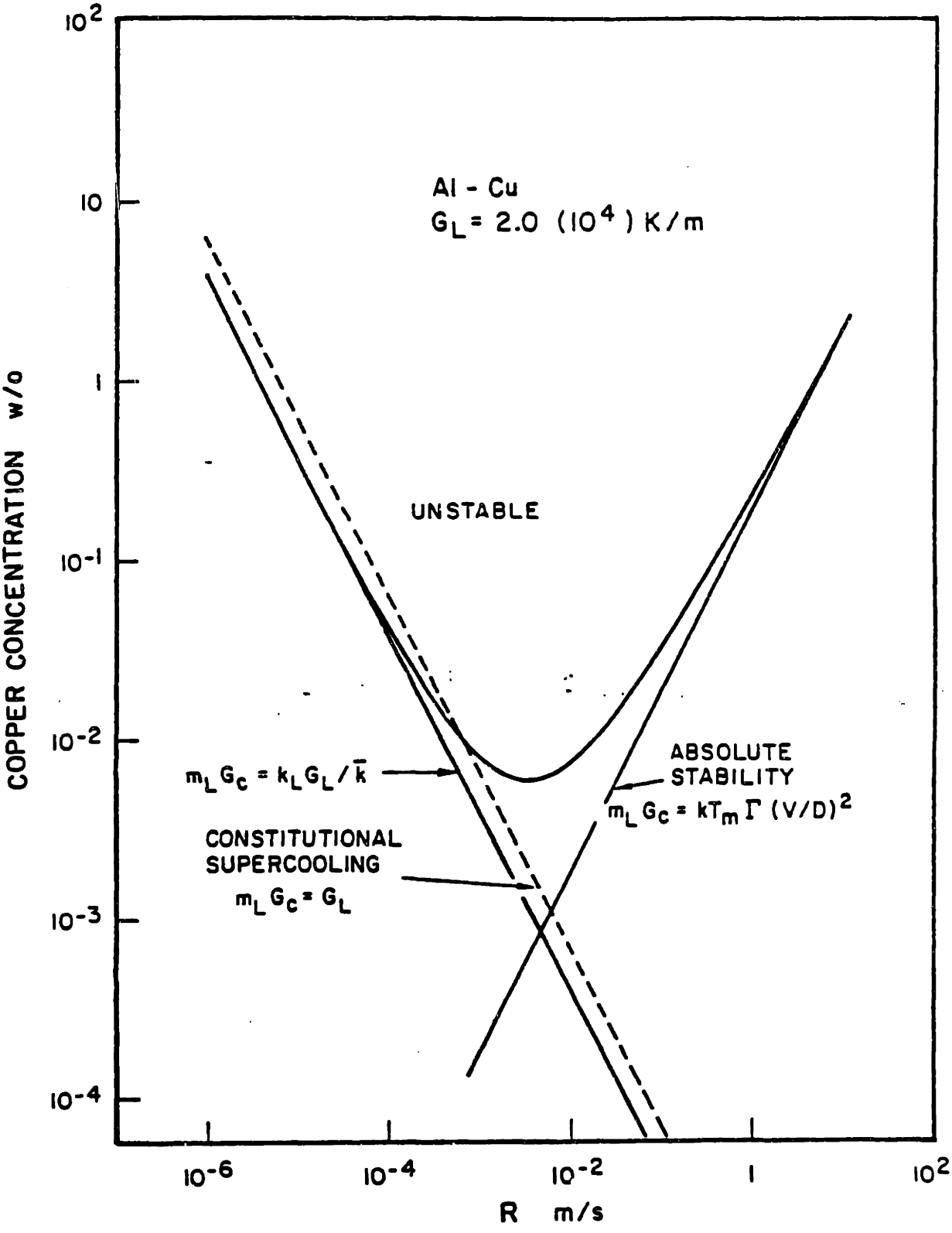

Figure 3. The critical concentration of copper above which interface instability occurs as a function of interface velocity. The curve is based on morphological stability theory while the lines correspond to constitutional supercooling and absolute stability.

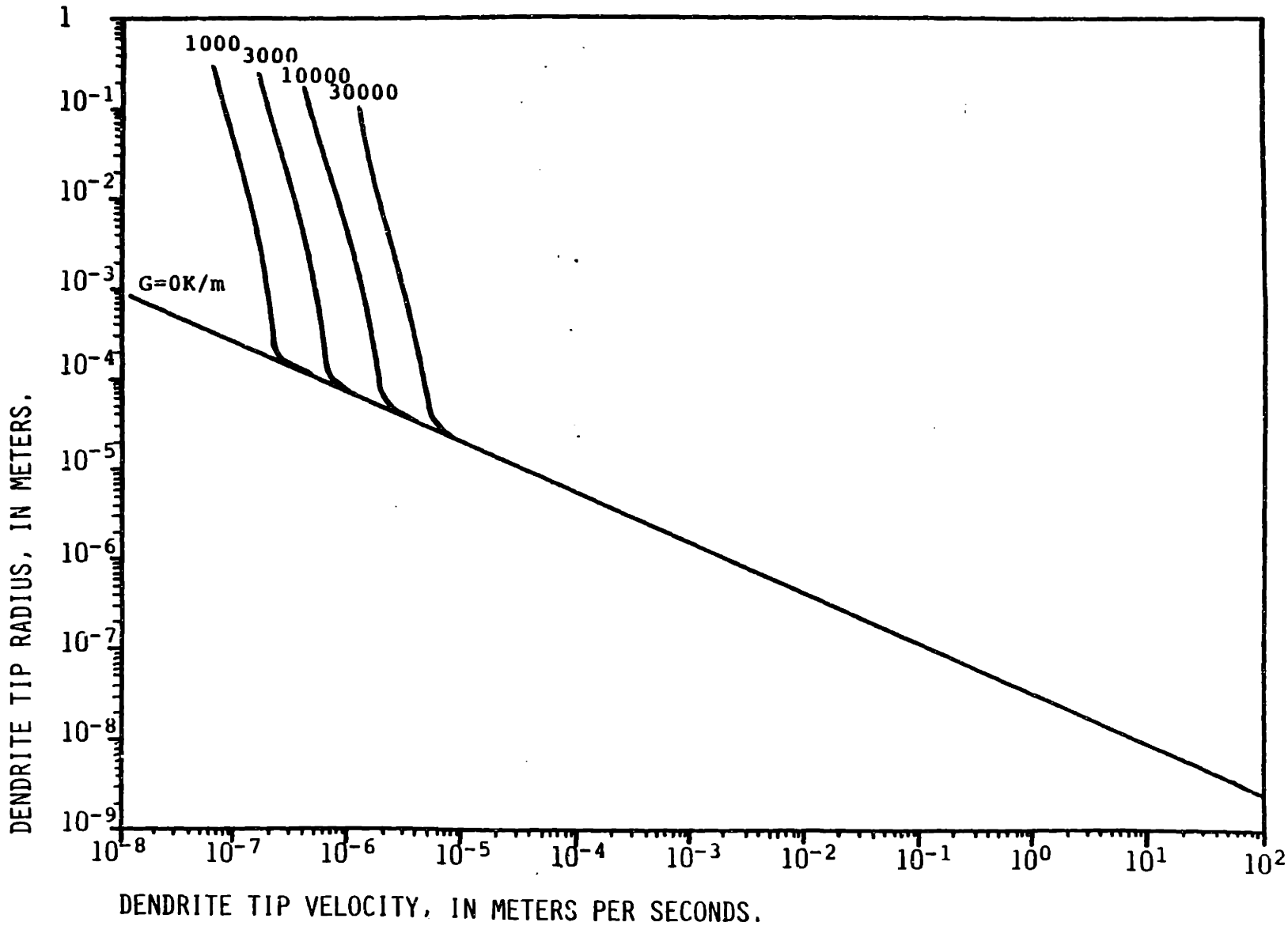

Figure 4. Dendrite tip radius as a function of growth rate and temperature gradient G, from Trivedi's model [128,134] using data in Appendix B.

EXPERIMENTAL PROCEDURES

I - Sample preparation.

The fibers, provided by AVCO specialty Materials, Lowell, Massachusetts, were described earlier in the literature survey. Individual fibers were cut from a monofilament wound on a spool.

The Al-4.5 wt% Cu alloy was purchased from Reynolds Aluminum, Metallurgy Laboratory, Richmond, Virginia. The metallurgical practice for alloying was reported as follows :

- 400 lbs of super pure aluminum melted in 100 KW induction unit,
- base metal chemical button taken,
- alloy addition added in the form of hardner,
- melt fluxed with pure chlorine,
- chemical analysis button taken,
- metal continuously cast into a 3"x8" mold,
- ingot stress relieved overnight at 550 F.

The analysis of the alloy was reported as follows:

Si	Fe	Cu	Mn	Mg	Cr	Ni	Zn	Ti
.010	.014	4.61	.002	.002	.002	.003	.006	.002

To avoid any fluctuations in composition due to macrosegregation, transverse slices remote from the ends of the ingot were used.

The fibers and the metal were combined by the squeeze-casting technique with a few modifications for the purposes of this investigation.

A mold of graphite was machined with a drill press so as to obtain the samples in their final form. Gates and vents were provided, as drawn in figure 5. Fibers were cut and weighed, so as to obtain a volume percent of fibers at 40 % in the samples. They were then wrapped at their ends into a tightly packed bundle with enough fiberglass tape to center them in the mold. In this manner, samples with a composite core containing around 80 vol.% fibers surrounded with the unreinforced metal were obtained. These fiber bundles were inserted in the graphite mold which was 3 3/8 inches in diameter and 1/2 inches thick. One mold could produce about seven samples.

The squeeze casting process is depicted in figure 6. The apparatus consists in a piston-cylinder activated by a hydraulic press. The interior of the cylinder was lined with a fibrous alumina insulation material, and the graphite mold was positioned at its bottom. The piston was centered above the cylinder with a steel ring. A port was machined into that ring to pour the molten metal and insert heaters etc. prior to infiltration.

The insulation material lining the cylinder allowed to preheat in-situ the fibers and the mold. To this end, a heating element made from Kanthal wire, and argon inlet of graphite and a chromel-alumel thermocouple were inserted through the port. Adding a layer of insulation material on the top of the cylinder allowed to preheat the fibers up to about 600 ^{o}C under an Argon

flux.

Once the graphite mold temperature had stabilized around 550-600 °C, the metal was melted following standard foundry practice in a gas furnace. A graphite crucible was used and the metal was stirred with at least thirty strokes. It was degassed with nitrogen for at least two minutes, and then skimmed and poured at about 750 - 800 °C (high superheat) right after removing the heater etc. from the cylinder.

The piston was lowered about ten seconds after pouring. The infiltration pressure, about 1000 psi, was maintained for thirty seconds. Everything within the cylinder was infiltrated after the operation - including voids in the graphite mold proper. Consequently, the graphite mold had to be extricated from the resulting slug, and gently crushed to remove the seven infiltrated composite specimens. After filing their outer surface clean, removing gates and vents and cutting off the fiberglass containing ends, the samples were ready for remelting and controlled solidification.

II - Steady State Solidification.

The resulting composite samples were inserted into tubular crucibles designed for the Bridgman furnace depicted in figure 7. A composite consisting of a 3 mm thermocouple alumina tube in Al-4.5 wt% Cu was placed immediately below the sample. This provided both a means to monitor the temperature and a prolongation of about five centimeters to the sample having the

same overall longitudinal thermal conductivity. End-effects in the thermal gradient at the lower end of the sample were thus minimized. A small slug of the alloy was placed over the sample, followed by a graphite plunger and a steel weight. This forced molten metal down to fill any gaps around or beneath the sample.

The quench tank of the furnace was a molten gallium bath cooled with water circulating in an immersed coil. The water was driven by a mechanical pump from a large tank, itself kept at temperature with an immersed coil of water circulating from the warm tap of a nearby sink. In this manner, the water tank could be kept at a steady temperature slightly above 29 °C, the melting point of gallium. The inertia in the system prevented any fluctuations in the cooling conditions over the time period of a solidification experiment. Small local band heaters were also used to prevent any freezing of the gallium at the bottom of the tank.

The hot region of the apparatus was provided by a resistance furnace around a quartz tube containing an argon atmosphere. The gap between the crucible and the quartz tube was filled with an appropriate steel cylinder to prevent any convection induced temperature fluctuations. The steel cylinder was separated from the quench tank by alumina rings and in some experiments a small booster heater (depicted in figure 7). A DC motor with a controller, a gearbox and a threaded rod allowed to move the sample at a steady and controlled rate down to about 20 microns per second.

Once the measurement of a control thermocouple inside the

quartz tube had stabilized, the sample was raised at a rate higher than the chosen growth rate. When the thermocouple below the sample had reached a temperature above the liquidus of the alloy (650°C), the motor was stopped, and the temperature allowed to stabilize for five minutes. The sample was then retracted at a chosen rate, and after a sufficient length had solidified, it was suddenly pulled by hand into the gallium bath by loosening the chuck holding the crucible. This technique is widely used. Problems typically encountered are :

1- Convection. Differences in the specific gravity of different constituents of the alloy tend to induce convection in the liquid in the presence of temperature and concentration gradients. These have been shown to affect the interface geometry and the primary dendrite arm spacing [197, 198]. Since copper is heavier than aluminum, a vertical system with the temperature increasing with height was used. The small size of fiber-free areas within the sample and this precaution ensured that no significant convection was present. Isotherms therefore were flat and perpendicular to the fibers. This was confirmed by observing the location of the dendrite tips and the eutectic solidification front on quenched samples.

2- Transients. Due to the absence of fibers, the thermal conductivity changes in the region above the specimen. Since F. Mollard [203] observed that transient effects were affecting the last centimeter of his samples on a similar apparatus, the specimens were quenched before the solidifying metal reached the last two centimeters of the sample. This was, if anything, an

overly precautious measure. At the bottom, the first half centimeter was discarded as well, to avoid the region where different grains outgrow one another. Another type of transient is due to the moving crucible, since the heat transfer pattern is modified by this additional heat transport mechanism [196]. To minimize this effect, the downward movement was started from a point high enough for the heat flow pattern to stablilize by the time the liquidus temperature reaches the sample bottom.

The growth velocity was measured with a ruler attached next to the moving crucible. The temperature gradient was measured by recording the distance separating the dendrite tips from the eutectic front on a longitudinal cross-section of the quenched sample. This value differed by at most 20% from the value output by the thermocouple below the sample.

Despite the relatively large crucible diameter, quench rates in the gallium tank were high, and the solidification morphology was appropriately quenched-in. Transient effects at the interface are reviewed by Sharp and Hellawell [199].

With the composite samples, the main experimental difficulty was obtaining high temperature gradients. High gradients, for a given quench tank, require a high furnace temperature. Sharp and Hellawell, for example, heated their top region between 1000 and 1250 °C [199]. The problem lies in the fact that above 800-900 °C, the fiber-matrix reaction proceeds at a rate high enough to build up a substantial interfacial reaction zone. It is shown below that this reaction zone consists of Al_4C_3 and does not significantly affect the overall alloy composition. Some reaction

zone formation was therefore allowed. The phenomenon places, however, an upper limit on permissible temperature gradients. The sample is six to seven centimeters long. Hence, temperature gradients cannot fall much below 30 °C/cm. Experiments were thus performed with two values for the thermal gradient, i.e. "high" gradients (100-70 °C/cm) and "low" gradients (50-30 °C/cm). The temperature gradient could not be adjusted with any higher degree of precision. "High" gradients were obtained with use of the small booster furnace described above.

On one sample, the motor was stopped for ten minutes before quenching to obtain an isothermal hold. All other aspects of the procedure were identical.

III - Metallography.

After a sample was removed from its crucible, a bevel was ground into the unreinforced peripheral region. After polishing and etching in Keller's etch, this revealed the positions of the tips and the eutectic front. The quenched-in structure was then sectioned lengthwise to obtain two longitudinal sections from the tips to the eutectic front. Below the eutectic front, fully solidified microstructures were also revealed with transverse sections. After examination under the optical microscope, one of the longitudinal halves was sliced at measured distances from the tips into transverse sections for examination and analysis in the electron microprobe. All sectioning was with a low speed diamond saw. Polishing the composite structure with its soft matrix and

extremely hard fibers was difficult and time consuming. Therefore, automatic polishers were used. The grinding and polishing sequence was as follows:

1- Grinding was by hand on metal or resin bonded diamond wheels. This was essentially to obtain a flat sample surface, and eliminate the shattered portions of the sectioned fibers. Silicon carbide is extremely brittle, and creates at this stage numerous particles which get embedded into the aluminum matrix.

2- Rough polishing was with 9 and 6 micron diamond pastes on a rough perforated synthetic cloth ("Buehler Perf. Chem. Texmet"). Water was used as a thinner because it has a low viscosity and did not degrade the cloth nor its adhesive. At the end of this operation, the fibers were flat, and the embedded particles of SiC were removed from the matrix.

3- Intermediate polishing with 1 micron diamond paste as above. At the end of this operation, major scratches were removed from the matrix.

4- Final polishing was with magnesium oxide in water on a fine felt cloth. As MgO does not polish the fibers, there is a trade-off between a flat and a scratch-free matrix surface. This limits final polish times to short values (a minute or two). MgO is more difficult to use than alumina, but results are far better (consult reference [200] for details).

After each polishing step, the samples were ultrasonically cleaned in water with an appropriate soap. Due to the low polishing rates permissible in the presence of silicon carbide fibers, water had to be avoided altogether in some instances

because the corrosion rate of the matrix was higher than the polishing rate. In these cases, kerosene was used as the thinning agent for polishing and cleaning was in ethanol.

After the final polish, the samples were thoroughly cleaned to remove the MgO powder which tended to stick to the sample surface. Immediately thereafter, the sample was etched. Etchants were:

1- Keller's etch [78,79]. This etch reveals very clearly the secondary dendrite arms, the eutectic and to some extent coring patterns. Keller's etch is easy to use and was most appropriate for longitudinal cross-sections.

2- a modification of a reported etchant [201,202,79]: 4 g $KMnO_4$ and 2 g NaOH in a liter of water. This etch reveals coring patterns and the second phase in brilliant colors by depositing a film that allows for extinction of a wavelength of the incident light beam. Both the fibers and the matrix are etched, and isoconcentration contours within the matrix are clearly visible, figure 8. The correspondance between a color fringe and isoconcentrates has been proven elsewhere [66, 202]. This etchant was used on all transverse and some longitudinal sections. The fact that the etchant reveals concentration contours also allows for a good rendition of the quenched-in solid/liquid interface near the dendrite tips due to the solute rich band present in that area [199]. This etchant is more delicate in its use. It must be mixed fresh, with the proportion of NaOH and $KMnO_4$ tightly controlled. It is also best to keep the etchant cold with some ice around its container when it is used. This etchant

deteriorates rapidly in air.

Dendrite arm spacings were counted with an eyepiece fitted with a micrometer. To allow for comparison, counting procedures were as in reference [149]. In the unreinforced regions, the secondary dendrite arm spacing was averaged over a few adjacent arms. Because of the much decreased amount of material available in the composite regions, all dendrite arms were used and plotted individually. Hence a much increased scatter in this data is found.

IV - Electron beam X-ray microanalysis.

Analyses were performed on a Cameca Camebax. Sample preparation was as above without etching. Samples were not coated as the fibers are conductive enough to prevent any charging to occur.

Standardization was with the pure elements, Al and Cu. This gives results within the alha phase on fully homogenised microstructures that are consistent with the alloy composition [81,204]. Conditions for analysis were as follows: beam acceleration voltage: 20 kV; beam intensity : 20 nA; counting time: 10 seconds per element; Al,Kα and Cu,Kα peaks were used. ZAF corrections were automatically performed by the computer attached to the instrument.

Electron microprobe analysis was performed on specimens to measure the amount of microsegregation present. In this thesis,

the adopted measure of microsegregation is the minimum copper concentration present. It is a usual and significant figure which for the case at hand is easy to measure since the copper-poor regions are located in the center of the interfiber regions where the matrix surface is horizontal. To obtain this minimum, analysis points were chosen down the concentration gradients along a square grid of adequate size until a point surrounded by four points having a higher concentration were found. To minimize the effect of noise in the measured concentrations, the value for the minimum concentration in each interfiber region was averaged with the second lowest value measured in that region. As the square grid was finer than the coring patterns, the uncertainty in the location of the minimum concentration point was low and of no consequence.

As many as five areas were investigated for each sample. The average of the obtained values is plotted. Since standard variations were up to 15% of the values obtained, this was taken as the margin of error.

V - Auger electron spectroscopy.

Auger electron spectroscopy can be used to analyse an area on the sample that is only a few atomic layers deep. It was therefore suited for investigating the interfacial reaction zone. Analyses were performed on a Perkin Elmer Physical Electronics digital scanning Auger electron spectroscope Model 590. To eliminate oxygen and carbon contamination on the surface of the

sample, argon sputtering was used. Prior to data acquisition the sample surface was thus cleaned until the oxygen peak was reduced to negligible values. During the analysis proper, sputtering was continued at a much lower rate. Conditions pertinent to the analysis were: electron beam energy: 5 keV; beam current: about 1 μA; data acquisition time: 15 minutes. Partial spectra were collected in a multiplex mode for the four elements present : Al, Cu, Si, C. The spectra were smoothed and expanded after acquisition.

The composite sample utilized was from a longitudinal cut of the top-most part of the sample grown at the slowest rate under the steepest temperature gradient (H-3). This region, liquid at the time of the quench, contained the thickest interfacial reaction zone of all samples due to the long exposure to elevated temperatures. The sample was polished and cleaned in the absence of water to prevent dissolution of the hygroscopic reaction zone. The Al_4C_3 standard was made from a powder of chemical purity purchased from Alpha Ventron. The powder was pressed into a small pellet together with a fine mesh tin powder. This allowed for easy handling of the sample and suppression of charging effects.

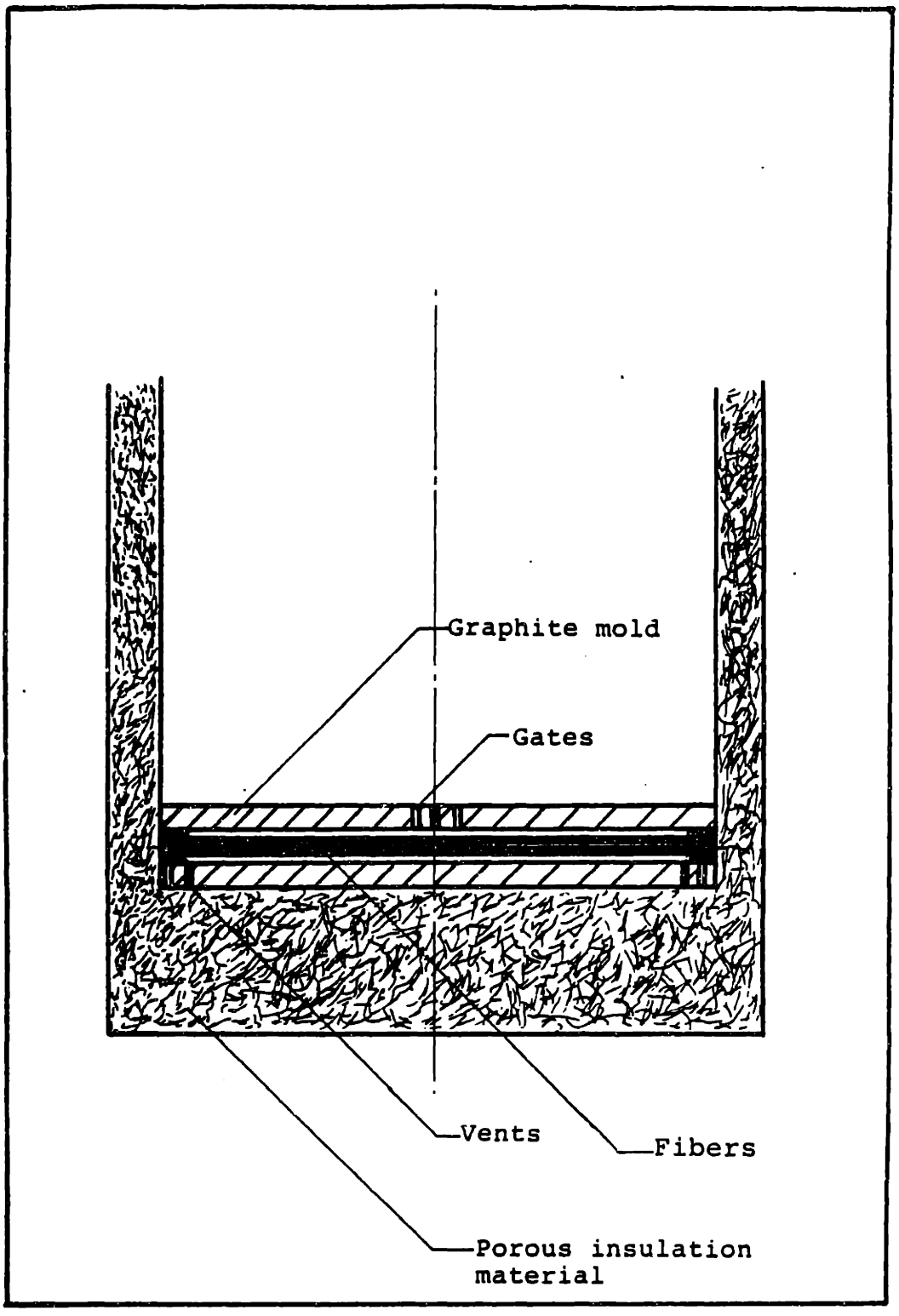

Figure 5. Mold configuration

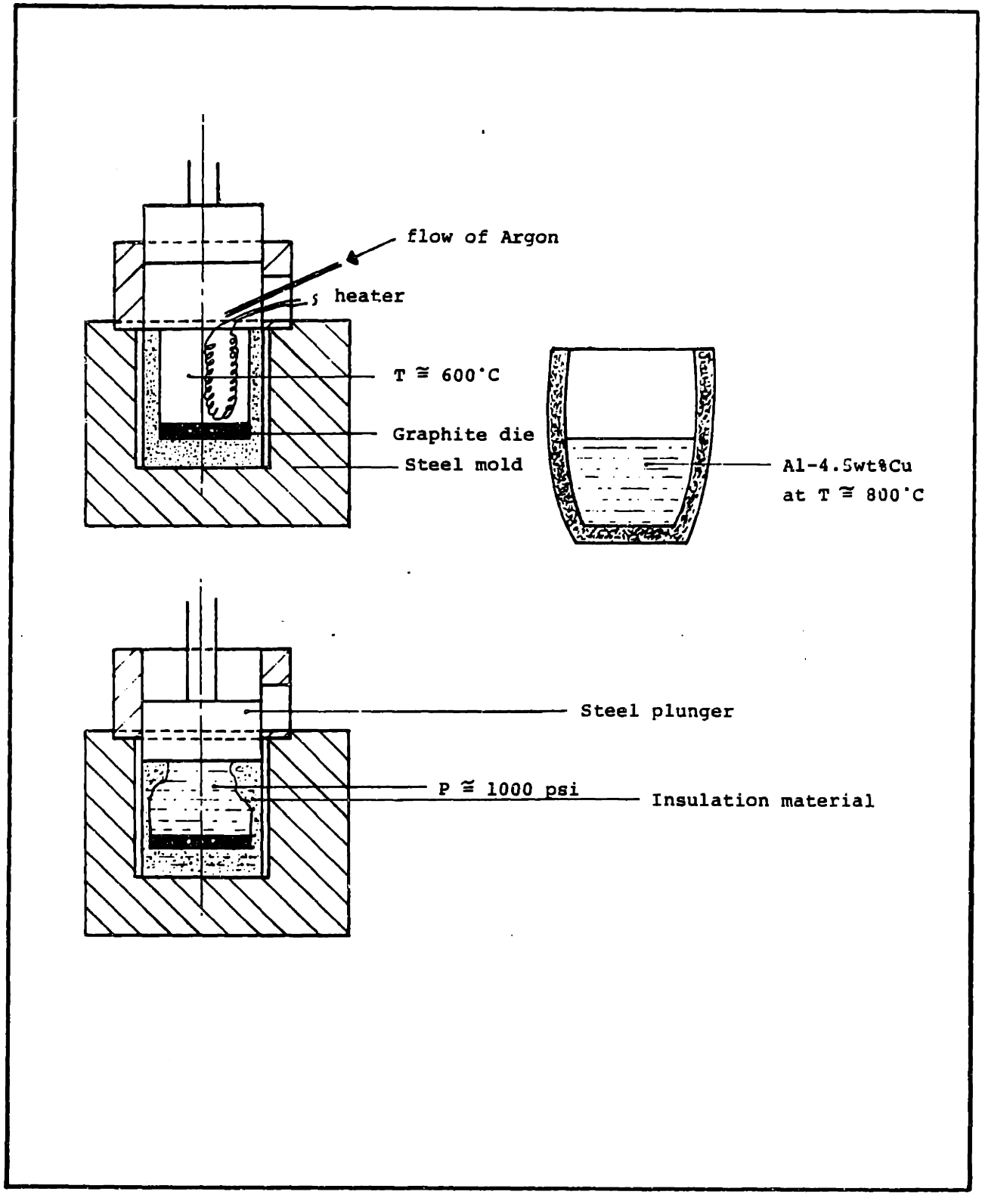

Figure 6. Casting procedure.

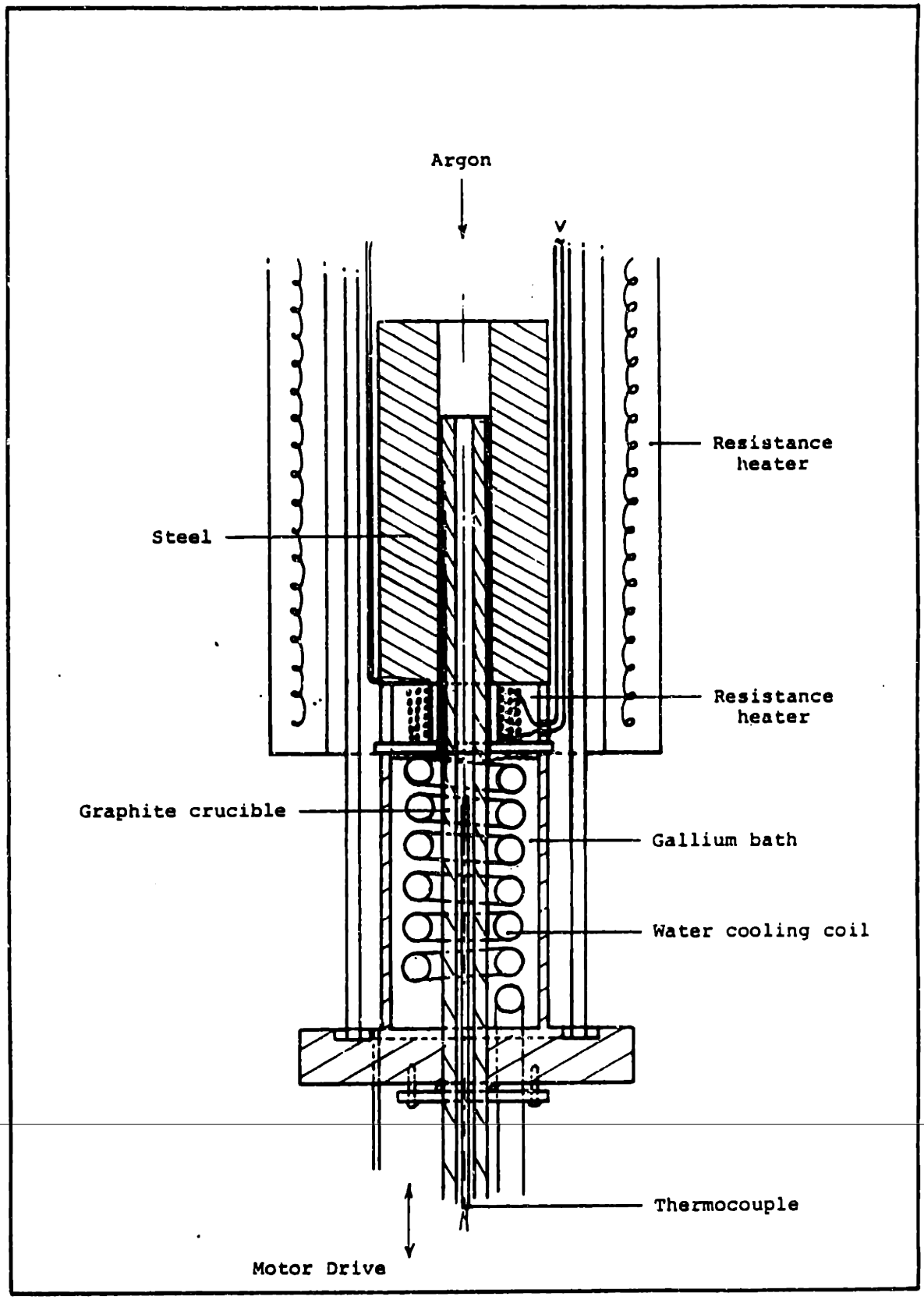

Figure 7. Steady state solidification apparatus. Cross section, 1:0.77.

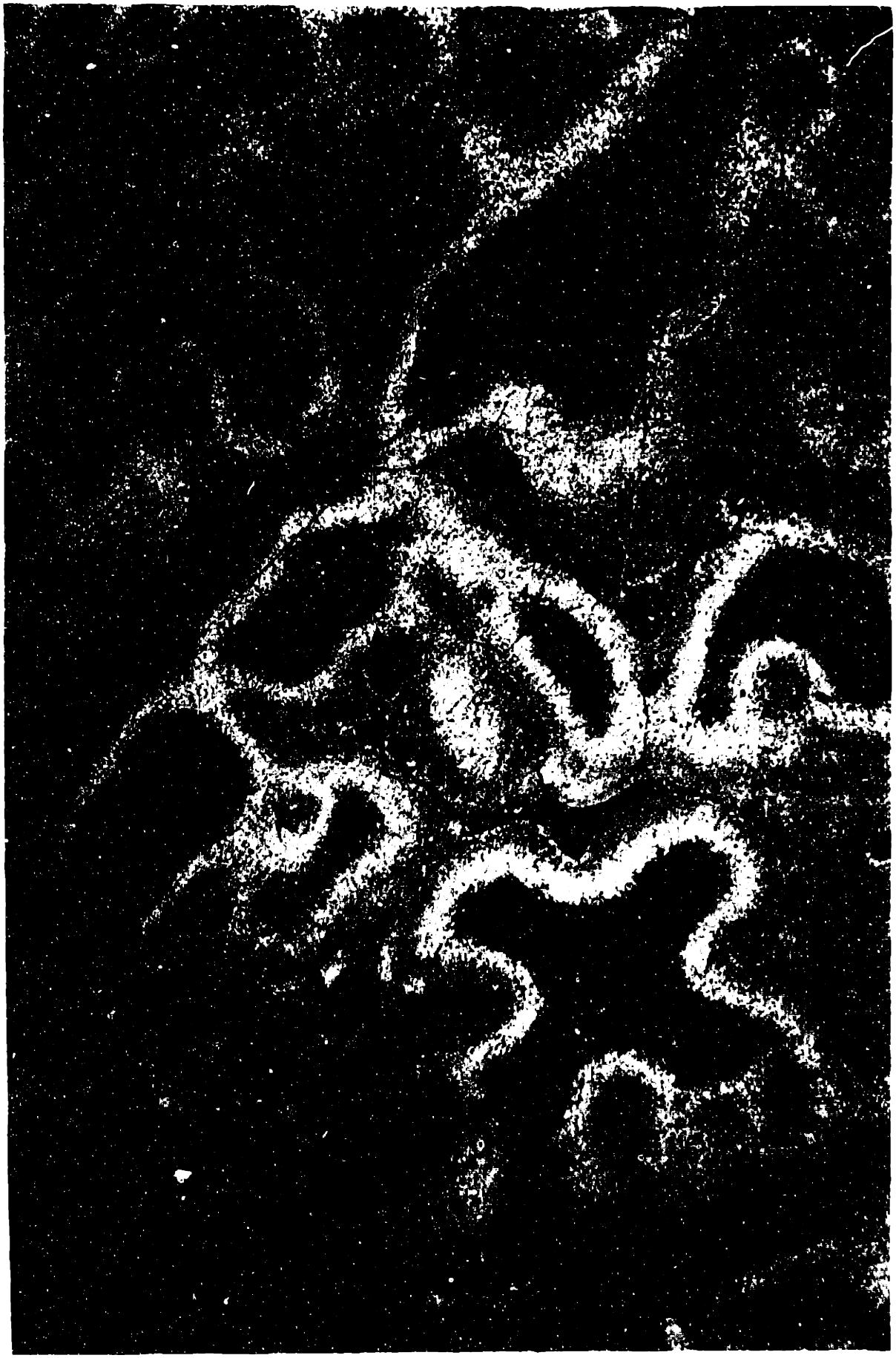

Figure 8 - Al-4.5wt%Cu, etched to reveal coring and the second phase. ——— 100 μm

Figure 8 - Al-4.5wt%Cu, etched to reveal coring and the second phase. ——— 100 μm

INTENTIONAL DUPLICATE EXPOSURE

EXPERIMENTAL RESULTS

I - Samples.

A total of eight samples were solidified in the Bridgman furnace. They were taken from three identical pressure cast batches, labelled "G", "H" and "I". All were solidified at steady state, and quenched. One additional sample was solidified in a similar manner and then held still for ten minutes in the furnace prior to quenching. All nine samples are listed in Table 1 with their solidification parameters.

Each sample consists of a reinforced composite core surrounded with a fiber-free region. Within the composite core, fibers often touch and define isolated interstices. The simplest of these are the interstices delineated by three and four fibers. Interstices delineated by three fibers will be defined in this thesis as "Triangular" interstices. Interstices delineated by four fibers, the centers of which are approximately located on the four corners of a square, are defined as "Square" interstices. Only these two types of interfiber regions are considered in any quantitative manner in what follows. These interstices are drawn in figure 9 together with their dimensions and area.

II - Microstructures.

While each sample was drawn at steady state through the

SAMPLE	GROWTH RATE $x10^{-6}$m/s	TEMPERATURE GRADIENT $x10^{2}$ K/m	COOLING RATE K/s	SOLIDIFICATION TIME s
I-1	203	91	1.85	54
I-4	206	58	1.19	84
H-2	100	75	0.75	133
I-3	105	51	0.536	187
G-2	52	71	0.373	268
H-4	54	45	0.242	413
H-3	23	96	0.240	417
I-2	25	41	0.106	940
I-5	53	35	0.186	
	Sample held for 3600 seconds in the temperature gradient before quenching.			

Table 1 - Samples with their solidification parameters.

thermal gradient (G) of the furnace, a zone of coexisting liquid and solid metal progressed up through both the unreinforced and the composite regions of the sample. When the sample was suddenly pulled through the gallium bath, this liquid/solid region was quenched. In this manner, all stages of solidification from the dendrite tips to the fully solid structure below the eutectic front could be examined. In a longitudinal cross section through this quenched liquid/solid region, increasing distance from the tips measured parallel to the fibers corresponds to an increasing local solidification time, and hence an increasing fraction solid. Since the temperature gradient and the growth rate were kept constant, the temperature at the time of the quench at any point in such a longitudinal cross section is a linear function of distance measured parallel to the fibers. A transverse cross section through the sample in a plane perpendicular to the fibers corresponds to an isotherm in the sample at the time of the quench. The corresponding isotherm temperature can be obtained by measuring the distance from the dendrite tips and using the known temperature gradient.

In the unreinforced region of the samples, large rounded dendrites typical of the dendritic/cellular transition are obtained at low growth rates. At higher growth rates, their size decreases and they adopt a well branched morphology typical of the fully dendritic growth regime. The primary dendrite arm spacings were mesured as in Young and Kirkwood's work [149]. Results are given and compared with Young and Kirkwood's

experimental correlation in table 2. It can be readily seen that primary dendrite arms growing in the fiber free regions are significantly wider than the narrow square and triangular interstices found between the fibers in the composite region and described in figure 9.

In the composite region of the samples, the growing solid is initially dendritic. Primary dendrite stems with secondary dendrite arms attached to them were observed to form in all composite samples in the initial stages of solidification. Only one primary dendrite arm was seen to grow in each triangular interfiber space of all samples. Square interstices also contained only one primary dendrite arm each, except in some square interstices of sample I-1 which solidified the most rapidly.

The relative position of the dendrite tips in the composite and unreinforced regions can be approximately compared on a longitudinal section through the samples. Examples are given on figures 10 and 11. These micrographs are taken from the liquid/solid region near the dendrite tips. Between the fibers, dendrite tips were not found to lag significantly behind those in the unreinforced regions. Hence, within experimental error (about one Kelvin), no enhancement in the dendrite tip undercooling was found between the fibers at the growth rates and gradients investigated.

Transverse cross-sections near the tips confirmed this observation in that the dendrites appeared at about the same time

SAMPLE	MEASURED PRIMARY D.A.S. x 10^{-6} m	FROM REFERENCE [149] x 10^{-6} m
H 3	227	
I 2	317	
G 2	234	275
H 4	283	343
H 2	202	212
I 3	244	253
I 1	126	146
I 4	186	187

TABLE 2 - Primary dendrite arm spacings.

in both regions of several samples after successive grinding and polishing through the quenched liquid. The dendrite tips were thus located on the same isotherm in both the fiber free and the composite regions. Cross-sections obtained in this manner are given in figures 12 and 13. As seen in these figures, the solid phase initially grows from within the interfiber regions without touching the fibers. It is also apparent that secondary dendrite arms also form between the fibers in the composite at this initial stage of solidification. Secondary dendrite arms formed in the initial stages of solidification inside a triangular interstice can be seen on figure 14.

As solidification progresses, the secondary dendrite arms gradually disappear, first in the triangular interstices and later in the square and larger interstices, by deposition of solid in the liquid trough separating them. This is a process identical to secondary dendrite arm coalescence mechanisms described previously by several authors [147-150]. The secondary dendrite arms thus gradually shorten with increasing local solidification time. Provided there is sufficient time for this process to reach its completion before the end of solidification, all secondary dendrite arms will be eliminated. At this point, the solid maps precisely the fiber surfaces delineating the interstices and all the liquid is found against the fibers. The entire process can be viewed on figure 15. This micrograph is a low angle cut through a square interstice ranging from the dendrite tip region (A) through the primary stem (B) of the dendrite growing in that interstice and then through an array of

secondary dendrite arms branching off that primary stem (below B). Below a certain temperature corresponding to an isotherm around point C, the liquid trough separating secondary dendrite arms can be seen to gradually disappear. At D, corresponding to a still lower temperature than at C, in the later stages of solidification, the only traces left of the secondary dendrite arms are solute-rich bands delineating the previous location of the liquid pool that separated them (these are revealed by the etch). Figure 16 superimposes two stages of the process. This micrograph was obtained from a transverse cut through a square interstice which was in the later stages of solidification prior to quenching. In this scanning electron micrograph obtained with back-scattered electron imaging, lighter (copper rich) areas in the primary alpha phase correspond to the portions that solidified last. Two channels that separated secondary dendrite arms are thus seen to have been filled in. The copper concentration in the lighter areas of this micrograph was determined by electron probe microanalysis to be 3.5 - 3.9 wt%Cu. This is the composition of the depositing solid at the time when the trough separating secondary dendrite arms was filled in.

In narrow interfiber spaces, secondary dendrite arm coalescence is accelerated to the point where the initially dendritic microstructure can be eliminated when the time spent in the liquid/solid state is sufficiently long. As the total solidification time increases, therefore, the final solid metal matrix becomes increasingly non-dendritic. Any second phase is then found at the fiber-matrix interface. This phenomenon

determines the morphology of the final matrix microstructure, as can be seen on figures 17 to 20. In figures 17 and 18, the solidification time is short and secondary dendrite arms are still visible in the larger interstices. In square interstices of this sample, the coring patterns are dendritic although the second phase is mostly found at the fiber-matrix interface. In triangular interstices, the isoconcentrates are non dendritic and parallel to the fiber surfaces. In larger interstices, secondary dendrite arms and eutectic islands are found within the matrix. Figures 19 and 20 are from a sample solidified at a lower cooling rate. In this sample, coring patterns are non dendritic in square interstices as well as in triangular interstices.

In the square and triangular interstices of all samples, the secondary dendrite arms coalescence process reached its completion before the eutectic temperature was attained. In larger interstices, however, secondary dendrite arms persisted, as witnessed by the presence of islands of eutectic within the interfiber spaces (figures 17, 18 and 20). In square interstices, the transition from dendritic to non dendritic coring patterns took place from sample I-4 to sample H-2, ie. at a solidification time between 84 and 133 seconds. The presence of non dendritic coring patterns indicates that the secondary dendrite arm coalescence process was completed before the solid deposited with a high copper content. The location of the eutectic is thus predominantly on the fiber surface in the final fully solidified microstructure.

Figure 21 is a schematic rendition of these observations. The

microstructural evolution during solidification of a dendrite in a triangular interstice is compared to that of a dendrite free of the constraining action of the fibers. The dendrite tips both grow at the same (small) undercooling. Behind the tips, secondary dendrite arms form and start to grow. Later in the solidification process, still at relatively low fraction solid, secondary dendrite arm coarsening is predominantly by ripening in the fiber-free matrix. As will be shown later, ripening can proceed in the interstices of the composite, but not beyond a certain secondary dendrite arm spacing due to the constraining action of the fibers. The secondary dendrite arm spacing may, therefore, be smaller on the average than in the fiber free alloy. Simultaneously, in the narrow interfiber spaces of the composite, secondary dendrite arm coalescence is already clearly discernible. Secondary dendrite arms are thus gradually eliminated. At higher fractions solid (third stage depicted), coarsening is by coalescence in the fiber free matrix whereas in the narrow interfiber spaces, the structure is no longer dendritic. In the fully solidified metal (last stage depicted), the eutectic is found in pools located between the dendrite arms in the fiber free alloy. In the composite, the eutectic is located at the interface between the fibers and the primary phase.

In the sample that was held isothermally for ten minutes, the microstructure coarsened substantially in the fiber-free regions. In the composite region, nearly all secondary dendrite arms

disappeared at higher volume fractions solid (i.e. at some distance from the tips), figure 22.

III - Secondary dendrite arm spacings.

A longitudinal cross section through the quenched liquid-solid region of the samples is approximately perpendicular to the <100> planes in which the secondary dendrite arms were growing during solidification. Furthermore, the time during solidification increases linearly with distance measured from the dendrite tips because the growth rate was constant. It was thus possible to follow the evolution with time during solidification of the secondary dendrite arm spacing on longitudinal cross sections of the samples.

Secondary dendrite arm spacings from the unreinforced region were measured in all samples. Given the relative abundance of dendrite arms, measurements were made over several dendrite arms at a time and averaged. Data collected in this manner are plotted in figure 23 for samples solidified within the dendritic growth regime. As seen, the secondary dendrite arm spacing measurements from these samples compare well with Young and Kirkwood's experimental correlation [149]. The fit with this correlation was however less good for samples I-2 and H-3, both in the cellular/dendritic transition growth regime which lies outside of the range of validity of Young and Kirkwood's correlation, figure 24.

In the composite regions of the samples, averaging of secondary dendrite arm spacings was not found to be a satisfactory method because the number of dendrite arms available in each type of interstice was much smaller. All secondary dendrite arm spacings available were therefore measured and plotted individually, figures 25 to 38. This increases significantly the scatter in the data. For comparison with the unreinforced matrix, secondary dendrite arm measurements were made in this manner for three of the eight samples. The resulting plots are given in figures 39, 40 and 41.

Compared to similar plots from the unreinforced alloy, data from the composites present several novel features:

1 - Secondary dendrite arm spacings are significantly larger than in the unreinforced alloy. This phenomenon is particularly evident in triangular interstices, figures 25 to 32. The secondary dendrite arms therefore violate the usual $t^{1/3}$ coarsening law in the narrow interstices since the data gathered in the interstices do not fit any line of slope 1/3 in a log-log plot versus time during solidification.

2 - Secondary dendrite arms disappear after a certain time during solidification.

Both features are explained by the accelerated coalescence of secondary dendrite arms described above. When the liquid channel separating individual dendrite arms has been filled in with solid, the secondary dendrite arm spacing increases abruptly since several previous arms count as one. After a certain time during solidification, all secondary dendrite arms have coalesced

and the solid phase is non dendritic.

In the sample solidified at the lowest rate (I-2, solidification time = 940 seconds) secondary dendrite arms could be measured in triangular interstices after a time during solidification as high as 100 seconds, figure 32. It is interesting to note that the secondary dendrite arm spacing measurements gathered from that sample deviate significantly both upwards and downwards from the scatter bands normally encountered in the unreinforced alloy, figure 41.

After a certain time during solidification, no secondary dendrite arms are found in the narrow interstices. If this time is taken as an approximate measure of the time for full coalescence of secondary dendrite arms t_c, it can be plotted as a function of the solidification time t_f, for square and triangular interstices, figure 42.

IV - Microsegregation.

The minimum copper concentration was measured in all samples along several isotherms using transverse cuts of the quenched dendritic structures. The values obtained are given in Table 3. As seen, compared to the unreinforced regions, the narrower the interstice and the lower the cooling rate, the higher the minimum copper concentration present. Microsegregation is thus reduced in the composite. It is even entirely suppressed in the triangular interstices of the sample cooled at the lowest rate, sample I-2.

SAMPLE t_f (s)	T (°C) at quench	MINIMUM COPPER CONCENTRATION (wt%Cu) Triangular Interstices	Square Interstices	Primary dendrite arms
I-1	619	1.1	1.3	1.0
54	571	1.4	1.3	1.2
	545	1.5	1.4	1.2
I-4	627	1.0	1.2	1.0
84	601	1.4	1.3	1.1
	574	1.7	1.3	1.1
	541	1.9	1.3	1.2
H-2	623	1.2		1.0
130	592	1.8	1.3	1.0
	542	2.3	1.3	1.3
I-3	627	1.2	1.0	1.0
190	606	1.7	1.1	1.0
	579	2.4	1.4	1.4
	549	3.0		1.2
G-2	646	0.8	0.8	0.8
270	627	1.2	0.9	0.9
	602	1.8	1.1	1.0
	577	2.4	1.3	1.2
H-3	623	1.8		1.0
420	593	2.1		1.4
	559	3.2	1.8	1.1
H-4	648	0.9	0.9	0.9
420	636	1.1	0.9	0.8
	618	1.6	1.2	1.0
	600	2.2	1.3	1.0
	585	2.8	1.4	1.2
	568	3.1	1.6	1.2
	548	3.6	1.6	1.3
I-2	648	0.9	0.9	0.9
940	632	1.2	1.0	0.8
	617	1.9	1.4	1.2
	602	2.3		1.3
	572	3.8	2.5	1.8
	548	4.3	2.9	1.8

TABLE 3 - Minimum copper concentration in triangular interstices, square interstices and the unreinforced regions of the samples as a function of the temperature during solidification.

Figure 43, a backscattered electron image of the same sample, reveals the absence of the second phase in the triangular interstices.

These measurements are corroborated by the microstructures given above, figures 17 to 20 : the coring patterns disappear in the triangular interstices at low cooling rates.

In the last sample, after an isothermal hold, the minimum copper content measured in an identical fashion is given in table 4. Concentration gradients were shallow in triangular interstices. As seen, the solute content is close to the solidus composition at that temperature in triangular interstices. Only small amounts of eutectic were found in the close packed composite regions at temperatures below the solidus.

V - The interface.

The interfacial zone is given in figure 44. It is seen to consist in a uniform layer covered by plates identical to the plates of Al_4C_3 observed in many instances with graphite-aluminum composites. Copper and silicon were not present in the interfacial zone since they gave no signal. The spectra collected for aluminum and carbon are given in figures 45 and 46. In the matrix, only Al and Cu gave a signal. In the fiber, only Si and C were present. As seen in these figures, the secondary peaks of both elements present at the interface indicate a bonding state that is different from that of aluminum in the alloy and carbon at the surface of the fiber. The reaction zone was therefore

ISOTHERM TEMPERATURE K	MINIMUM COPPER CONCENTRATION			SOLIDUS COMPOSITION
	PRIMARY DENDRITE ARMS wt % Cu	SQUARE INTERSTICES wt % Cu	TRIANGULAR INTERSTICES wt % Cu	wt % Cu
571	1.47	3.18	4.23	4.6
563	1.39	3.31	4.66	4.9
548	1.59	3.13	5.26	5.65

Table 4 - Microsegregation data from sample I-5 : effect of an isothermal hold in the Bridgman furnace.

believed to be composed of Al_4C_3.

To verify this conclusion, data were collected from pure aluminum carbide Al_4C_3 for comparison. Secondary peaks were identical with those observed in the interfacial zone, figures 47 and 48.

In conclusion some Al_4C_3 formed at the interface. Since the alloy composition is not significantly affected by the reaction, the limited formation of an interfacial zone around the fibers was deemed acceptable for the purposes of this thesis.

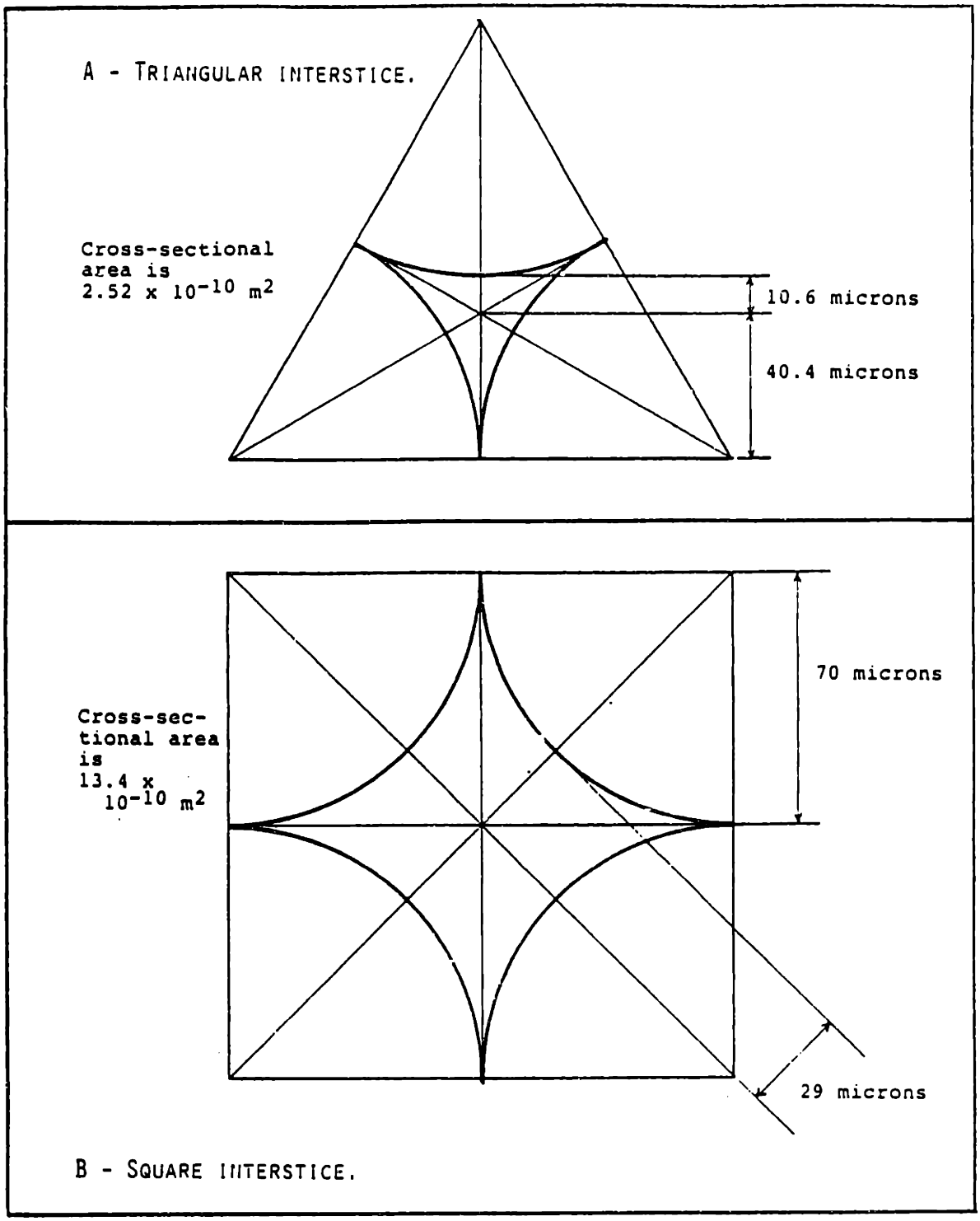

Figure 9. The two interstices studied in this thesis.

A - Triangular interstice.
B - Square interstice.

The fiber diameter is 140 microns. From this, dimensions of the interstices are derived and given above.

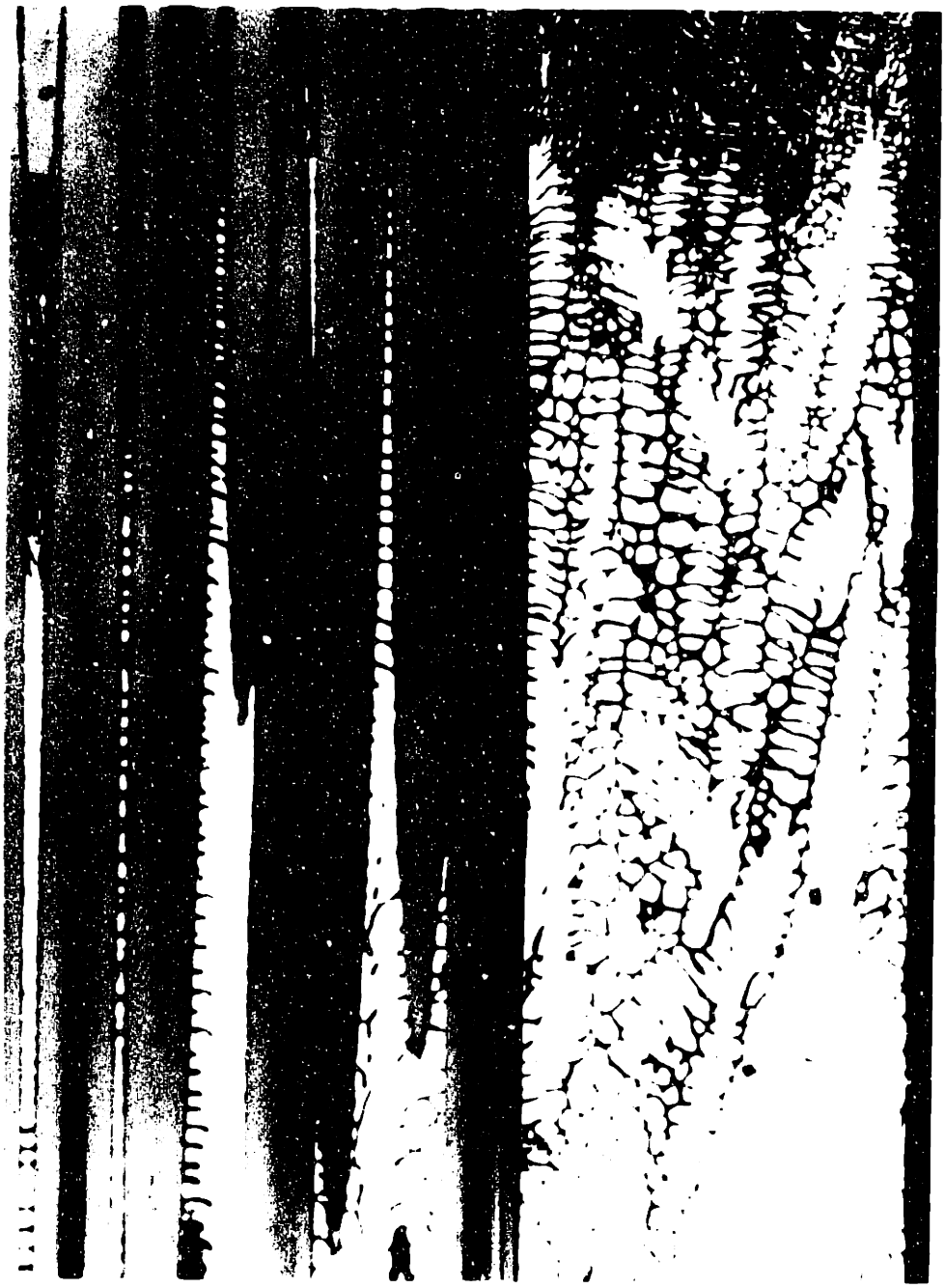

Figure 10 - Longitudinal section through the dendrite tip region. Sample H-2. —— 100 μ

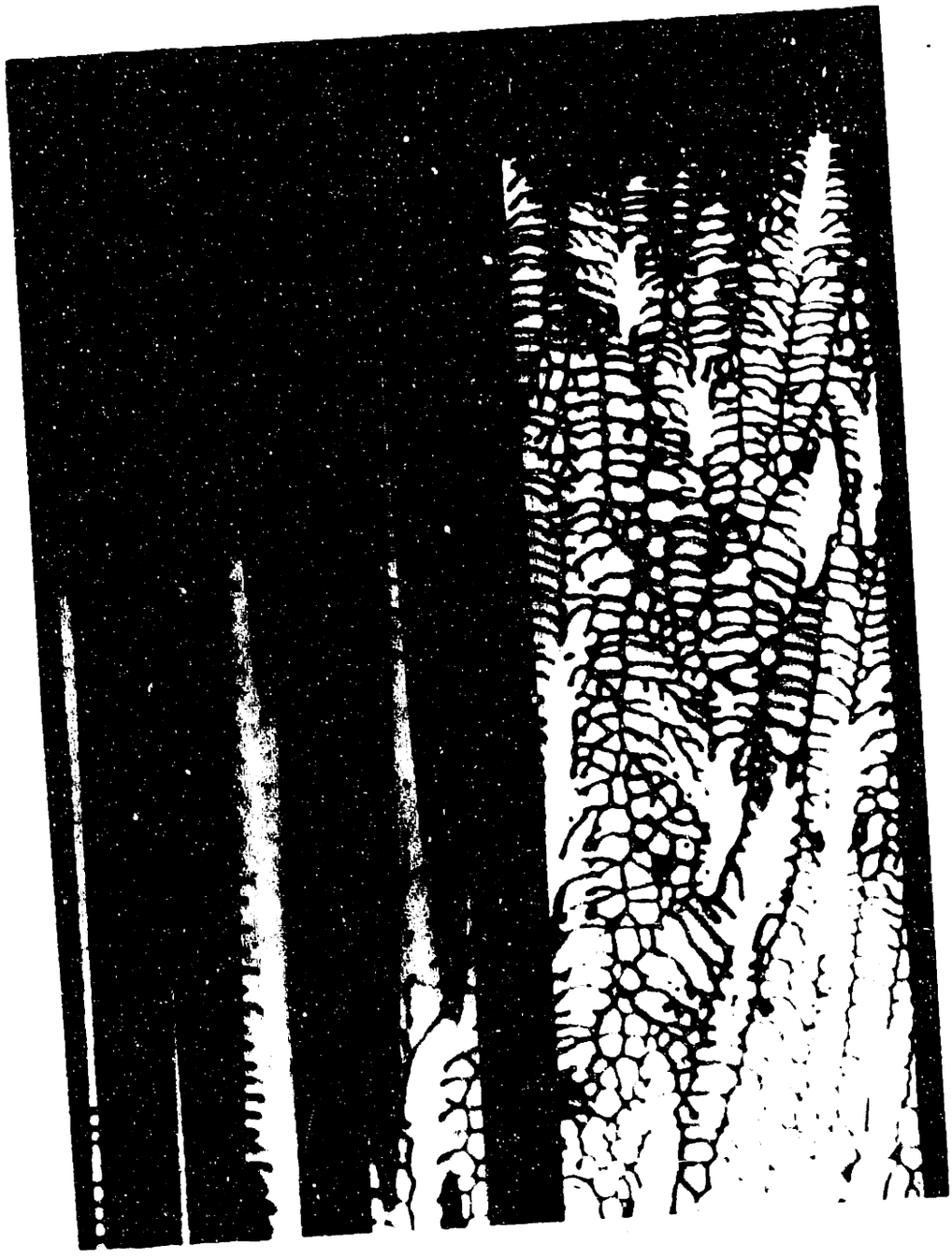

Figure 10 - Longitudinal section through the dendrite tip region. Sample H-2.

—— 100 μm

INTENTIONAL DUPLICATE EXPOSURE

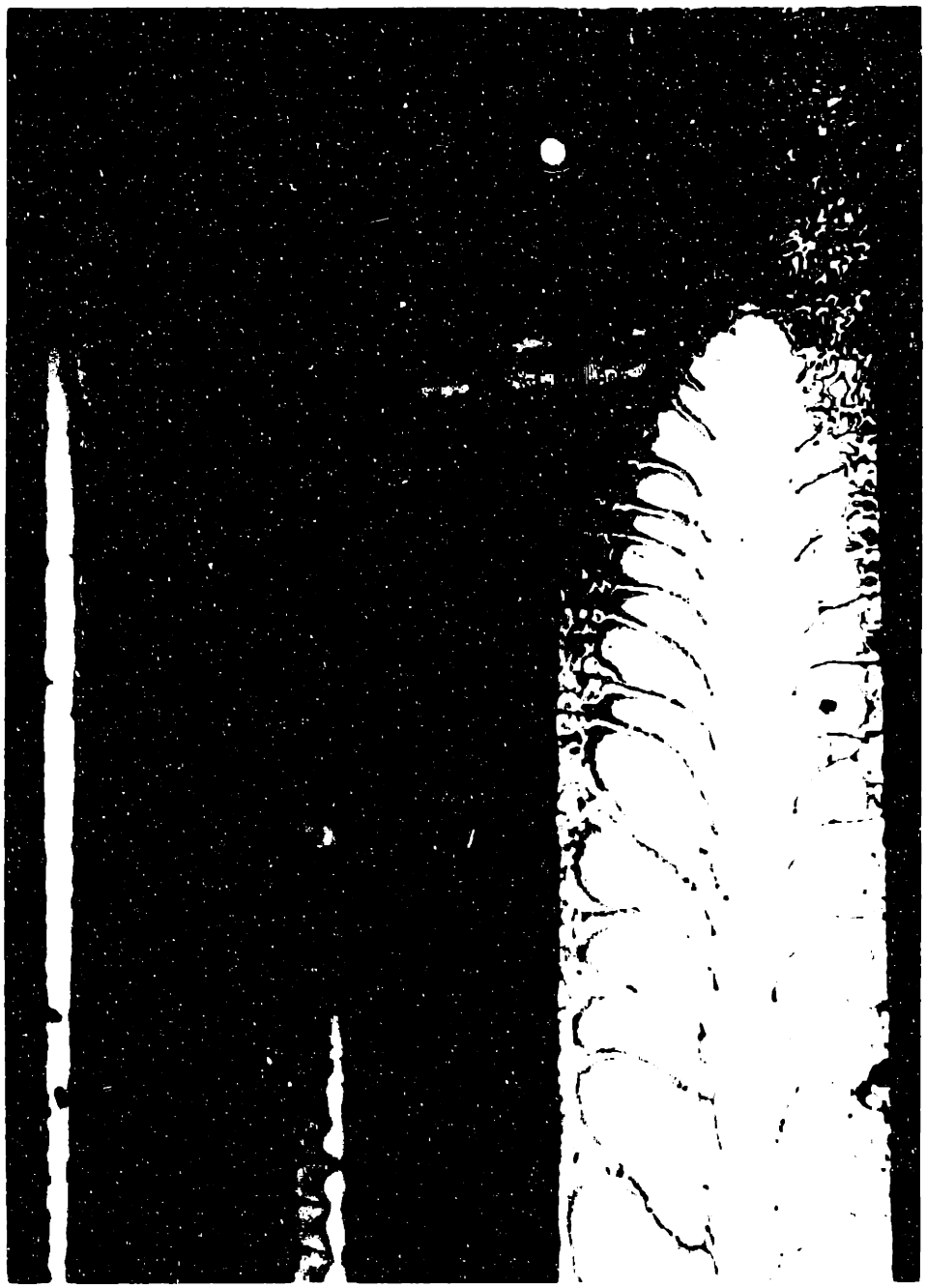

Figure 11 - Longitudinal section through the dendrite tip region. The smaller interstice (left) is a square interstice. Sample H-3.

100 µm

INTENTIONAL DUPLICATE EXPOSURE

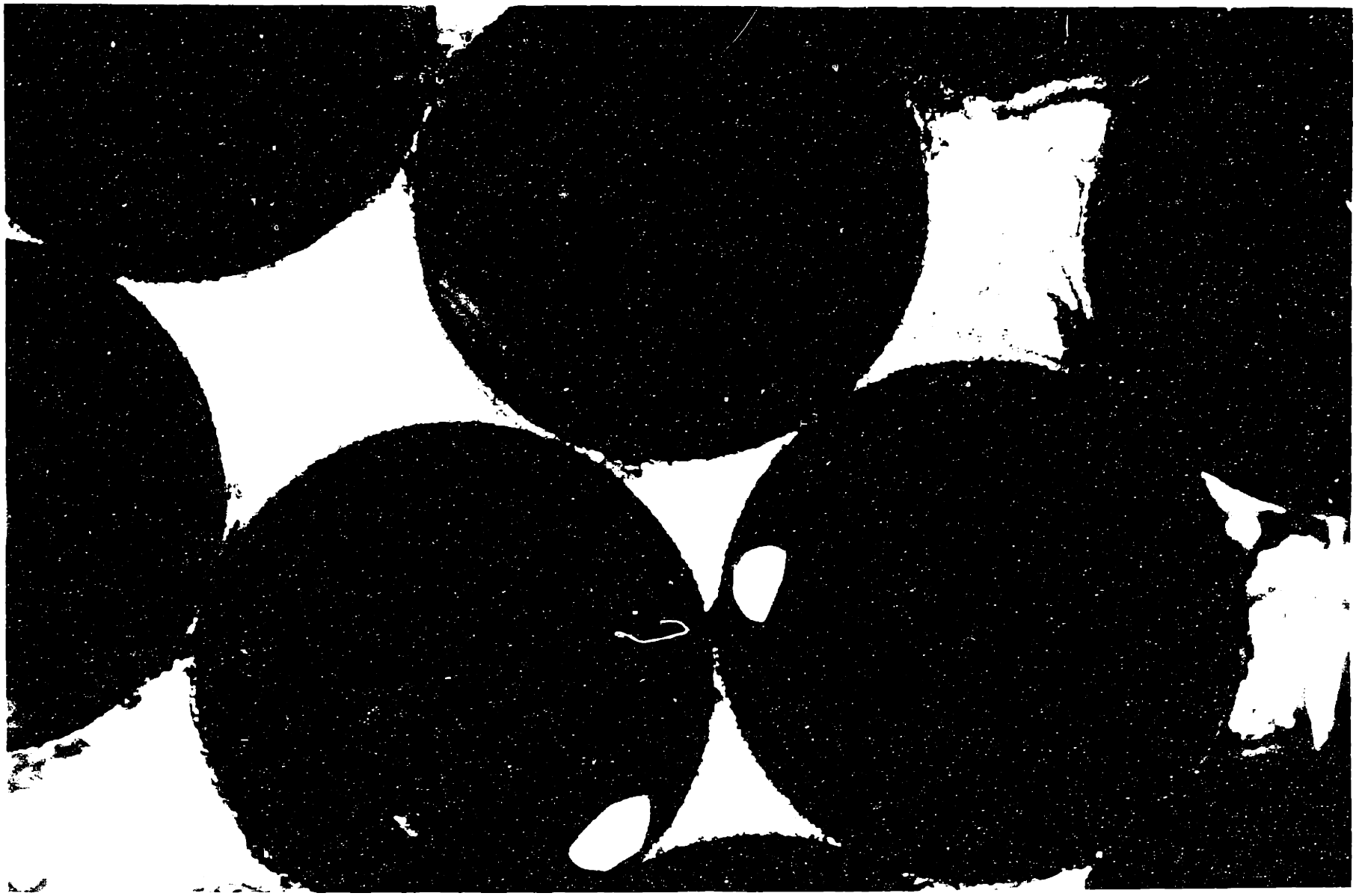

Figure 12 - Transverse cross section a short distance behind the dendrite tips. Sample I-1.

50 μm

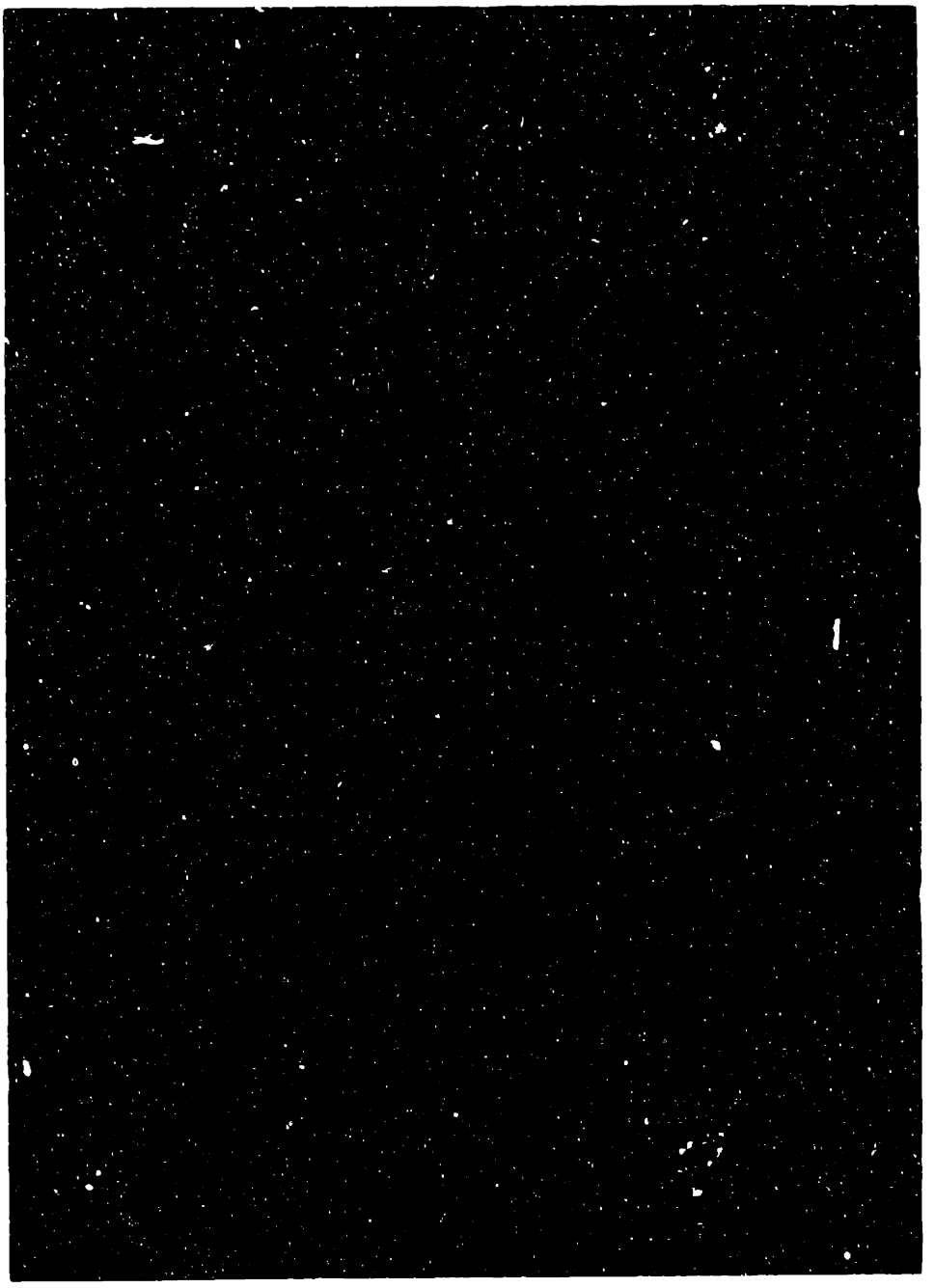

Figure 13 - Transverse cross-section a short distance behind the dendrite tips. Sample I-1.

——— 50 μm

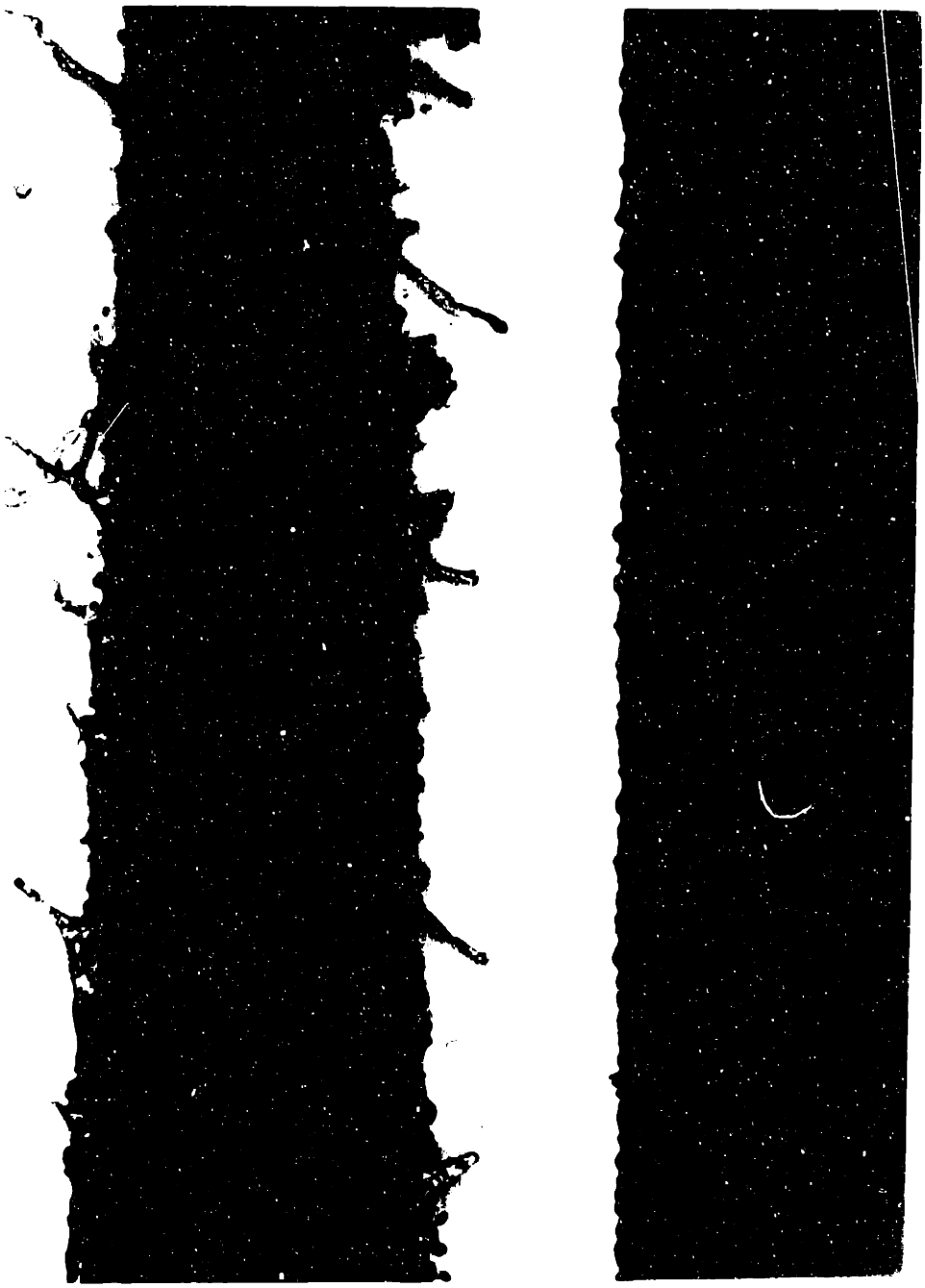

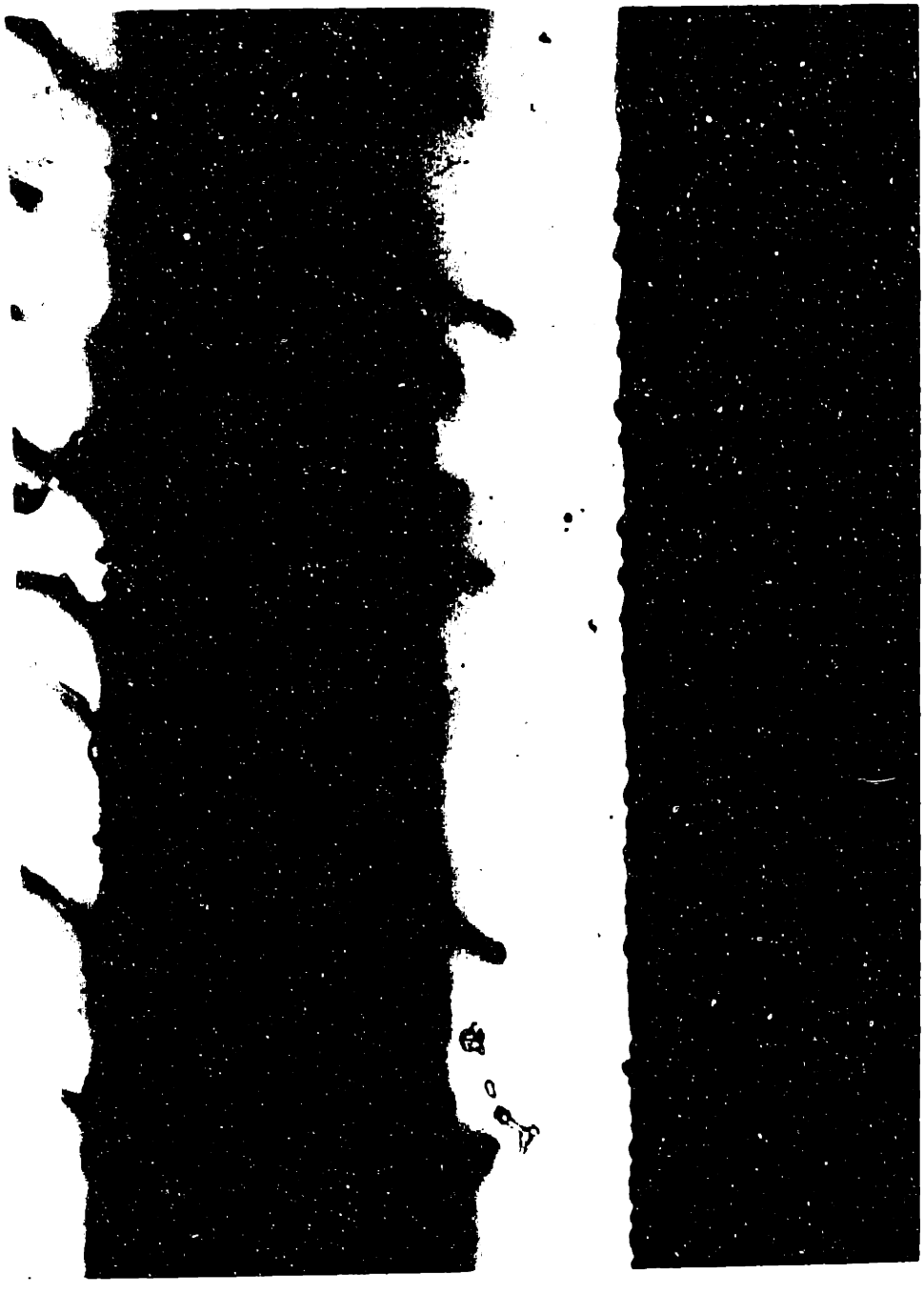

Figure 14 - Secondary dendrite arms formed in a triangular interstice of sample I-1. This longitudinal cross section is from the quenched liquid-solid region of the sample close to the dendrite tips.

10 μm

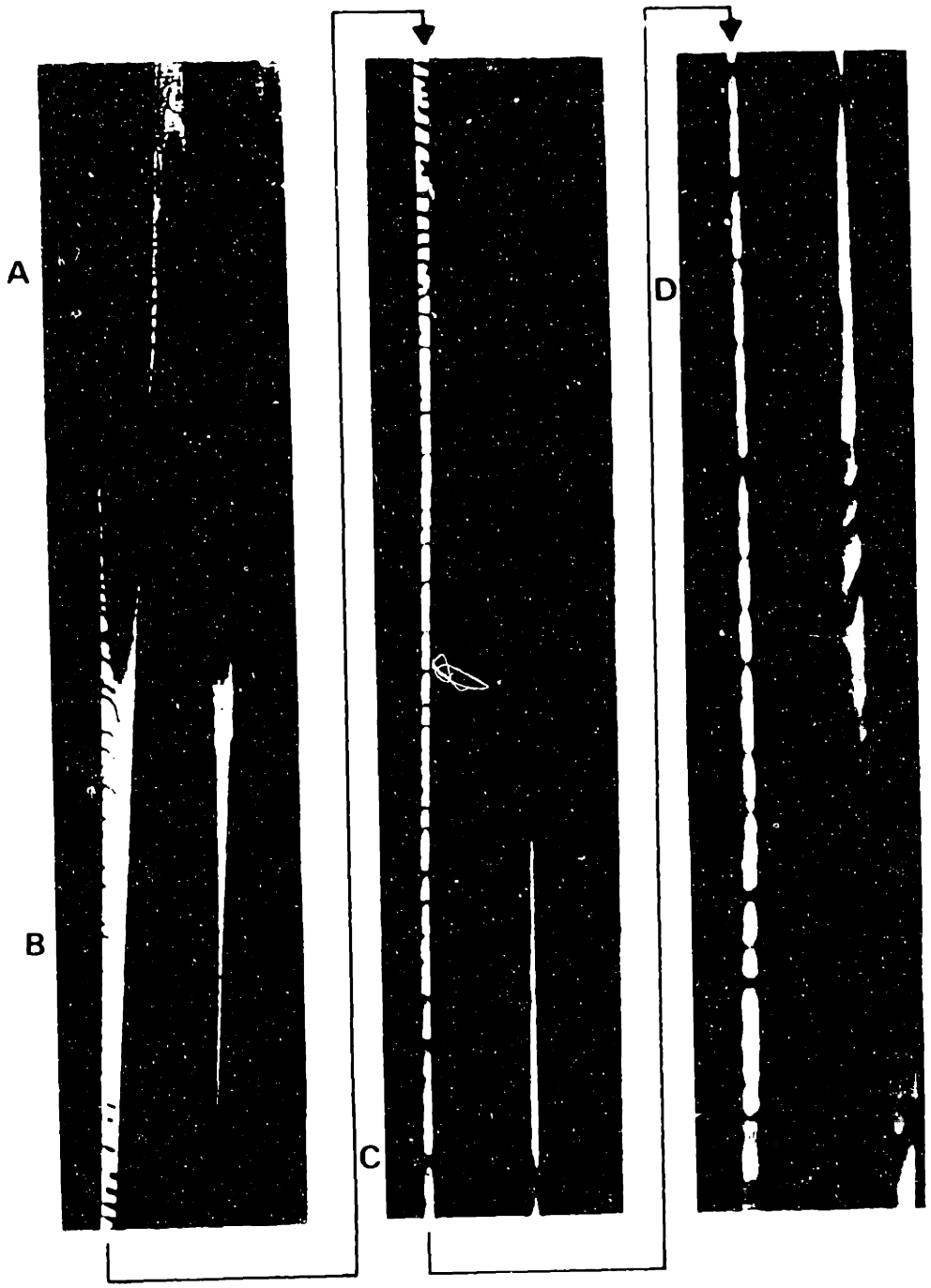
A
B
C
D

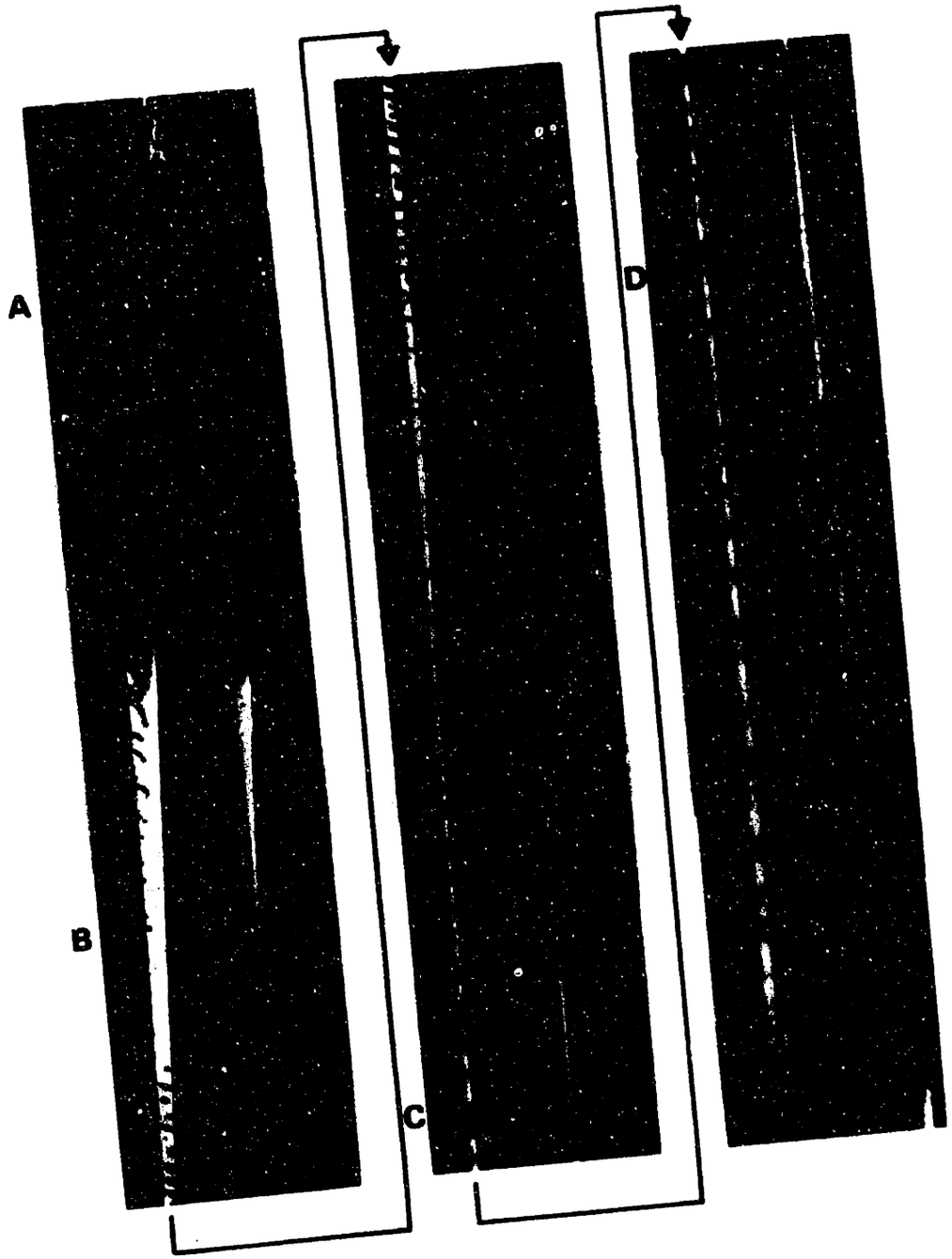

Figure 15 - A longitudinal section through a square interstice. Below the primary stem, the secondary dendrite arm coalescence process can be observed. Sample I-1. ——— 200 μm

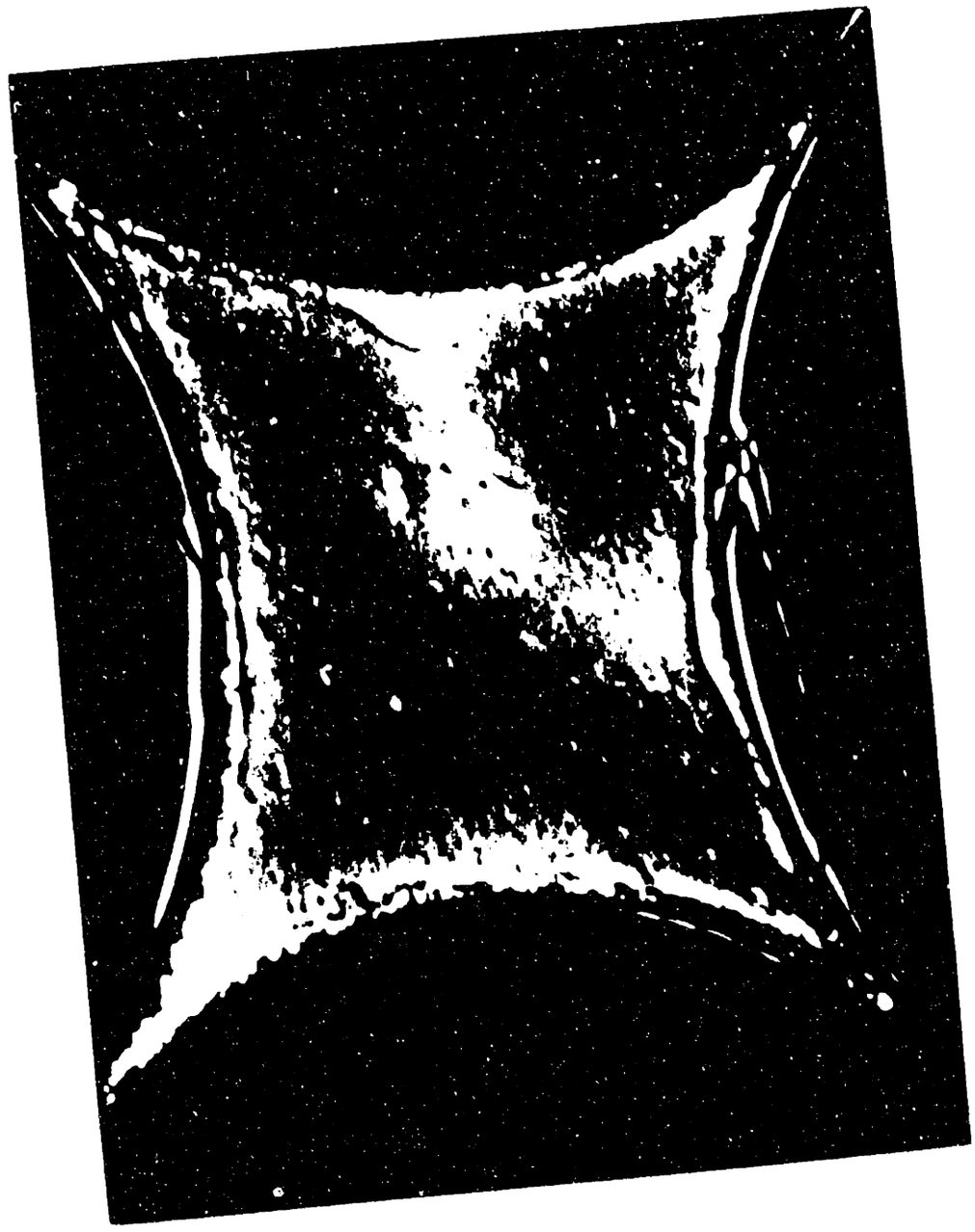

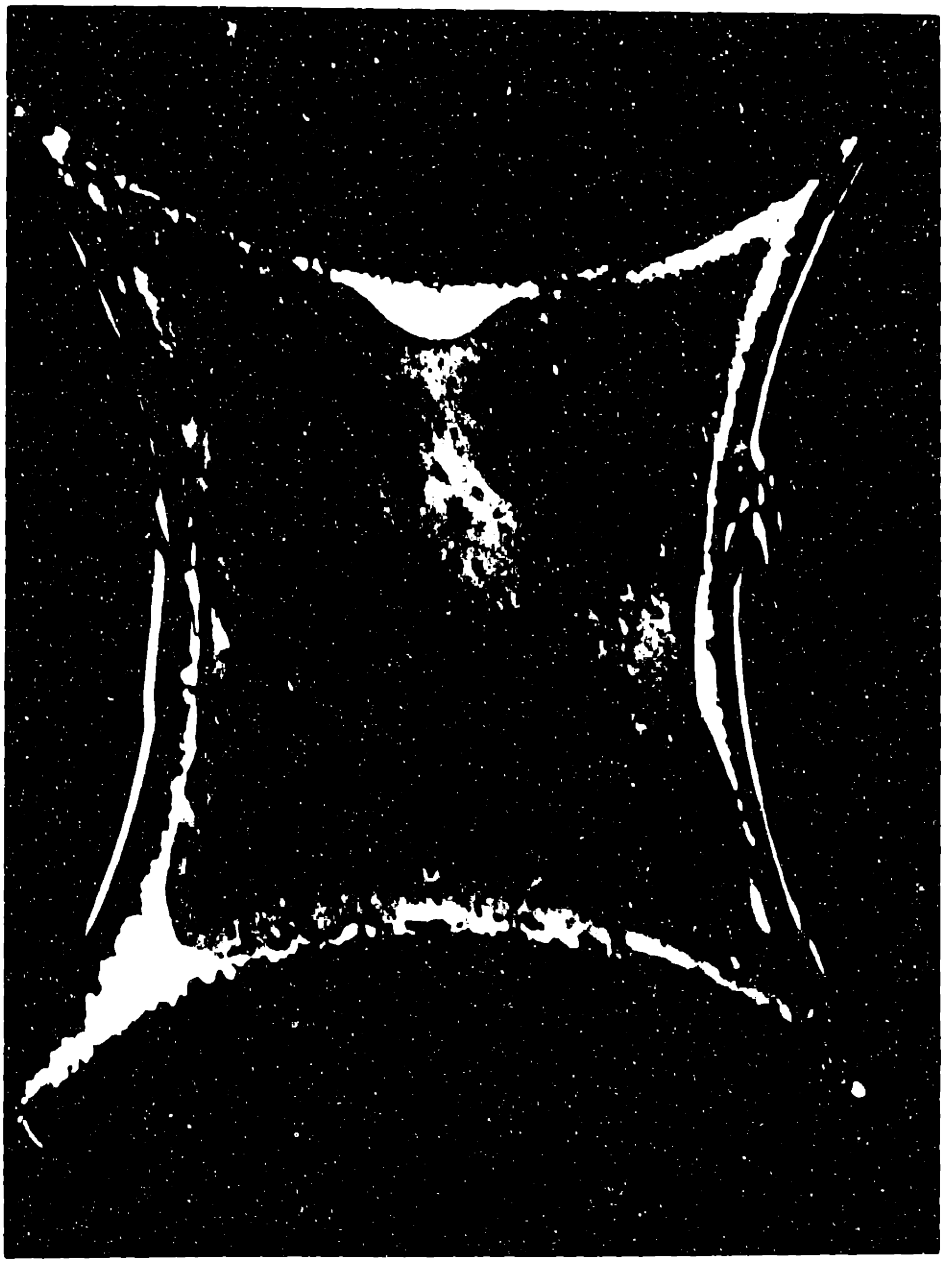

Figure 16 - Two steps of the dendrite arm coalescence process can be traced with this backscattered electron image. Darker metal areas are solute poor and hence solidified first.

20 μm

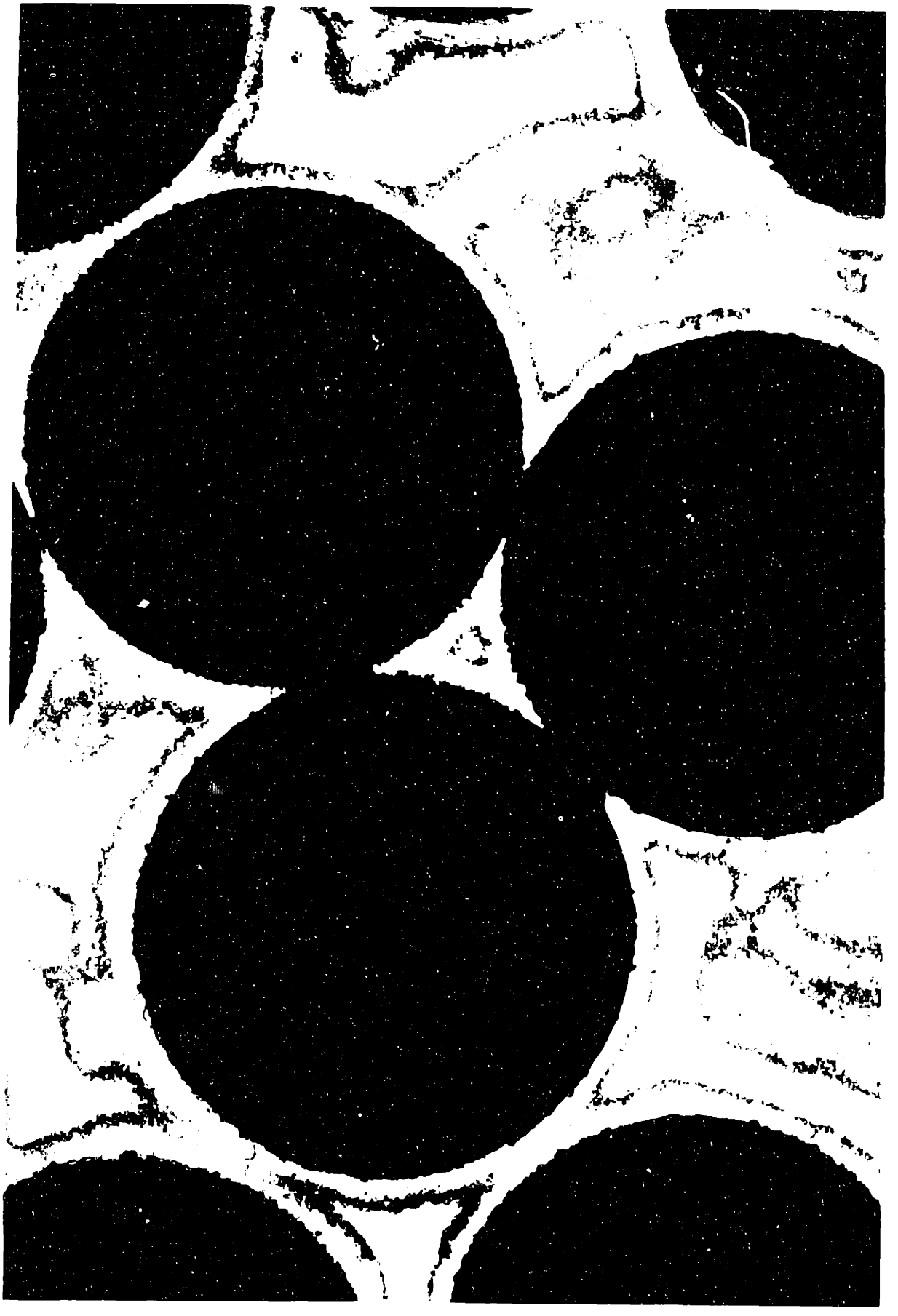

Figure 17 - Transverse microstructure of a fully solidified composite (quenched from a temperature below T_E) . Sample I-1. ——— 50 μm
Solidification time t_f = 54 seconds.

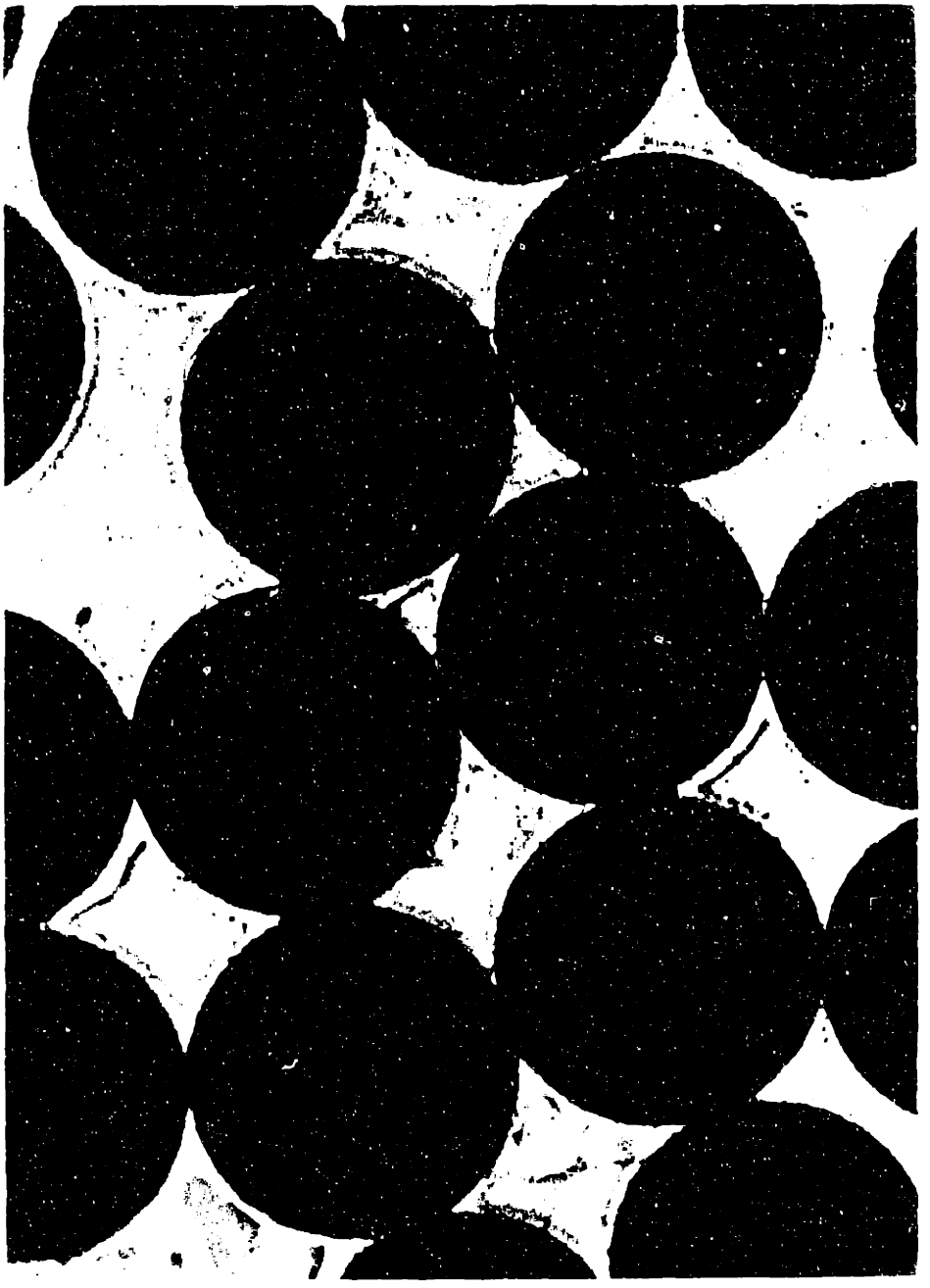

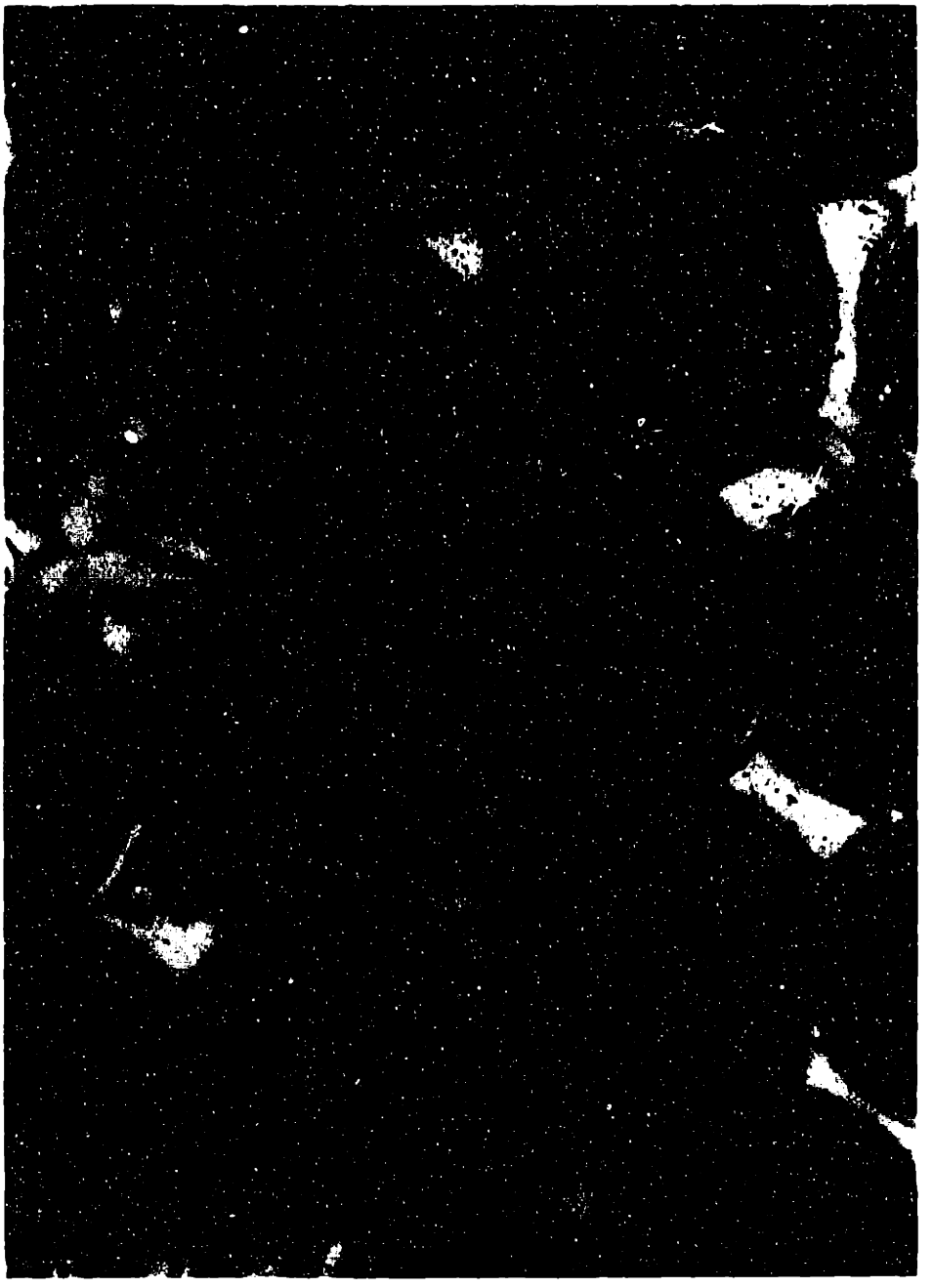

Figure 18 - Transverse microstructure of a fully solidified composite (quenched from a temperature below T_E). Sample I-1. ——— 50 μm

INTENTIONAL DUPLICATE EXPOSURE

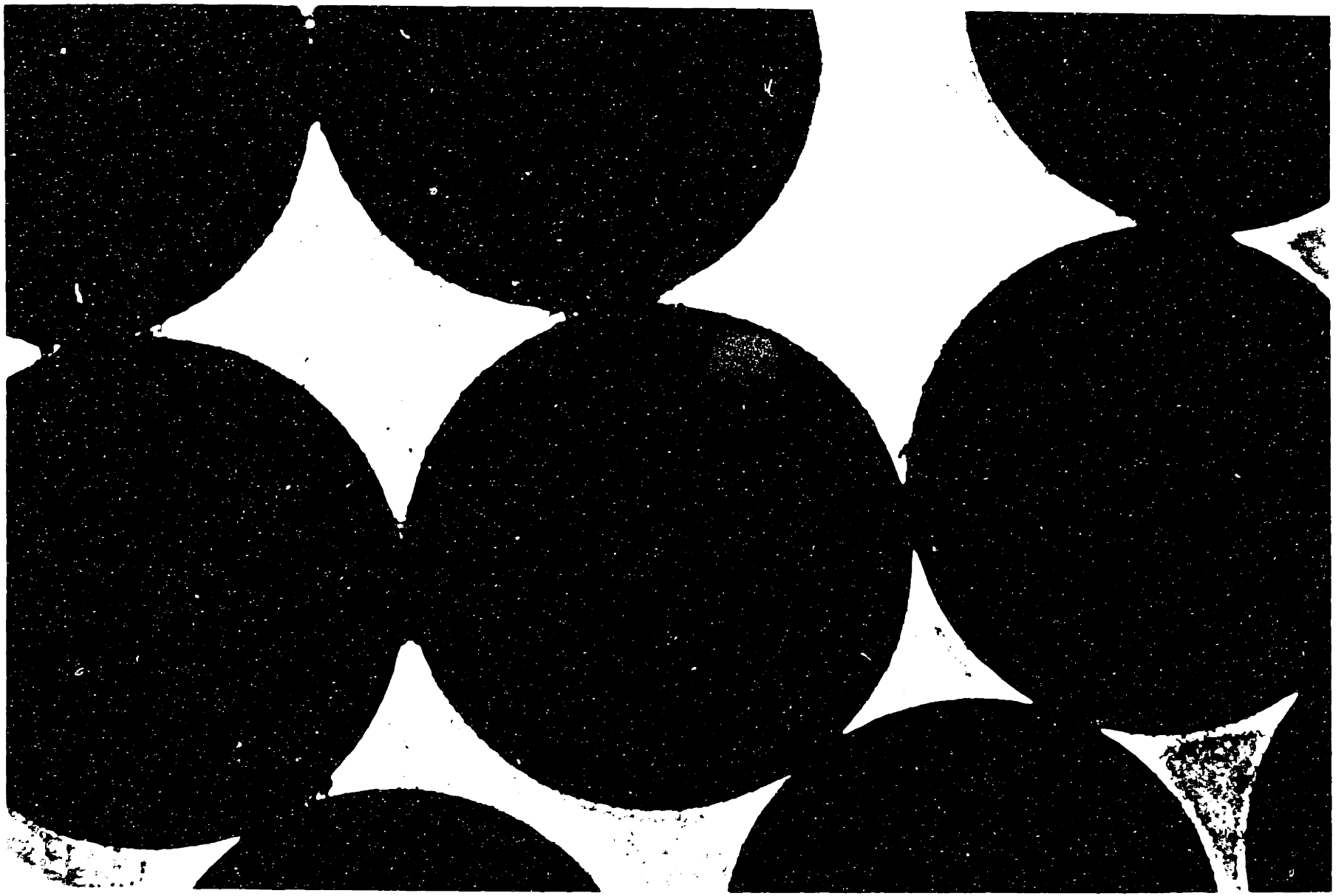

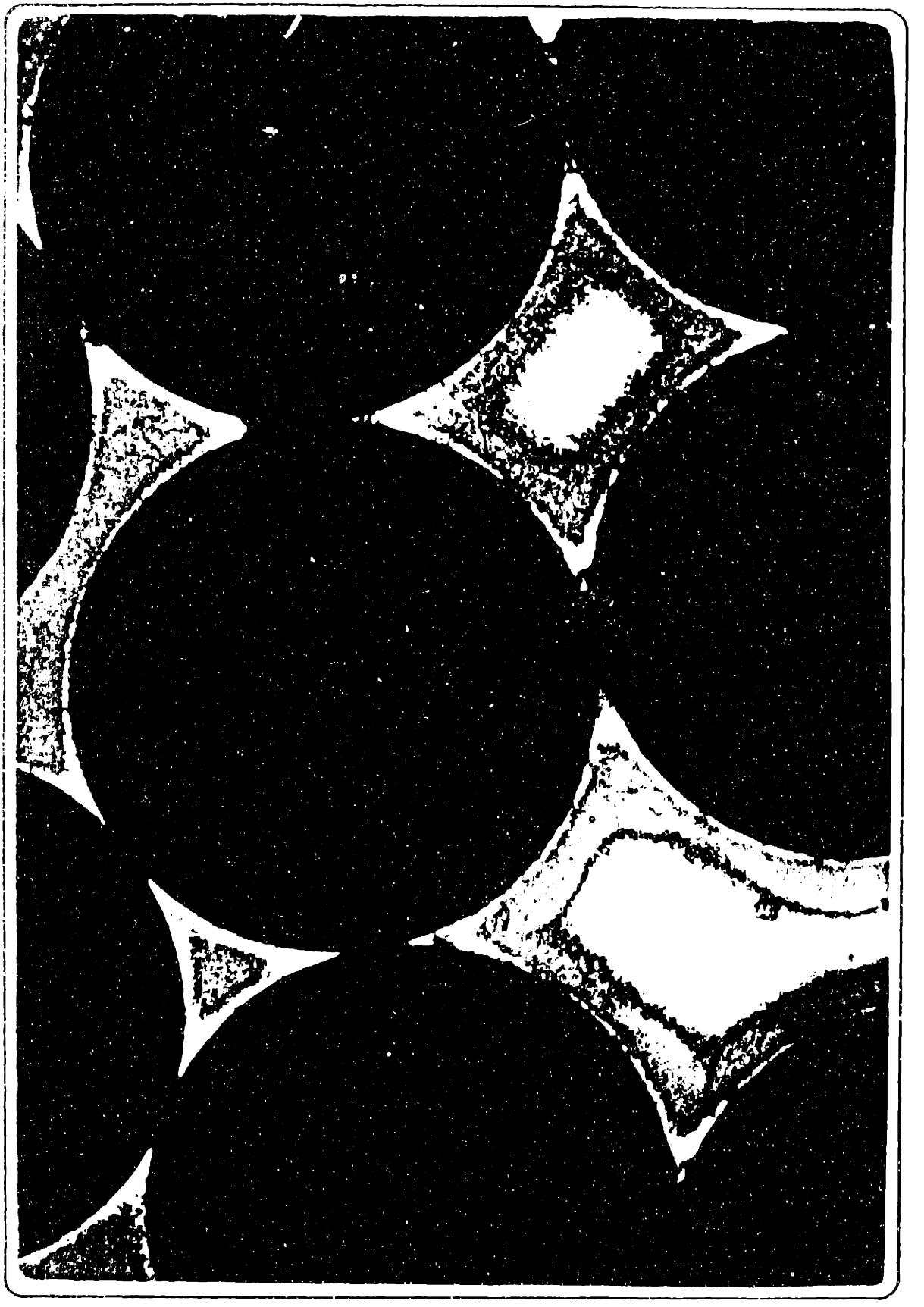

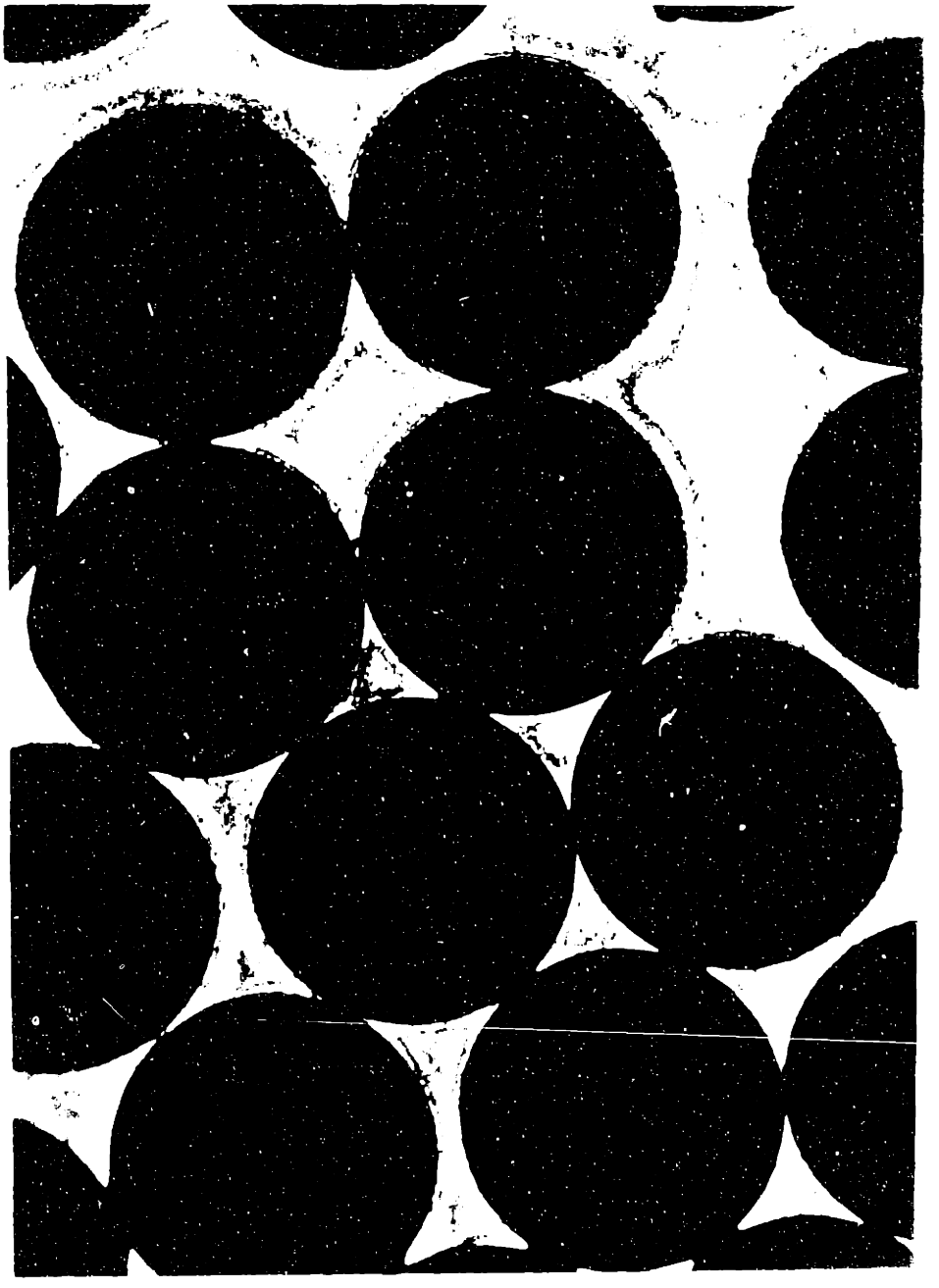

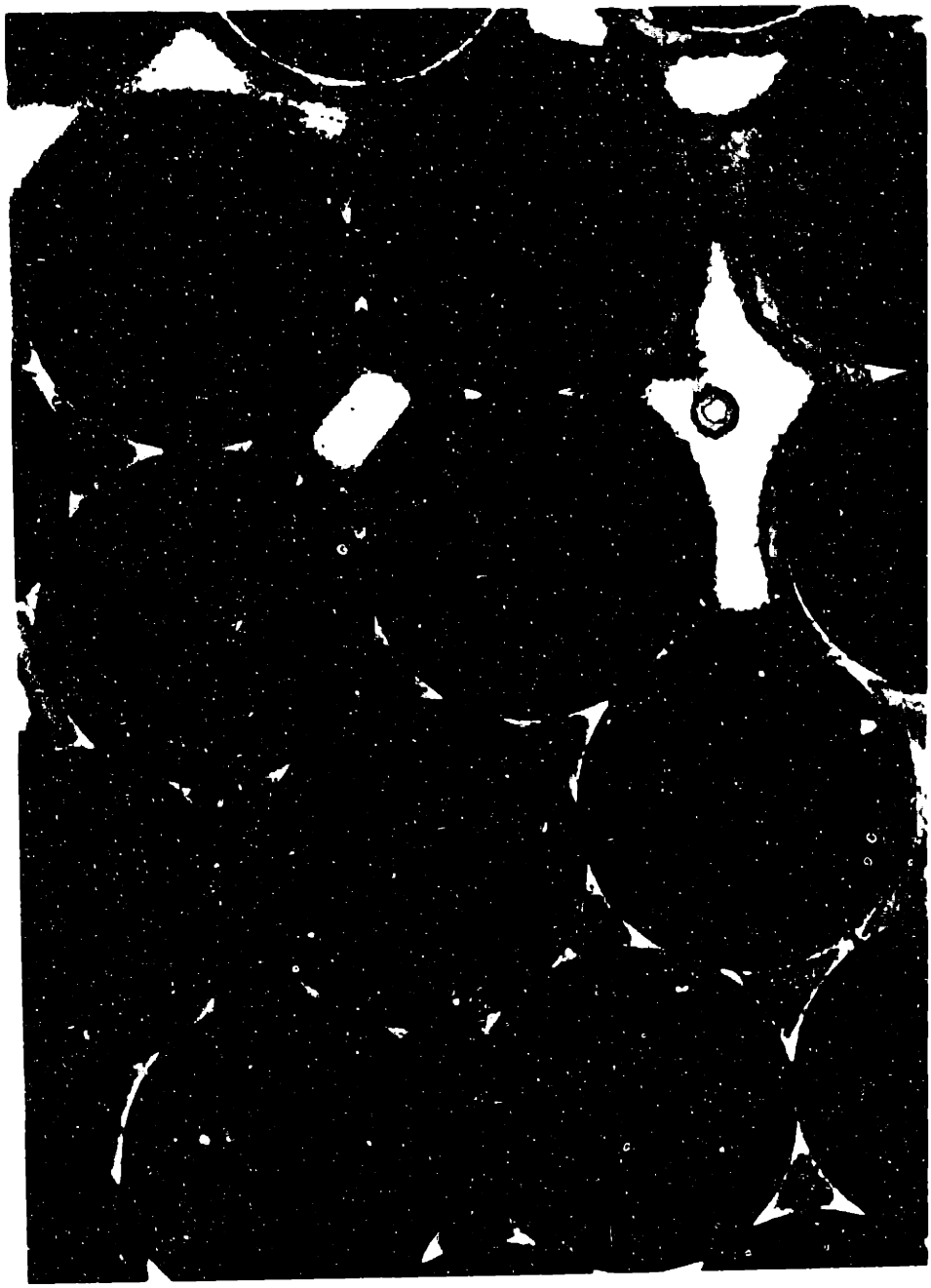

Figure 20 - Transverse microstructure of a fully solidified composite (quenched from a temperature below T_E). Sample H-4 ——— 50 μm

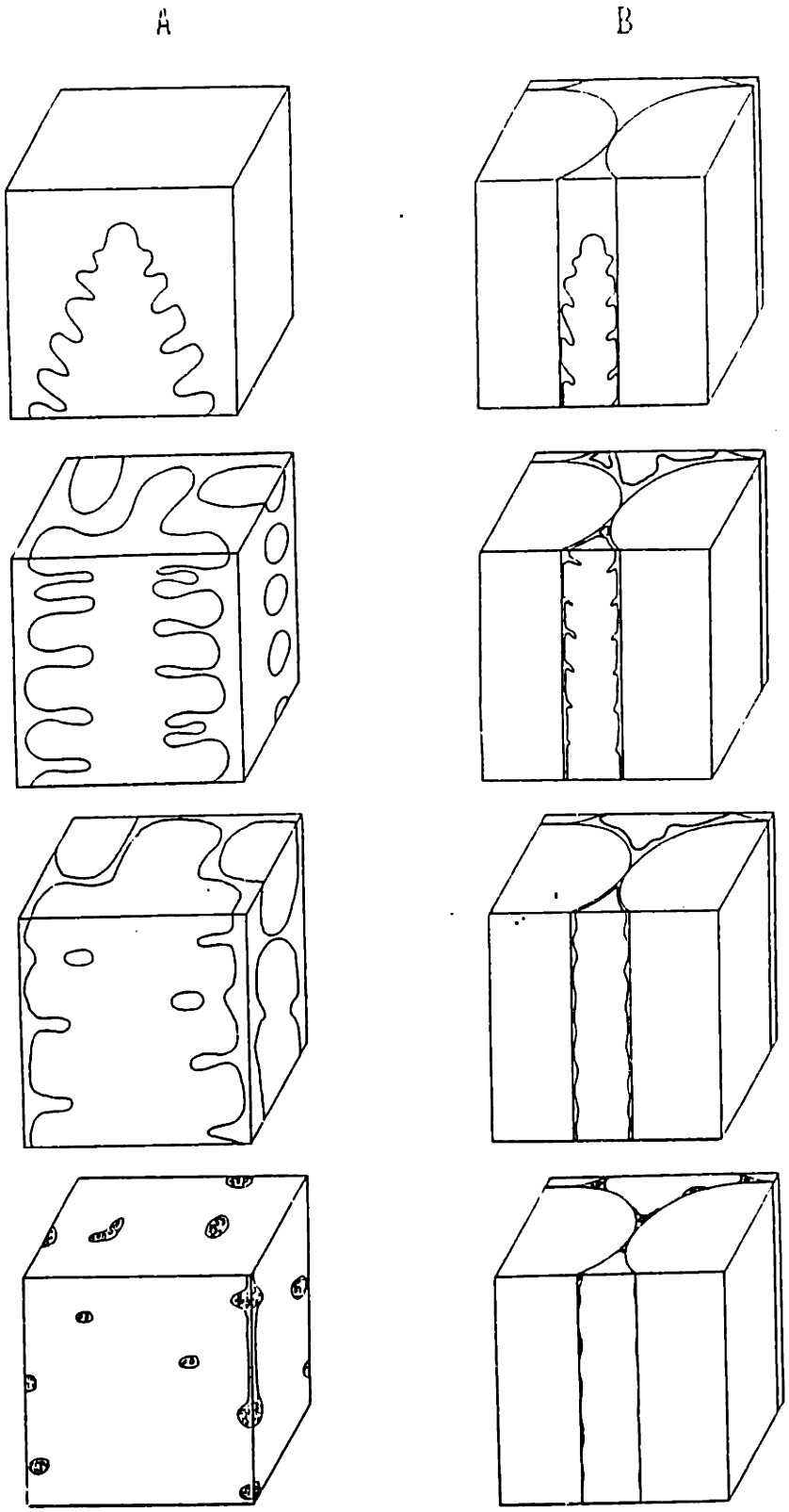

Figure 21 - Schematic rendition of the secondary dendrite arm coarsening process in:
A - fiber-free primary dendrite arms,
B - between fibers.

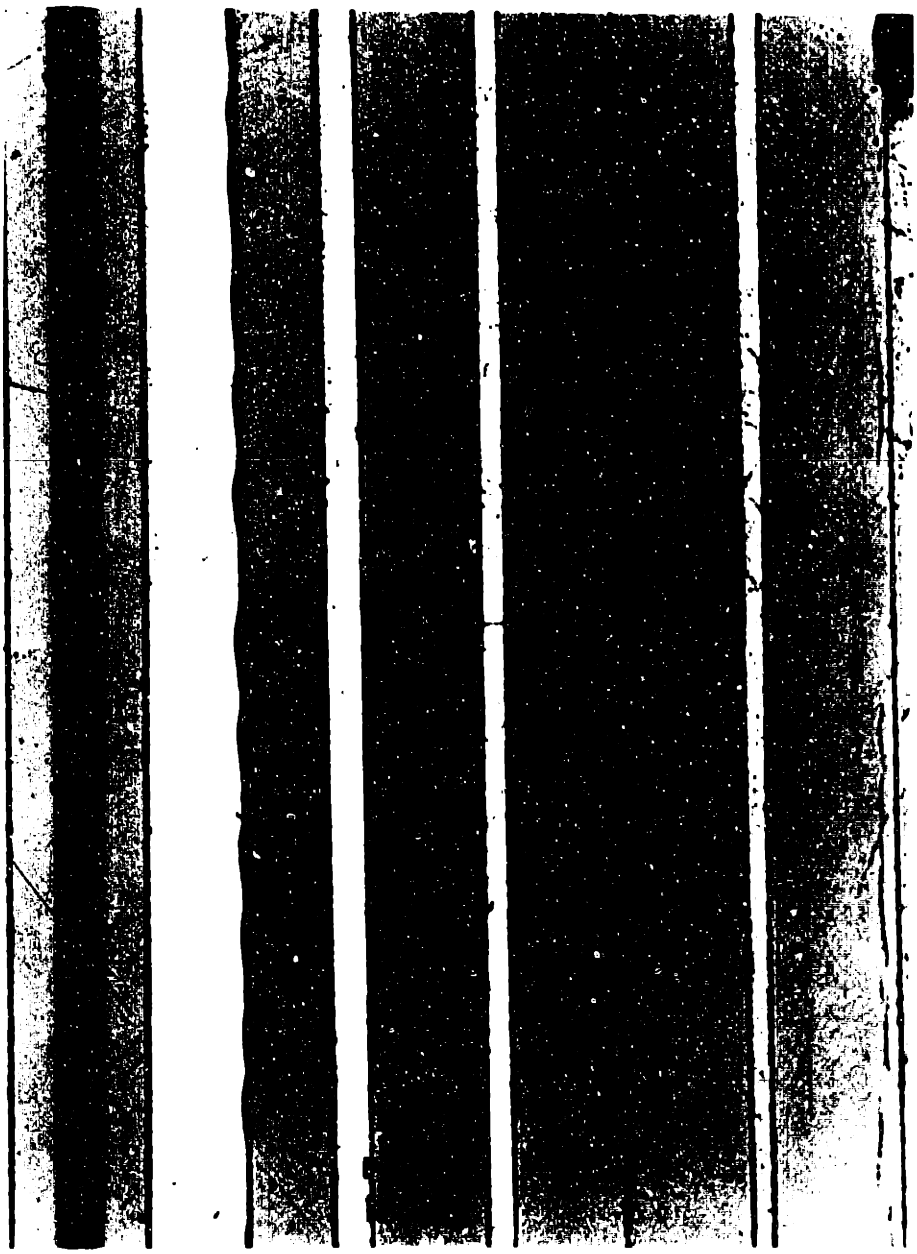

Figure 22 - A longitudinal cut in the liquid/solid region of sample I-5 (after an isothermal hold).

200 m

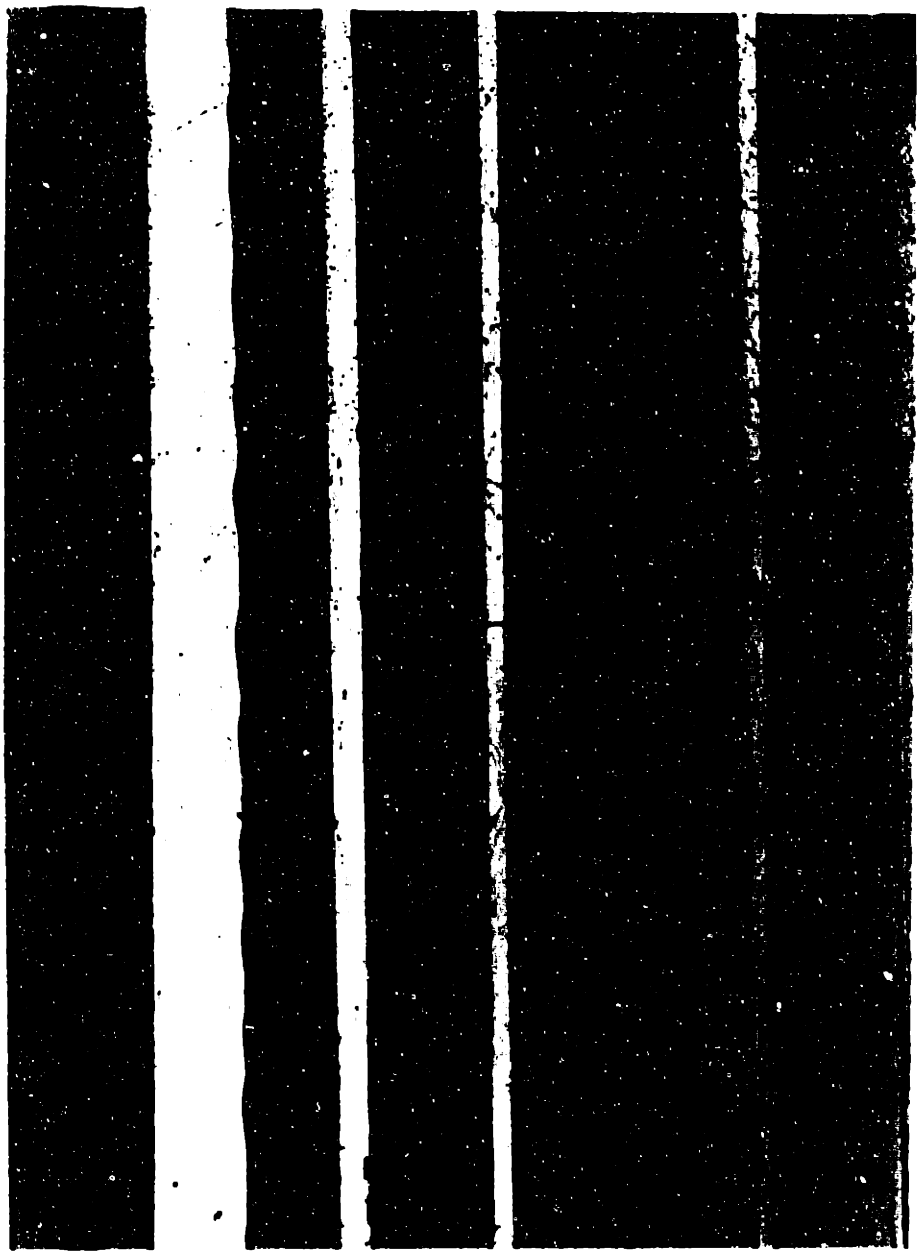

Figure 22 - A longitudinal cut in the liquid/solid region of sample I-5 (after an isothermal hold).

200 μm

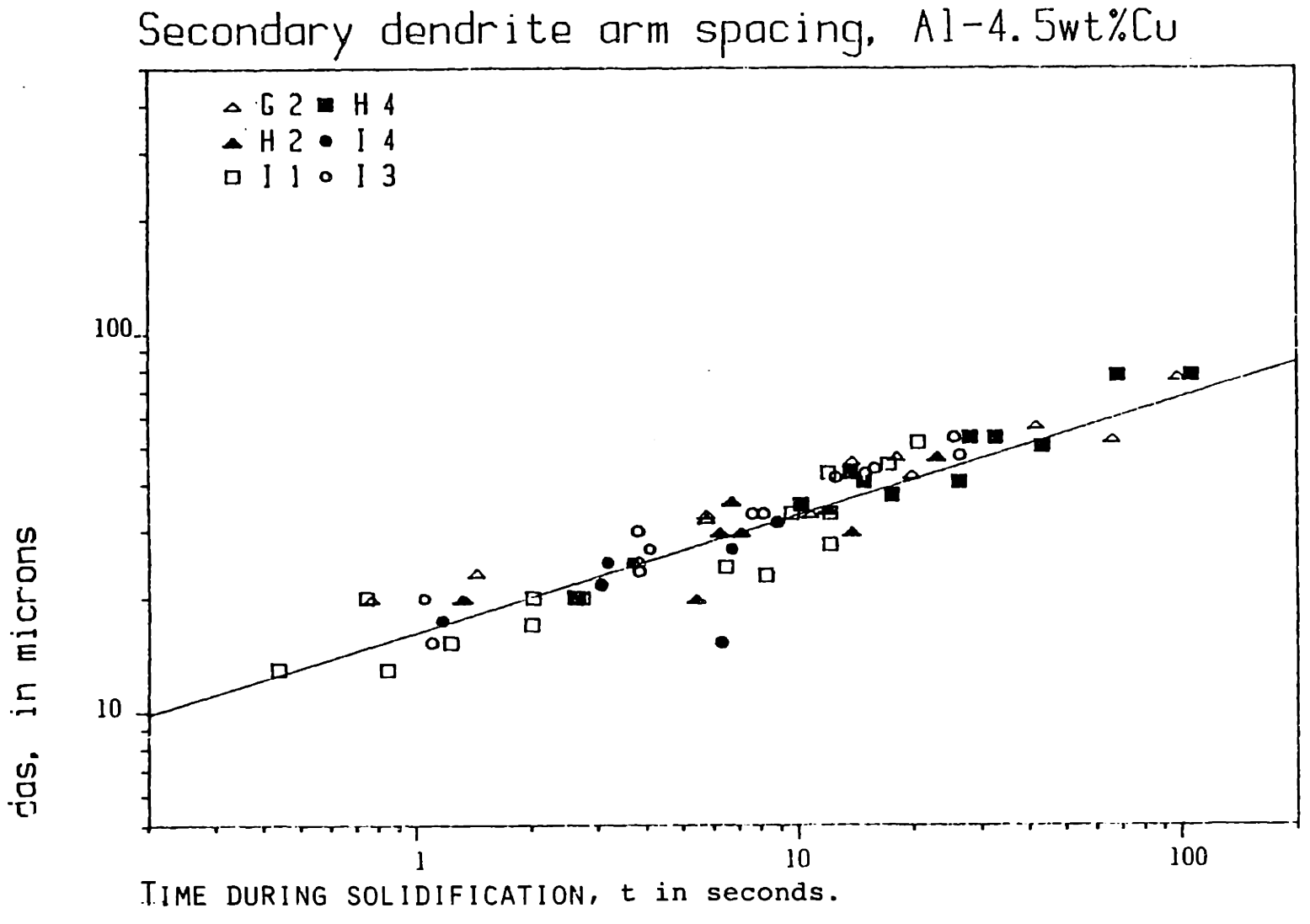

Figure 23 - Secondary dendrite arm spacing measurements from the fiber-free matrix. The straight line is from Young and Kirkwood's experimental correlation [149]. Experimental data points are from samples solidified in the dendritic growth regime.

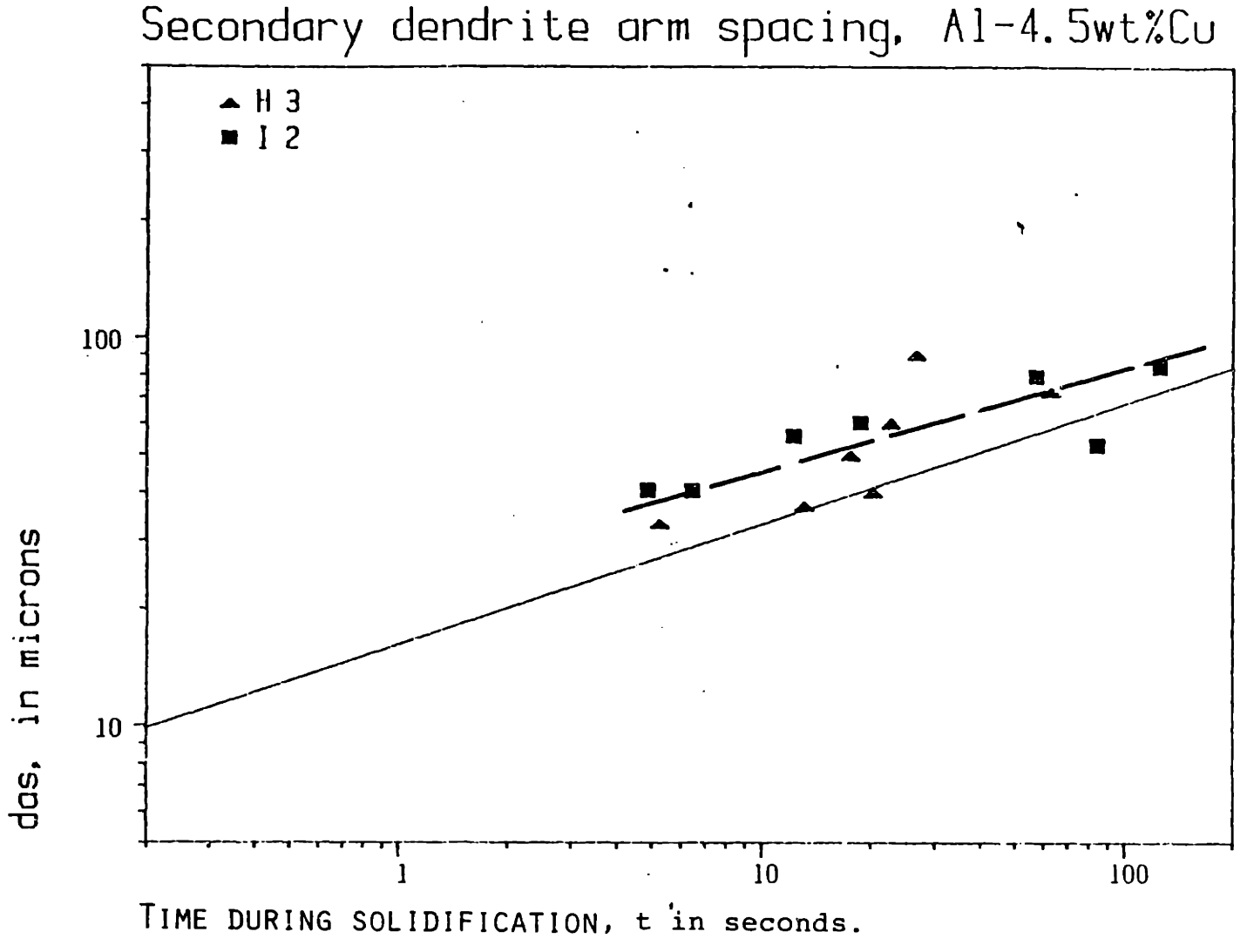

Figure 24 - Secondary dendrite arm spacing measurements from the fiber-free matrix. The straight line is from Young and Kirkwood's experimental correlation [149]. Experimental data points are from samples solidified in the cellular-dendritic growth regime.

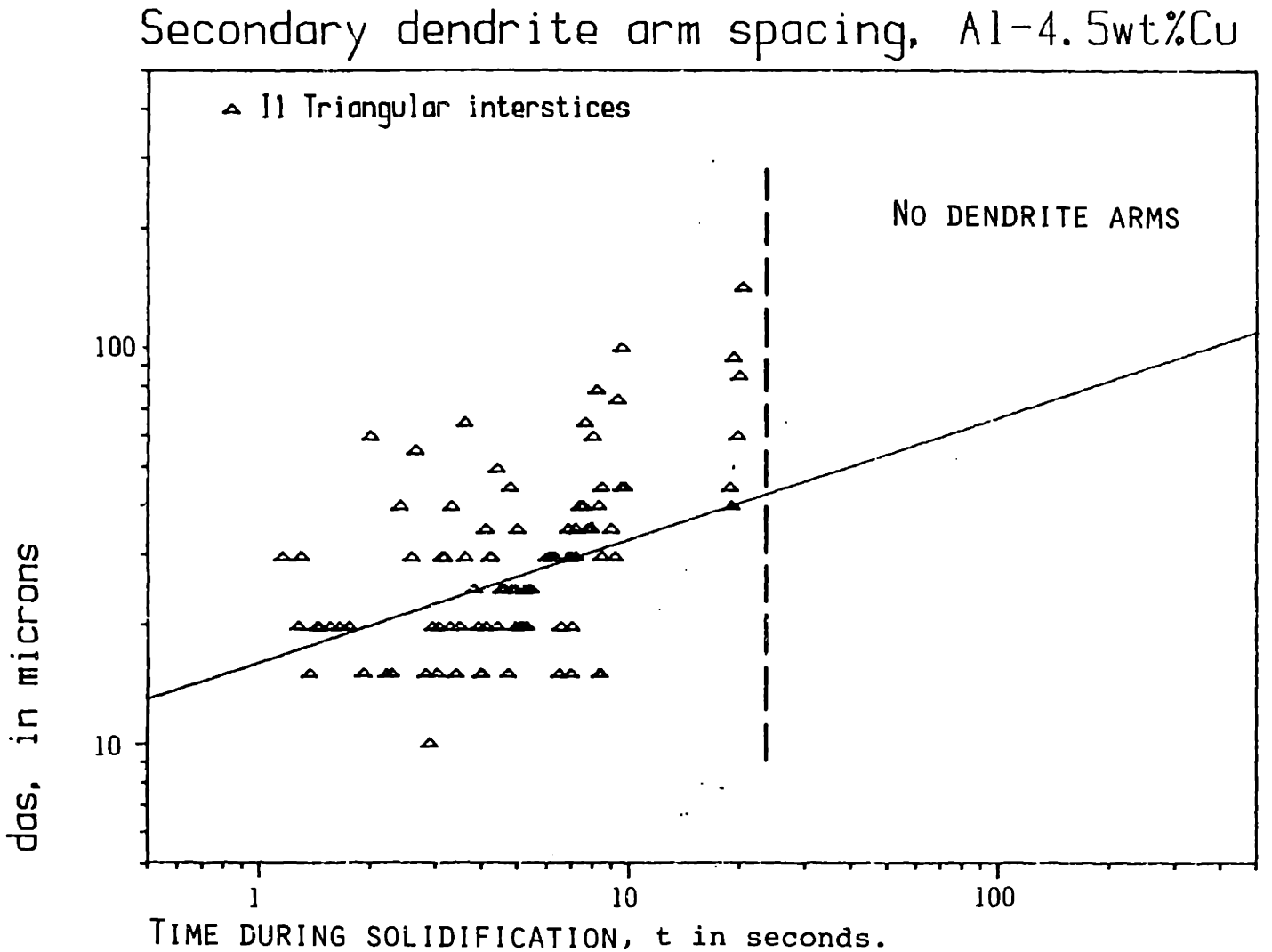

Figure 25 - Individual secondary dendrite arm spacings in triangular interstices of sample I-1. The straight line is Young and Kirkwood's experimental correlation [149]. The solidification time t_f is 54 seconds.

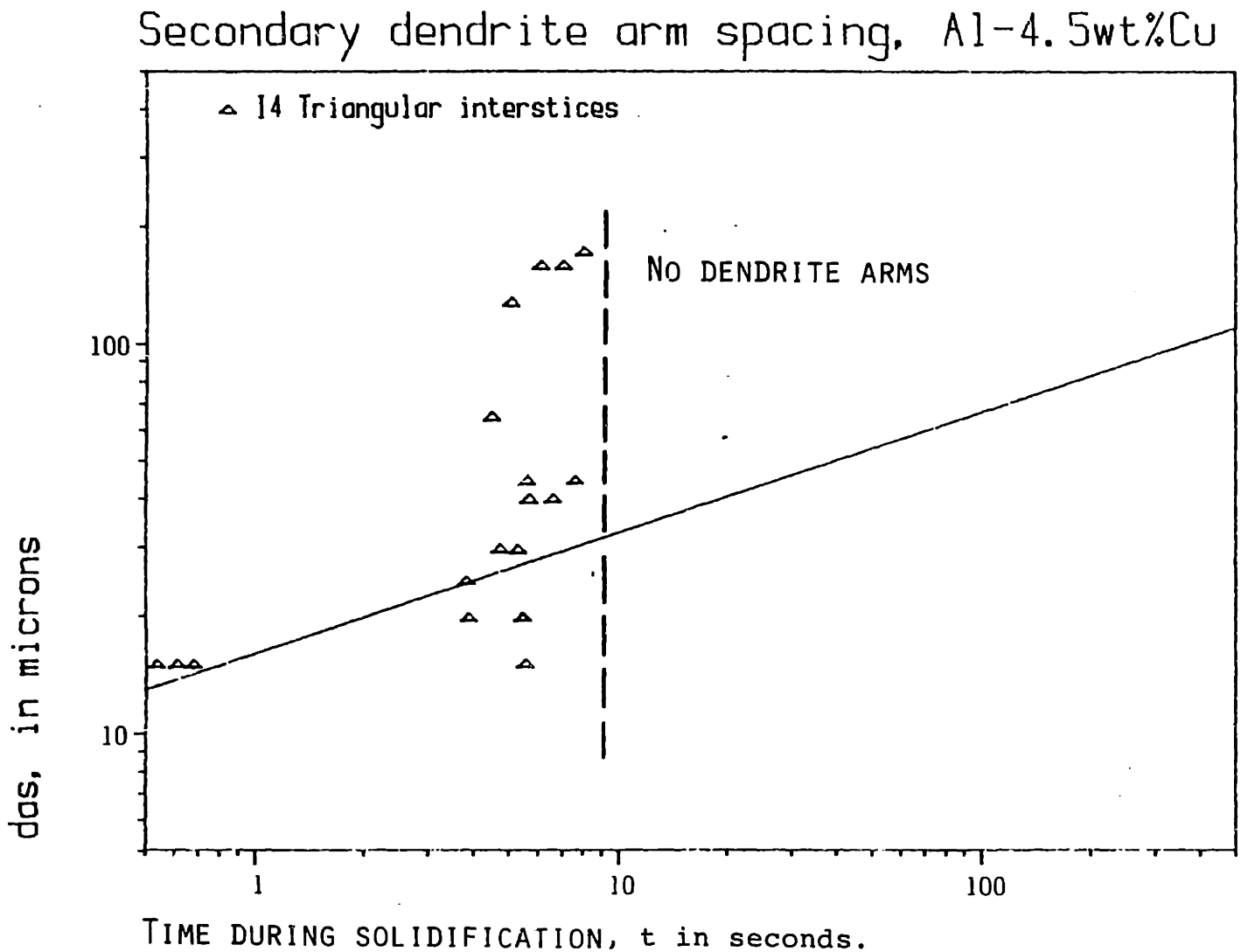

Figure 26 - Individual secondary dendrite arm spacings in triangular interstices of sample I-4. The straight line is Young and Kirkwood's experimental correlation [149]. The solidification time t_f is 84 seconds.

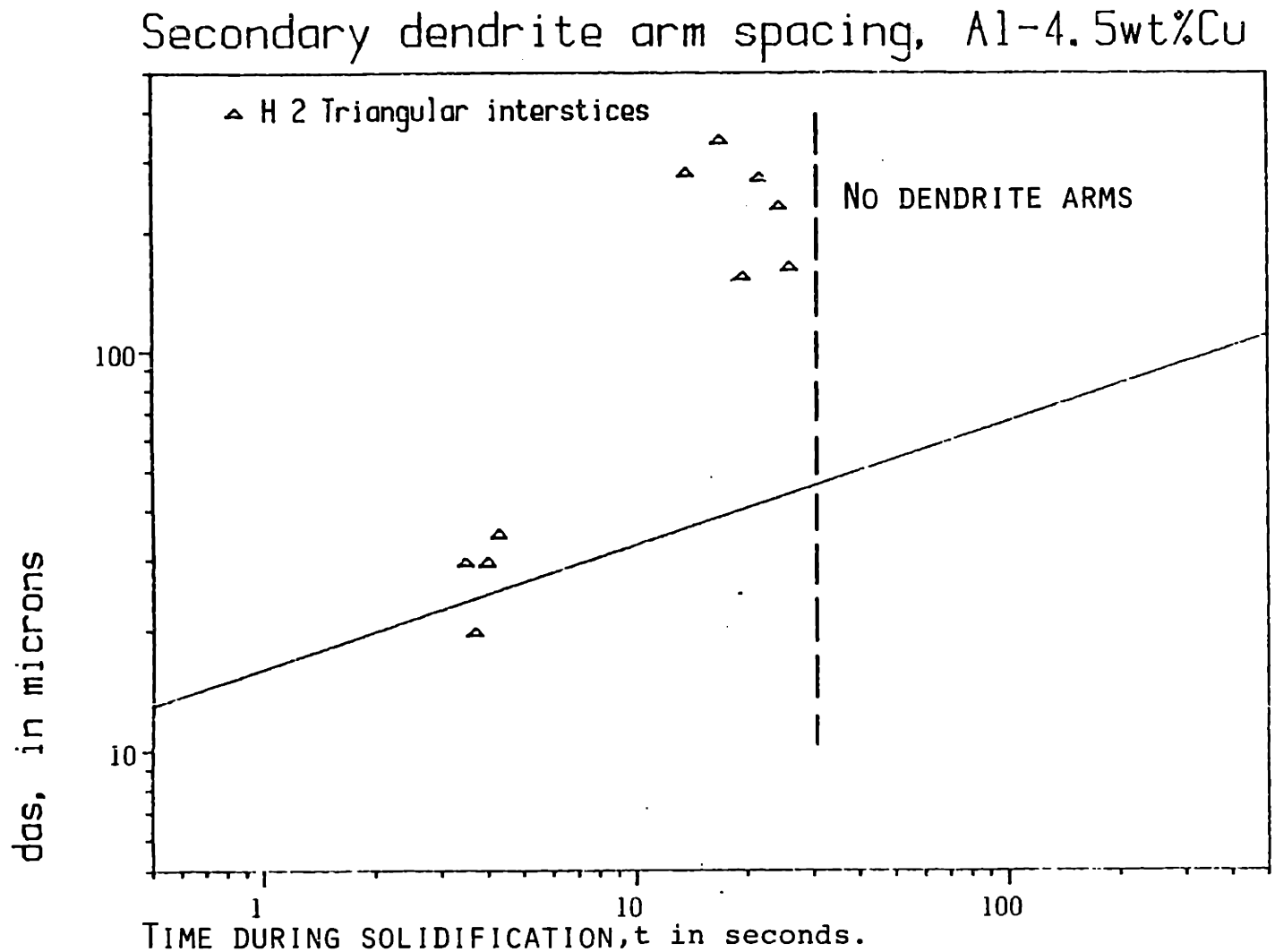

Figure 27 - Individual secondary dendrite arm spacings in triangular interstices of sample H-2. The straight line is Young and Kirkwood's experimental correlation [149]. The solidification time t_f is 133 seconds.

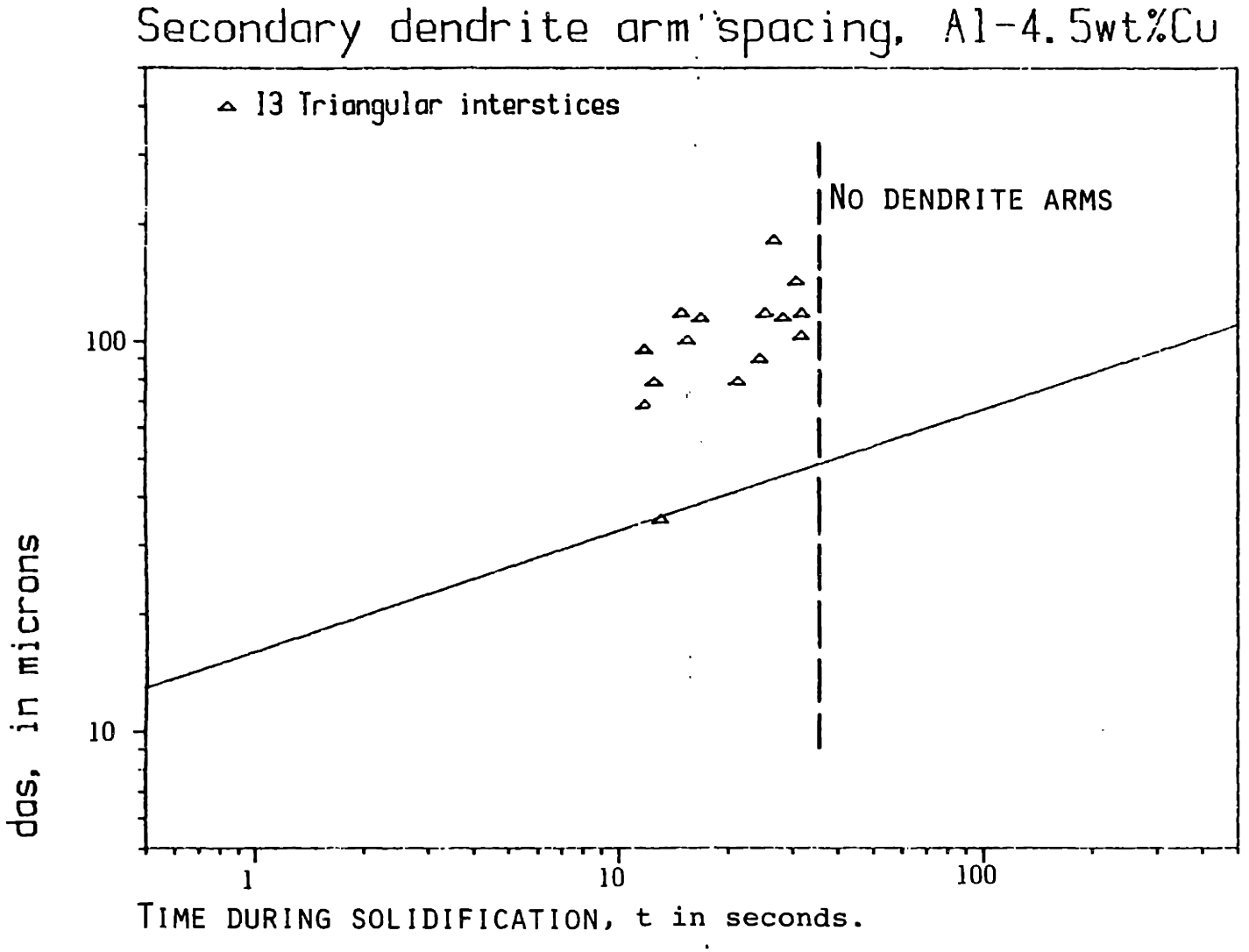

Figure 28 - Individual secondary dendrite arm spacings in triangular interstices of sample I-3. The straight line is Young and Kirkwood's experimental correlation [149]. The solidification time t_f is 187 seconds.

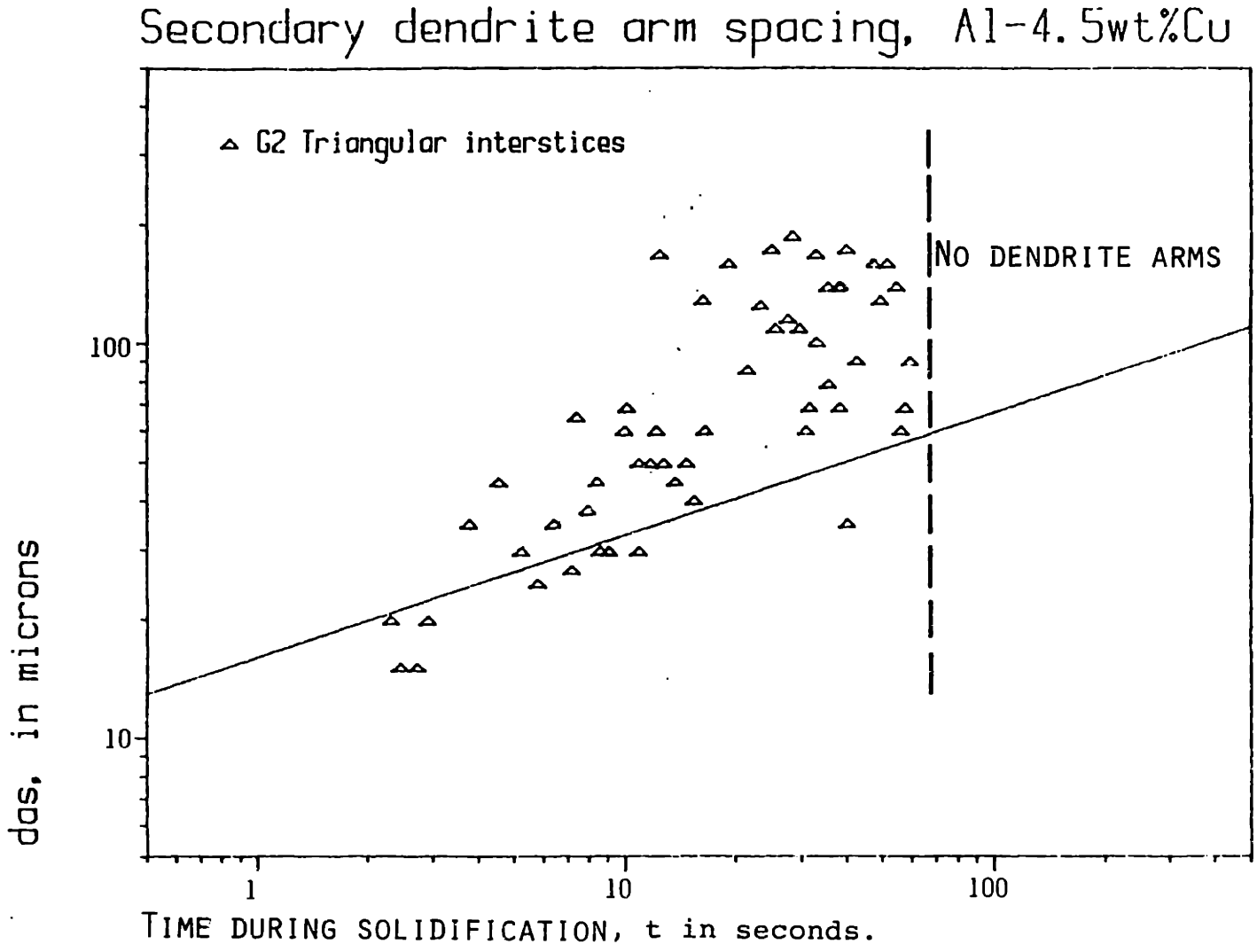

Figure 29 - Individual secondary dendrite arm spacings in triangular interstices of sample G-2. The straight line is Young and Kirkwood's experimental correlation [149]. The solidification time t_f is 268 seconds.

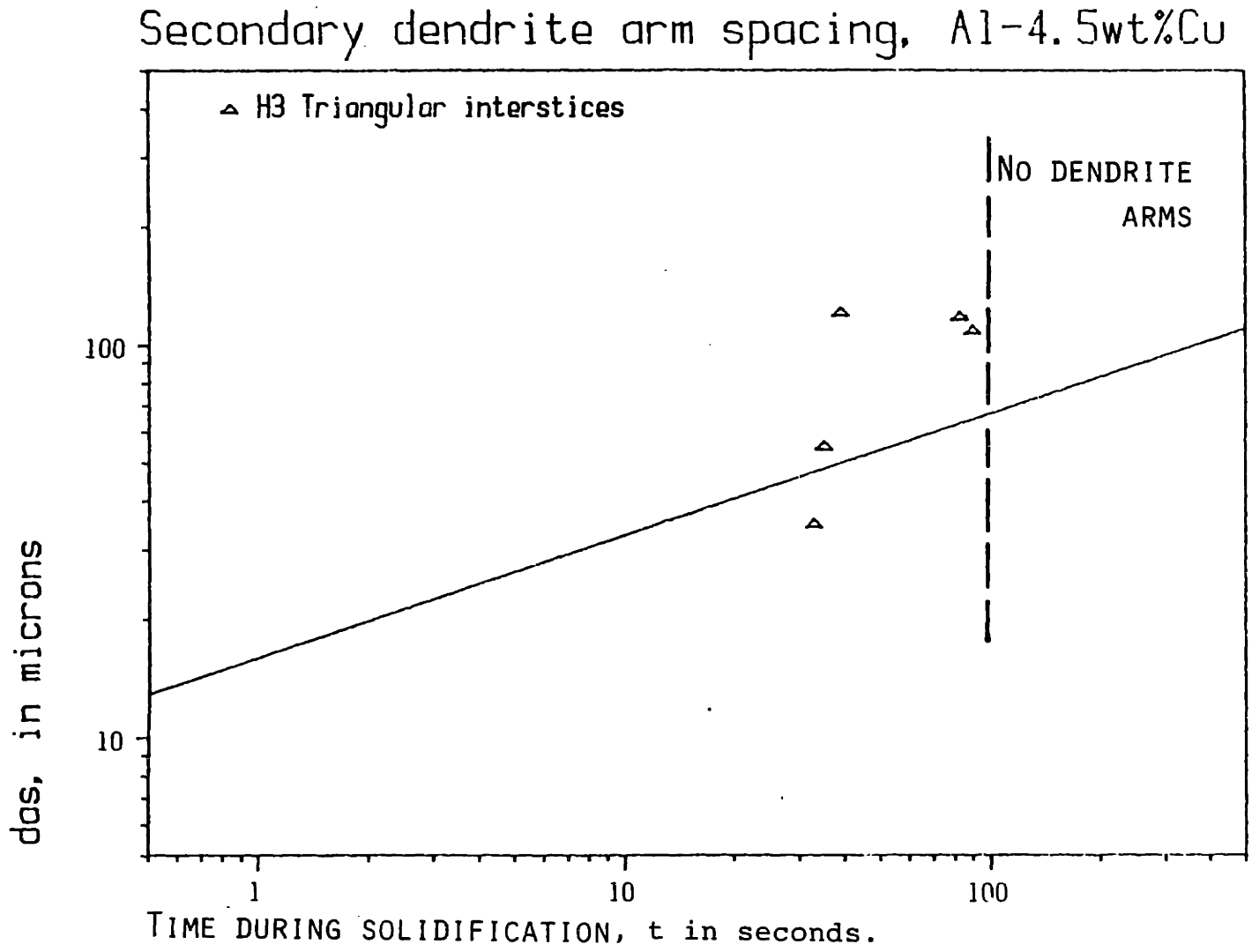

Figure 30 - Individual secondary dendrite arm spacings in triangular interstices of sample H-3. The straight line is Young and Kirkwood's experimental correlation [149]. The solidification time t_f is 417 seconds.

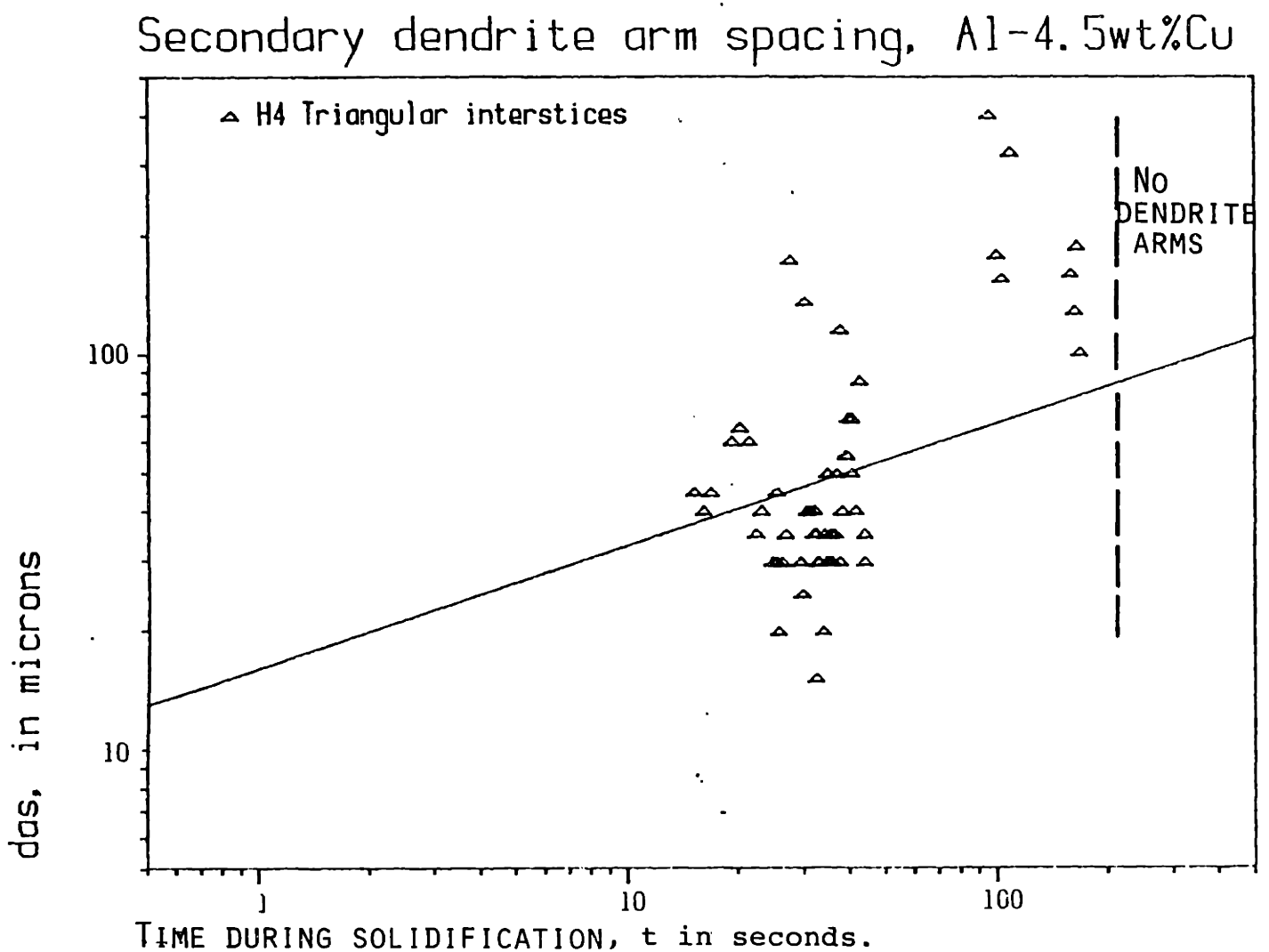

Figure 31 - Individual secondary dendrite arm spacings in triangular interstices of sample H-4. The straight line is Young and Kirkwood's experimental correlation [149]. The solidification time t_f is 417 seconds.

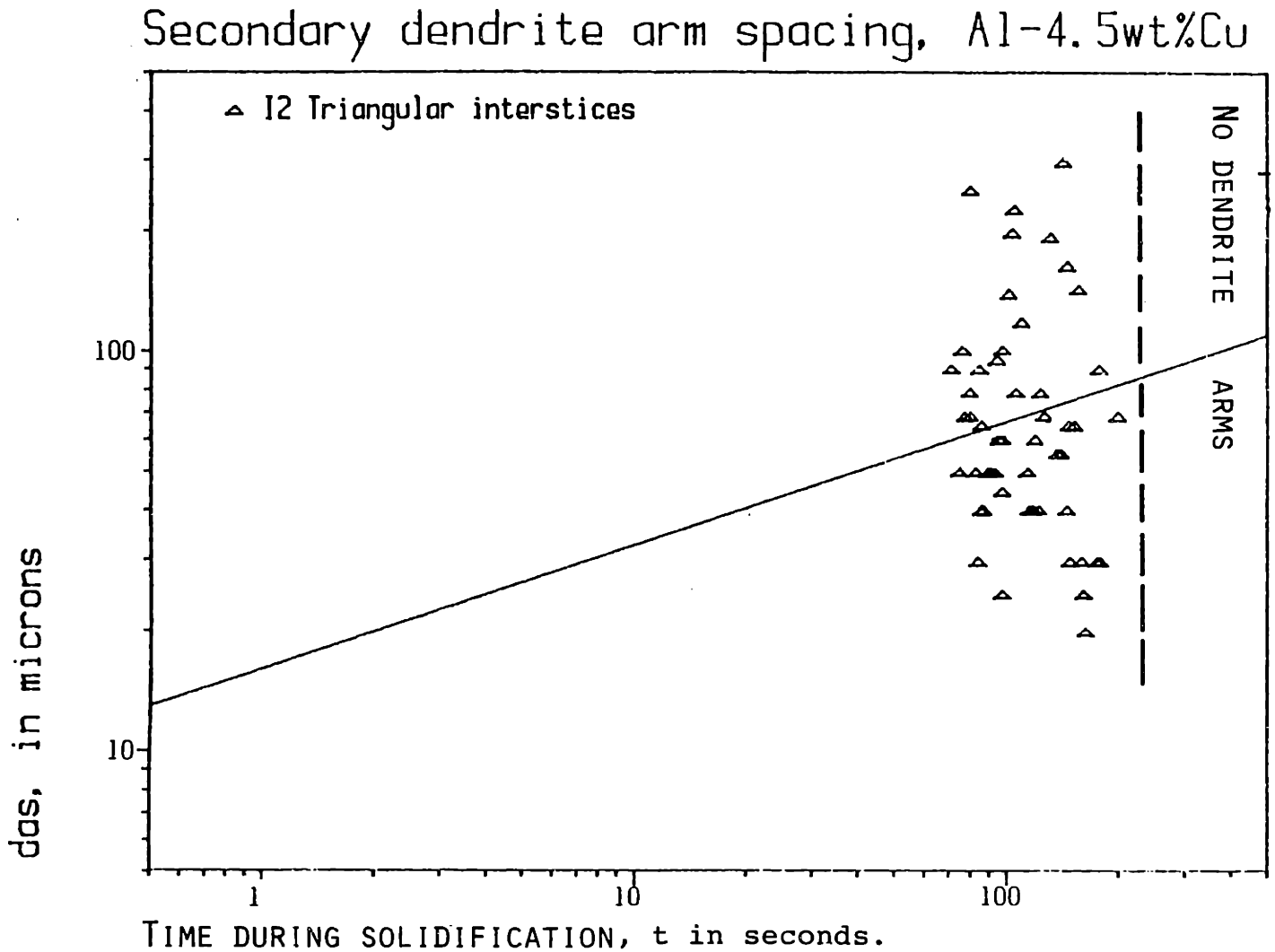

Figure 32 - Individual secondary dendrite arm spacings in triangular interstices of sample I-2. The straight line is Young and Kirkwood's experimental correlation [149]. The solidification time t_f is 940 seconds.

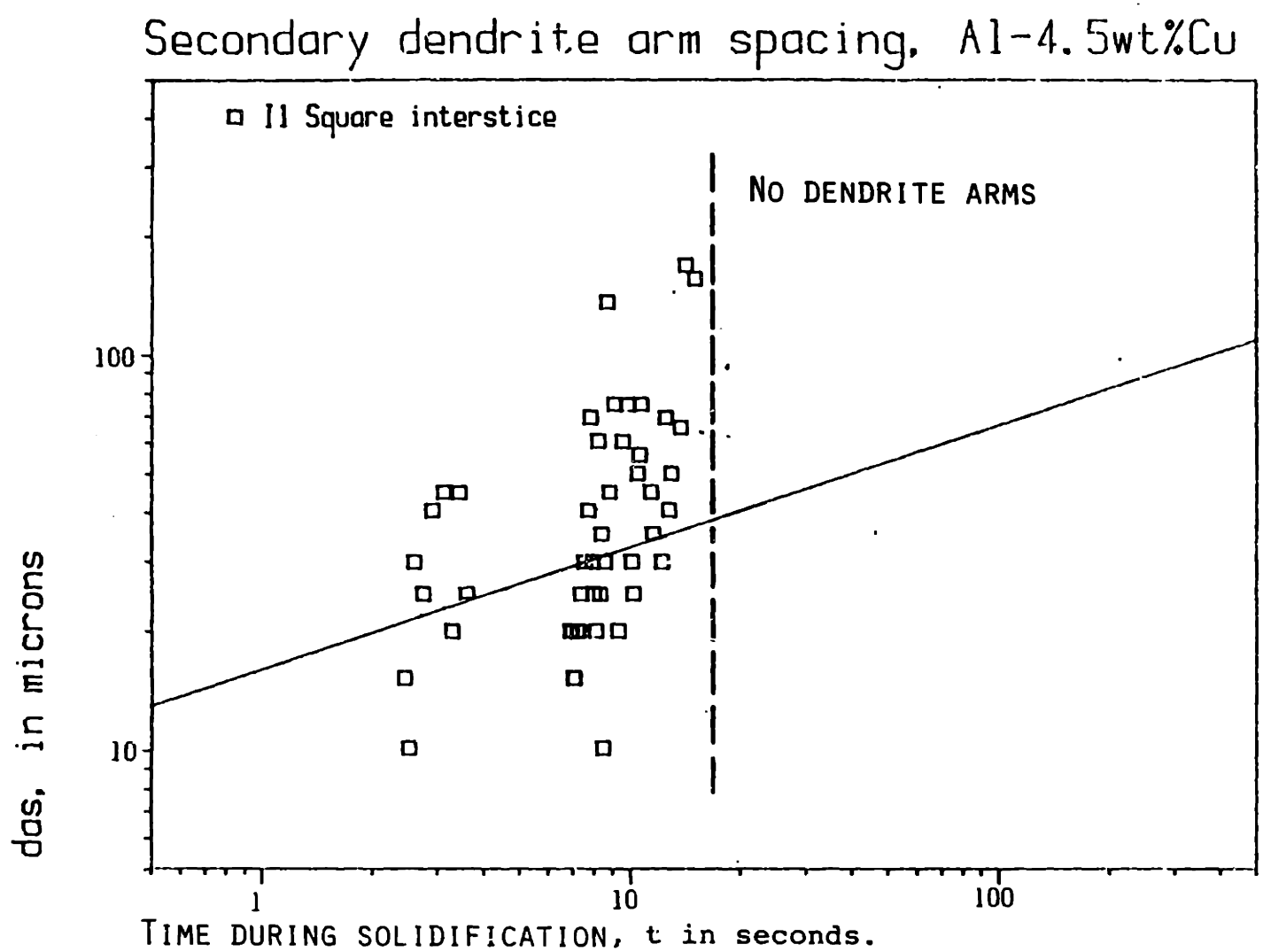

Figure 33 - Individual secondary dendrite arm spacings in square interstices of sample I-1. The straight line is Young and Kirkwood's experimental correlation [149]. The solidification time t_f is 54 seconds.

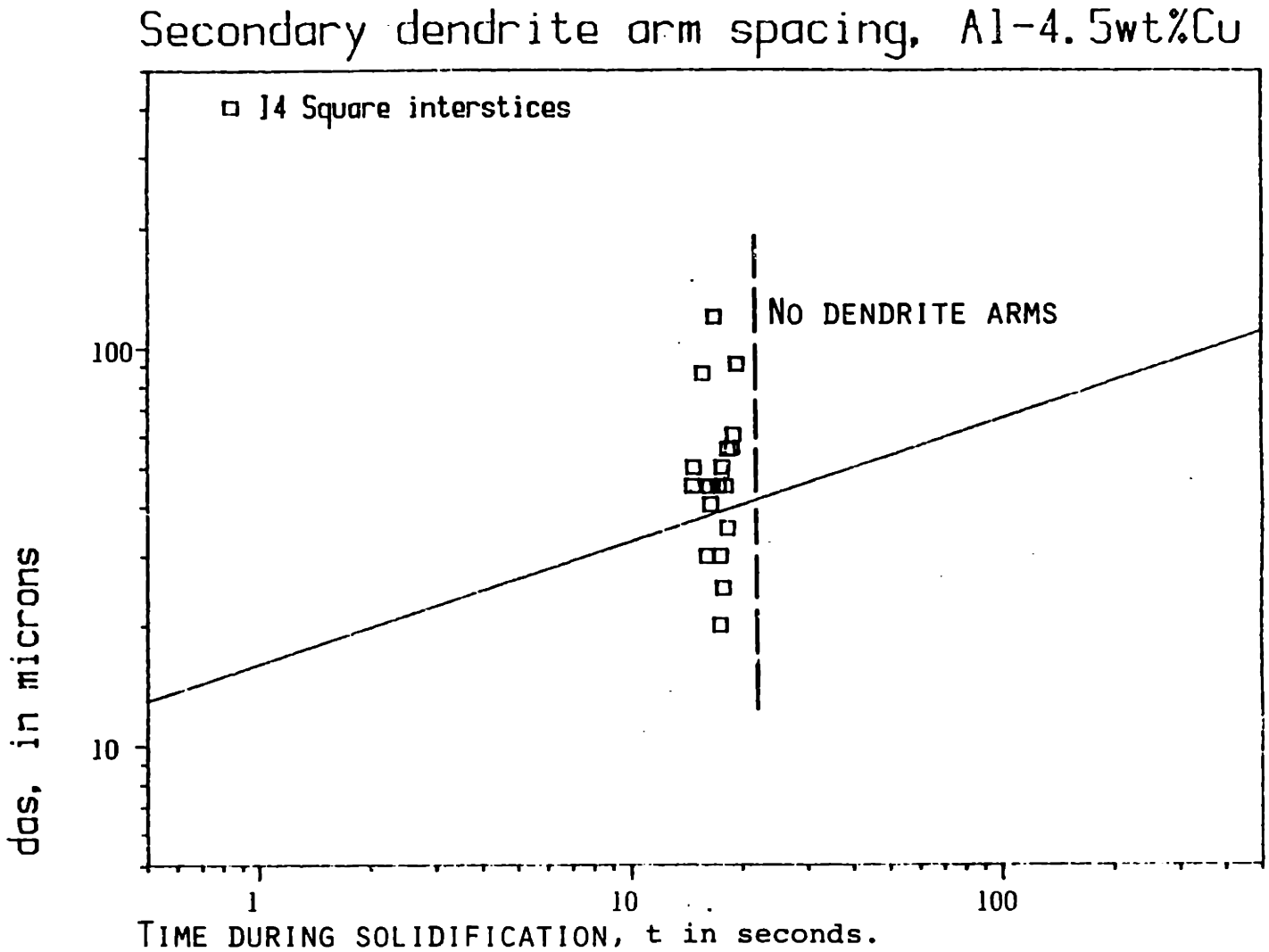

Figure 34 - Individual secondary dendrite arm spacings in square interstices of sample I-4. The straight line is Young and Kirkwood's experimental correlation [149]. The solidification time t_f is 84 seconds.

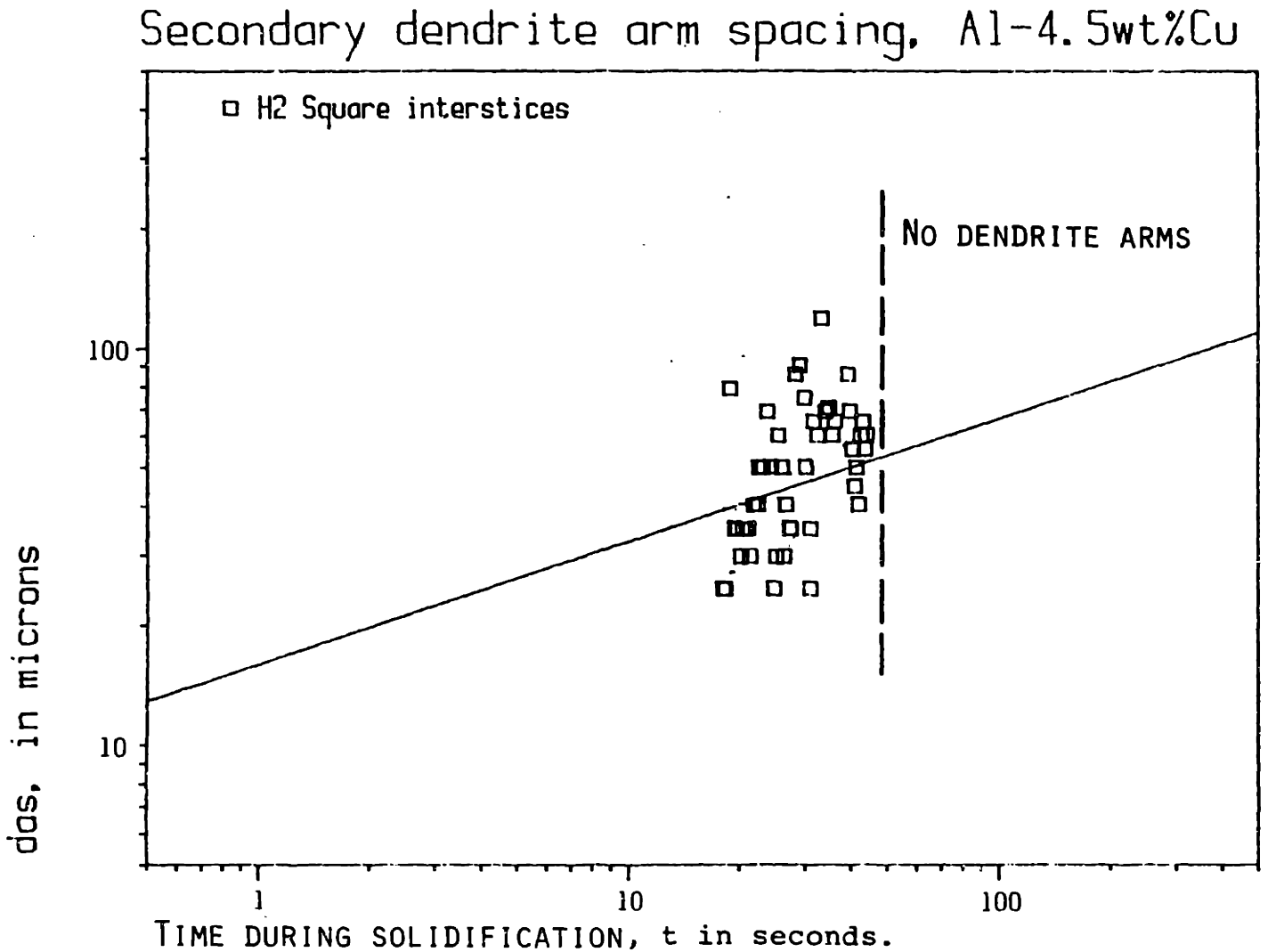

Figure 35 - Individual secondary dendrite arm spacings in square interstices of sample H-2. The straight line is Young and Kirkwood's experimental correlation [149]. The solidification time t_f is 133 seconds.

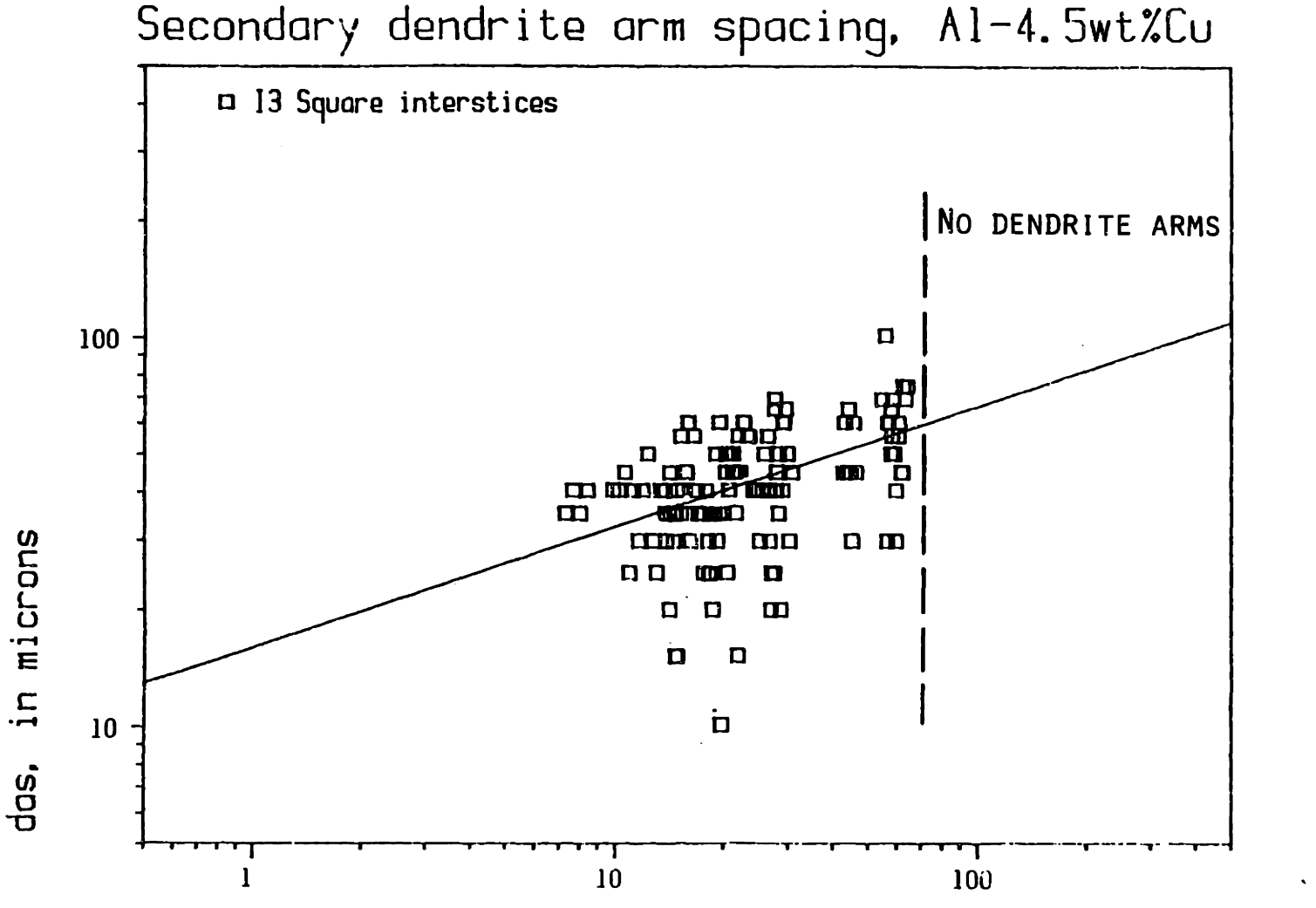

Figure 36 - Individual secondary dendrite arm spacings in square interstices of sample I-3. The straight line is Young and Kirkwood's experimental correlation [149]. The solidification time t_f is 187 seconds.

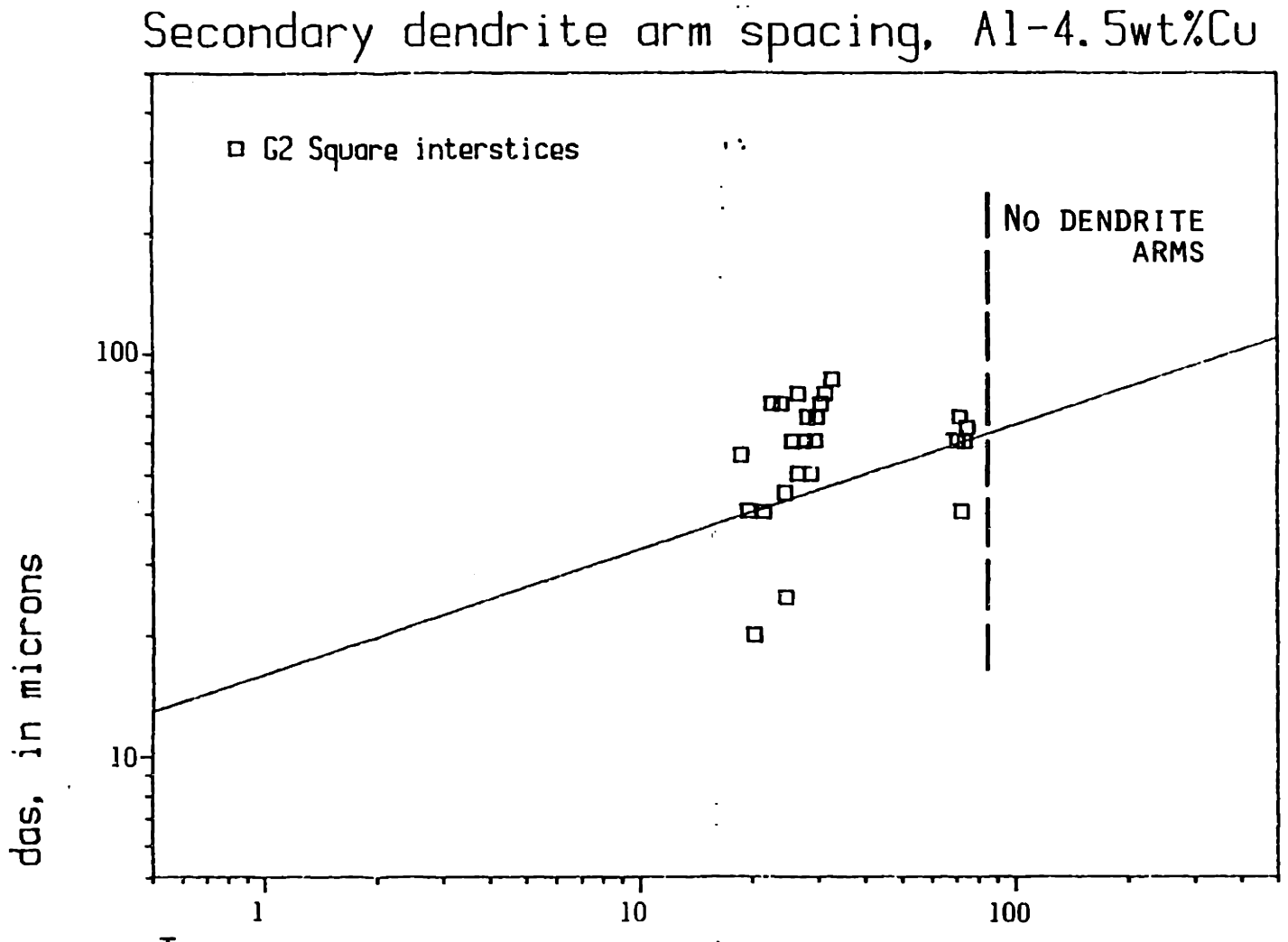

Figure 37 - Individual secondary dendrite arm spacings in square interstices of sample G-2. The straight line is Young and Kirkwood's experimental correlation [149]. The solidification time t_f is 268 seconds.

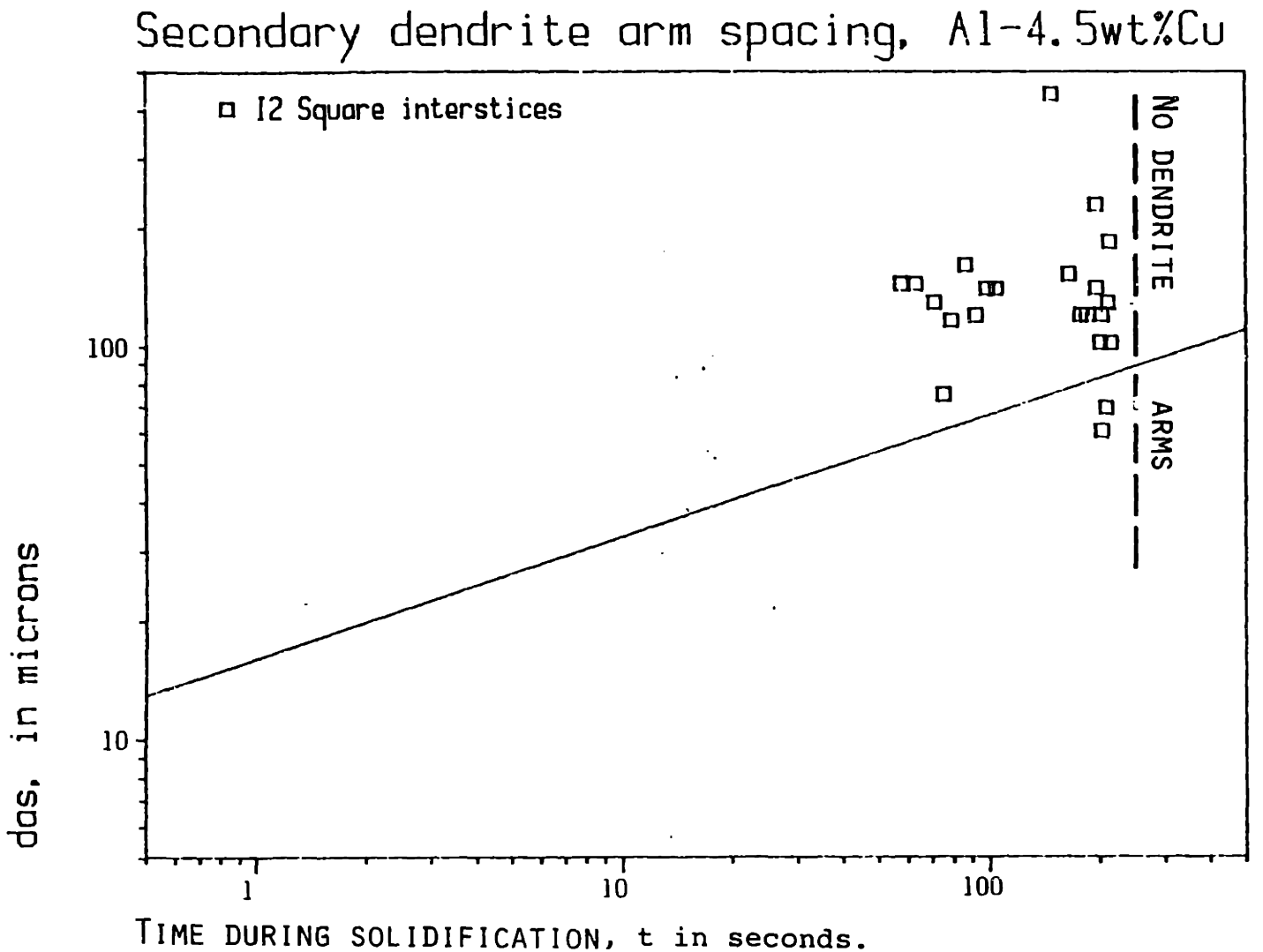

Figure 38 - Individual secondary dendrite arm spacings in square interstices of sample I-2. The straight line is Young and Kirkwood's experimental correlation [149]. The solidification time t_f is 940 seconds.

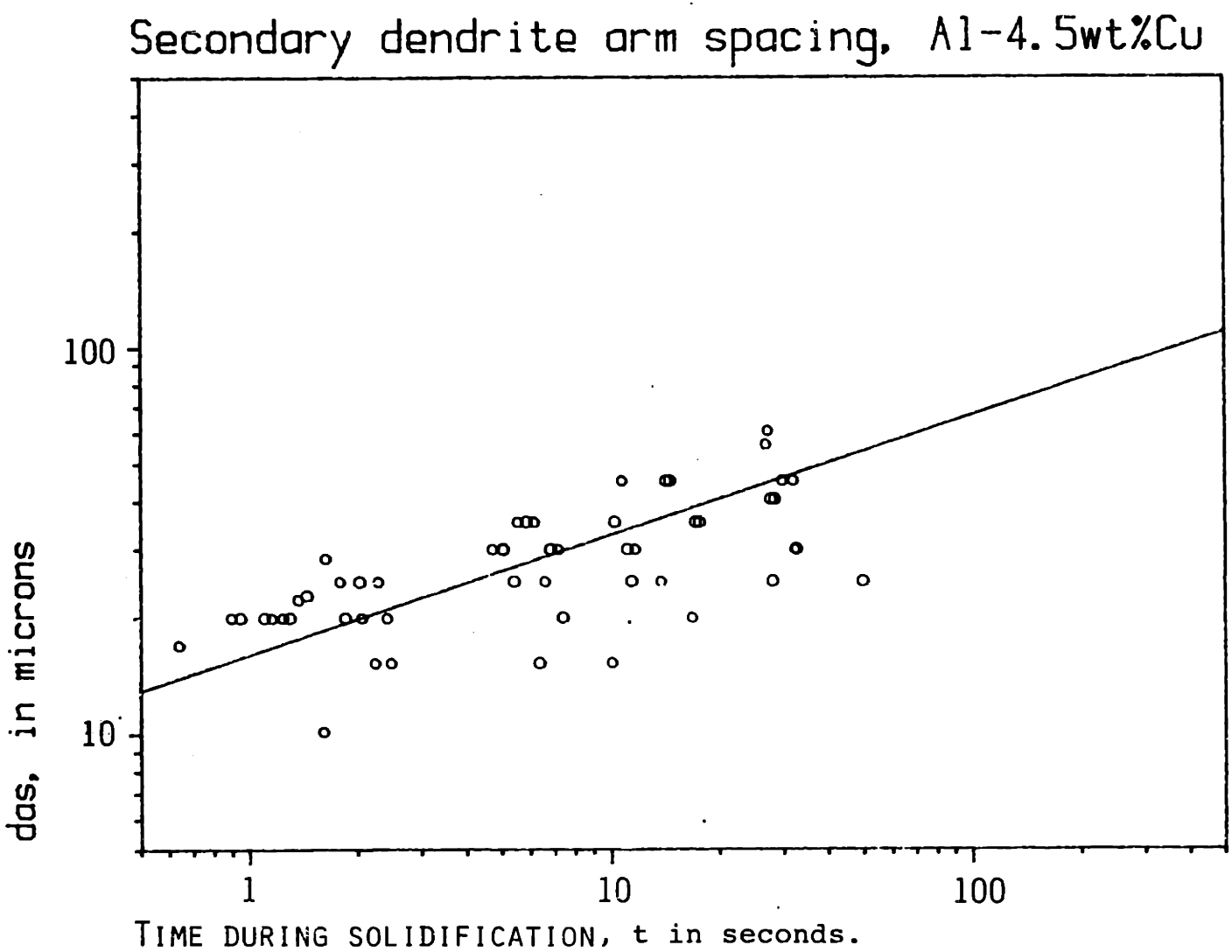

Figure 39 - Individual secondary dendrite arm spacings in the unreinforced region of sample H-2. The straight line is Young and Kirkwood's experimental correlation [149]. The solidification time t_f is 133 s.

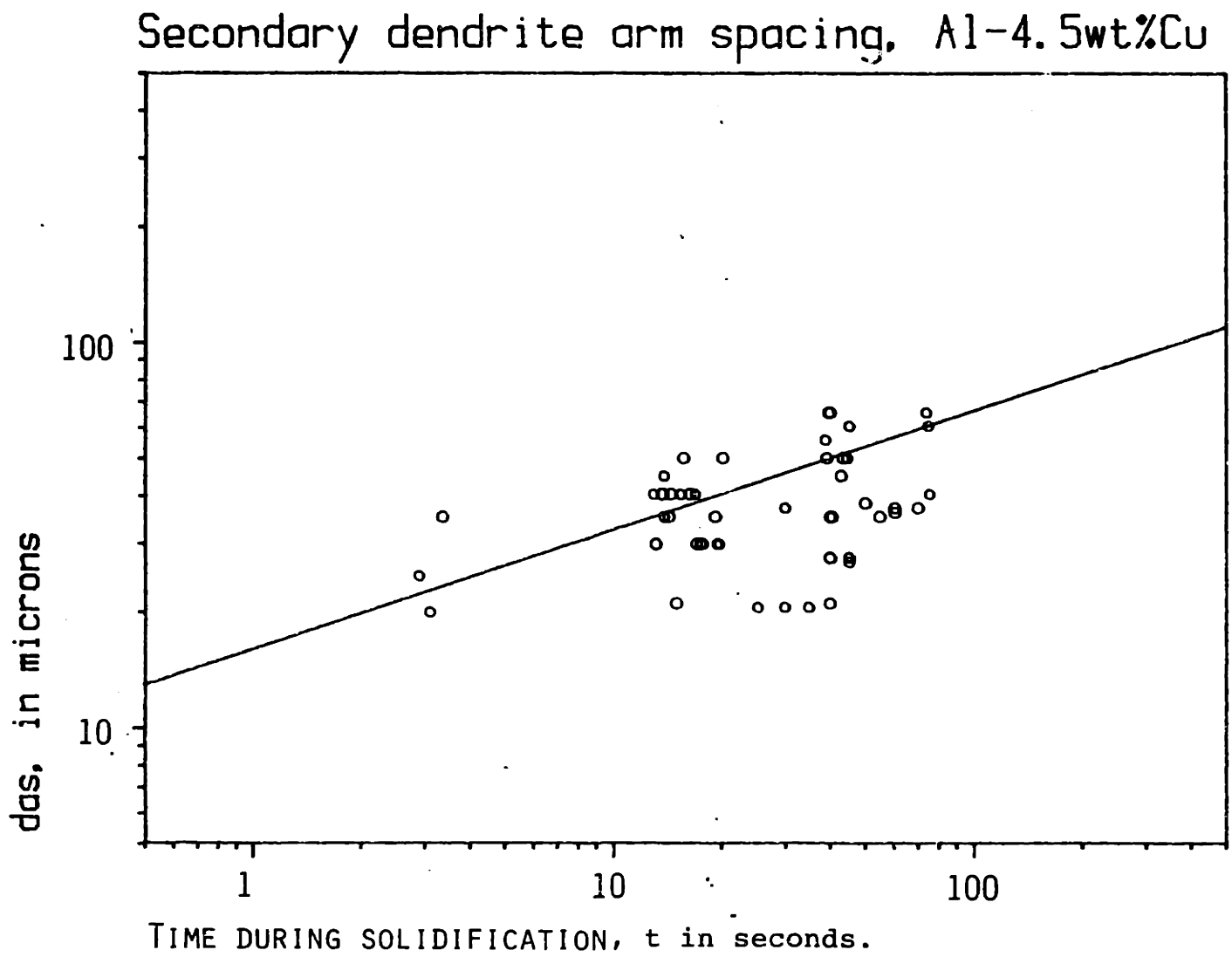

Figure 40 - Individual secondary dendrite arm spacings in the unreiforced region of sample I-3. The straight line is Young and Kirkwood's experimental correlation [149]. The solidification time t_f is 187 s.

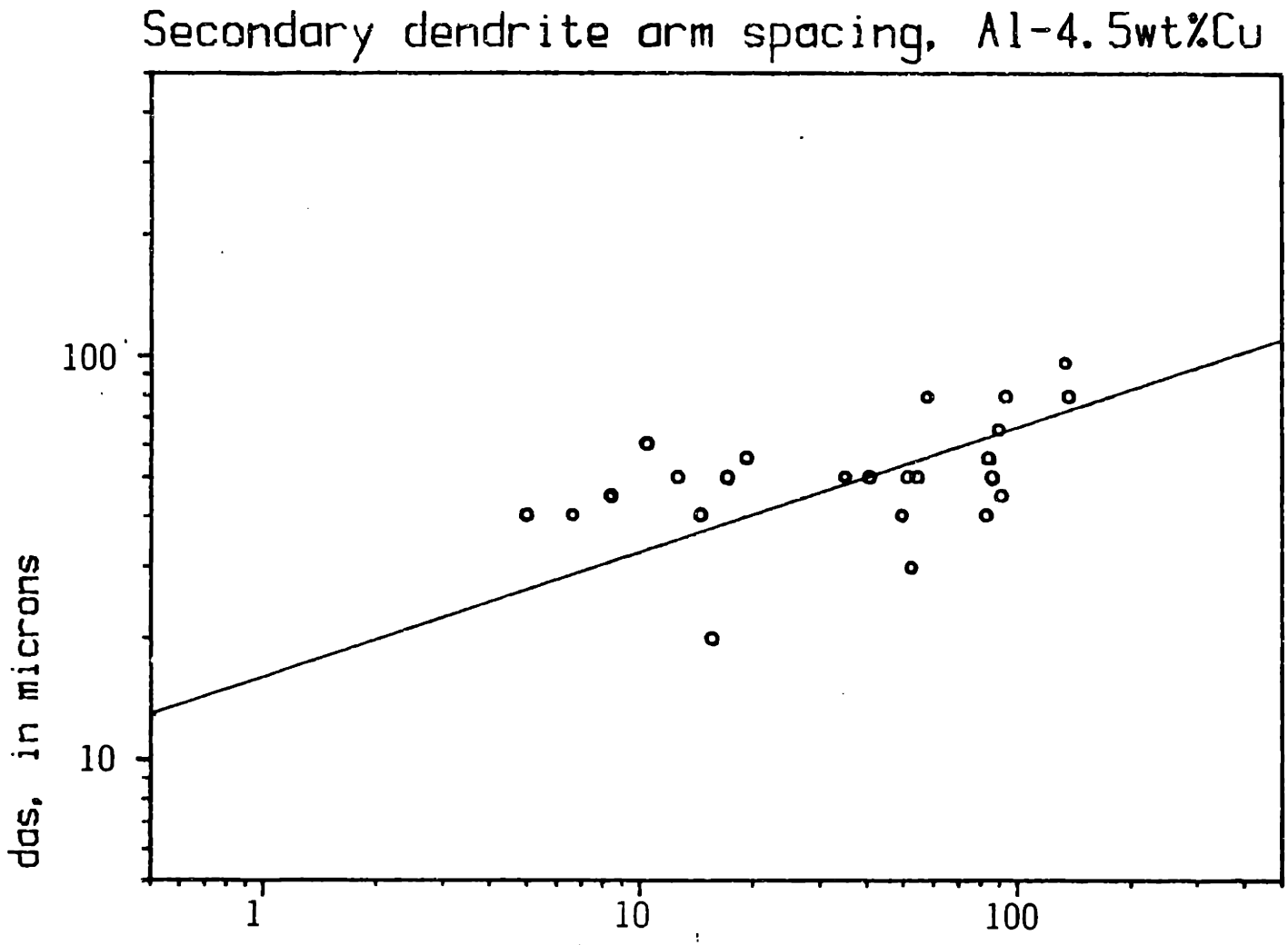

Figure 41 - Individual secondary dendrite arm spacings in the unreinforced region of sample I-2. The straight line is Young and Kirkwood's experimental correlation [149]. The solidification time t_f is 940s.

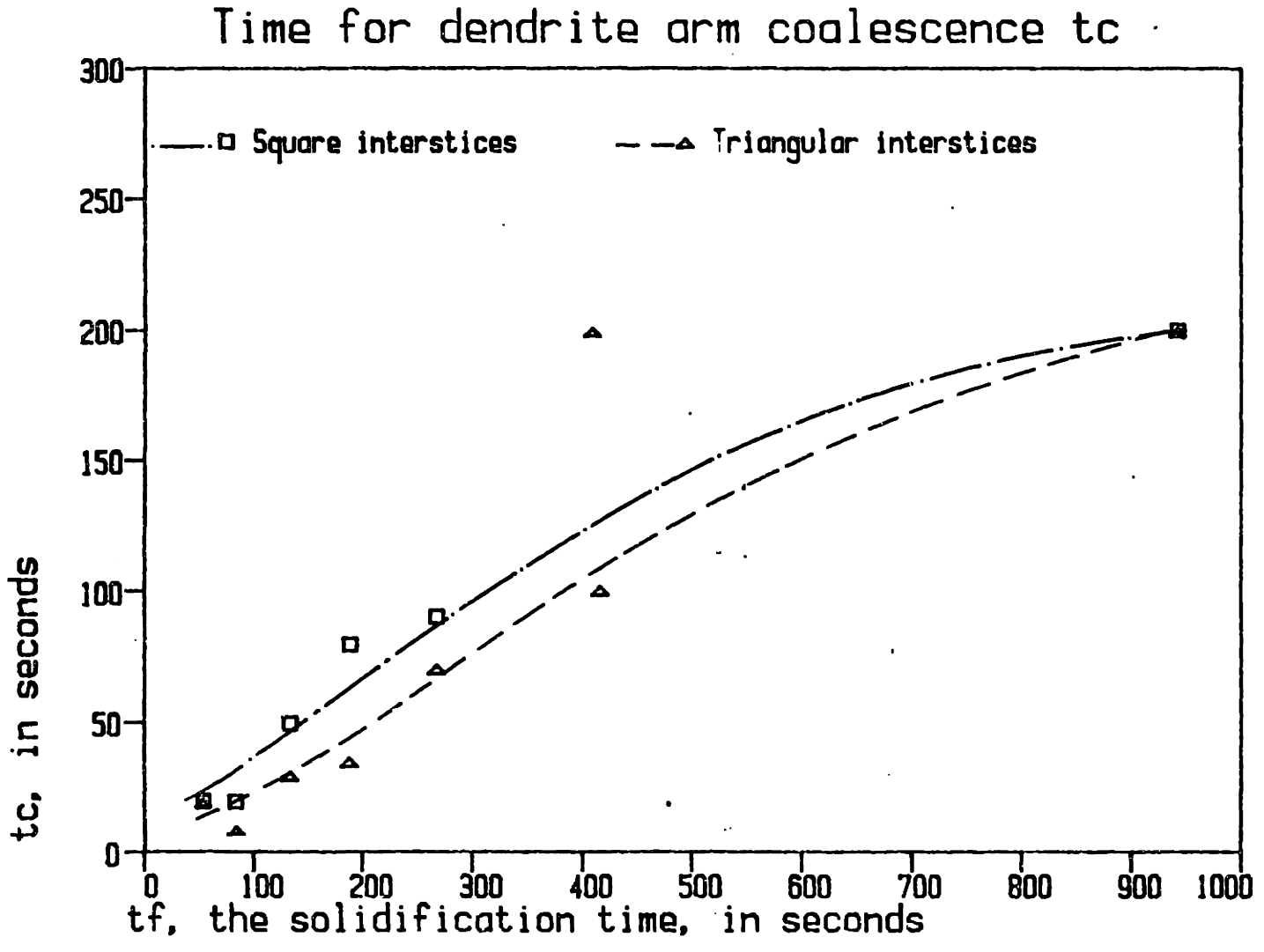

Figure 42 - Time for secondary dendrite arm coalescence in square and triangular interstices from the plots in figures 25 to 38.

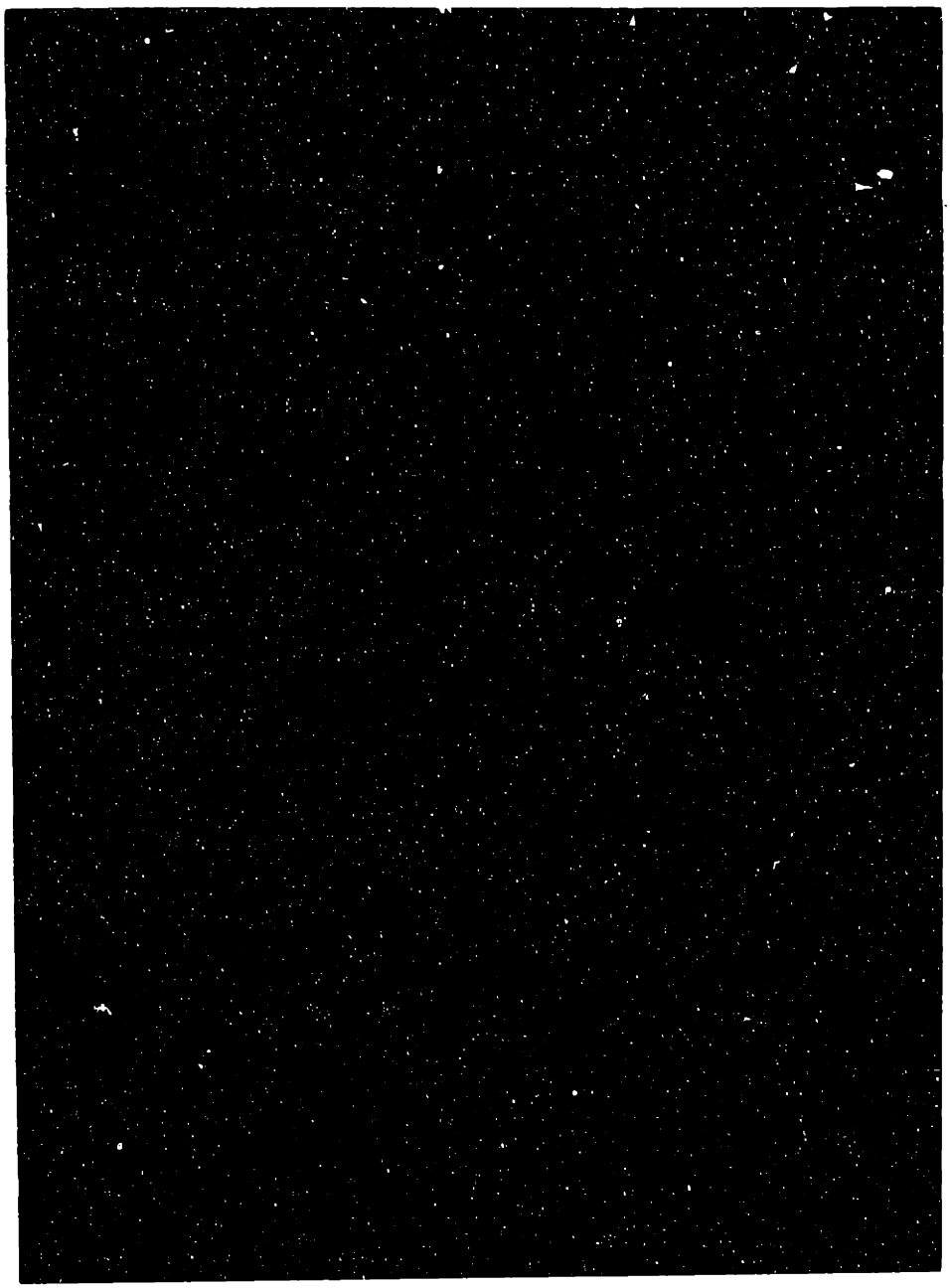

Figure 43 - Back scattered electron image of a cross section through sample I-2 quenched from the eutectic temperature. The second phase Al_2Cu is white and thus clearly visible. ——— 200 μm

Figure 44 - A low angle cut through the interface from the top portion of sample H-3. A continuous layer of Al_4C_3 is visible followed by discrete carbide platelets. Auger data was collected from the continuous interfacial region on this micrograph.

100 μ

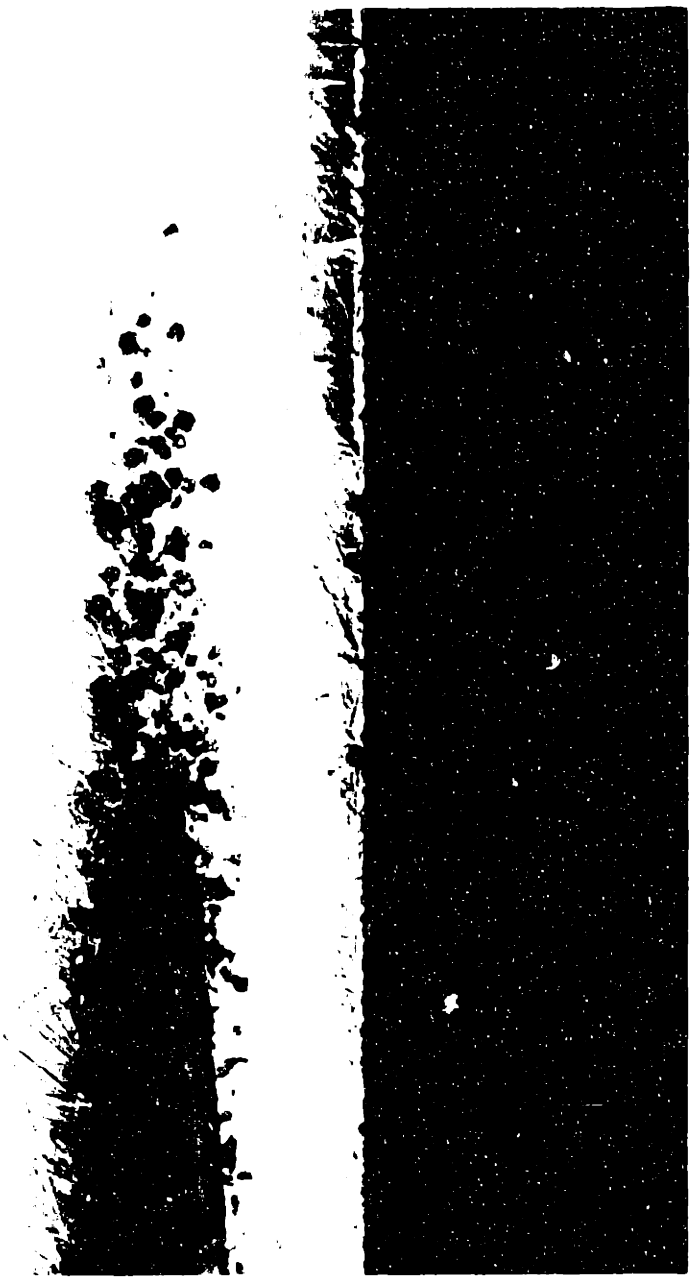

Figure 44 - A low angle cut through the interface from the top portion of sample H-3. A continuous layer of Al_4C_3 is visible followed by discrete carbide platelets. Auger data was collected from the continuous interfacial region on this micrograph.

100 μm

INTENTIONAL DUPLICATE EXPOSURE

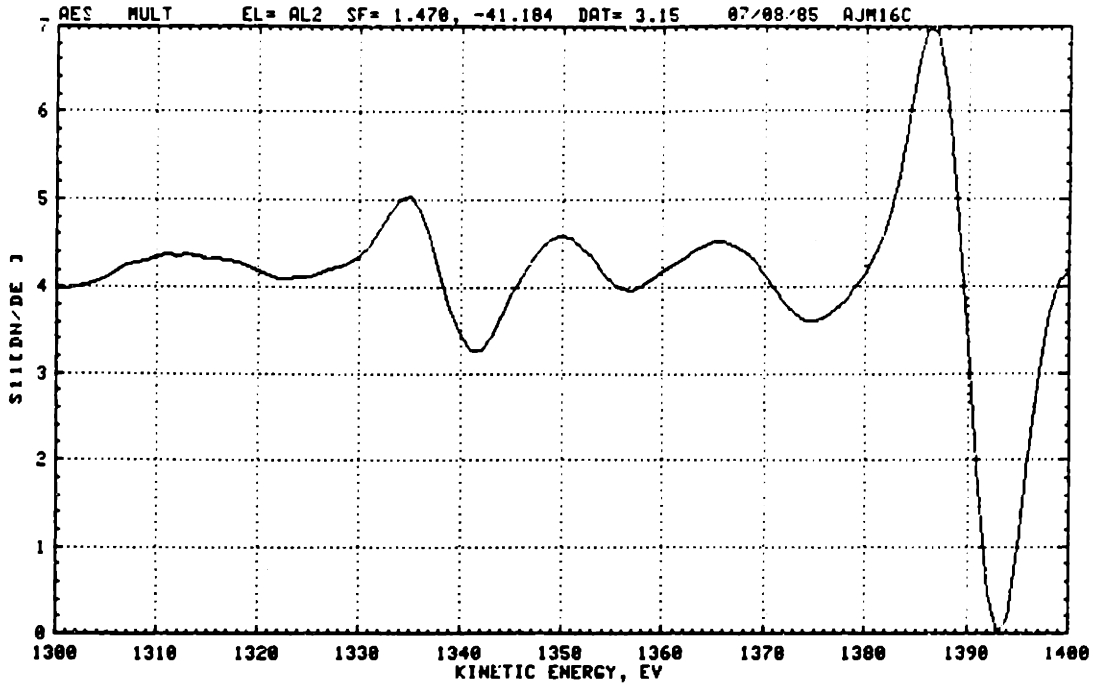

a - Aluminum in the interfacial zone.

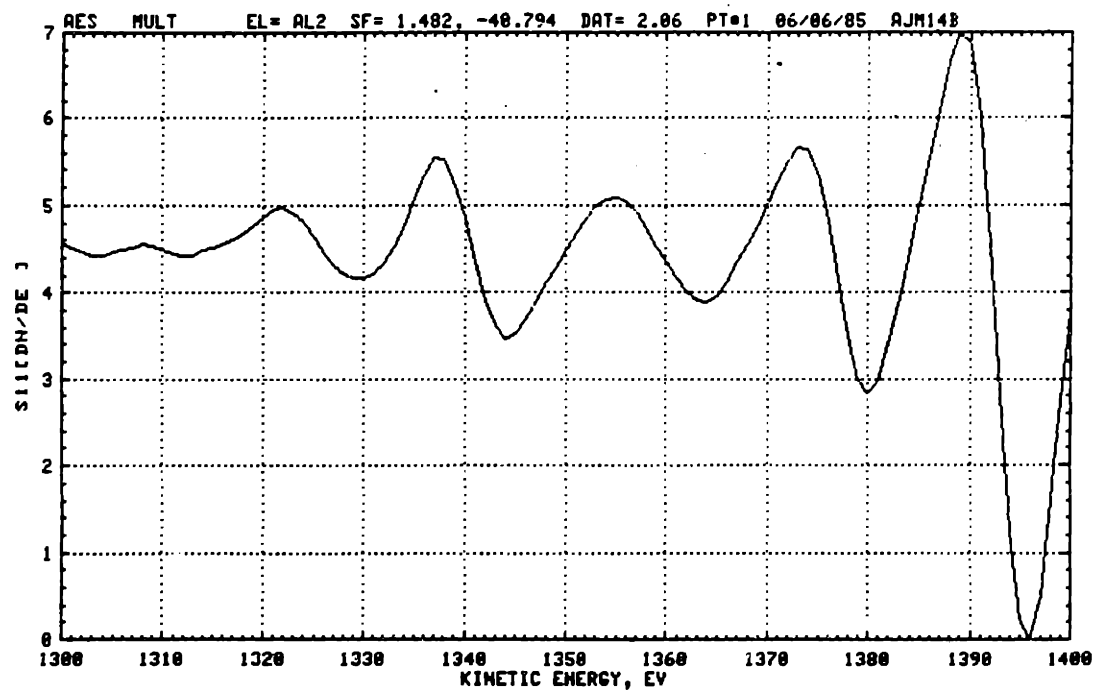

b - Aluminum in Al-4.5 wt% Cu.

Figure 45 - Auger electron spectra for aluminum from the interface and the matrix alloy.

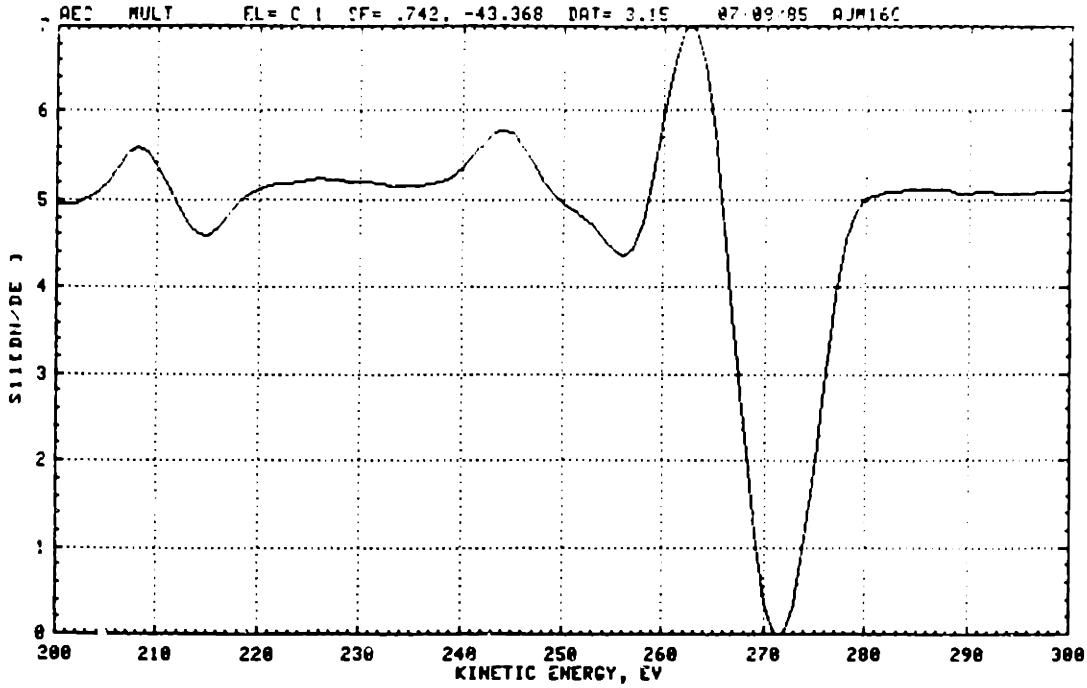

a - Carbon in the interfacial zone.

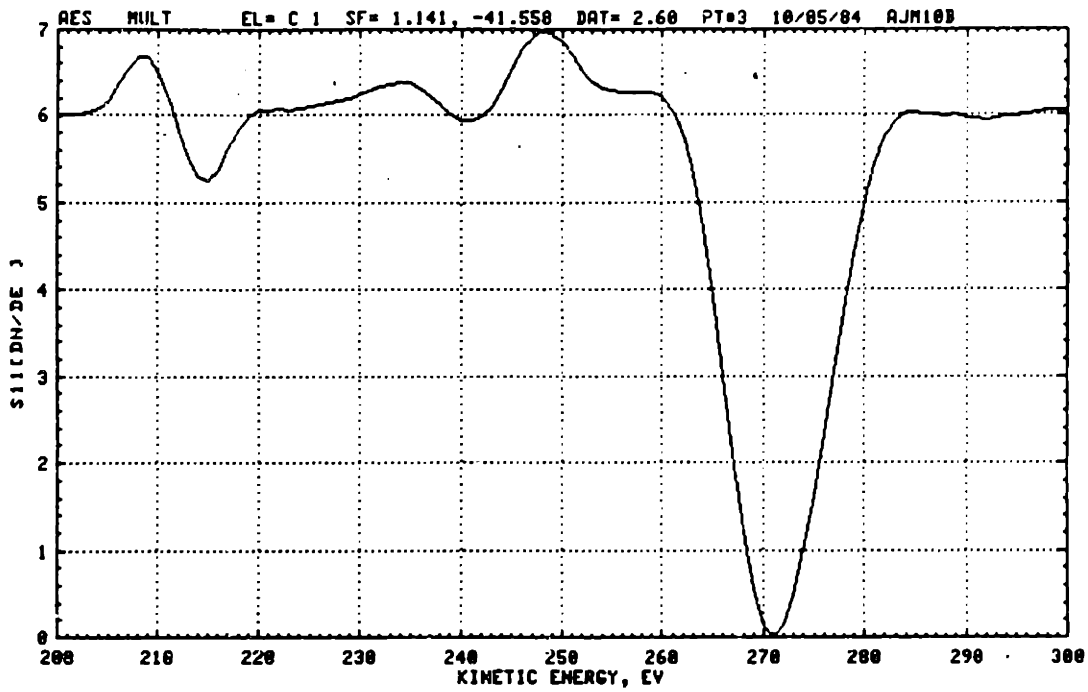

b - Carbon in the SCS coating.

Figure 46 - Auger electron spectra for carbon from the interface and the carbon-rich SCS-2 coating.

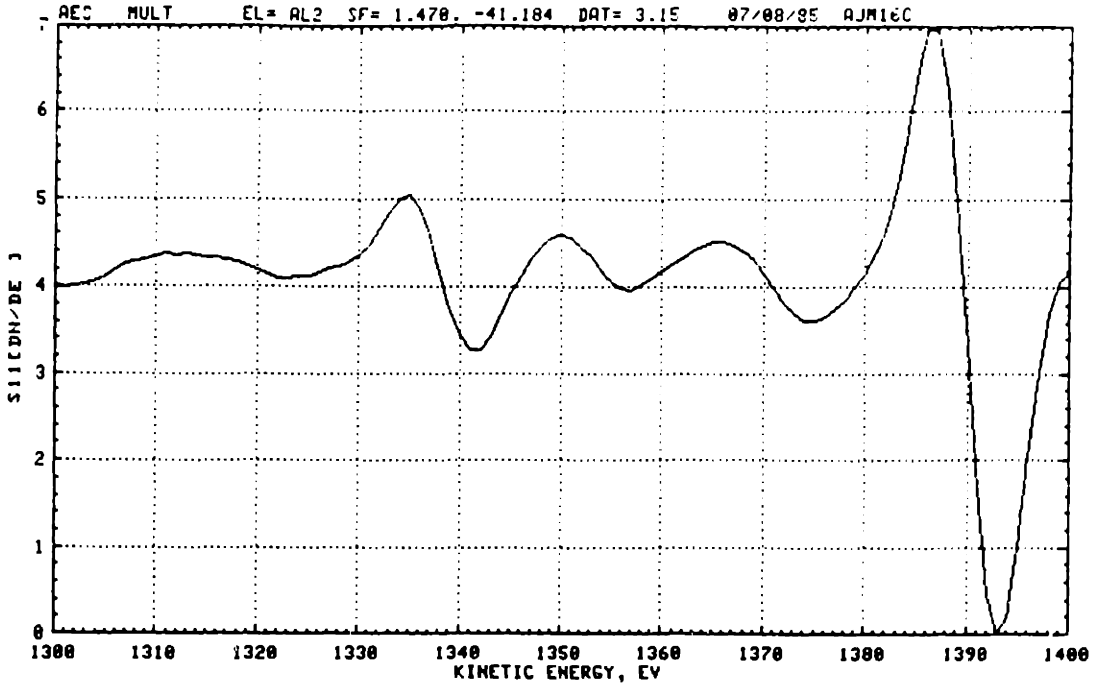

a - Aluminum in the interfacial zone.

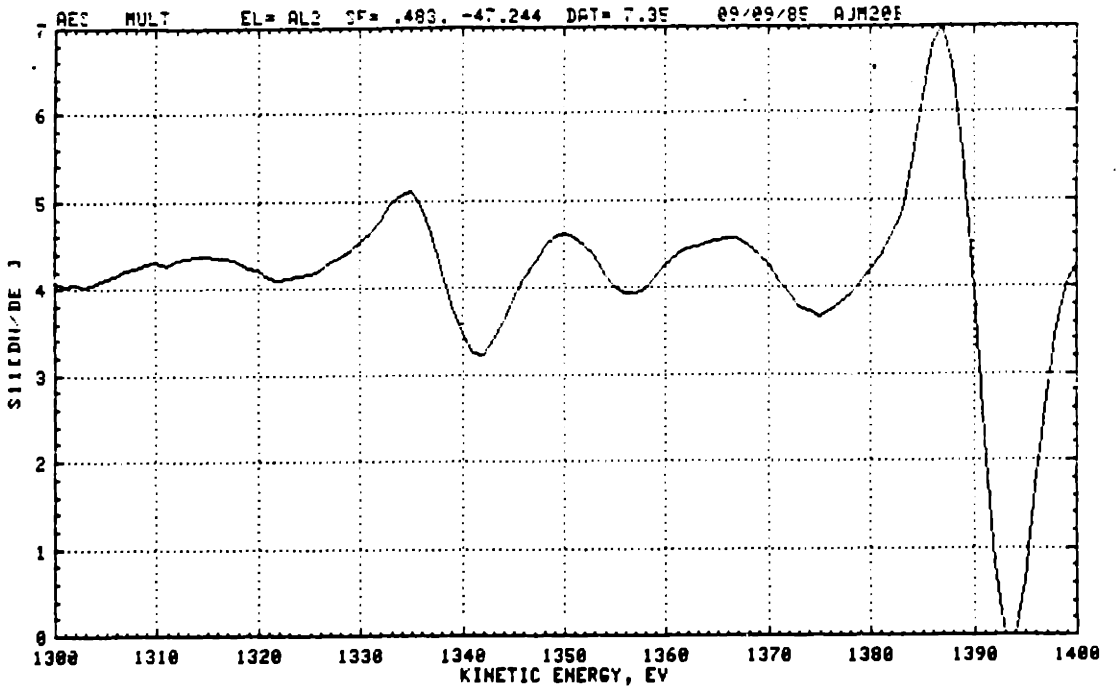

b - Aluminum in Al_4C_3.

Figure 47 - Auger electron spectra for aluminum from the interface and Al_4C_3 .

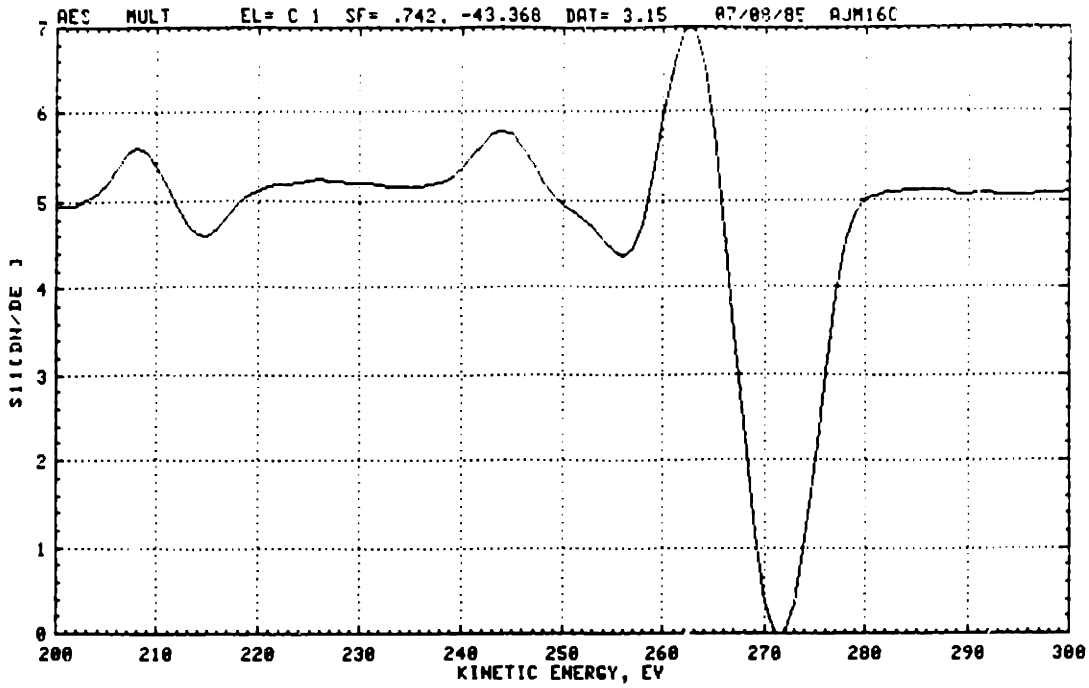

a - Carbon in the interfacial zone.

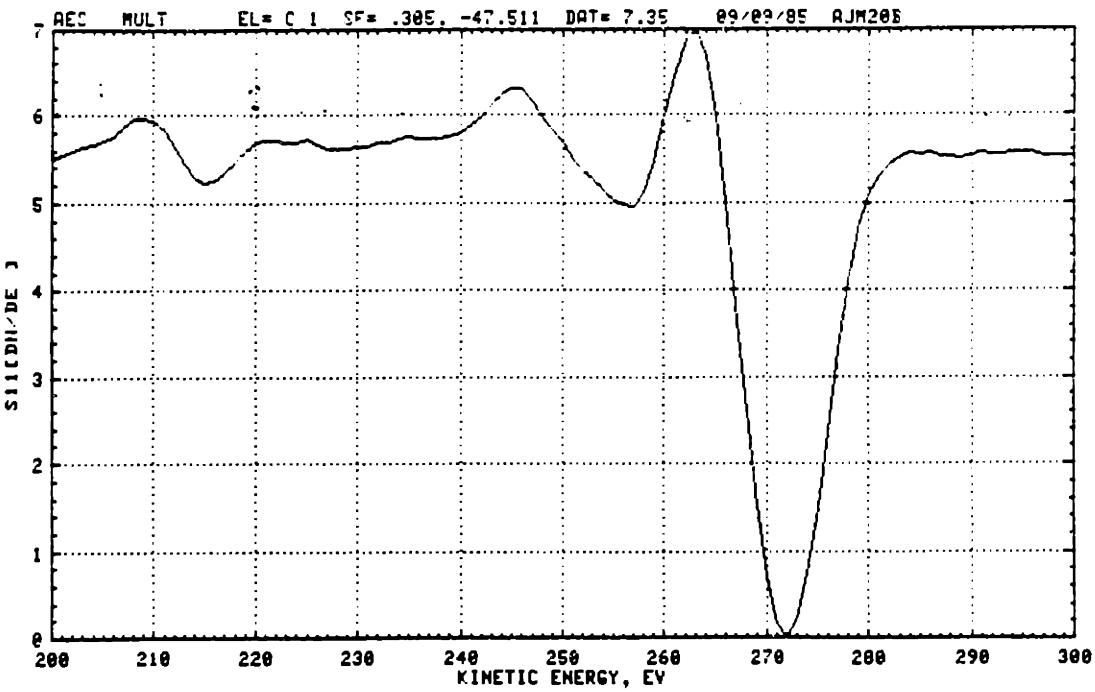

b - Carbon in Al_4C_3.

Figure 48 - Auger electron spectra for carbon from the interface and Al_4C_3.

THEORY

In this chapter, the observations described above are modelled on a quantitative basis. Coarsening effects are dealt with first since they determine the morphology of the final matrix microstructure. Then a simple and general model is proposed to describe the role of coarsening in reducing microsegregation. It is thus proved that for the case at hand, solid-state diffusion is solely responsible for the considerably lowered levels of microsegregation observed in some of the samples. A finite difference model is then constructed to predict these microsegregation levels.

I - Dendrite coarsening in metal matrix composites.

a - Background.

Contributions to the subject of dendrite coarsening were reviewed in the literature survey. Two approaches have been adopted to treat the problem:

1 - The "Lifschitz-Slyozov-Wagner" (LSW) approach, initiated by the related problem of precipitation from a supersaturated solution. The initial treatment assumed a near-zero volume fraction of dispersed spherical particles undergoing Ostwald ripening [154-157]. These assumptions were later relaxed to incorporate effects due to (i) a finite volume fraction of coarsening phase and (ii) coalescence of the spheres by diffusion

in the liquid. The results of all these treatments present the following features:

(i) - an asymptotic normalized particle distribution is attained after an initial transient, independent of initial conditions.

(ii) - the scaling factor of this distribution (average particle size R) increases linearly with the cube root of time:

$$\overline{R}^3 - \overline{R}_0^3 = K\ t$$

(iii) - the normalized particle distribution and the coarsening constant K are functions of the particle volume fraction and of the importance of particle coalescence. With increasing volume fraction and importance of coalescence, the distribution curve flattens and K increases.

2 - The "Kattamis-Flemings" approach [143]. Coarsening is again driven by surface tension and its rate is limited by diffusion in the liquid phase. Here, however, the kinetics of the process are modelled with a few detailed diffusion paths based on experimental observation of coarsening dendrites. This approach has the disadvantage of not offering a complete description of the coarsening microstructure as the LSW treatment does. But it also has advantages:

(i) - All LSW treatments of the problem assume only spherical particles are present. Dendrites are not spherical.

(ii) - Since solidification takes place concomitantly with

coarsening, a steady-state distribution is not attained.

The treatment offered herein is thus inspired from the Kattamis- Flemings approach of dendrite coarsening.

Coarsening takes place by the diffusion of matter from points of high curvature to points of low curvature. The process is modelled by simplifying the diffusion field into the interaction between two regions of differing curvature observed on relevant microstructures. At a given temperature T, the liquid composition in equilibrium with an interface of curvature κ is given by the Thomson-Freundlich equation [83]:

$$C_L^{\kappa} = C_L + \frac{\kappa \Gamma}{m_L}$$

where C_L= equilibrium composition in the liquid for a flat interface (wt%),

m_L= slope of the liquidus (m_L is negative for Al-Cu) (K/wt%),

Γ = Gibbs-Thompson constant (m K) [84],

Also, $\Gamma = \frac{\sigma_{ls}}{\Delta S_f}$ where σ_{ls} is the surface tension at the liquid-solid interface and S_f is the entropy of fusion.

This implies that the solute concentration in the liquid will vary from point to point since the curvature varies along the solid-liquid interface of dendrites. At points of high positive curvature, the copper concentration in the liquid is decreased. Solute will diffuse through the liquid toward these regions of low concentration. Since the solid phase has a lower solute content than the liquid, these regions will melt back to maintain

the concentration in the adjoining liquid at an adequately low level. Conversely, regions of low or negative curvature will tend to grow. Overall, the result is a reduction of the total interfacial surface area present.

It is assumed that the kinetics of the process are limited by the diffusion of solute through the liquid. Solid state difusion is neglected and interface kinetics are assumed to be rapid. Solute is assumed to diffuse down a gradient determined by a simple diffusion distance, d, and a composition difference determined by two different curvatures, κ_A and κ_B on the liquid-solid interface. Thus, the flux of solute from A to B is approximated as:

$$J = -\frac{D_L \Gamma}{m_L d}\left[\kappa_B + \kappa_A\right] \qquad \text{(m wt\% /s)}$$

Assuming B is the region of higher curvature ($\kappa_B > \kappa_A$), region B will melt away according to the relation:

$$J_B = - C_L^{K_B}(1-k)\frac{1}{S_B}\frac{dV_B}{dt}$$

where $\frac{dV_B}{dt}$ is the rate of change of volume of region B (in m^3/s), S_B is the surface area of region B (in m^2), and J_B is the flux of solute to region B. Similarly, region A will grow at a rate defined by the relation:

$$J_A = C_L^{K_A}(1-k)\frac{1}{S_A}\frac{dV_A}{dt}$$

where $\frac{dV_A}{dt}$ is the rate of change of volume of region A (in m^3/s), S_A is the surface area of region A (in m^2), and J_A is the flux of solute leaving region A. Mass conservation dictates:

$$\frac{dV_A}{dt} = \frac{dV_B}{dt}$$

Therefore, if $S_A \ll S_B$, then $J_A \gg J_B$ and the rate limiting factor is the diffusion limited growth of the solid at A. When this is the case, $J = J_A$ and assuming $C_L^{K_A} \simeq C_L$ (which is reasonable as long as $\kappa < 10^6 m^{-1}$), the final equation is:

$$\frac{1}{S_A}\frac{dV_A}{dt} = \frac{D_L \Gamma (\kappa_B + \kappa_A)}{(-m_L)(1-k)\, d\, C_L} \qquad (1)$$

Conversely, if $S_A \gg S_B$, the rate limiting step is the dissolution of matter at B. Therefore, $J = J_B$ and assuming as above that $C_L^{K_B} \simeq C_L$, the final equation describing the process is:

$$-\frac{1}{S_B}\frac{dV_B}{dt} = \frac{D_L \Gamma (\kappa_B + \kappa_A)}{(-m_L)(1-k)\, d\, C_L}$$

Depending on the assumptions made as to the nature of A and B, different coarsening mechanisms can be modelled. If both regions A and B have positive curvatures, this equation will approximately describe the kinetics of coarsening by ripening. Specific ripening models, given in figure 49, are:

Model I: The disappearance of smaller arms in favor of larger arms by lateral remelting of the smaller arms (ripening

mechanism).

Model II: The disappearance of smaller arms in favor of larger arms by the remelting of the smaller arms from their tips back toward their roots (ripening mechanism).

Model III: The removal of smaller arms by remelting at their roots and transport of the remelted arm away from the dendrite by convection (ripening mechanism).

If region A has a negative curvature, coalescence is described. Coalescence mechanisms are described in figure 50:

Model IV: The disappearance of an apparent dendritic structure by in-filling of the inter dendritic space (coalescence mechanism).

Model V: The coalescence of neighboring dendrite arms at their tips (coalescence mechanism).

All coarsening mechanisms described in figures 49 and 50 are based on documented microstructural observations and have been used previously as the basis of calculations [83,84,89,143-150].

b - Ripening in metal matrix composites.

In the presence of a high volume fraction of fibers, the metal matrix in a composite is constrained to grow inside narrow interfiber spaces. Provided the fibers are parallel, these interfiber spaces are cylindrical. The experimental results in this work are collected from two types of well defined spaces between cylindrical fibers, termed "triangular" and "square" interstices. A transverse cross section of these interstices is

given in figure 9 with relevant dimensions.

It was experimentally observed that secondary dendrite arms form between the fibers in the initial stages of solidification. It was further shown that the solid phase avoids the fibers which are thus about always in contact with the liquid phase only. For these reasons, the most stable configuration that can possibly be achieved by the semi-solid metal matrix in order to minimize its surface energy (at some relatively high volume fraction solid) is as drawn in figure 51. The fibers place a lower limit on the curvature that can be achieved at the liquid-solid interface of the growing solid.

For simplicity of the discussion, coarsening by ripening in a circular cylindrical interstice is first considered, figure 52. As noted above, the minimum average curvature permissible in the interfiber space is approximately given by $\kappa_{min} = \frac{1}{\ell_0}$, ℓ_0 being the interfiber space radius (figure 52). For this reason, the evolution of the dendritic structure must deviate at some point from that which it would experience in the absence of the fibers. A primary dendrite arm with secondary dendrite arms growing and coarsening in the circular interfiber space is depicted in figure 52. In figure 52-a, the secondary dendrite arm spacing λ_2 is still small compared to the interfiber space radius ℓ_0. As time increases, this structure can coarsen by ripening as described above to yield a coarser microstructure, figure 52-b. It is apparent, however, that the average dendrite arm cannot ripen beyond the size of the interfiber space itself. At this stage, the kinetics of coarsening by ripening must be slowed down by the

fibers. Should the dendrite arm spacing reach a size slightly above the interfiber space diameter, figure 52-c, coarsening by ripening will come to a halt since the curvature along all dendrite arms is about the same. The average secondary dendrite arm spacing cannot, therefore, increase much beyond the interfiber space radius diameter, $2\ \ell_0$.

Returning to the triangular and square interstices of interest herein, the same argument applies. The configuration given in figure 53 corresponds to that which was experimentally observed in the initial stages of solidification (figures 12 to 15). Transverse to the fiber axis, the curvature is high due to the constraining action of the fibers. If the dendrite arms are wide in a direction parallel to the fibers, the curvature at their surface is everywhere about the same. For this reason, ripening must be very sluggish when the secondary dendrite arm spacing becomes larger than about twice the radius of curvature at the solid-liquid interface transverse to the fibers. The moment at which ripening mechanisms will cease to operate is difficult to evaluate since the transverse curvature along the dendrite arms is a complex function of the volume fraction solid and the interfiber space geometry. However, a lower limit on the minimum achievable curvature along secondary dendrite arms is given by the radius of the largest circle that can be inscribed in a transverse cross section of the cylindrical interfiber space of interest, r_{max} . From figure 9, this is: r_{max} = 10 microns for triangular interstices; and r_{max} = 30 microns for square interstices.

In conclusion, coarsening by ripening must come to a halt when the average dendrite arm spacing reaches at most $2r_{max}$. From then on, it is only by coalescence mechanisms that the microstructure can evolve.

The kinetics of secondary dendrite arm coalescence are modelled in the remainder of the section. The secondary dendrite arms are assumed to coalesce according to mechanism IV of figure 50 and the time for complete coalescence of secondary dendrite arms t_c is calculated.

c - Kinetics of coalescence in metal matrix composites.

The dendrite geometry is simplified as depicted in figure 54. The diffusion process limiting the rate of secondary dendrite arm coalescence is assumed to take place between the tips of secondary dendrite arms and the bottom of the trough separating those arms. This process is described as model IV in figure 50. The bottom of the trough is approximately circular, of radius r_A . The diffusion distance is taken as the secondary dendrite arm length ℓ, and the curvature at the dendrite tips is assumed to be negligible compared to that in the trough:

$$\kappa_A = -\frac{1}{r_A}$$

$$\kappa_B \ll -\kappa_A$$

$$d = \ell$$

$$\frac{1}{S_A} \frac{dV_A}{dt} = \frac{d\ell}{dt}$$

Furthermore, the radius at the bottom of the trough is approximately:

$$r_A = \frac{\lambda_2}{2} f_L$$

where f_L is the fraction liquid. The coalescence process will only take place at an appreciable rate once the dendrite arms are sufficiently large compared to the troughs separating them. The physical reason for this was given above: if the total trough area is larger than the dendrite tip area, the rate limiting step in the coarsening processes is remelting at the dendrite tips. It is only at higher volume fractions solid that there will be enough matter remelting from the dendrite arm tips for coalescence to proceed at an appreciable rate. The fact that coalescence only proceeds at an appreciable rate at higher volume fractions solid has been experimentally proven in dendritic [147-150] and liquid-phase sintered [206-212] structures.

A volume fraction solid f_{si} is thus defined as that at which coalescence starts proceeding at an appreciable rate. Hence:

$$\frac{d\ell}{dt} = 0 \qquad \text{for } f_s < f_{si}$$

It is assumed for simplicity that the secondary dendrite arm spacing remains constant at λ_2 during the coalescence process. The secondary dendrite arm spacing will in particular remain approximately constant if secondary dendrite arm ripening is halted by the fibers before $f_s = f_{si}$. A treatment of coalescence occuring concomitant with secondary dendrite arm coarsening by ripening is given in Appendix D.

Equation (1) thus becomes

$$\frac{d\ell}{dt} = -\frac{\Gamma \quad D_L}{(-m_L) \quad (1-k)} \quad \frac{2}{\lambda_2 \quad C_L f_L} \quad \frac{1}{\ell} \qquad (2)$$

with $f_s > f_{si}$. The fraction liquid f_L is approximately given by the Scheil equation:

$$f_L = \left[\frac{C_L}{C_o}\right]^{\frac{1}{k-1}} \qquad (3)$$

and the cooling rate is assumed to be constant:

$$C_L = C_o + \frac{GR}{(-m_L)} \; t \qquad (4)$$

Equation (2) then becomes:

$$\lambda_2 \ell \; d\ell = -\frac{2 \; D_L \; \Gamma}{GR \; (1-k)} \left(\frac{C_L}{C_o}\right)^{\frac{1}{1-k}} \frac{dC_L}{C_L}$$

and after integration:

$$\lambda_2 (\ell^2 - \ell^2) = \frac{4 \; D_L \; \Gamma}{G \; R} \left[\left(\frac{C_L}{C_o}\right)^{\frac{1}{1-k}}\right]_{C_{Li}}^{C_L}$$

where ℓ_i is the initial secondary dendrite arm length and C_{Li} is the liquid composition at which $f_s = f_{si}$. From the Scheil equation (3), this equation can also be written:

$$\lambda_2(\ell_i^2 - \ell^2) = \frac{4\ D_L\ \Gamma}{G\ R}\left[\left(\frac{C_L}{C_o}\right)^{\frac{1}{1-k}} - \frac{1}{1 - f_{si}}\right] \qquad (5)$$

The time for complete coalescence of secondary dendrite arms t_c corresponds to $\ell = 0$ and is thus given by:

$$t_c = \frac{(-m_L)\ C_o}{G\ R}\left[\left(\frac{GR\ \ell_i^2 \lambda_2}{4\ D_L \Gamma} + \frac{1}{1 - f_{si}}\right)^{1-k} - 1\right] \qquad (6)$$

from equations (4) and (5). There are three parameters entering this equation for a given metal alloy:

GxR, the cooling rate;

λ_2, the secondary dendrite arm spacing, assumed not to vary during the coalescence process. If coarsening by ripening is halted by the fibers, $\lambda_2 \simeq 2r_{max}$;

ℓ_i, the initial secondary dendrite arm length.

There is one unknown constant: the fraction solid f_{si} below which coalescence is sluggish.

d - Criterion for complete coalescence of secondary dendrite arms in metal matrix composites.

In the final fully solidified metal matrix, secondary dendrite arms will not be found if

$$t_c (\ell_i , \lambda_2 , GxR) \leq t_f$$

This equation is most easily solved by putting $C_L = C_E$, the eutectic composition, in equation (5) and solving for t_c with $\ell = 0$. The resulting criterion is:

$$t_f \geq \frac{\Delta T \ \ell_i^2 \ \lambda_2}{4 D \Gamma \left[\left(\frac{C_E}{C_o} \right)^{\frac{1}{1-k}} - \frac{1}{1 - f_{si}} \right]} \qquad (7)$$

since $t_f = \Delta T/(GxR)$ where ΔT is the solidification temperature range of the alloy (ΔT = 100 K for Al-4.5wt%Cu).

Satisfaction of this criterion will ensure that no liquid is left between secondary dendrite arms in the very last phases of solidification. All the second phase will thus form at the fiber-metal interface. It may be desirable, however, to place more stringent conditions on the final microstructure by ensuring that all secondary dendrite arms have coalesced before the solidifying metal reaches a high copper concentration. In this manner, the coring patterns will map the fiber surfaces instead of delineating the former morphology of secondary dendrite arms. The simple form of equation (5) allows for a rapid evaluation of the maximum cooling rate GxR (or the minimum solidification time t_f) for coalescence to be complete before the liquid composition reaches an arbitrary value $C_L > C_{Li}$. All isoconcentrates in the solid phase corresponding to a concentration above kC_L will then map the interfiber space contour and not the formerly present secondary dendrite arms. The criterion:

t_c (GxR, λ_2 , ℓ_i) $\leq$ the time at which the liquid composition is C_L (from equation (4))

is simply obtained from equation (5) as:

$$t_f \geqslant \frac{\Delta T \ \ell^2 \ \lambda_2}{4 \ D_L \ \Gamma \left[\left(\frac{C_L}{C_o} \right)^{\frac{1}{1-k}} - \frac{1}{1-f_{si}} \right]} \qquad (8)$$

With $C_L = C_E$, this relation becomes relation (7).

e - Numerical results.

For a given metal alloy and a given interstice, there are two unknown parameters:

f_{si} which is characteristic of the alloy, and

$\lambda_2 \ \ell_i^2$ which is characteristic of the interstice.

f_{si} should be somewhat above 0.5 because coalescence is expected to take place rapidly starting roughly from the moment when the total area at the bottom of the troughs is commensurate with that at the dendrite tips.

The value to be ascribed to $\lambda_2 \ \ell_i^2$ depends on the initial length of the secondary dendrite arms ℓ_i and the approximately constant secondary dendrite arm spacing. In narrow interfiber interstices, both are defined by the interstice geometry.

The time during solidification t_c at which secondary dendrite arm coalescence is complete is plotted in figure 55 as a function of the solidification time t_f for various values of $\lambda_2 \ \ell_i^2$ and f_{si}

= 0.65. The results from equation (6) are also plotted in a similar manner in figure 56 for various values of f_{si} and $\lambda_2 \ell_i^2$ at $2 \times 10^{-15} m^3$. In both plots, the identity line "$t_c = t_f$" limits the possible values for t_c since if $t_c > t_f$, the coalescence process is incomplete at the end of solidification. For a given interstice and metal alloy, the intersection of the line giving t_c as a function of t_f and this identity line gives the minimum solidification time for complete coalescence (criterion (7)). This criterion for secondary dendrite arm coalescence to be complete before the end of solidification is only weakly dependent on f_{si} . On the other hand, when $t_c << t_f$, t_c is determined mainly by f_{si} since the coalescence process proper is short compared to the time needed to reach f_{si} (equation (6)).

It will be shown in the "discussion" chapter of this thesis that the model fits experimental data with reasonable values for f_{si} and $\lambda_2 \ell_i^2$.

II - On the influence of coarsening on microsegregation.

As the experimental results have shown, one of the most interesting observations found in this work is the possibility of completely suppressing microsegregation in metal-matrix composites during solidification. It was shown in the literature survey that two mechanisms contribute to the suppression of microsegregation: solid-state diffusion and dendritic coarsening

by ripening. Our present knowledge of the influence of dendritic coarsening on microsegregation is poor. It seems that only Kirkwood et al. [171] have successfully addressed the problem. Their approach, although correct, has the disadvantage of being a modification of a computer model for the suppression of microsegregation by solid state diffusion. The two operating mechanisms were not separated and the influence of coarsening alone was not evaluated. In the following, an analytical solution is derived for the suppression of microsegregation by coarsening alone. The additional effect of solid state diffusion is then considered separately in a computer solution.

A large number of cylindrical secondary dendrite arms are considered, each arm having a radius r^* , figure 57. Diffusion in the liquid is assumed to be rapid enough that the liquid concentration is essentially uniform. Interfacial kinetics are assumed to be rapid, and so the liquid composition C_L is given by the phase diagram as a function of the temperature T. All phases, both solid and liquid, are assumed to have the same density.

A small hexagonal "volume element", V, is drawn in figure 57 in such a way that the fraction solid within this element is equal to the average fraction solid in the solidifying metal. A solute balance within this element gives:

$$\bar{C}_S f_S + C_L f_L = C_o \qquad (9)$$

With $V \simeq \pi r_T^2 \ell$, and since the volume of the solid cylindrical dendrite arm is $\pi r^{*2} \ell$, equation (9) is written:

$$\overline{C}_S \pi r^{*2} \ell + C_L \pi (r_T^2 - r^{*2}) \ell = C_0 \pi r_T^2 \ell \qquad (10)$$

Now, what differentiates the solution to follow from the many similar analyses made on such "volume elements" is that the volume element is allowed to grow as ripening proceeds. Suppose that the volume element considered contains one of the few dendrite arms destined to survive throughout the entire solidification process. During a time increment dt, a few other arms remelt and the microstructure coarsens by ripening. All volume elements containing surviving dendrite arms will therefore increase in size by the addition of a small quantity of matter, necessarily of the average concentration C_o. $V = \pi r_T^2 \ell$ therefore increases with time, at a rate depending on the coarsening rate. Differentiating equation (10) and dividing with $\pi \ell dt$ gives:

$$\frac{d(\overline{C}_S r^{*2})}{dt} + (r_T^2 - r^{*2}) \frac{dC_L}{dt} - 2 C_L r^* \frac{dr^*}{dt} + 2 (C_L - C_0) r_T \frac{dr_T}{dt} = 0 \qquad (11)$$

The first term on the left of equation (11) represents the increase in mass of solute in the solid during dt [83]:

$$\frac{d(\overline{C}_S r^{*2})}{dt} = 2 r^* C_S^* \frac{dr^*}{dt} + 2 D_S r^* \left(\frac{\partial C_S}{\partial r} \right)_{r=r^*} \qquad (12)$$

Now, assuming that there is no solid state diffusion ($D_S = 0$),

the last term to the right of equation (12) vanishes. Since $C_S^* = kC_L$, substitution of equation (12) into equation (11) gives:

$$2\,C_L\,(1-k)\,r^*\frac{dr^*}{dt} = (r_T^2 - r^{*2})\frac{dC_L}{dt} + (C_L - C_o)\,2\,r_T\frac{dr_T}{dt} \qquad (13)$$

With three additional and simple assumptions, the problem is defined:

1 - secondary dendrite arms coarsen according to the usual law:

$$r_T = B\,t^{1/n} \qquad n \in \mathbb{R}^* \qquad (14)$$

2 - the cooling rate is constant:

$$C_L = C_o + At \qquad A = \frac{G \cdot R}{(-m_L)} \qquad (15)$$

3 - solidification starts at $C_L = C_o$ (no undercooling at the dendrite tip). Equation (13) then becomes:

$$(C_o + At)\,(1-k)\;2r^*\frac{dr^*}{dt} + Ar^{*2} = (1+2/n)\;A\;B^2\;t^{2/n} \qquad (16)$$

and equation (16) is the basic "solute redistribution equation", in differential form, for the case of solidification with coarsening but no solid diffusion. Now, noting that :

$$\frac{d}{dt}\left[r^{*2}\;(C_o+At)^{\frac{1}{1-k}}\right] = \frac{(C_o+At)^{\frac{k}{1-k}}}{1-k}\left[(1-k)\,(C_o+At)\;2r^*\frac{dr^*}{dt} + Ar^{*2}\right]$$

one finds:

$$r^{*2} = (1+2/n)\frac{A\,B^2}{1-k}\,(C_o+At)^{\frac{1}{k-1}} \int_0^t (C_o+A\tau)^{\frac{k}{1-k}}\,\tau^{2/n}\,d\tau$$

Now, since $r_T = B\,t^{1/n}$

and $t = \dfrac{C_L - C_o}{A}$

one obtains:

$$\left(\frac{r^*}{r_T}\right)^2 = (1+2/n)\,\frac{1}{1-k}\,\frac{C_L^{\frac{1}{k-1}}}{(C_L-C_r)^{2/n}} \int_{C_o}^{C_L} C^{\frac{k}{1-k}}\,(C - C_o)^{2/n}\,dC \quad (17)$$

The final equation is independent of both the cooling rate and the coarsening law constant. The integral can be integrated analytically if 2/n is an integer (integration by parts). $(r^*/r_T)^2$ is the fraction solid f_S at a given liquid composition C_L.

Since diffusion in the solid phase is neglected, solid deposited at a given composition remains at that composition in surviving dendrite arms. Therefore, solid at a composition $C_S = kC_L$ is found at a distance $r^*(C_L)$ from the center of the arm, with $r^*(C_L)$ given by equation (17). Although the overall dendrite arm radius r_T may increase with time, the radius $r^*(C_L)$ of this isoconcentrate does not change. When the liquid composition attains a higher value C_L, the fraction solid having a

concentration less than a given $C_s = kC_L < k\,\mathcal{C}_L$ is located inside the cylinder of radius $r_T^*(C_L)$. This corresponds to a volume fraction

$$\mathcal{F}_S(C_L) = \left[\frac{r^*(C_L)}{r_T(\mathcal{C}_L)}\right]^2 = f_S(C_L)\left[\frac{r_T(C_L)}{r_T(\mathcal{C}_L)}\right]^2$$

of the metal at this time. The fact that $\mathcal{F}_S$ is less than f_S is at the essence of the reduction of microsegregation by ripening: some solid having a composition below C_S has melted and deposited elsewhere at a higher concentration.

Therefore, when the liquid composition is $\mathcal{C}_L$, the fraction solid $\mathcal{F}_S(C_L)$ with a composition $C_s < kC_L < k\,\mathcal{C}_L$ is given by:

$$\mathcal{F}_S(C_L) = (1+2/n)\frac{1}{1-k}\,\frac{C_L^{\frac{1}{k-1}}}{(\mathcal{C}_L - C_o)^{2/n}}\int_{C_o}^{C_L} C^{\frac{k}{1-k}}\,(C - C_o)^{2/n}\,dC \quad (18)$$

Should ripening proceed throughout the solidification process, the solute concentration profile is given by equation (18) above with $\mathcal{C}_L = C_E = 33$wt%Cu. In particular, the fraction of eutectic is given by $f_E = 1 - \mathcal{F}_S(C_E)$ with $\mathcal{C}_E = C_E$.

Using k=0.171, C =4.5 wt%Cu and n=3, the resulting final solute distribution profile is plotted in figure 58-c, assuming as Kirkwood et al. did that ripening indeed proceeds throughout the solidification process. The fraction eutectic present is then

f_E=0.0491. The Scheil equation, plotted in figure 58-a yields f_E= 0.0903.

Using an approach in all points similar to that given above,

1 - for plates of thickness r_T, the interface is at r* given by:

$$\frac{r^*}{r_T} = \frac{(1+1/n)}{1-k} \frac{C_L^{\frac{1}{k-1}}}{(C_L - C_o)^{1/n}} \int_{C_o}^{C_L} C^{\frac{k}{1-k}} (C - C_o)^{1/n} \, dC$$

2 - for spheres of radius r_T, the interface is at r* given by:

$$\left[\frac{r^*}{r_T}\right]^3 = \frac{(1+3/n)}{1-k} \frac{C_L^{\frac{1}{k-1}}}{(C_L - C_o)^{3/n}} \int_{C_o}^{C_L} C^{\frac{k}{1-k}} (C - C_o)^{3/n} \, dC$$

if n=3, for a spherical geometry:

$$\left[\frac{r^*}{r}\right]^3 = \frac{2}{C_L - C_o} \left[\frac{1}{2-k} C_L + \frac{1-k}{2-k} C_L^{\frac{1}{k-1}} C_o^{\frac{2-k}{1-k}} - C_o\right]$$

For k = 0.171, Co = 4.5 wt%Cu and n=3, figures 58-b and 58-d give the final solute distribution profile for the plane and the spherical geometries respectively. Resulting fractions eutectic are 0.0664 and 0.0352 respectively.

The effect is therefore considerable, even for the plate geometry which Kirkwood et al. used [171]. Experimentally however, measured values of the fraction eutectic can come close to that predicted by the Scheil equation [82]. Therefore,

ripening cannot have proceeded throughout the solidification range. This is because toward the end of solidification, coarsening proceeds by coalescence. Dendrite arms then no longer remelt down to their core and microsegregation is barely affected.

Assuming for simplicity that coarsening is by ripening only up to a certain volume fraction f_S^c, the corresponding liquid composition C_L^c is given by:

$$f_S^c = \frac{5}{3(1-k)} \frac{{C_L^c}^{\frac{1}{k-1}}}{(C_L^c - C_o)^{2/3}} \int_{C_o}^{C_L^c} C^{\frac{k}{1-k}} (C - C_o)^{2/3} \, dC$$

for n=3 and cylindrical dendrites. From this point on, r_T remains fixed and solidification is according to the Scheil equation. Hence, a fraction

$$f_E' = \left(\frac{C_E}{C_L^c} \right)^{\frac{1}{k-1}}$$

of this remaining liquid solidifies at the eutectic composition. This is $f_E = (1 - f_S^c) f_E'$ of the total solid present at the end of solidification. This f_E is plotted as a function of f_S^c in figure 59. It is seen that for ripening to exert an influence on the microsegregation of Al-4.5 wt%Cu, it must proceed at least up to a volume fraction solid around sixty percent. It can thus be concluded that:

1 - In dendritic structures in general, coarsening by ripening exerts an influence on microsegregation that can be evaluated for a given alloy as a function the coarsening law

exponent and the fraction solid (or liquid composition) at which coarsening starts to take place predominantly by coalescence. Evaluating this fraction solid in general lies ouside the scope of this thesis, but is a necessary operation to assess the importance of coarsening on the suppression of microsegregation. Should an appreciable influence of coarsening on microsegregation be calculated for the case at hand, ripening up to f_s^c must be included in any finite difference model predicting microsegregation with solid state diffusion.

2 - When ripening ceases early enough ($f_s^c < 70\%$ for Al-4.5wt%Cu), the influence of coarsening on microsegregation is negligible. This is in particular the case when secondary dendrite arms coalesce together early on in the solidification process. The level of microsegregation can then safely be accounted for by solid state diffusion alone. This is done in the last section of this thesis.

III - The combined effect of coarsening and solid state diffusion on microsegregation.

Returning to equations (11) and (12), and relaxing the assumption that diffusion in the solid state be negligible, one obtains:

$$2\, C_L (1-k)\, r^* \frac{dr^*}{dt} = (r_T^2 - r^{*2}) \frac{dC_L}{dt} + (C_L - C_o)\, 2\, r_T \frac{dr_T}{dt} + 2\, r^*\, D_S \left(\frac{\partial C_S}{\partial r}\right)_{r=r^*} \qquad (19)$$

and the "basic solute redistribution equation" in differential form for solidification with both coarsening and solid state diffusion is then obtained by combining equations (14),(15), and (19):

$$2(C_o+At)(1-k)\ r^*\frac{dr^*}{dt} + Ar^{*2} = \left(1+\frac{2}{n}\right)AB^2t^{2/n} + 2r^*\ D_s\left(\frac{\partial C_s}{\partial r}\right)_{r=r^*}$$

The composition gradient in the solid at the interface $\left(\frac{\partial C_s}{\partial r}\right)_{r=r^*}$ cannot, however, be derived from these equations. To obtain a rigorous solution to the problem, the diffusion of solute in the entire solid phase during solidification must be solved. This is a free boundary problem and usually requires the use of numerical methods. A numerical solution to this problem was reported by Kirkwood [171] assuming (i) a planar dendrite geometry and (ii) that ripening proceeds throughout the entire solidification process. It must be emphasized that in view of results obtained in the preceding section of this chapter, the latter assumption may substantially overestimate the contribution of ripening to the suppression of microsegregation.

A different approach consists in making simplifying assumptions to estimate the composition gradient at the interface. Following steps analogous to those of Brody and Flemings [83, 164], a simple solution of that type is proposed in appendix F.

It was shown that in the composites investigated in this

work, coarsening processes are influenced in a manner such that in the narrowest triangular interstices, the growing solid is non dendritic throughout most of the solidification process. The considerably reduced levels of microsegregation found in these interstices can therefore only be due to solid state diffusion. Diffusion of solute in the solid state is thus modelled in what follows for a cylindrical volume element and no coarsening.

IV - Effect of solid state diffusion on microsegregation, no coarsening.

In this section, a finite difference model predicting the solute distribution in the solid phase during solidification is described. Similar models found in the literature are discussed in the review of literature. Differences between this and previous models are:

1 - Unlike Brody's original analysis and subsequent publications [164,169], the problem is treated as a free boundary problem. No dendrite arms thickening law is assumed and the position of the interface is calculated along with the solute profile.

2 - Kirkwood et al. [170,171] treated this problem as a free boundary problem, but for a planar dendrite arm geometry and a constant rate of enthalpy extraction. In the model presented herein, a cylindrical geometry and a constant cooling rate are assumed.

a - Assumptions and governing equations.

It is assumed that: (i) there is no undercooling at the dendrite tip; (ii) the liquid composition C_l is uniform at a given temperature; (iii) thermodynamic equilibrium is obeyed at the interface; (iv) the cooling rate is constant: $T = T_o - GxR\ t$; (v) for steady state solidification under a fixed gradient G, no mass transfer takes place along the sample axis parallel to G. Diffusion fields are then identical to those obtained if the sample were two dimensional and cooled at a constant rate GxR; (vi) the solid grows radially in a circular interstice. Within the solid, Fick's second law is obeyed:

$$\dot{C} = \mathrm{div}(D_S\ \mathrm{grad}\ C)$$

where D_S is the chemical diffusion coefficient of Cu in solid Al.

If D_S is assumed to be independent of concentration (see Appendix B) and the geometry is that of a circular cylinder, Fick's second law becomes:

$$\frac{\partial C}{\partial r} = D_S \left[\frac{\partial^2 C}{\partial r^2} + \frac{1}{r} \frac{\partial C}{\partial r} \right] \qquad (20)$$

Also, r^* is chosen to denote the position of the interface within the cylindrical primary dendrite arm of radius ℓ_0. A mass balance is then written:

$$C_l\,(1-k)\,(2\pi r^*)\ dr^* = \pi(\ell_0^2 - r^{*2})\ dC_l + D_S \left(\frac{\partial C}{\partial r}\right)_{r=r^*} 2\pi r^*\ dt$$

and since $$dt = -\frac{dT}{G \cdot R} = -m_L \frac{dC_L}{G \cdot R}$$

this equation becomes:

$$2\, C_L\,(1-k)\;\rho^*\, d\rho^* = (1-\rho^{*2})\; dC_L + 2\left[-\frac{D_S\; m_L}{\ell_0^2\; G \cdot R}\right] \rho^* \left[\frac{\partial C}{\partial \rho}\right]_{\rho=\rho^*} dC_L \qquad (21)$$

where ρ is r/ℓ_0 and ρ^* is r^*/ℓ_0 . Equation (20) then becomes:

$$\frac{\partial C}{\partial C_L} = -\frac{D_S\;\; m_L}{G\;\; R\;\; \ell_0^2} \left[\frac{\partial^2 C}{\partial \rho^2} + \frac{1}{\rho}\;\; \frac{\partial C}{\partial \rho}\right] \qquad (22)$$

The process is governed by equations (21) and (22). These with the initial condition

$$\rho^* = 0 \quad ; \quad C_L = C_o$$

and the boundary condition

$$\frac{\partial C}{\partial \rho} = 0 \quad ; \quad \rho = 0$$

determine ρ^* and the concentration profile within the solid at every instant t or, equivalently, for every concentration C_L . The problem is of the moving boundary type as ρ^* is unknown. It is solved numerically using an explicit finite difference procedure. Details of the finite difference solution are given in appendix E. It should be noted that for a given alloy system the only parameter entering the equations is $\eta = G \times R \times \ell_0^2$.

b - results.

For a given value of η , the model gives the interface position and the solute concentration at all points, throughout the solidification process.

Common measures of microsegregation are the fraction eutectic or second phase and the minimum solute concentration present at the end of solidification. These can be deduced from the computer model at T_E, and are respectively plotted in figures 60 and 61 as functions of ℓ_0^2/t_f. At high cooling rates and for large primary dendrite arm radii, the results correspond to those given by the Scheil equation. For $\ell_0^2/t_f < 2\ 10^{-13}\ m^2/s$ a microstructure free of microsegregation should be obtained.

The minimum copper concentration present before the eutectic temperature is attained is also of interest since it can be measured from quenched structures obtained in steady state solidification experiments. This is done in the next chapter of this thesis, figures 66 to 73.

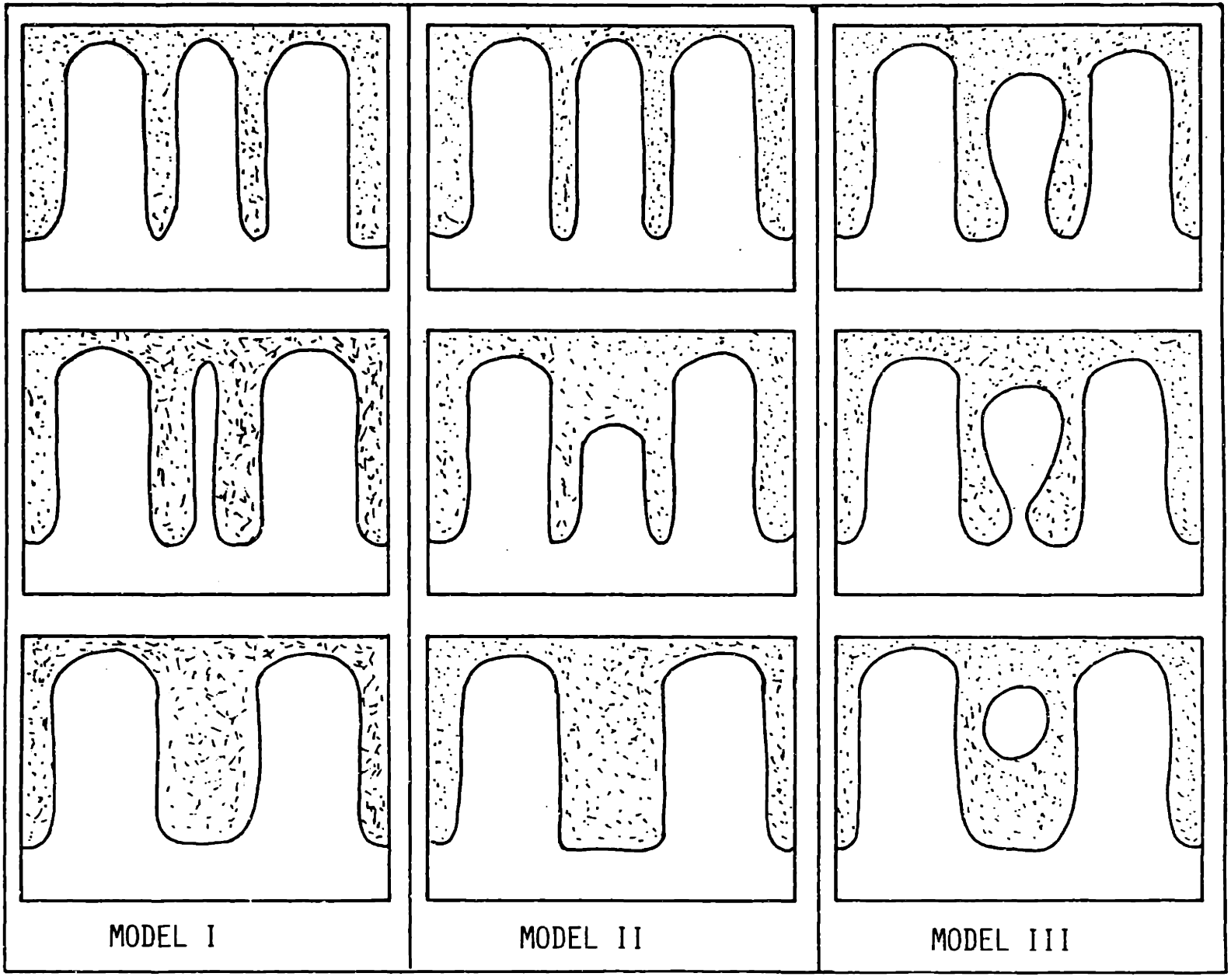

Figure 49 - Ripening mechanisms for secondary dendrite arms.

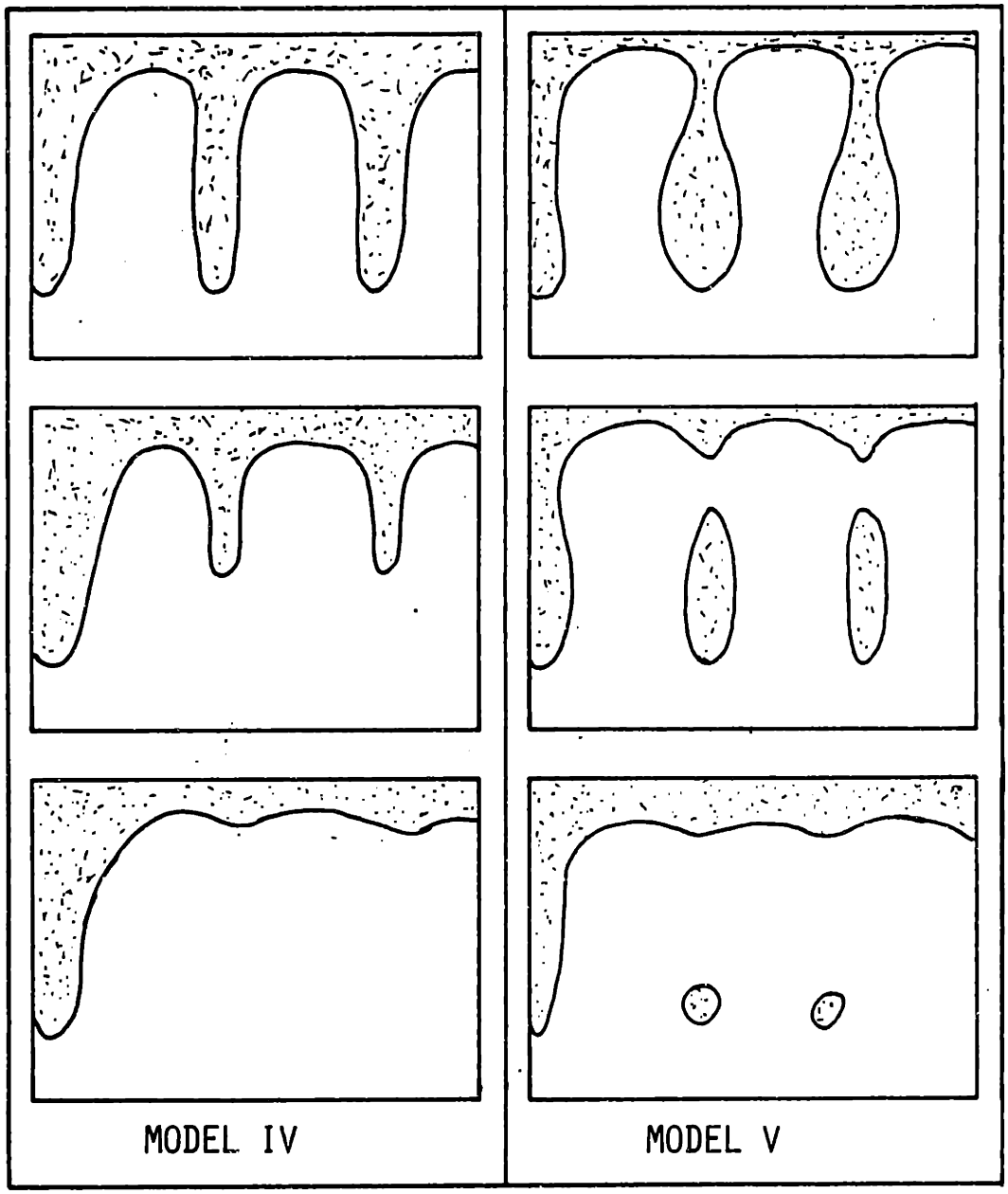

Figure 50 - Coalescence mechanisms for secondary dendrite arms.

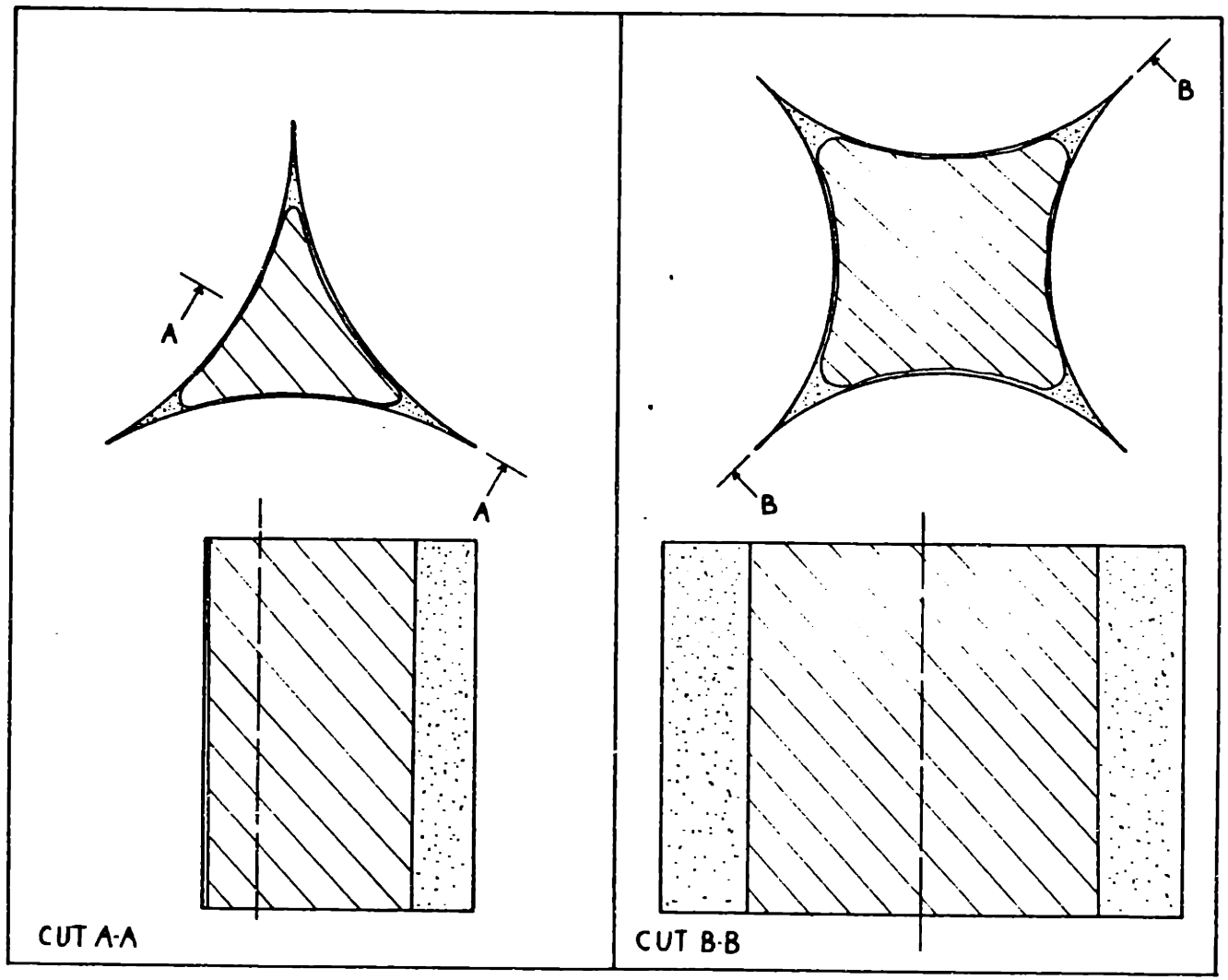

Figure 51 - Fully coarsened liquid-solid structure in triangular and square interstices.

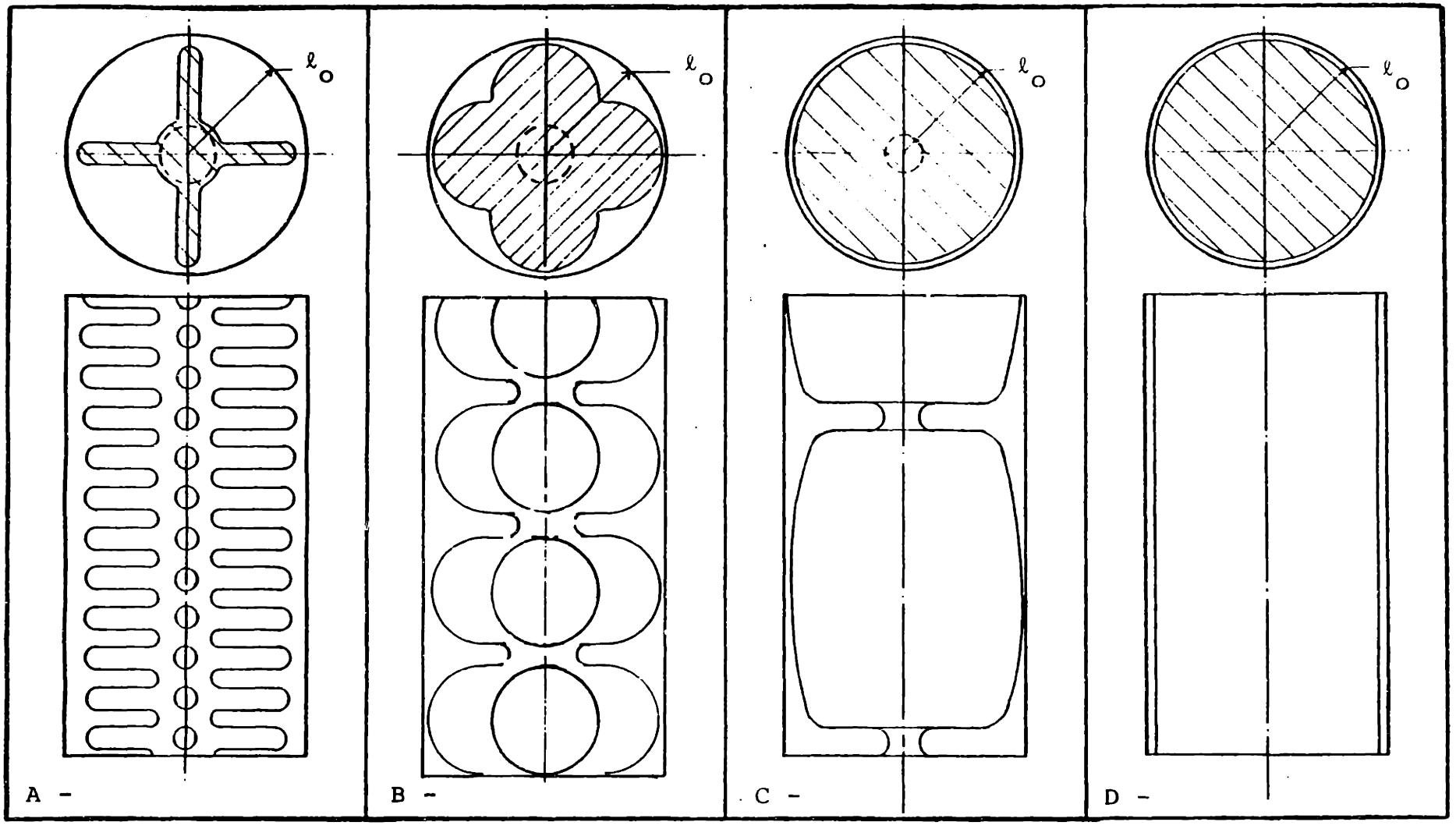

Figure 52 - Schematic rendition of dendrite coarsening in an interfiber space of radius ℓ_o
A: $\lambda_2/2 < \ell_o$. B: $\lambda_2/2 \leq \ell_o$, C: $\frac{\lambda_2}{2} \cong \ell_o$, D: fully coarsened solid phase.

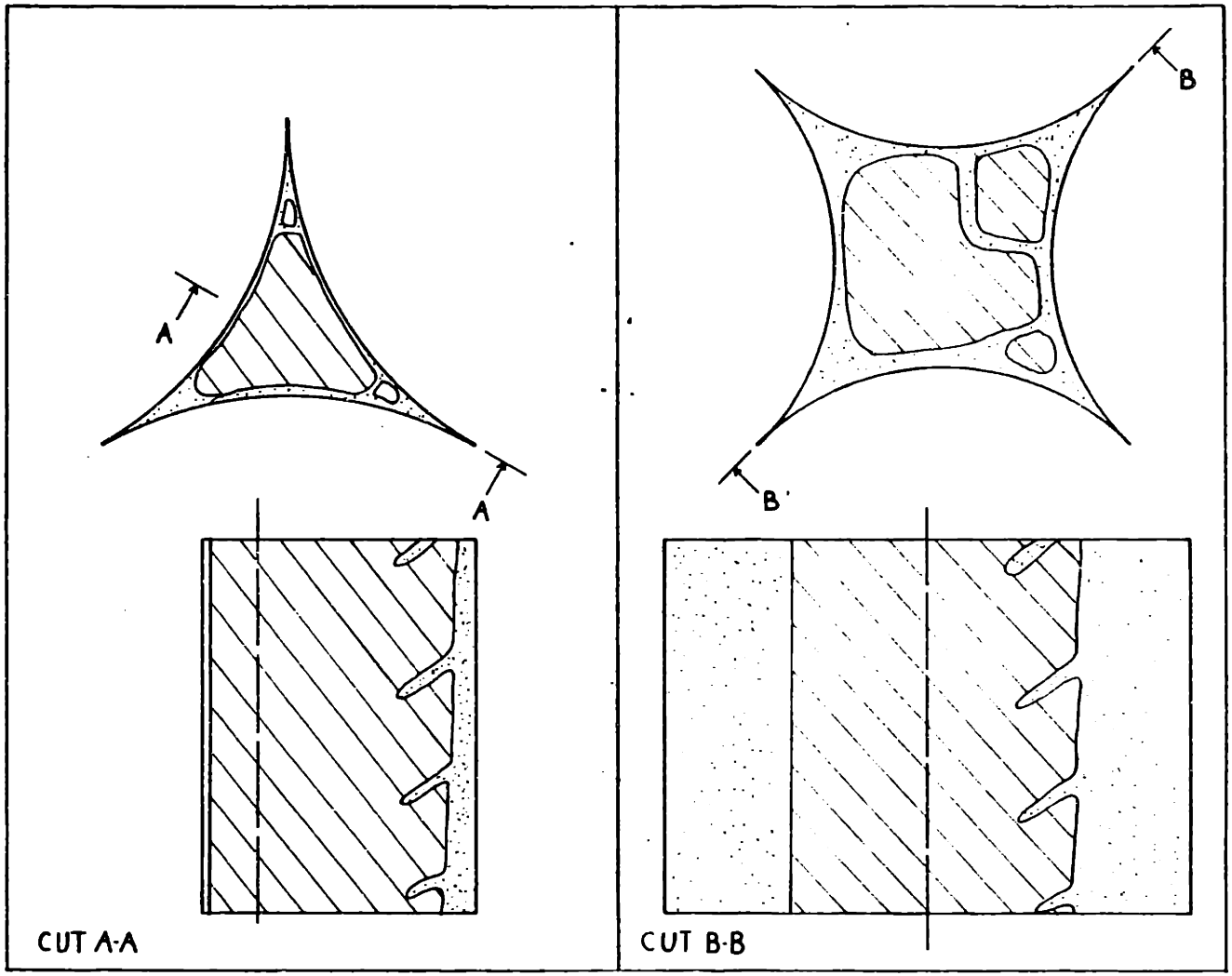

Figure 53 - Dendrite morphology during the initial stages of solidification in triangular and square interstices.

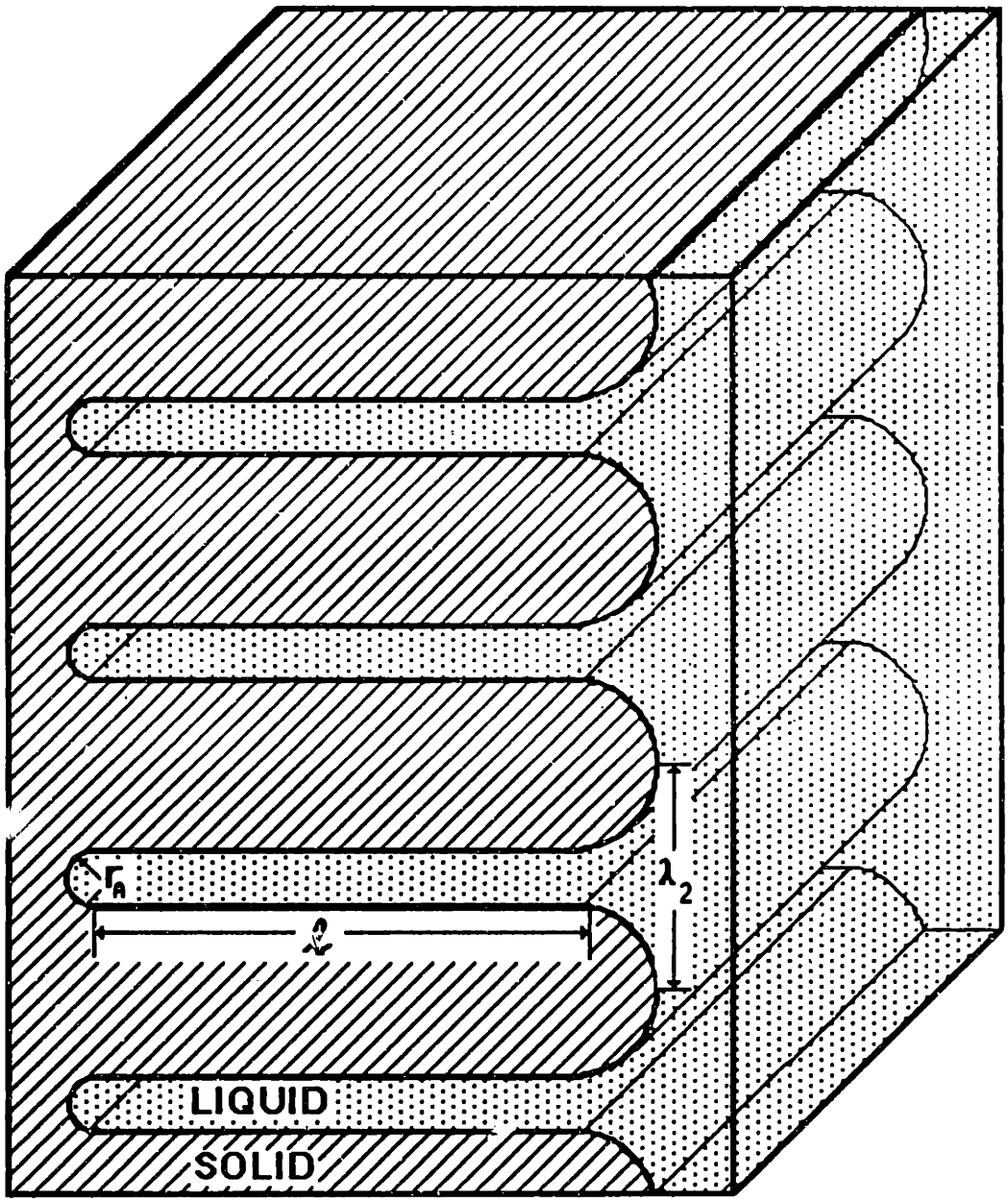

Figure 54 - Idealized dendritic structure used for modelling secondary dendrite arm coalescence.

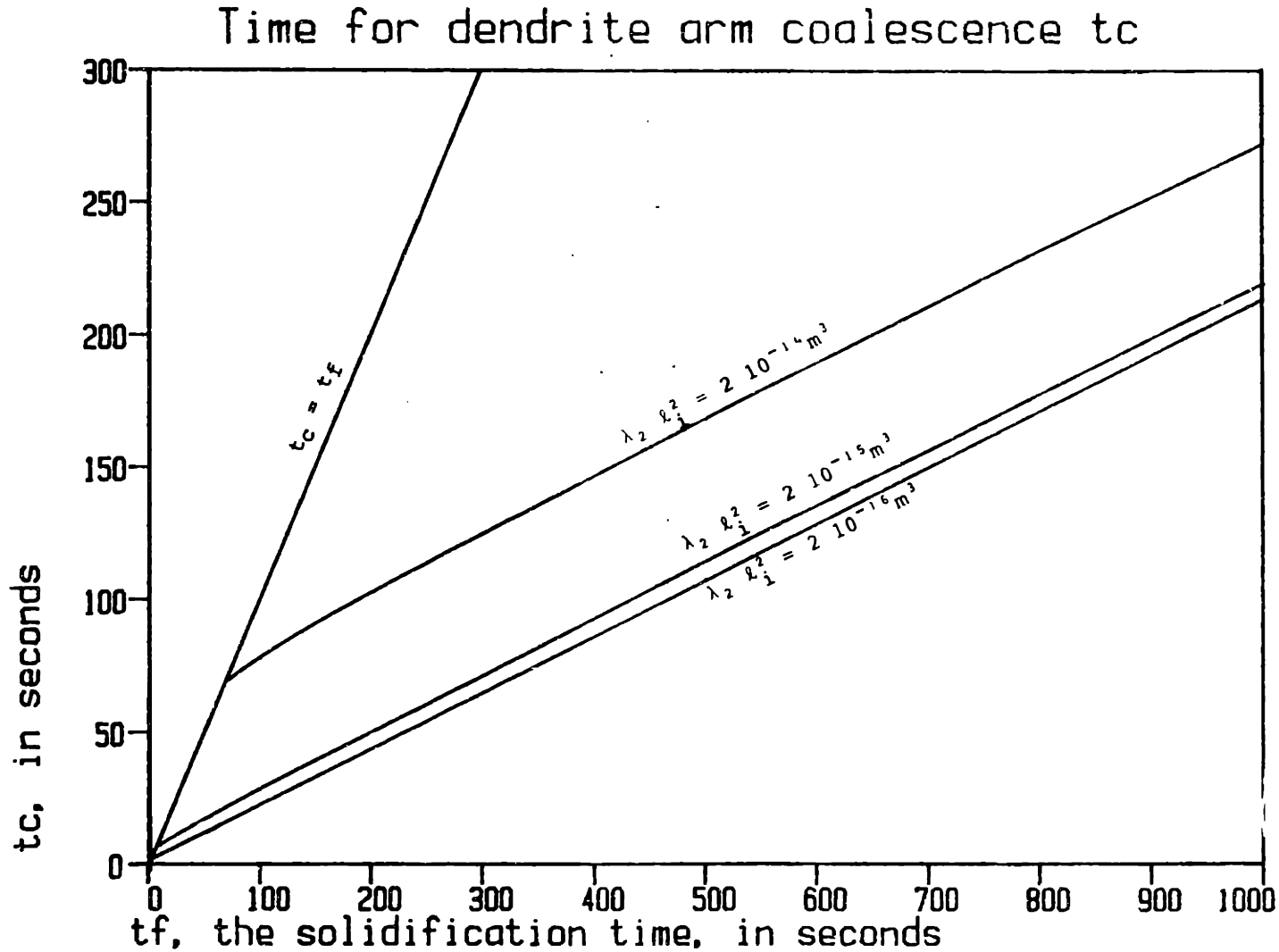

Figure 55 - Calculated time for coalescence of secondary dendrite arms as a function of the solidification time t_f. f_{si} is 0.65 for all three curves.

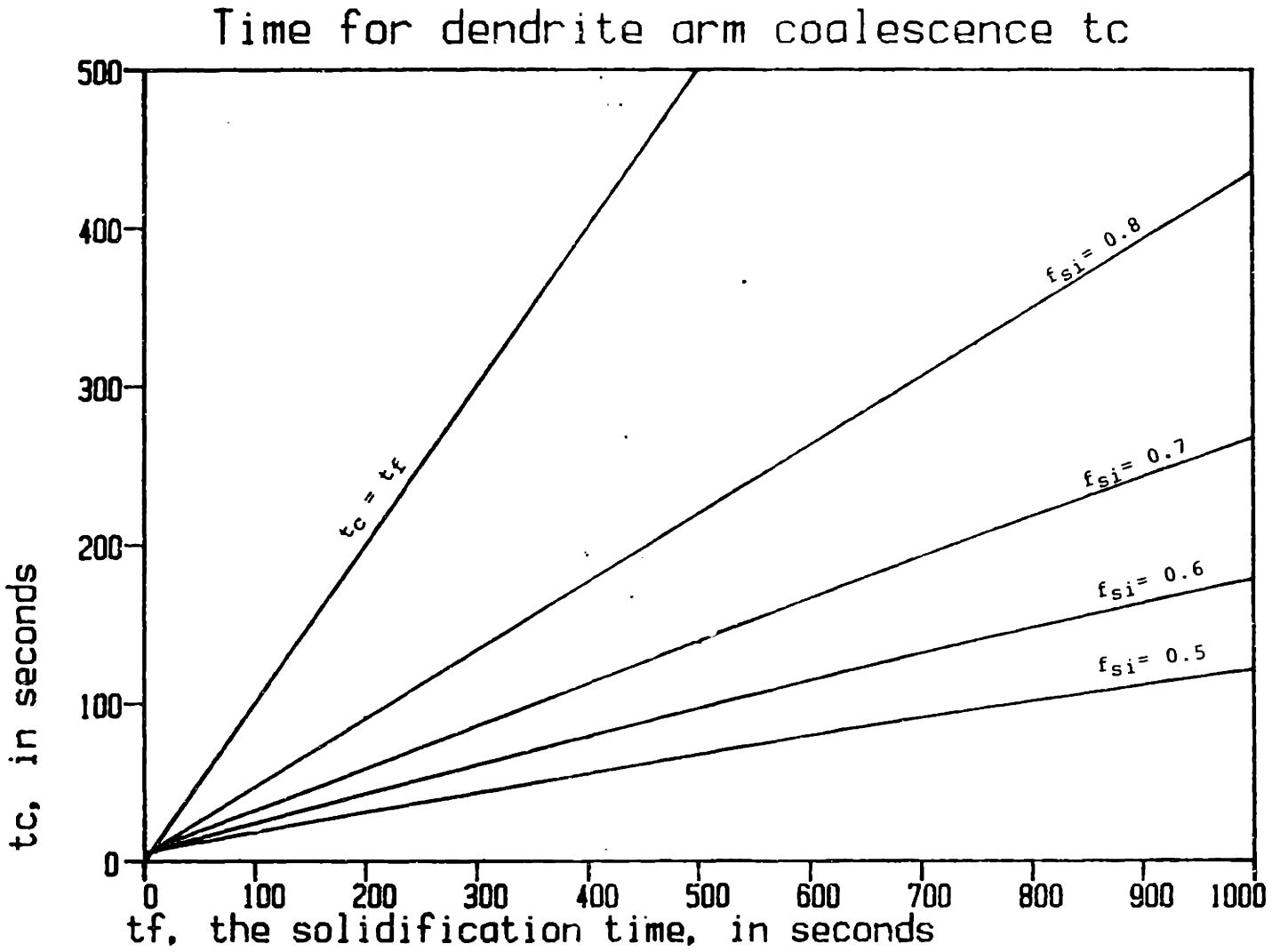

Figure 56 - Calculated time for coalescence of secondary dendrite arms as a function of the solidification time, t_f. $\ell_i^2 \lambda_2 = 2\ 10^{-15}\ m^3$.

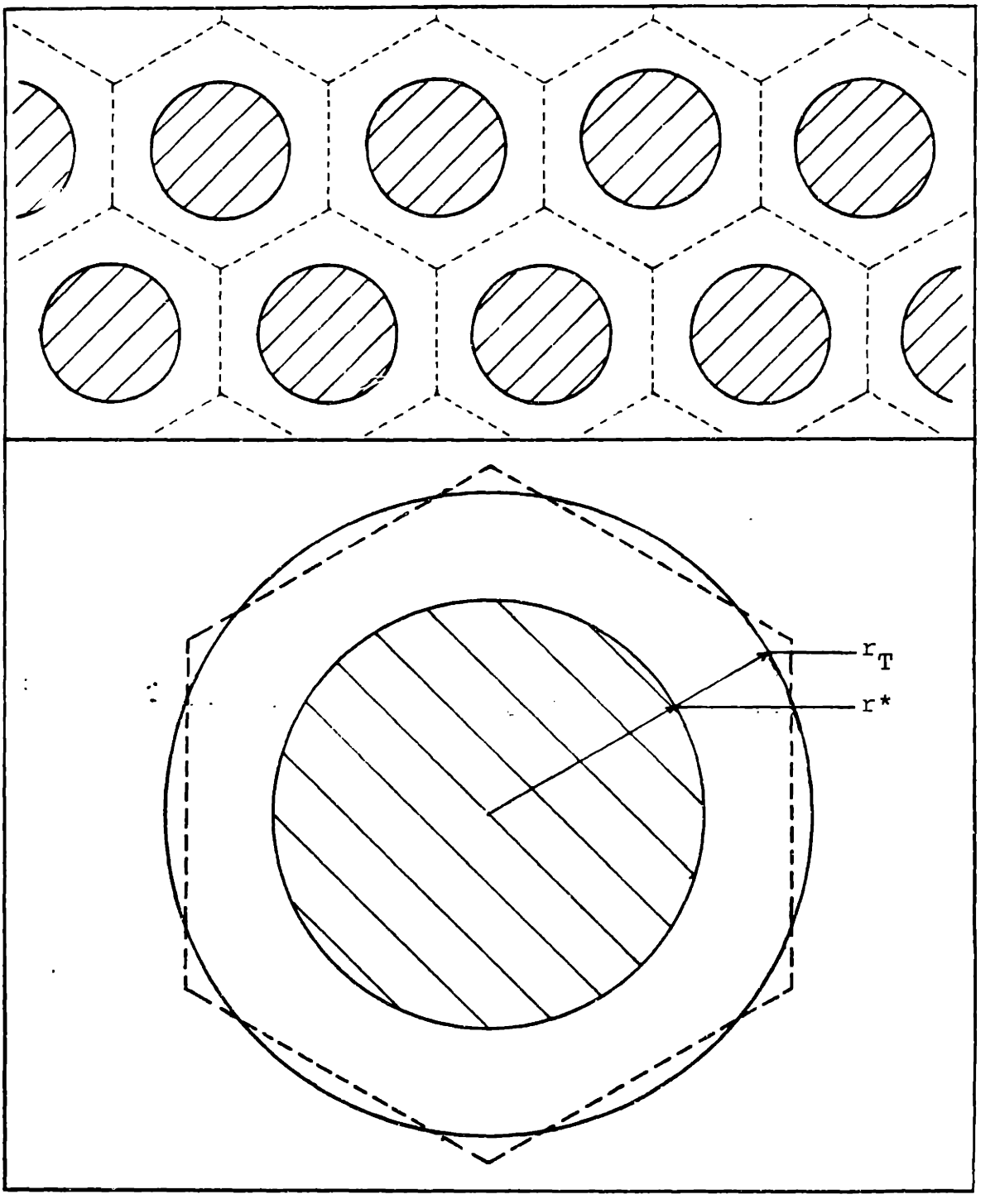

Figure 57 - Idealized geometry of a secondary dendrite arm array used to model the influence of ripening on microsegregation.

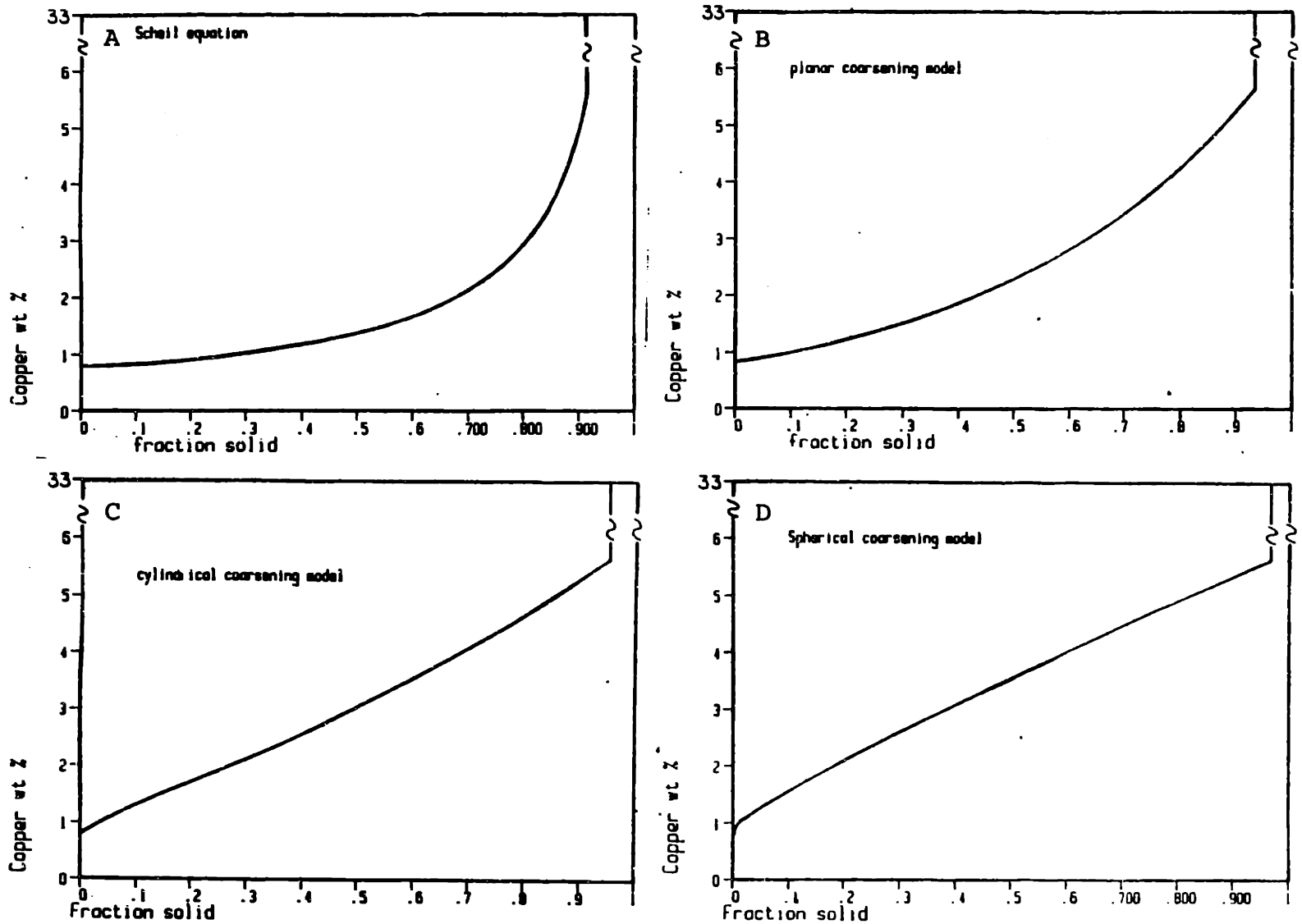

Figure 58 - Final solute profile in Al-4.5wt%Cu solidified : A: without coarsening, B,C,D : with coarsening by ripening throughout the solidification range, for planar, cylindrical and spherical growth morphologies respectively and no solid state diffusion.

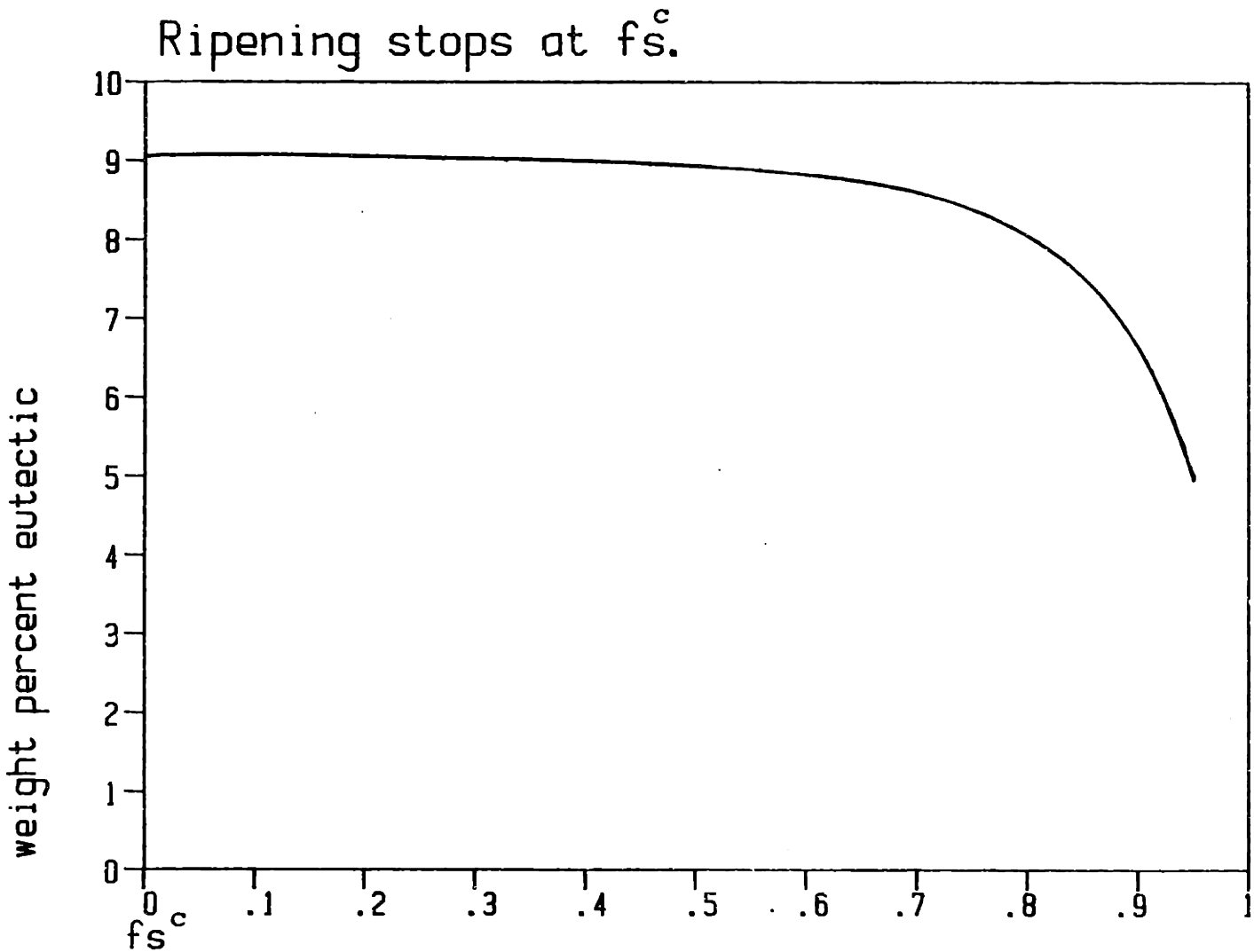

Figure 59 - Weight percent eutectic for cylindrical growth elements assuming coarsening is by ripening up to a fraction solid f_s^c.

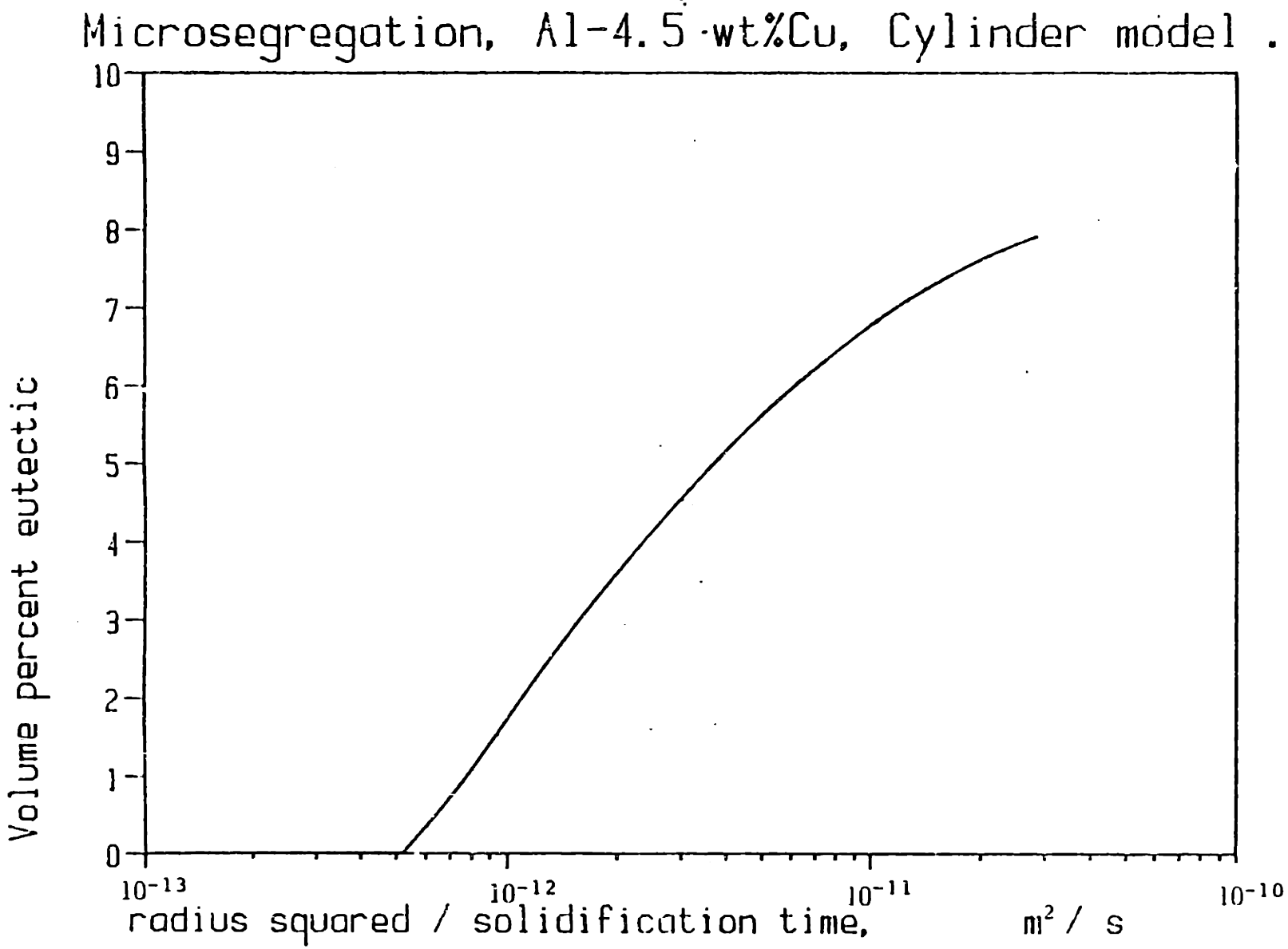

Figure 60 - Volume percent eutectic as a function of dendrite arm or interfiber radius and solidification time. No coarsening, cylindrical growth morphology.

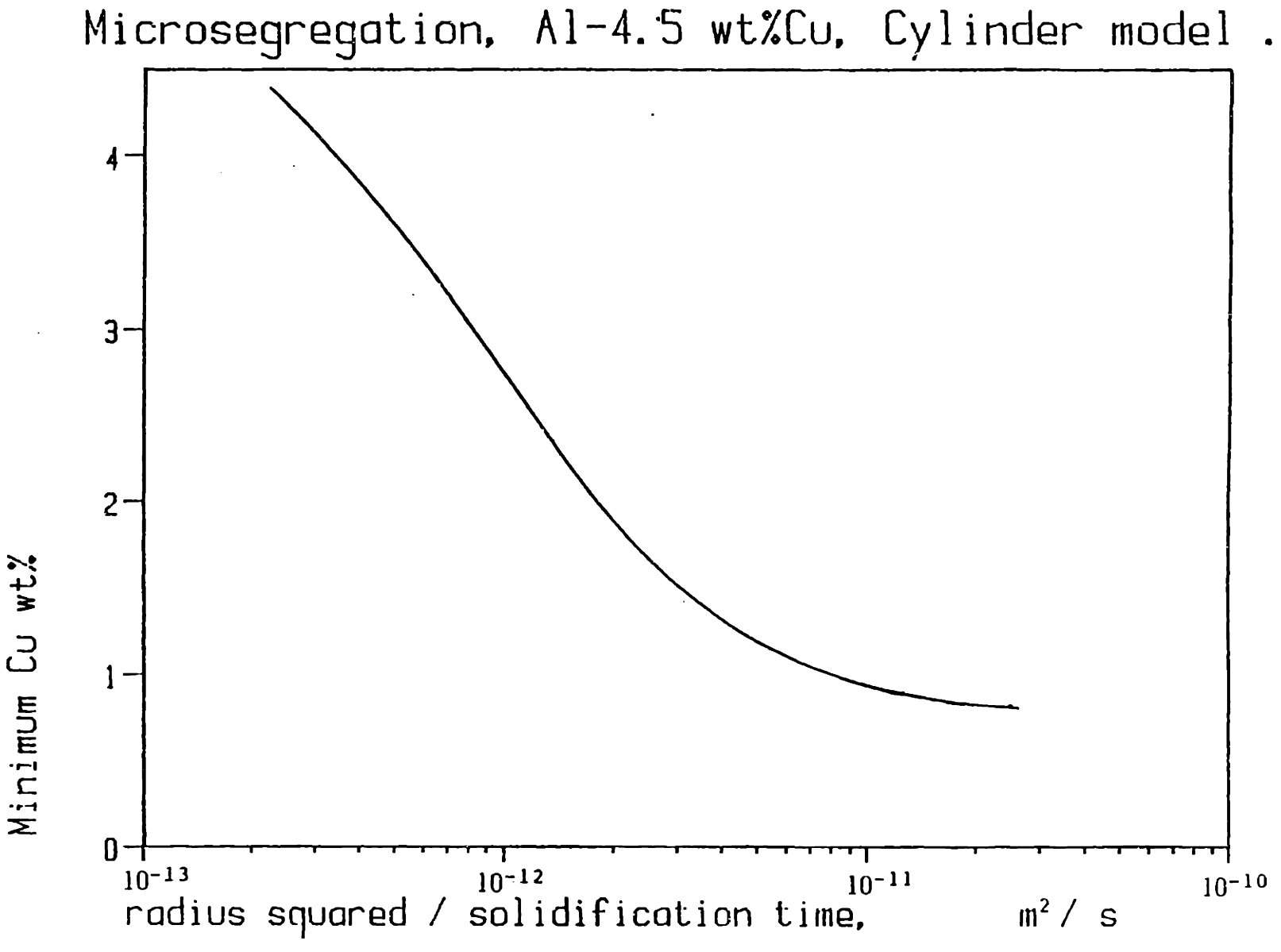

Figure 61 - Minimum copper concentration as a function of dendrite arm or interfiber radius and solidification time. No coarsening, cylindrical growth morphology.

DISCUSSION

I - Comparison of experiment and theory.

No increase in the dendrite tip undercooling was detected in the presence of fibers. This observation is in agreement with calculations performed by Mc Cartney and Hunt [123] discussed in the review of literature. Solidification of the metal alloy between the fibers therefore started close to the liquidus temperature, since no significant undercooling is normally present at the dendrite tips of Al-4.5wt%Cu at the growth rates and temperature gradients of the samples in this work.

In the fully solidified matrix, isoconcentration contours were never found to intersect the fiber surfaces. Instead, they ran parallel to the fiber surfaces, avoiding the fibers at a distance of the order of several microns. In quenched partially solid structures, a copper rich film was found to surround the fibers. The dendrites therefore avoided the fibers as they grew. This can be attributed to two phenomena:

1 - Interfacial energies present in the system under consideration do visibly not favour heterogeneous nucleation or growth of the solid on the fiber surface. A situation where the fibers are everywhere in contact with the liquid phase is therefore thermodynamically the most stable in the initial phases of solidification. This explains why solidification did not begin

on the fiber surfaces.

2 - As the solid phase approaches a fiber, solute rejection in the liquid phase away from the growing interface is inhibited by the fibers. Growth consequently takes place elsewhere. Growing dendrites can thus rapidly center themselves in the interfiber spaces and yield coring patterns several microns away from the fibers.

In conclusion, if the reinforcing phase does not act as a heterogeneous nucleation catalyst for the metal alloy or otherwise act as a preferred growth site, the solid phase will start growing from a point remote from the fibers. Growth will then proceed away from the fiber surfaces due to solute rejection at the liquid/solid interface. These mechanisms apparently determine the microstructure of the majority of metal matrix composites (see the literature survey).

While the solid phase grew behind the dendrite tip it formed secondary dendrite arms between the fibers. It was found experimentally that the coarsening of these secondary dendrite arms in narrow interstices presents the following unique features:

1 - significant deviations from the usual $t^{1/3}$ law leading to much larger secondary dendrite arm spacings in the later stages of solidification, in comparison to the metal in the unreinforced alloy,

2 - disappearance of secondary dendrite arms after some time

during solidification,

3 - secondary dendrite arm spacings (in one sample) that were significantly below that predicted by the $t^{1/3}$ law, before they coarsened rapidly.

By examining the microstructure of the metal, it was shown that the tendency of secondary dendrite arms to coalesce is enhanced in narrow interstices. The filling in of the trough separating secondary dendrite arms takes place sufficiently fast to erase all secondary dendrite arms in the matrix. This coalescence mechanism, depicted as model IV in figure 50 is responsible for the much increased secondary dendrite arm spacings measured and the total disappearance of secondary dendrite arms after some time during solidification in the narrowest interstices.

It was found that in all triangular interstices as well as in square interstices having solidified in more than about 100 seconds, all coring patterns are concentric with the fiber surfaces. The reason for this isoconcentrate morphology was shown to lie in the rapid completion of the coalescence process, early enough for the solid phase to grow in a non dendritic fashion when it forms from a liquid of high copper concentration.

In square interstices of samples with a solidification time below about 100 seconds (samples I-1 and I-4), the matrix displays dendritic coring patterns and, occasionally, islands of the liquid or the second phase between the fibers. The dendritic coring patterns are due to the fact that the coalescence process reached completion only late in the solidification process, when

the solid forming was of relatively high copper concentration. The few islands of quenched liquid or second phase are present because in some instances secondary dendrite arms coalesced [illegible]cting from their tips (according to model V of figure 50) in square interstices of these samples, thus leaving isolated pools of liquid between coalescing dendrite arms.

In the preceding chapter, it was shown that secondary dendrite arm coarsening by ripening cannot proceed far beyond the point where the average secondary dendrite arm spacing equals twice the maximum radius of curvature permissible inside the interstice. This explains the presence of secondary dendrite arm spacings significantly smaller than in the unreinforced alloy seen on figure 32. Secondary dendrite arm coalescence in this sample was slow enough in some interstices to allow for secondary dendrite arms to "survive" up to 200 seconds during solidification. These secondary dendrite arms could not ripen beyond a certain size and hence remained at much smaller values than in the unreinforced alloy.

The time t_c for secondary dendrite arms to coalesce according to model IV of figure 50 was calculated in the preceding chapter under the assumption that the average secondary dendrite arm spacing remains approximately constant during coalescence. An experimental estimation of t_c can be obtained from the secondary dendrite arm measurements by postulating that t_c is approximately given by the time during solidification after which secondary dendrite arms could no longer be discerned in the quenched

microstructures, figures 25 to 38. These approximate data points were plotted in figure 42.

The calculated time for coalescence t_c depends on three variable: f_{si}, the volume fraction solid below which coalescence is sluggish; $\lambda_2 \ell_i^2$, where ℓ_i is the initial dendrite arm length and λ_2 is the (constant) dendrite arm spacing; and t_f, the solidification time. Both ℓ_i and λ_2 depend on the interstice dimensions when secondary dendrite arm ripening is inhibited by the fibers during coalescence. f_{si} should be approximately constant for a given alloy. Using equation (6) of the theory chapter, a good fit with experimental data is obtained with $f_{si} = 0.65$, figures 62 and 63. For square interstices, $\lambda_2 \ell_i^2$ is about $6 \times 10^{-15}\ m^3$ and for triangular interstices, $\lambda_2 \ell_i^2$ is about $2 \times 10^{-15}\ m^3$. Both values are reasonable:

(i) in square interstices, from the secondary dendrite arm spacing measurements, $\lambda_2 \cong 40$ microns, figure 33 to 38. The initial secondary dendrite arm length is then around 12 microns, which is reasonable (figures 12, 13 and 15).

(ii) in triangular interstices, from the secondary dendrite arm spacing measurements, $\lambda_2 \cong 20$ microns. The initial secondary dendrite arm length is thus around 10 microns which is reasonable as well (figure 14).

Further agreement between the model and experimental data can be obtained by comparing the criteria (7) and (8) for full coalescence and non dendritic coring patterns with experimental data. According to the model, with the solidification times in this work, all square and triangular interstices should be fully

coalesced before the end of solidification. This is indeed observed. The model predicts that the coalescence process is complete when the copper concentration C_s in the depositing solid is:

$$C_s = k\, C_o \left[\frac{29.6 \times 10^{15} \ell_i^2 \lambda_2 + 2.86}{t_f} \right]^{0.829}$$

In square interstices, with t_f = 133 seconds, C_s is 2.5 wt%Cu (sample H-2), with t_f = 84 seconds, C_s = 2.9 wt%Cu. It is within this range of solidification times that the coring patterns revealed by the etchant were observed to become non dendritic. As the etchant outlines coring patterns corresponding to copper concentrations around 3wt% [66], the calculations agree with experimental observations. Furthermore, the SEM micrograph given in figure 16 was from sample I-1, which with t_f = 54 seconds yields C_s = 3.5 wt%Cu. The copper content (determined by electron probe microanalysis) of the lighter areas on this micrograph which separated two coalesced secondary dendrite arms varied between 3.5 and 3.9 wt%Cu.

It can thus be concluded that the overall agreement of the model with experiment is good. Two factors were chosen so as to fit the measured values for t_c . The first parameter, f_{si} , is a constant for a given alloy. For Al-4.5wt%Cu, f_{si} is about 0.65, which is reasonable. The second parameter, $\lambda_2 \ell_i^2$, depends on the dendrite and interstice morphologies and is more difficult to predict. Since the critical time for coalescence t_c is strongly dependent on this parameter when it is close to the solidification time t_f , the ability of the model to predict a

priori and precisely the time for coalescence in a given interstice is somewhat limited. Nevertheless, since λ_2 and ℓ_i can be predicted within a factor of two for a given interfiber interstice diameter, the minimum solidification time for full coalescence can be predicted by equation (7) within an order of magnitude.

A calculation of the time for coalescence t_c for ripening secondary dendrite arms is given in Appendix D. This model is more adequate for large interstices or dendrite arms in the unreinforced alloy, since in these cases the secondary dendrite arm spacing does not remain constant during the coalescence process. A comparison of results from both models with values for ℓ_i and λ_2 for square and triangular interstices given above is shown in figures 64 and 65. The discrepancy between the two models is not very large.

The influence of dendrite arm coarsening on the suppression of microsegregation in general has been described. In particular, it was shown that for Al-4.5wt%Cu, when the coalescence of secondary dendrite arms occurs early in the solidification process as was the case in triangular interstices, dendrite arm coarsening exerts a negligible influence on the relief of microsegregation.

Solid state diffusion then accounts alone for the solute

profiles observed. A finite difference model was built to calculate solute redistribution by solid state diffusion in circular interstices (valid as well for cylindrical dendrite arms). The model was applied to square and triangular interstices by approximating these interstices with circular interstices of identical cross sectional area (given in figure 9). A comparison between calculated and measured minimum copper concentrations at various stages of the solidification process (from table 3) is given in figures 66 to 73. Agreement is good enough to conclude that the model is accurate. In particular, it is both predicted and experimentally observed that when ℓ_0^2 / t_f is less than about 2×10^{-13} m^2/s a homogeneous microstructure free of microsegregation is obtained with a minimum copper concentration close to 4.5 wt% and no eutectic.

The computer model allowing for an isothermal hold was used for sample I-5. This sample was held still for ten minutes in the temperature gradient of the Bridgman furnace before quenching. Results showed that no microsegregation should be found below the solidus in the triangular interstices of this sample. Experimental results on this sample indicate that below the solidus, the minimum copper content increased above 4.5 wt% to reach a value close to that of the solidus at the hold temperature. This must be due to the fact that the copper rich liquid was free to fall and fill in the space left by the shrinking metal during the long hold in the Bridgman furnace. This sample proves that it is possible to obtain a metal

microstructure free of dendrite arms and microsegregation in metal matrix composites after an isothermal hold at a temperature just below the solidus of the matrix alloy and with a reasonably short hold time. This implies in particular that a matrix alloy with a copper content as high as 5.6 wt%Cu can be easily homogenized.

II - Controlling the metal microstructure in fiber reinforced Al-4.5wt%Cu.

In this section, the application of models developped in this thesis will be illustrated for two simple cases: the fibers are assumed to define circular and rectangular cylindrical interstices. The aim is to predict and control the microstructure of the metal matrix after directional solidification of the matrix parallel to the fibers.

A unidirectional fiber reinforced metal matrix composite is considered, the matrix of which is cast Al-4.5wt%Cu. The metal is thus constrained to solidify in cylindrical interfiber channels. These are assumed for simplicity to be circular of radius ℓ_0. It is assumed that the fiber do not react with the metal, and that the metal does not nucleate heterogeneously on the fiber surface.

Both the coalescence of secondary dendrite arms and the suppression of microsegregation are controlled by two parameters: the interstice radius ℓ_0 and the solidification time t_f (or

equivalently the cooling rate GxR). Grouping the results from the calculations pertaining to these two facets of the microstructure, one can approximately predict that:

1 - if it is assumed that $\ell = \ell_0 / 2$, and that the secondary dendrite arm spacing remains constant around $2\ell_0$, from equation (7), all secondary dendrite arms will have coalesced before the end of solidification if:

$$t_f \geq 1.8.10^{15} \ell_0^2$$

in S.I. units. From equation (8), for isoconcentrates containing 3wt%Cu to be non dendritic, the solidification time t_f must exceed:

$$t_f \geq 6.4.10^{15} \ell_0^2$$

These criteria are probably somewhat conservative but should be correct within an order of magnitude in t_f.

If these criteria are met, solidification will be mostly non dendritic and the cylindrical solid state diffusion model applies. A metal free of any microsegregation will therefore be found between the fibers if:

$$t_f \geq 5.10^{12} \ell_0^2 \qquad \text{(S.I. units)}$$

These criteria can be combined in a single plot delineating regions of circular interfiber space radii and solidification times for which a given microstructure will be obtained in Al-4.5wt%Cu matrix composites. This plot is given in figure 74, and examples of corresponding microstructures from the samples are combined in figure 75. It is seen that four different types of microstructure can be obtained corresponding to the four regions shown in figure 74:

Region A: Both secondary dendrite arm coalescence and solid state diffusion do not have time enough to affect the microstructure. The metal solidifies at a rapid rate, and a dendritic microstructure unperturbed by the fibers is obtained.

Region B: Secondary dendrite arm coalescence has time to reach completion before the eutectic temperature is reached. About all the eutectic therefore forms at the fiber-matrix interface, but coring patterns are dendritic in the final matrix microstructure. This region is intermediary between the dendritic and the non dendritic microstructures. This was found for example in square interstices of samples I-1 and I-4.

Region C: The microstructure is non dendritic with concentric circular isoconcentrates. Some degree of microsegregation is still found in the metal matrix. There is some second phase present at the fiber-metal interface, and a central solute poor core in the matrix regions. The minimum copper concentration increases and the amount of eutectic decreases as the solidification time t_f increases for a given interfiber space radius

Region D: Both dendrite arms and microsegregation are erased at the end of solidification. The microstructure is completely featureless and homogeneous. After ageing, optimal strength can be obtained in the matrix and hence the composite. The interface is then devoid of the brittle theta phase ordinarily found with Al-4.5 wt%Cu.

As a second example, the assumption of a circular interfiber space is relaxed and replaced with that of a rectangular interfiber space with one side having a length (a) smaller than the other (b). The morphology of a growing dendrite is depicted in figure 76 and it is apparent that:

λ_2 is equal to a, the shorter side of the rectangle since dendrite arms can not ripen beyond the point where the curvature at their surface is everywhere around 2/a.

ℓ_i is somewhat smaller than b/2, half the longer side of the rectangle if the dendrite grows approximately in the center of the interstice as depicted in figure 76. Assuming $\ell_i = (b-a)/2$, the criteria become:

for coalescence of secondary dendrite arms during solidification:

$$t_f \geq 0.45 \times 10^{15} a\ (b-a) \qquad \text{(S.I. units)}$$

for coalescence to be complete before solid starts depositing with a copper content higher than 3wt%Cu:

$$t_f \geq 1.6\ 10^{15}\ a\,(b-a) \qquad \text{(S.I. units)}$$

If b is much larger than a, coalescence according to model V of figure 45 may however become significant. The kinetics of secondary dendrite arm coalescence are therefore probably underestimated by these equations in that case.

Provided the coalescence process has erased all secondary dendrite arms, microsegregation can be relieved by solid state diffusion. If a and b are approximately of the same order, the cylindrical model will still be a good approximation to reality as it was in square and triangular interstices, and the criterion for obtaining a microstructure free of microsegregation becomes:

$$t_f \geq 1.25\ 10^{12}\ a\ b \qquad \text{(S.I. units)}$$

If $b \gg a$, a planar model such as the one by Kirkwood et al.[171] would be more adequate.

From a practical point of view, it may be judicious to cool metal matrix composites at a medium rate from the liquidus temperature to the solidus temperature and heat treat for homogenization immediately below the solidus temperature. This was shown on one sample to be a viable method. One significant advantage over cooling the composite at a constant low rate is that less time is spent at higher temperatures where the fiber may react with the matrix.

Slow solidification to obtain featureless microstructures and performing a homogenization heat treatment above the eutectic temperature are novel concepts. They are impossible in non-composite cast metals because as soon as such materials are brought above the eutectic temperature for any prolonged period of time, significant coarsening of the microstructure takes place. The distance over which solid state diffusion operates then increases and the brittle second phase groups into large islands typical of "burnt" microstructures. In metal matrix composites, however, the fibers interfere with the microstructural coarsening the metal normally experiences. After a certain time, the morphology of the solid phase is dictated by the fibers. At this point solid state diffusion can proceed unhindered. The resulting microstructure can then be rendered featureless.

It was shown in the review of literature that the matrix microstructure of cast SiC/Al-4.5wt%Cu composites is representative of what is found in the majority of cast metal matrix composites. The mechanisms determining the microstructure of the matrix have been identified and interpreted on the basis of relatively simple theoretical models which should be easy to transpose to other metal matrices. The conclusions and processing methods given in this work should therefore be applicable to most cast metal-matrix composites.

To date, the materials engineer confronted with the task of fabricating metal matrix composites has chosen the matrix alloy

and its processing conditions strictly along the lines that apply for conventional unreinforced cast parts. No justification exists for this approach. The microstructure obtained between the fibers can be drastically different from, and much better controlled than is the case with the fiber-free metal. For example, within the Al-Cu system, a copper content as high as 5.5 wt% may be a perfectly judicious choice since all the copper in this alloy can be put in solid solution in the primary phase. Other alloy systems may also be chosen if they yield a secondary phase it would be interesting to find at the fiber/metal interface in the final microstructure. New possibilities and different criteria should thus dictate the choice and the solidification processing of the matrix alloy for these materials.

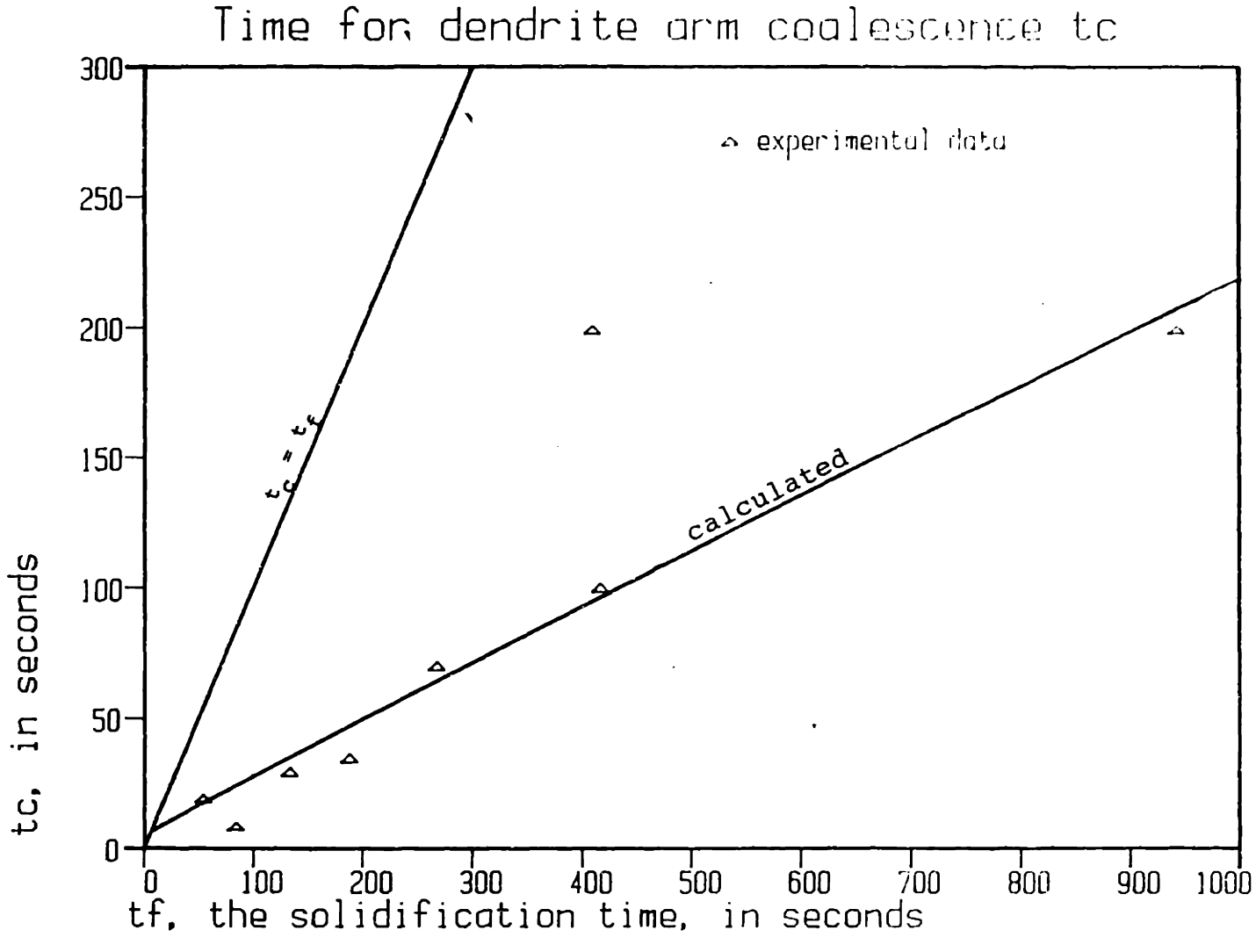

Figure 62 - Comparison of calculated and measured time for coalescence t_c for triangular interstices. f_{si}= 0.65 and $\ell_i^2 \lambda_2$= 2 10^{-15} m^3.

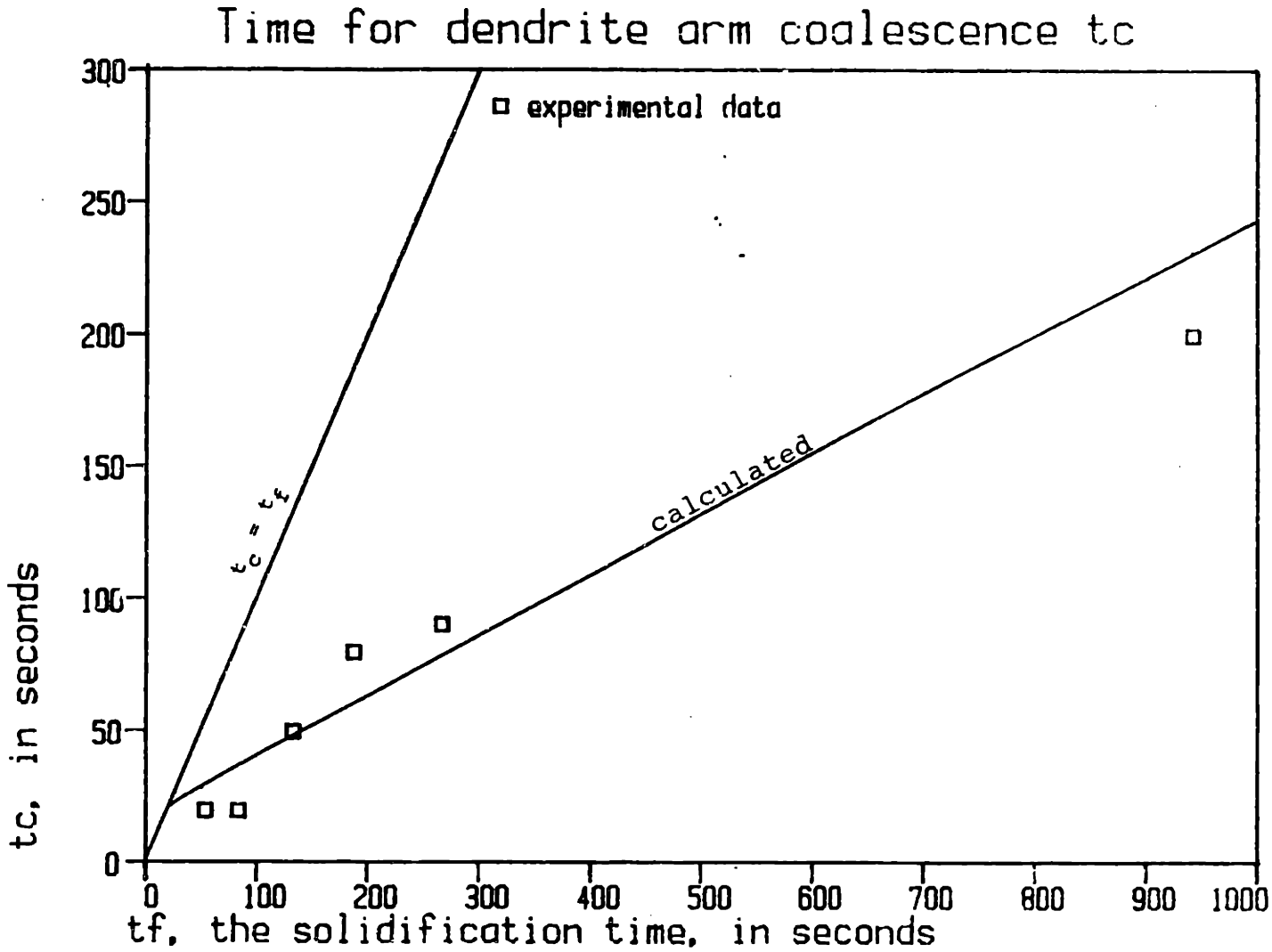

Figure 63 - Comparison of calculated and measured time for coalescence t_c for square interstices. f_{si}= 0.65 and $\ell_i^2 \lambda_2$= 6 $10^{-15} m^3$.

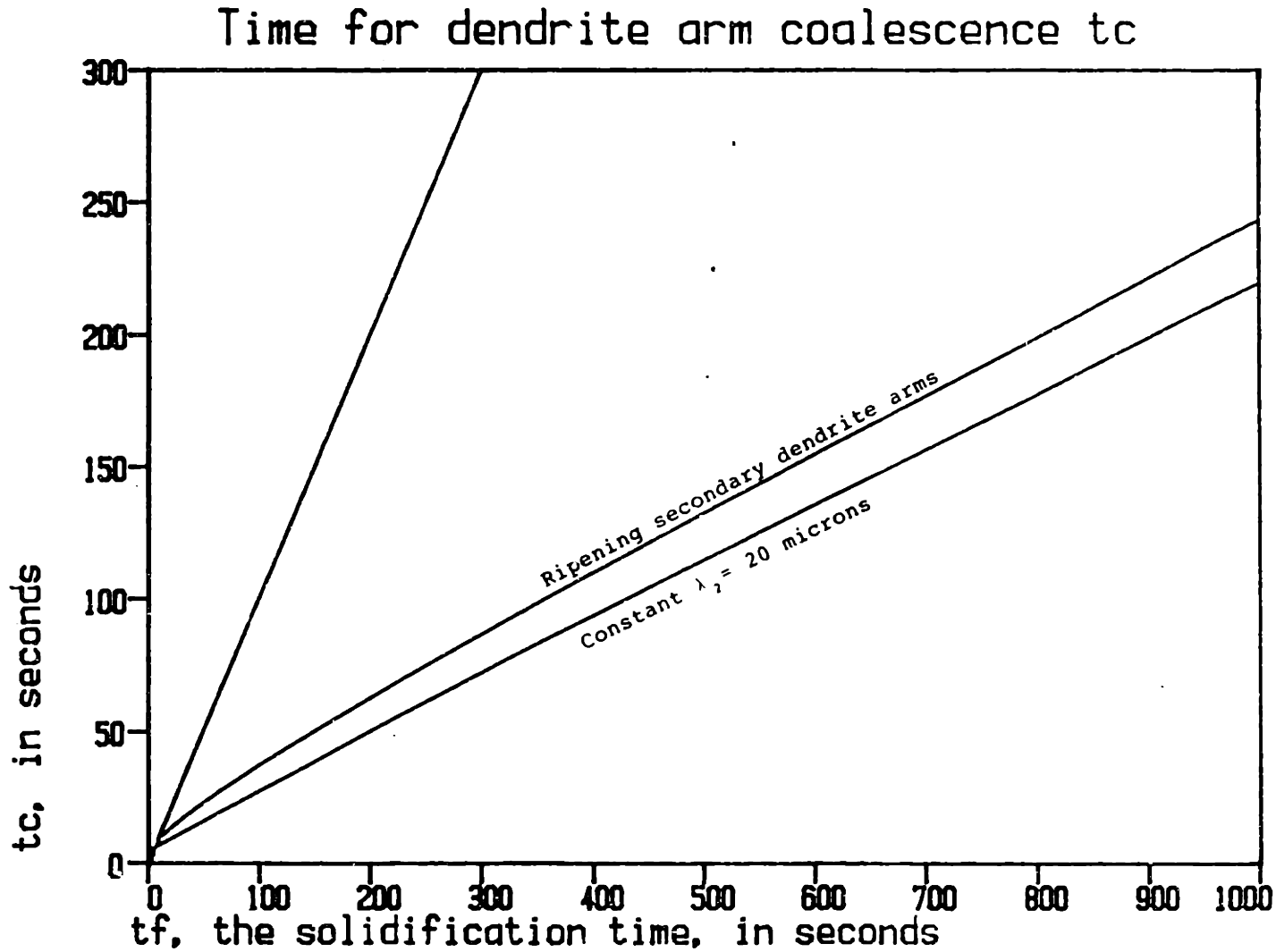

Figure 64 - Calculated time for coalescence t_c for ripening dendrite arms compared to the results with a constant λ_2. f_{si}= 0.65 and $\ell_i^2 = 10^{-10} m^2$.

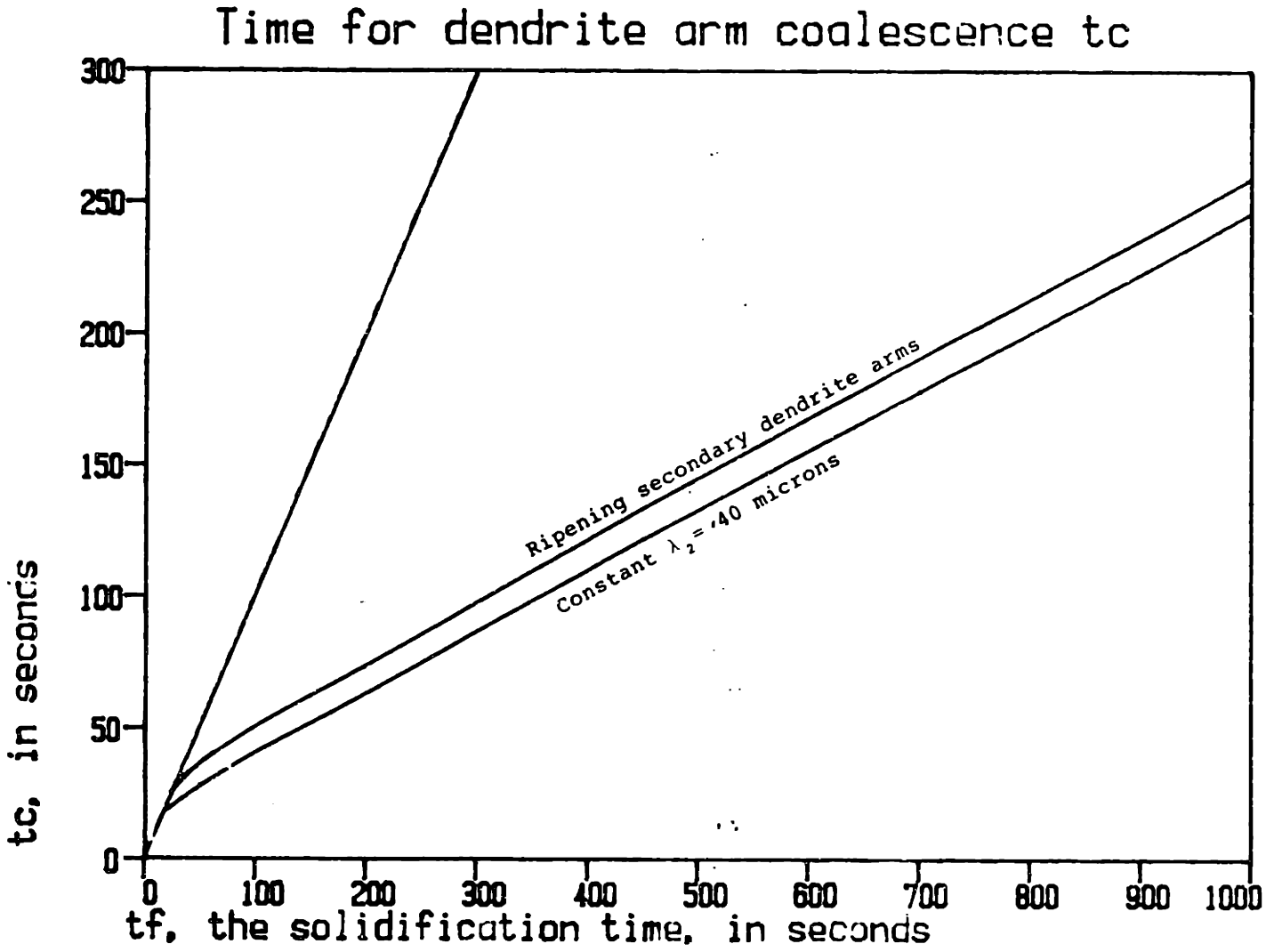

Figure 65 - Calculated time for coalescence t_c for ripening dendrite arms compared to the result with a constant λ_2. f_{si}= 0.65 and ℓ_i^2= 1.5 $10^{-10} m^2$.

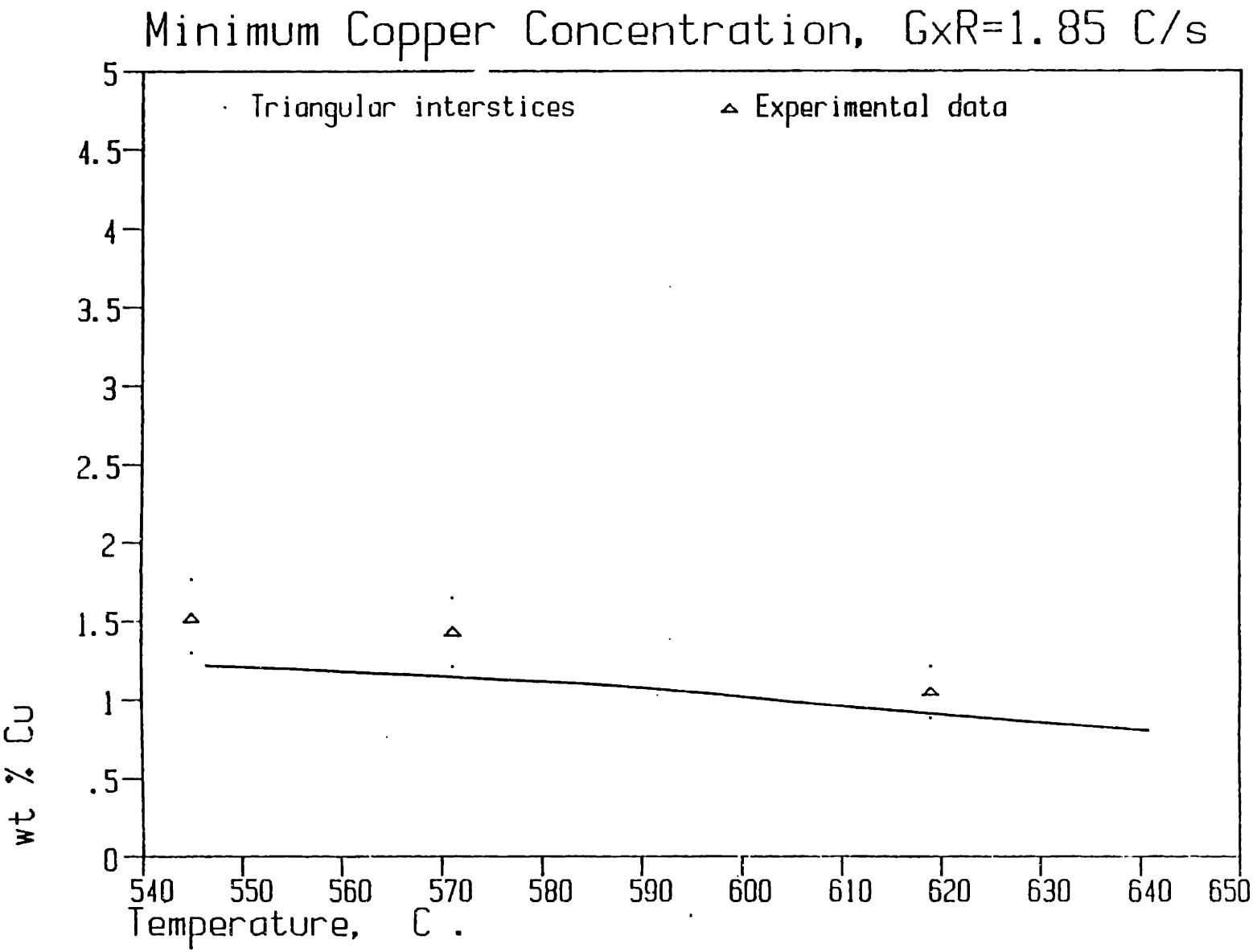

Figure 66 - Comparison of calculated and measured minimum copper concentration as a function of the quench temperature. Triangular interstices, sample I-1.

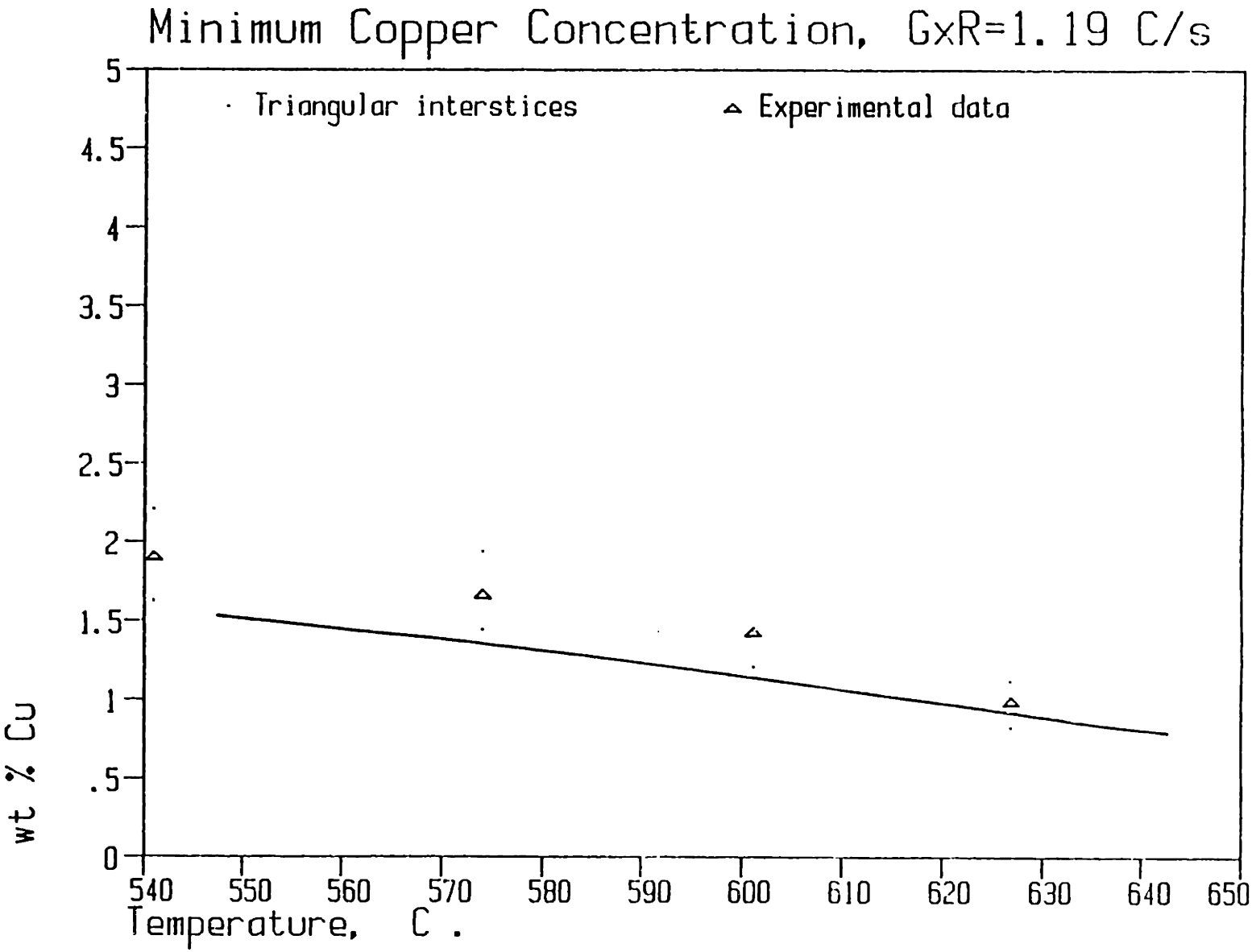

Figure 67 - Comparison of calculated and measured minimum copper concentration as a function of the quench temperature. Triangular interstices, sample I-4.

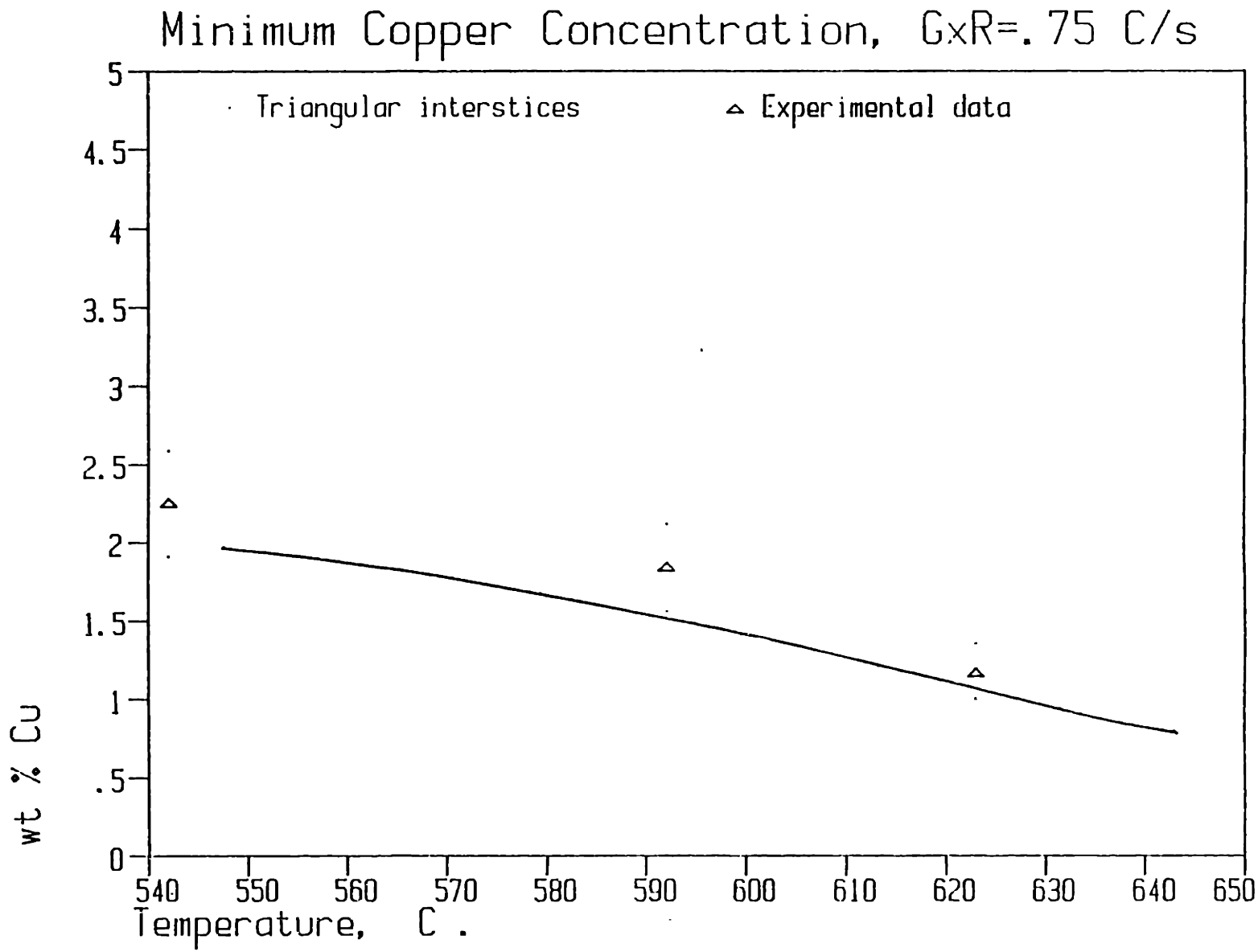

Figure 68 - Comparison of calculated and measured minimum copper concentration as a function of the quench temperature. Triangular interstices, sample H-2.

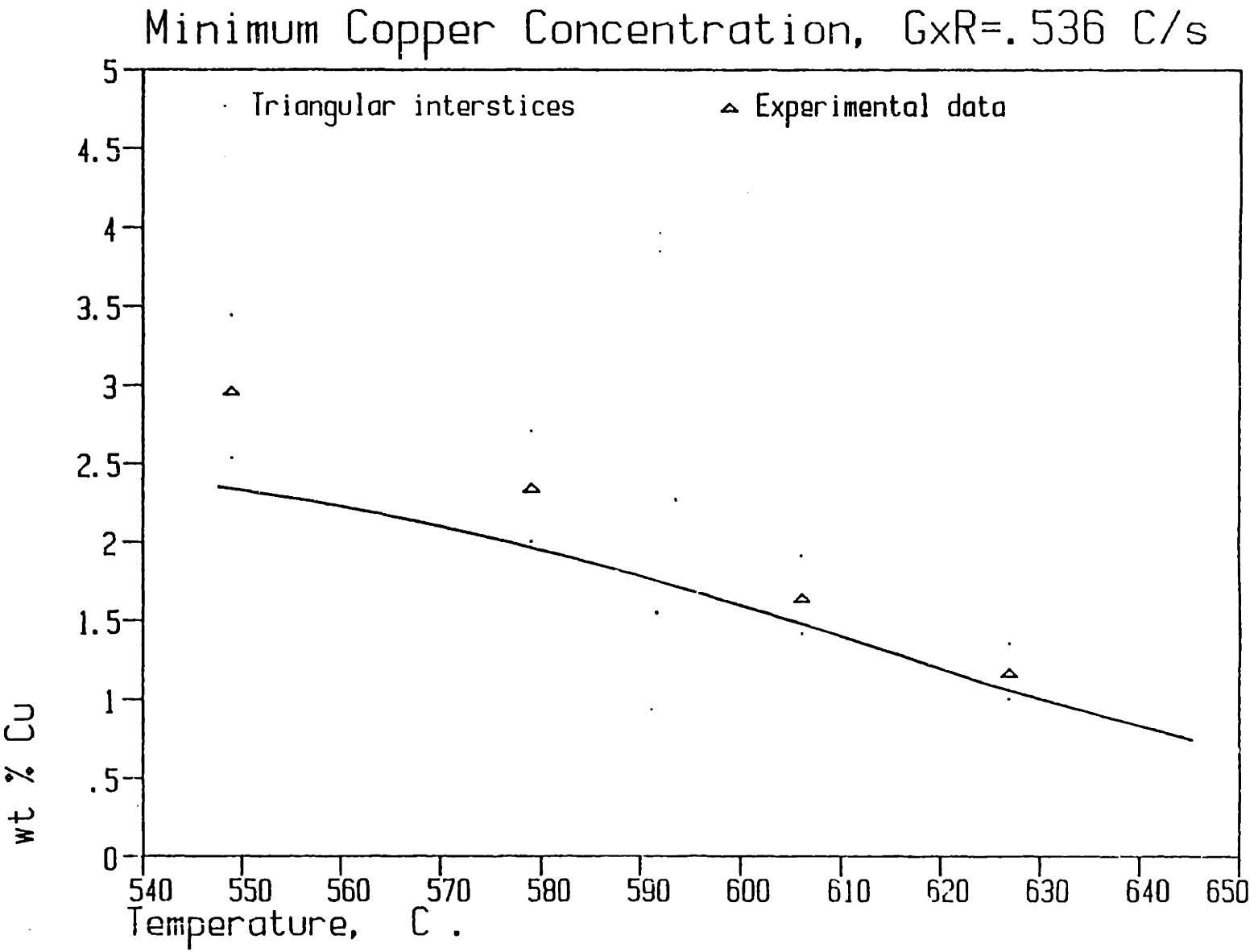

Figure 69 - Comparison of calculated and measured minimum copper concentration as a function of the quench temperature. Triangular interstices, sample I-3.

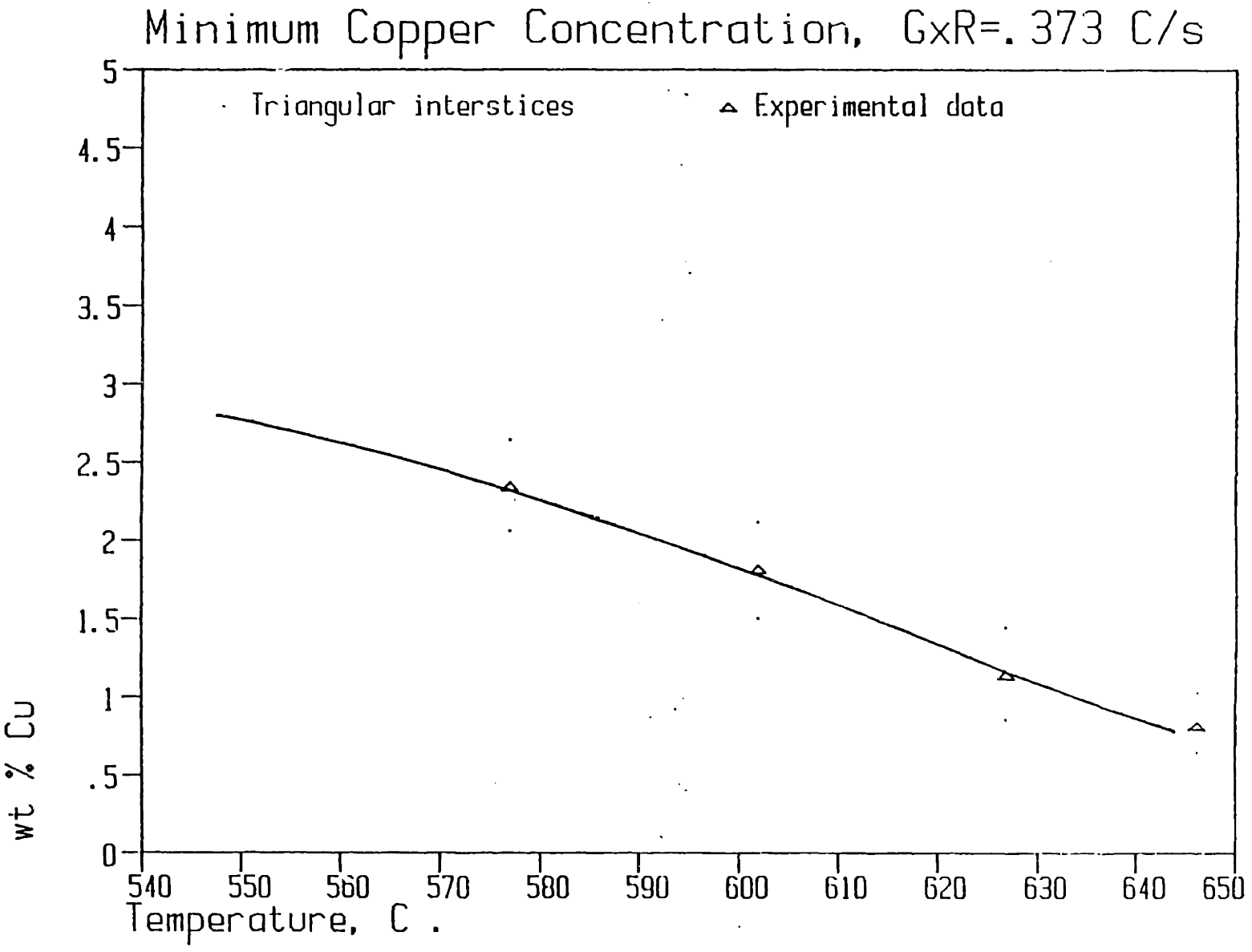

Figure 70 - Comparison of calculated and measured minimum copper concentration as a function of the quench temperature. Triangular interstices, sample G-2.

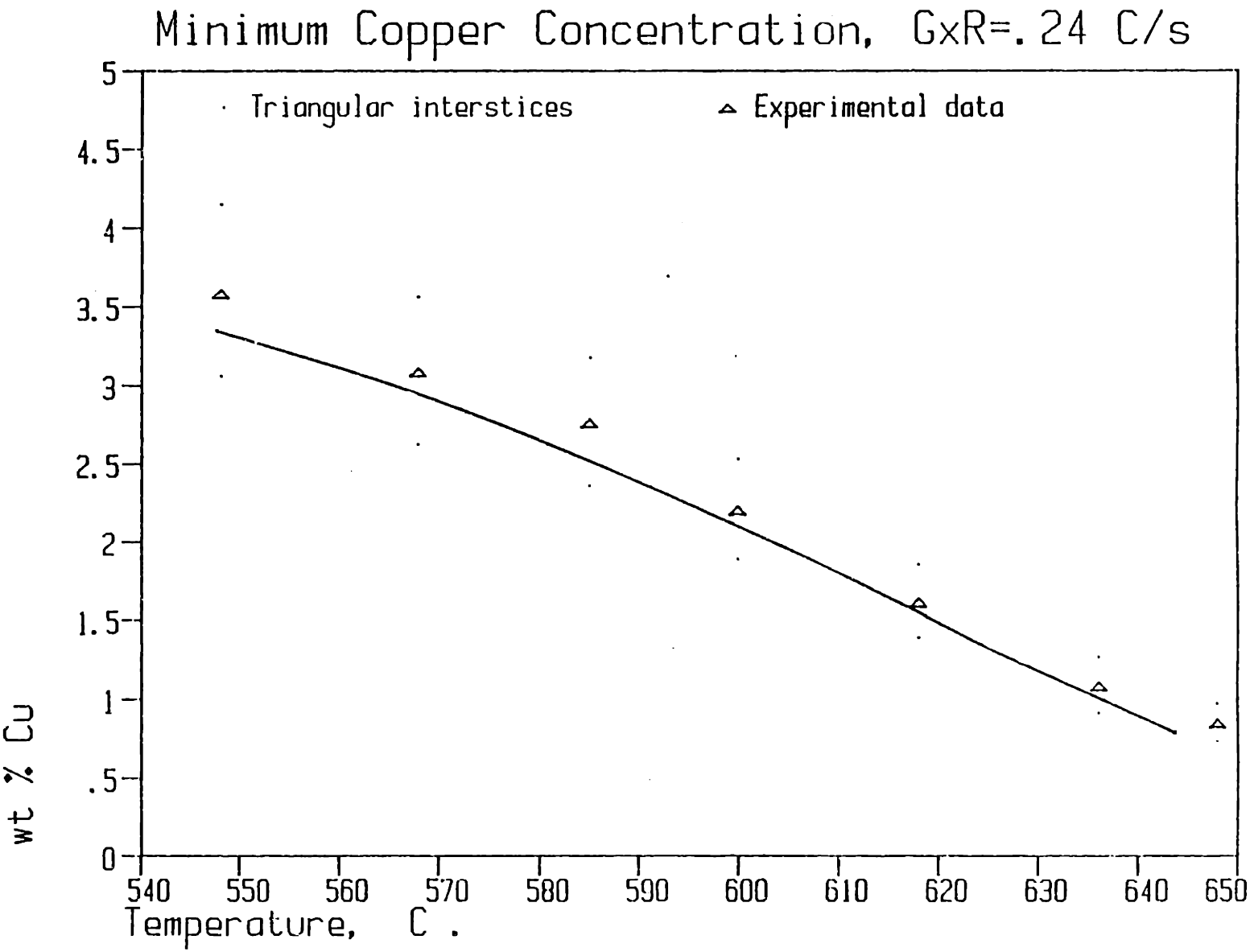

Figure 71 - Comparison of calculated and measured minimum copper concentrations as a function of the quench temperature. Triangular interstices, sample H-4.

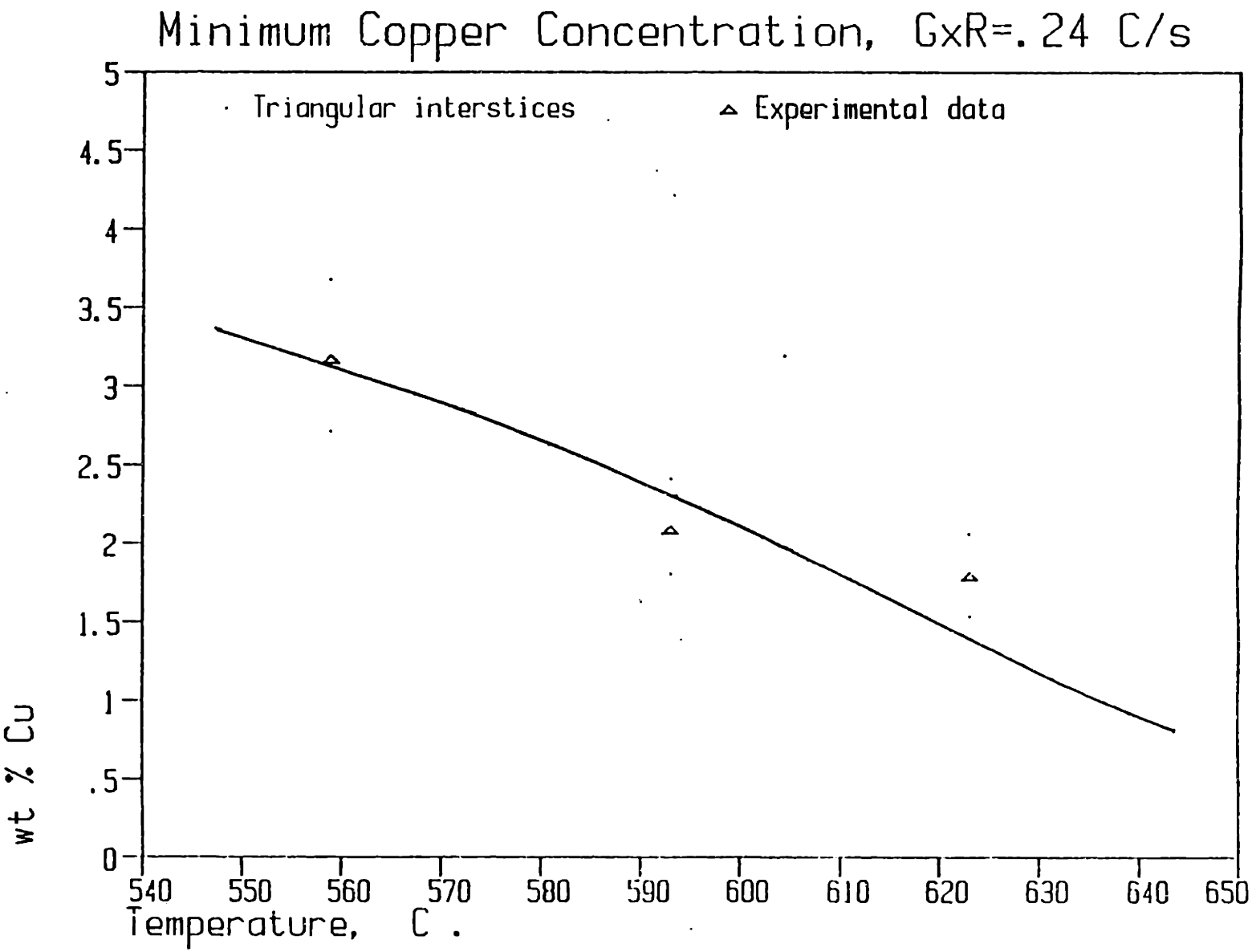

Figure 72 - Comparison of calculated and measured minimum copper concentration as a function of the quench temperature. Triangular interstices, sample H-3.

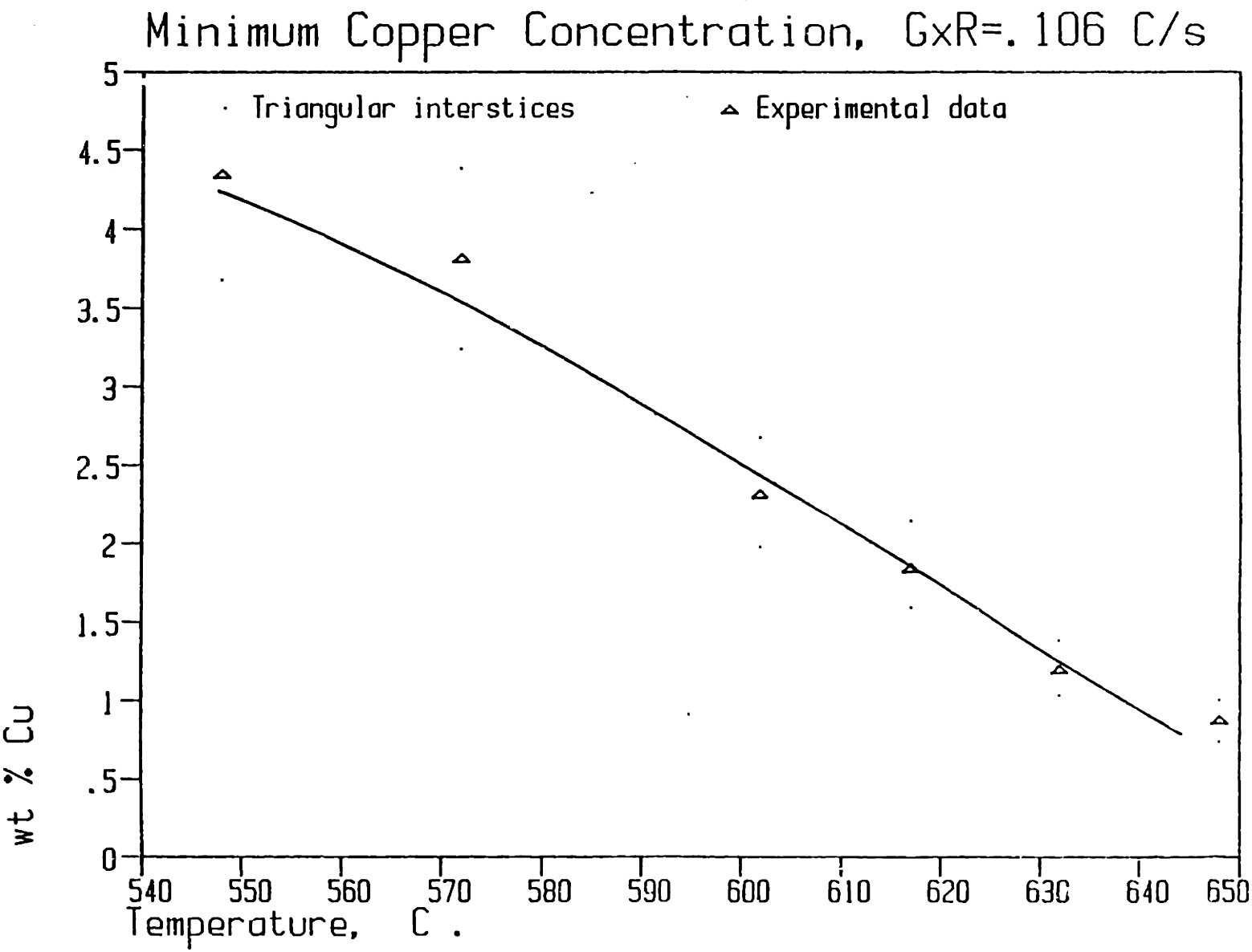

Figure 73 - Comparison of calculated and measured minimum copper concentration as a function of the quench temperature. Triangular interstices, sample I-2.

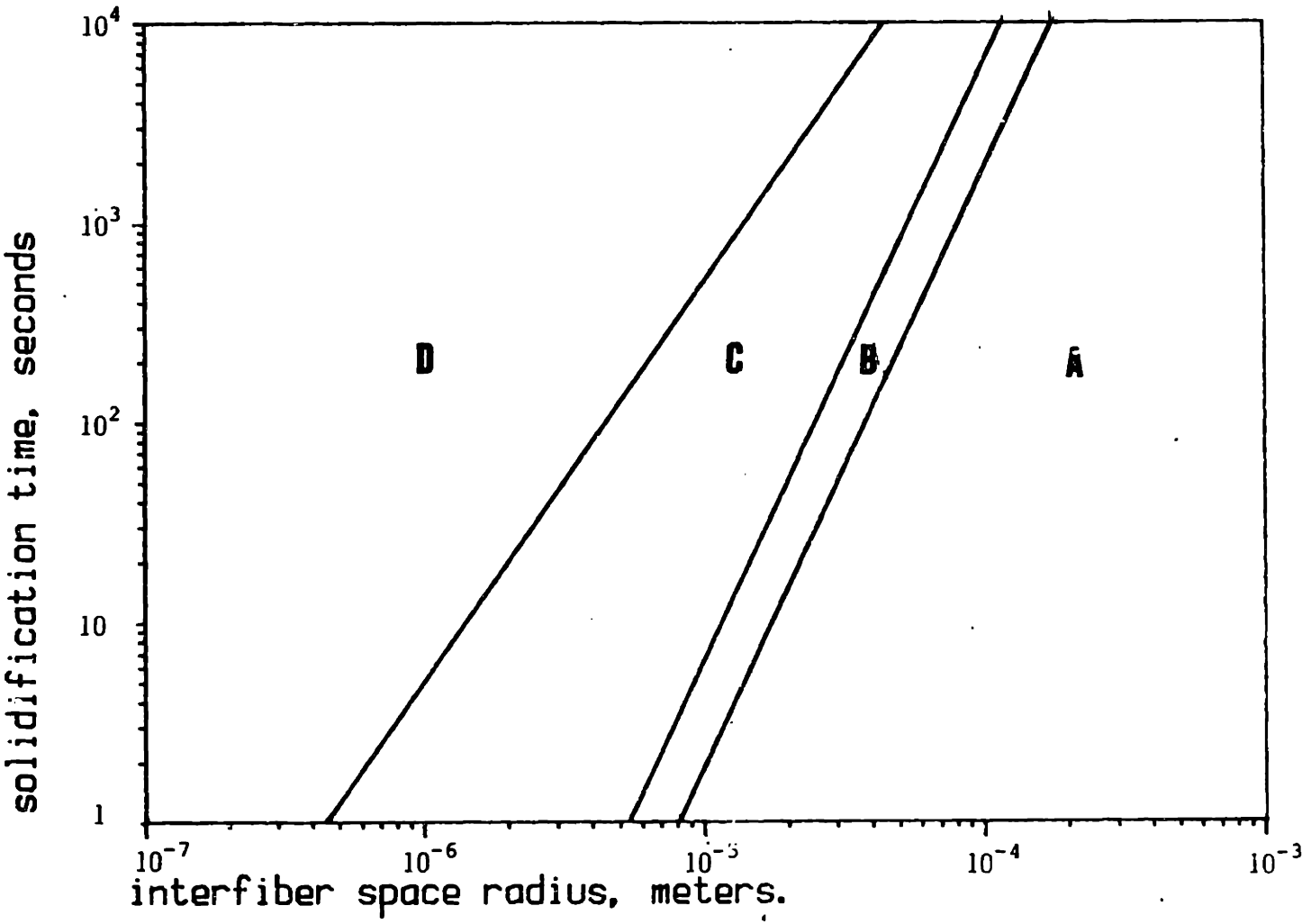

Figure 74 - Predicted microstructural features for Al-4.5wt%Cu solidified in circular interstices. Region A: dendritic microstructure. Region B: coalesced dendrite arms, dendritic coring patterns. Region C: non dendritic microstructure with some microsegregation. Region D: non dendritic homogeneous matrix.

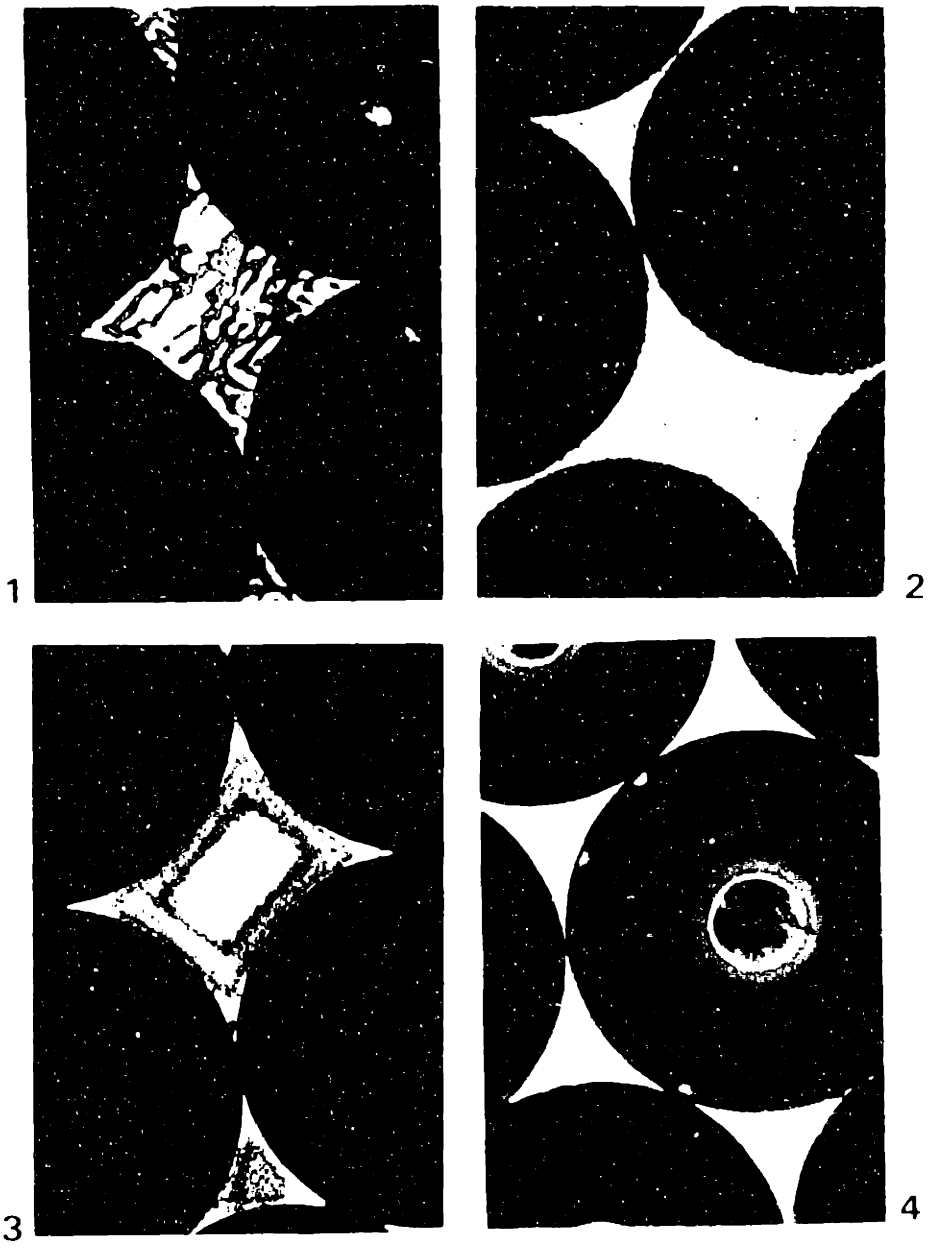
1
2
3
4

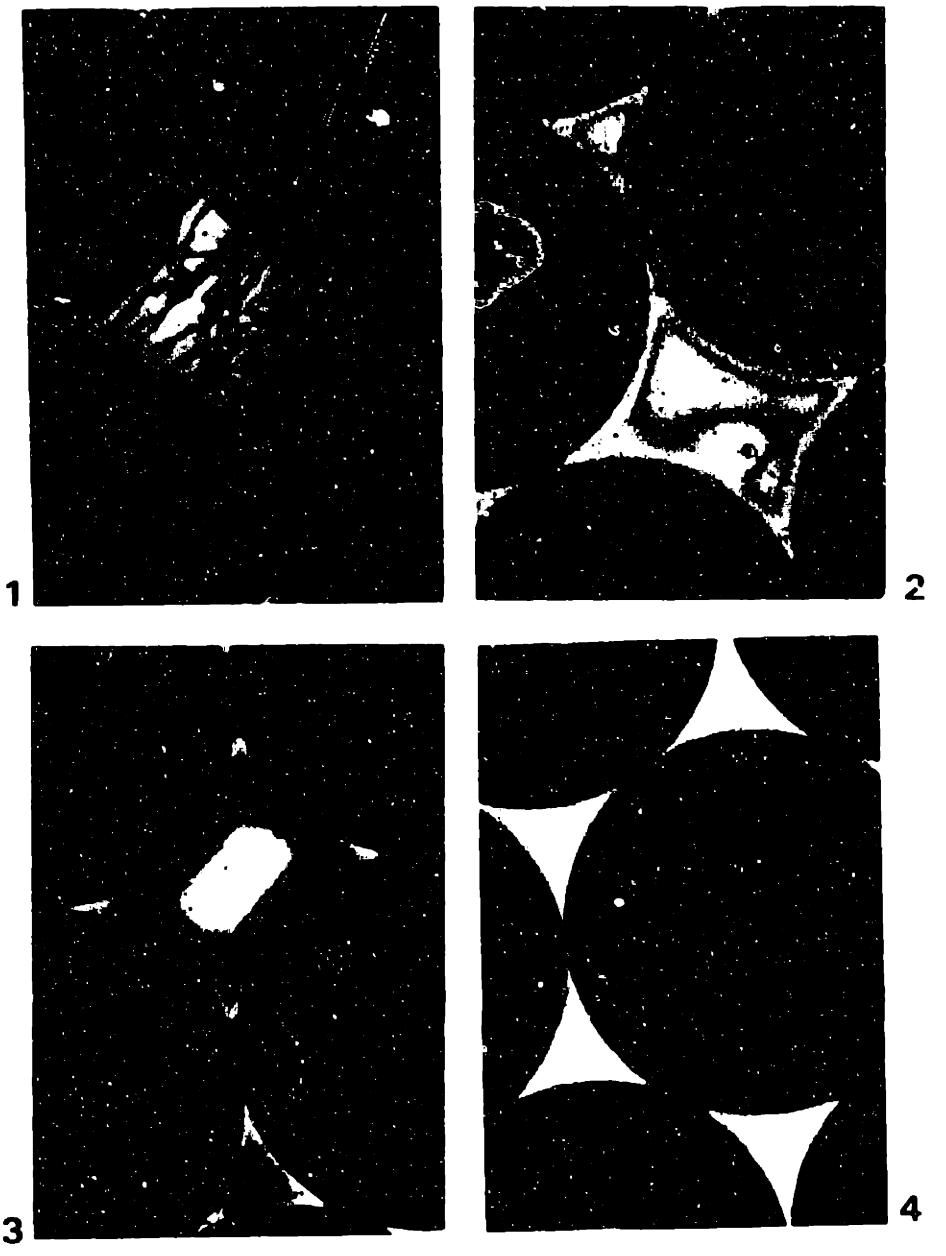

Figure 75 - Examples of microstructures in SiC / Al-4.5wt·Cu composites with reference to figure 74. See next page for details. 100 m

Figure 75 - 1 : Quenched liquid portion of a sample. Fine dendrites correspond to a high cooling rate. This microstructure is typical of region A in figure .

Figure 75 - 2 : Square interstices of sample I-1: about all the eutectic is at the fiber-metal interface but coring patterns are dendritic: this microstructure is typical of region B. In triangular interstices, the structure is non dendritic with microsegregation and is typical of region C of figure .

Figure 75 - 3 : Both square and triangular interstices of sample H-4 are non dendritic and display some degree of microsegregation: Both are of the type found in region C of figure . As triangular interstices are smaller than square interstices, the amount of microsegregation is more reduced in triangular interstices.

Figure 75 - 4 : Triangular interstices in sample I-2. The metal microstructure is featureless: neither dendrite arms nor microsegregation are observed. This microstructure corresponds to region D of figure .

Figure 75 - Detailed captions.

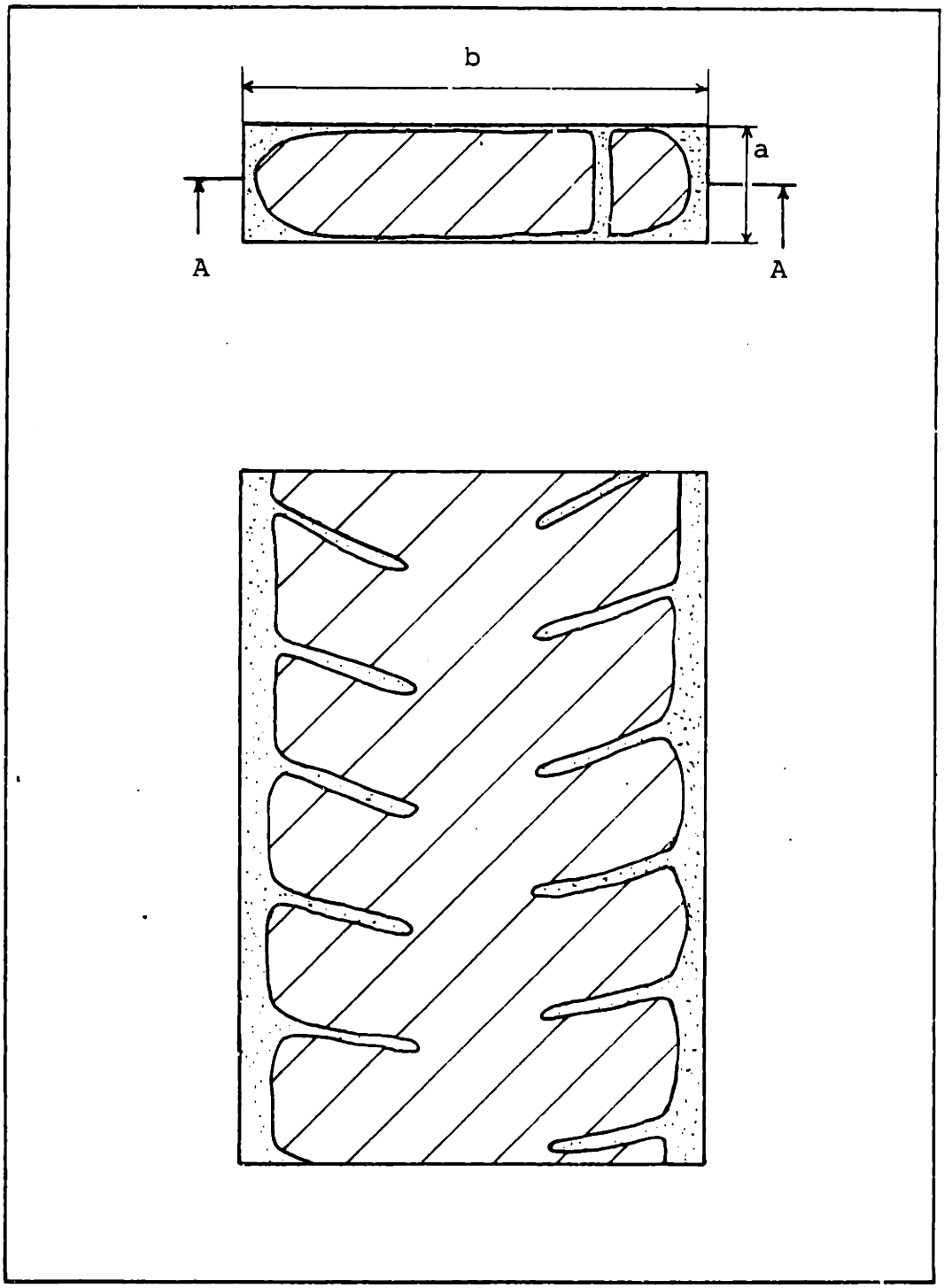

Figure 76 - Dendrite morphology in a rectangular interstice.

CONCLUSIONS

1 - No increase in the dendrite tip undercooling compared to fiber-free Al-4.5wt%Cu was found in SiC/Al-4.5wt%Cu matrix composites solidified at steady state for the growth rates (25-200 microns per second) and gradients (30-100 K/cm) of this work.

2 - The solidifying metal avoids the fiber surface as it grows. This is attributed to relative values of interfacial energies and rejection of solute at the growing interface.

3 - In the initial phases of solidification, Al-4.5wt%Cu grows in a dendritic fashion, with formation of secondary dendrite arms. The coarsening by ripening of this dendritic structure is inhibited by the fibers, which place an upper limit on the secondary dendrite arm spacing. The kinetics of coarsening by coalescence are accelerated by the fibers. If the coalescence process reaches its completion before the end of solidification, the dendritic microstructure is lost. This process was modelled using a simplified geometry and a constant dendrite arm spacing. The model is in agreement with experimental observations. A similar model for coalescence allowing for simultaneous coarsening by ripening is also given.

4 - The influence of coarsening on the suppression of microsegregation is studied from a theoretical point of view with

the assumption of negligible solid state diffusion. The model is generalized to include in an approximate but simple manner the effect of limited solid state diffusion.

5 - A matrix free of microsegregation can be obtained in metal-matrix composites with sufficiently long solidification times. Results from a finite difference model calculating the solute profile in the solid during solidification agree with experimental measurements. A criterion is thus provided for obtaining homogeneous solidified microstructures.

6 - Al-4.5wt%Cu reacts with AVCO's SCS-2 silicon carbide fiber to form aluminum carbide Al_4C_3. The reaction proceeds at an appreciable rate at temperatures above about 1050 K.

SUGGESTIONS FOR FUTURE WORK

1 - The solidification technique and the fiber lay-up were highly idealized in this work. The observations should be generalized to less regular fiber configurations and non steady state solidification experiments, both columnar and equiaxed.

2 - Next, composites with low fiber volume fractions should be investigated. The point where coarsening and microsegregation cease to be influenced must be found. This is particularly important since fiber configurations in which individual fibers touch frequently are undesirable. Coarsening will probably still be affected by the fibers so long as the distance separating the fibers is kept low and the liquid phase has a low interfacial energy in contact with the fibers.

3 - The mechanical properties that result from a given matrix microstructure must be assessed since they determine in the last instance the processing conditions that must be chosen. It was shown in this work that the matrix microstructure can vary significantly depending on processing conditions. This opens the way for several studies focussing on the role played by the matrix on the mechanical properties of metal matrix composites.

4 - Other alloys or alloy systems should then be investigated on a comparative basis.

5 - A similar investigation with a chemically stable fiber/metal combination into the regions where solidification is plane-front or cellular would be interesting. The stability of a plane front or of cellular structures might be somewhat enhanced

(see references [123] and [98-102]).

6 - What happens when the fiber surface acts as a catalyst for heterogeneous nucleation of the solidifying metal alloy ? This would be of great interest, both theoretical and practical. Hypereutectic Al-Si alloys could be used with carbon fibers, or TiC coated fibers with aluminum alloys.

7 - Experiments should be performed to measure the influence of ripening on the suppression of microsegregation. The ideal metal system would be one which solidifies as small spheres and in which solid state diffusion is very sluggish.

8 - Precise measurements of the pressure differential at the infiltrating metal front would be of interest. The equations derived in appendix C could then be compared to the measured data and the role of surface treatments on the fibers could be assessed.

APPENDIX A

DEFINITION OF VARIABLES

VARIABLE		UNITS
λ_1	primary dendrite arm spacing	m
λ_2	secondary dendrite arm spacing	m
λ_{2o}	initial secondary dendrite arm spacing	m
λ_{2f}	final secondary dendrite arm spacing	m
r	radius	m
r_T	total dendrite arm radius (liquid+solid) $=\lambda_2/2$	m
r*	secondary dendrite arm radius (solid) = f_s r_t	m
f_S	fraction solid	
f_L	fraction liquid	
f_E	fraction eutectic	
ℓ	secondary dendrite arm length	m
ℓ_i	initial secondary dendrite arm length	m
ℓ_o	radius of a circular interstice	m
r_{max}	radius of largest circle inscribed in an interstice	m
ρ	dimensionless radius = r/ℓ_o	
ρ^*	dimensionless solid/liquid interface radius = r^*/ℓ_o	
κ	solid/liquid interface curvature	m^{-1}
Γ	Gibbs-Thomson coefficient	K m
T	temperature	K
T_L	liquidus temperature	K

T_S	solidus temperature	K
T_E	eutectic temperature	K
k	partition ratio	
C	copper concentration	wt%
C_o	average copper concentration (4.5)	wt%
C_L	copper concentration in the liquid	wt%
C_L^κ	liquid composition in equilibrium with an interface of curvature κ	wt%
C_E	eutectic composition	wt%
C_s	solid composition at the interface $=kC_L$	wt%
c	dimensionless copper concentration $=C/C_o$	
m_L	liquidus slope	K/wt%
G	temperature gradient	K/m
R	growth rate	m/s
GxR	cooling rate	K/s
t	time	s
t_f	solidification time $= (T_L-T_E)/(GR)$	s
t_c	time for coalescence of dendrite arms	s
i	radius increment	
j	time (or liquid composition) increment	
D_L	diffusion coefficient in the liquid	m^2/s
D_S	diffusion coefficient in the solid	m^2/s
η	$= GxRx\ell_o^2$	m^2K/s
n	exponent in $\lambda_2 = B\ t^{1/n}$	
B	coefficient in $\lambda_2 = B\ t^{1/n}$	$m\ s^{(-1/n)}$
K	$= B^n$	m^n/s
A	$= GxR/(-m_L)$	wt%/s
V_f	volume fraction fiber	
S_f	fiber surface area per unit volume of composite material	m^{-1}
θ	contact angle	rad

P	pressure	Pa
σ_{LA}	liquid metal/atmosphere interfacial energy	N/m
σ_{LF}	liquid metal/fiber interfacial energy	N/m
σ_{FA}	fiber/atmosphere interfacial energy	N/m

APPENDIX B

Physical properties for Al-4.5wt%Cu.

1 - Phase diagram.

The phase diagram given in figure 2 is approximated with a straight line configuration, given in figure B. In this manner, both the partition ratio k and the liquidus slope m_L are constant. Thus :

$$k = 5.65 / 33 = 0.171$$

and

$$m_L = (660-548)/(-33) = -3.4 \text{ K/wt\%}$$

are used. For k, this is higher than 0.14 (more correct value for Al-2wt%Cu at the liquidus temperature) sometimes used [84,171], and below 0.2, value claimed by Bennett and Kirkwood to be appropriate according to their experimental work [171,174].

2- Diffusion coefficients.

For diffusion of copper in solid primary aluminum,

$$D_s = 0.29 \exp(-15,700/T) \times 10^{-4} \text{ m}^2/\text{s}$$

is used, following Murphy [175] and recent editions of the Smithells reference book [79]. This value was used in most recent

microsegregation models for Al-Cu [169-171]. It is rigorously only valid for solutions up to 0.5 wt%Cu between 908 K and 778 K (635 ^{0}C and 505 ^{0}C). For simplicity's sake it is assumed that the diffusion coefficient is concentration independent (authors disagree on the matter). Several publications have, after Murphy's review and experiments, published more data measured around 800-900 K (500-600 ^{0}C). Most fall close to Murphy's reported value [176-185].

For diffusion in the liquid phase, a recent article by Watson and Hunt [186] provides values obtained with a technique based on the temperature gradient zone melting phenomenon. They compare their value with previously reported data, and obtain quite consistently

$$D_L = 3.5 \times 10^{-9} \ m^2/s$$

between 833 and 898 K (560-625 ^{0}C). Care must be exercised to include, when appropriate, a correction factor due to thermal diffusion by the Soret effect when steep thermal gradients are present [186,191].

3 - Gibbs-Thomson constant.

Here, a recent publication by Gunduz and Hunt [187] is used. According to their extensive experiments that followed lines parallel to those used by Glicksman and coworkers on organic systems,

$$\Gamma = \frac{\sigma_{SL}}{\Delta S_f} = 2.41 \times 10^{-7} \quad K \cdot m$$

This is somewhat higher than values listed in ref. [84].

4 - Densities.

For the alpha phase : 2,750 kg/m^3

and for the theta phase : 4,340 kg/m^3

from reference [188] pages 254-255.

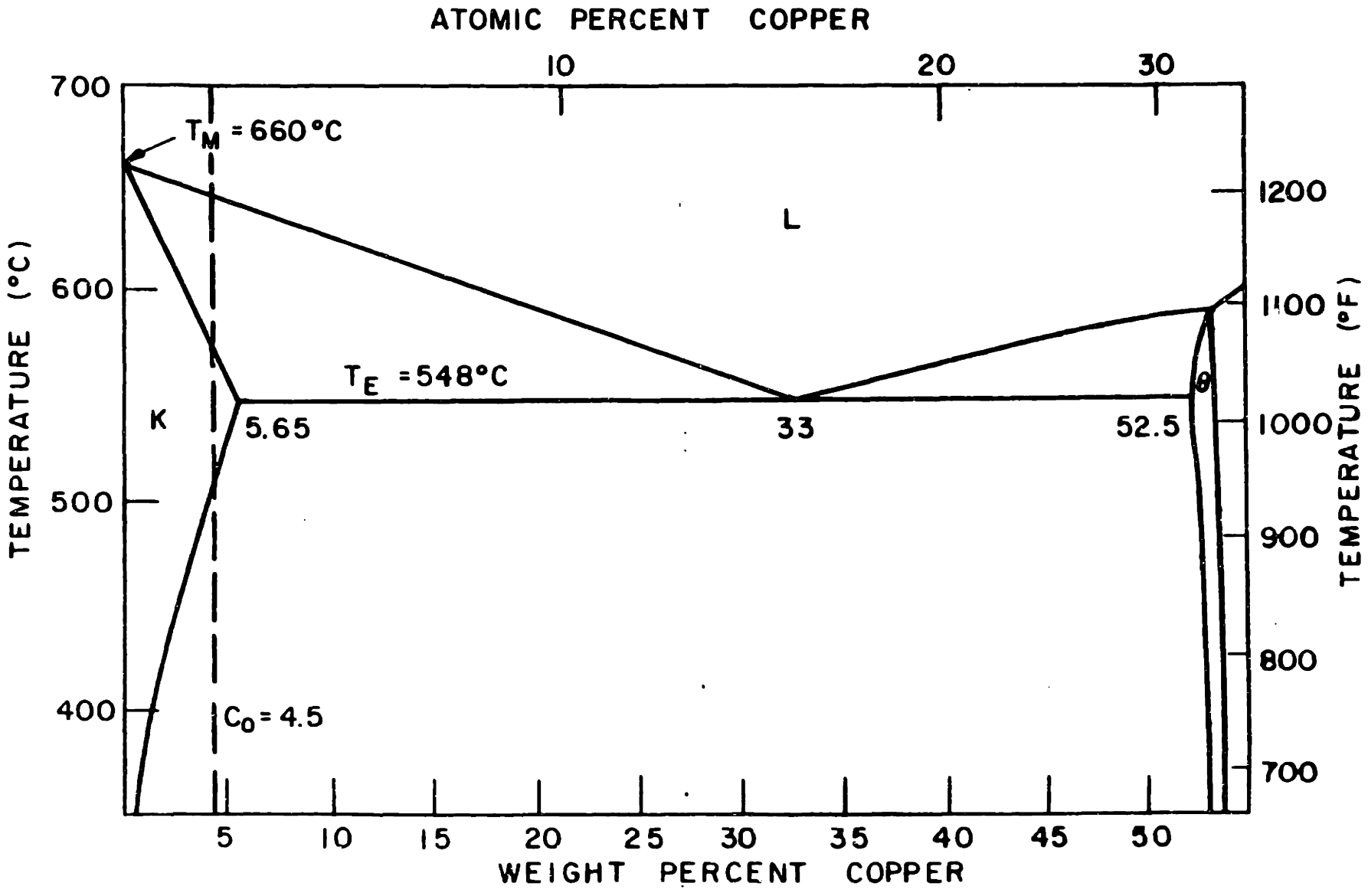

Figure B - Straight line approximation of the Al-Cu phase diagram. Compare with figure 2.

APPENDIX C

There is a pressure differential at the liquid metal front during infiltration of the reinforcement when casting metal matrix composites. It is this pressure differential that determines whether or not infiltration will be spontaneous (wetting systems) or will require adding pressure to the liquid metal (non-wetting systems). Published derivations of this pressure have been given in the literature [2-6], all based on the Young-Kelvin equation:

$$P = \sigma_{LA} K \cos\theta \qquad (1)$$

where σ_{LA} is the liquid metal/atmosphere interfacial energy, the atmosphere being any gas or liquid present around the fibers prior to infiltration, K is the curvature at that interface and θ is the contact angle. In general, K is unknown, and assumptions are made regarding the geometrical distribution of the reinforcement: fibers are assumed to lie on a square grid, a hexagonal grid, etc. K is then calculated as the curvature at the narrowest constriction between the fibers, in the assumed geometrical fiber distribution. Although this approach is rigorously correct, it presents several drawbacks:

1 - for equation (1) to be correct, the term $\sigma_{LA} \cos\theta$ must be equal to $\sigma_{FA} - \sigma_{LF}$, the difference between the fiber/atmosphere and fiber/liquid metal interfacial energies. If there is perfect wetting, θ is zero and this relationship is not obeyed since σ_{LA} is then inferior to $\sigma_{FA} - \sigma_{LF}$, and hence "$\cos\theta$" must be greater than one. The case of perfect non-wetting ($\sigma_{LA} < (\sigma_{FL} - \sigma_{FA})$) is of no practical importance [219].

2 - Equation (1) is used in conjunction with an assumed fiber distribution that does not exist (fibers do not usually lie on a square, hexagonal or other simple triangular grid).

Following is a derivation based solely on thermodynamic considerations of a general equation giving the average pressure required to infiltrate a fiber bundle or packed particles. As in real life situations the infiltration pressure will not be constant, this average pressure will in fact represent the minimum pressure differential (positive or negative) required at the liquid metal front to achieve complete infiltration.

I - Minimum pressure required for infiltration.

It is assumed that infiltration takes place reversibly. There are therefore no friction forces. Gravity effects are ignored. The only appreciable difference between the initial state (metal and fibers surrounded by the atmosphere) and the final state (the composite) is the replacement of the fiber/atmosphere with the fiber/liquid metal interface. The energy W given off by the process per unit volume of metal is

$$-W = (\sigma_{FL} - \sigma_{FA})\, S_f \qquad (3)$$

where S_f is the fiber surface area per unit volume of metal matrix. Now, since

$$W = -P\, \Delta V$$

where ΔV is the volume over which the metal was displaced, for a unit volume of metal matrix, one obtains:

$$P = (\sigma_{FL} - \sigma_{FA})\, S_f \qquad (4)$$

In particular, for a bundle of fibers of diameter d_f occupying a volume fraction V_f,

$$S_f = \frac{4\, V_f}{d_f\,(1 - V_f)} \qquad (5)$$

and the final expression is:

$$P = \frac{4 V_f (\sigma_{FL} - \sigma_{FA})}{(1-V_f) d_f} \qquad (6)$$

This expression is independent of fiber orientation, distribution, etc, since S_f is unaffected. Using data from reference [34], for graphite fibers in aluminum,

$$P = 3.12 V_f / (1-V_f) d_f \qquad \text{in S.I. units.}$$

Similarly, for spherical particles of diameter d_f packed to a volume fraction V_f;

$$S_f = \frac{6 V_f}{(1-V_f) d_f} \quad .$$

The term $(\sigma_{FL} - \sigma_{FA})$ can be calculated from the work of adhesion:

$$W_a = \sigma_{LA} + \sigma_{FA} - \sigma_{FL}$$

or the contact angle when it is finite (imperfectly wetting or non-wetting systems) if σ_{LA} is known, since

$$\sigma_{FA} - \sigma_{FL} = \sigma_{LA} \cos \theta \qquad (7)$$

Certain particular features of the case at hand may have to be taken into account:

- there is evidence that the oxide layer present at the surface of liquid aluminum is found at the fiber metal interface in cast aluminum matrix composites. The value for σ_{FL} may then need to be intermediate between that for Al and that for Al_2O_3 on the fiber material.
- If the fiber surface is modified by the presence of the

metal due to a coating layer or any interfacial reactions, adequate modifications to σ_{FA} and σ_{FL} need to be incorporated.
- If the fiber surface is not perfectly smooth, an adequate factor f>1 may be needed as a multiplier of S_f.

II - Terminal transient in non-wetting systems.

As pointed out above, the instantaneous pressure during infiltration will vary. The average pressure calculated above is therefore only the minimum pressure differential featured at the interface for complete infiltration.

In wetting systems ($\sigma_{FA} > \sigma_{FL}$), the metal will first be drawn into areas of high fiber surface area to metal volume ration (high S_f), later into areas where the driving force will be less. S_f therefore decreases with time and hence P, which is negative, increases with time.

Conversely, in non-wetting systems ($\sigma_{FA} < \sigma_{FL}$), S_f will increase with time as the metal will first flow into large channel and only in the last moments of infiltration be forced into the narrowest interfiber spaces. P, which is positive in this case since energy must be supplied to force the metal between the fibers, will increase with time. It is shown in what follows that it may increase to infinity in a few situations of practical importance.

a - Infiltration of a wedge.

Consider a simple two dimensional wedge, of half angle α at its base (figure C-1). It is assumed that the metal does not wet the fiber material with:

$$\sigma_{FL} - \sigma_{LA} < \sigma_{FA} < \sigma_{FL}$$

The contact angle θ is then between 90 and 180 degrees.

The pressure for infiltration of that wedge is again calculated from thermodynamic principles, i.e. under the assumption that the process takes place reversibly. The liquid/atmosphere therefore displays a constant curvature, and the contact angle with each face of the wedge is θ, figure C-1. The pressure that must be supplied to move reversibly the liquid metal a little further into the wedge is therefore the equilibrium pressure at the metal/atmosphere interface. From the simple geometry of figure C-1 and with terms defined on that figure, that pressure P is:

$$P = \frac{\sigma_{LA} \sin(\theta - \alpha - \pi/2)}{L \sin(\alpha)} \qquad (8)$$

It is clear that if $(\theta - \pi/2) > \alpha$, infiltration into the wedge will not be spontaneous ($P > 0$). Furthermore, the complete infiltration of such a wedge requires an infinitely high pressure, and is therefore thermodynamically impossible. The presence of surface defects of the fiber surface, for example in the form of a narrow groove, may therefore be deleterious to the properties of a cast composite since cracks will be present at the fiber-metal interface, of length approximately given by L in equation (8). Little healing of sharp surface defects on fibers should be expected from pressure-cast matrices that do not wet the fiber.

b - Fiber or particle contact points.

Consider now the contact point of two equal fibers or spherical particles, a cross-section of which is given in figure C-2 with the definition of geometrical variables. Proceeding as above, the pressure required to infiltrate reversibly this contact area is:

for two cylindrical fibers:

$$P = \frac{\sigma_{LR} \sin(\theta - \alpha - \pi/2)}{R \sin(\alpha) \, tg(\alpha/2)} \qquad (9)$$

for two spherical particles:

$$P = \frac{\sigma_{LR}}{R \sin(\alpha)} \left[\frac{\sin(\theta - \alpha - \pi/2)}{tg(\alpha/2)} - 1 \right] \qquad (10)$$

In both cases, this pressure becomes infinitely large when α approaches zero. For an infiltration pressure P, therefore, defects at the contact area of two fibers or particles will exist, of length above that derived from thermodynamic considerations and approximately equal to $2 R \sin(\alpha)$ obtained from equations (9) or (10) for a given infiltration pressure P. Furthermore, if two fibers touch over a certain length ℓ, the defect will be just as long along the fiber axis. Evidence for such voids can be seen on several micrographs, for example figures 12,13 and 17 to 20 of this thesis. The size of such defects can be decreased by increasing the infiltration pressure. These defects can only be suppressed by either suppressing fiber or particle contacts, or promoting fiber wetting in these areas.

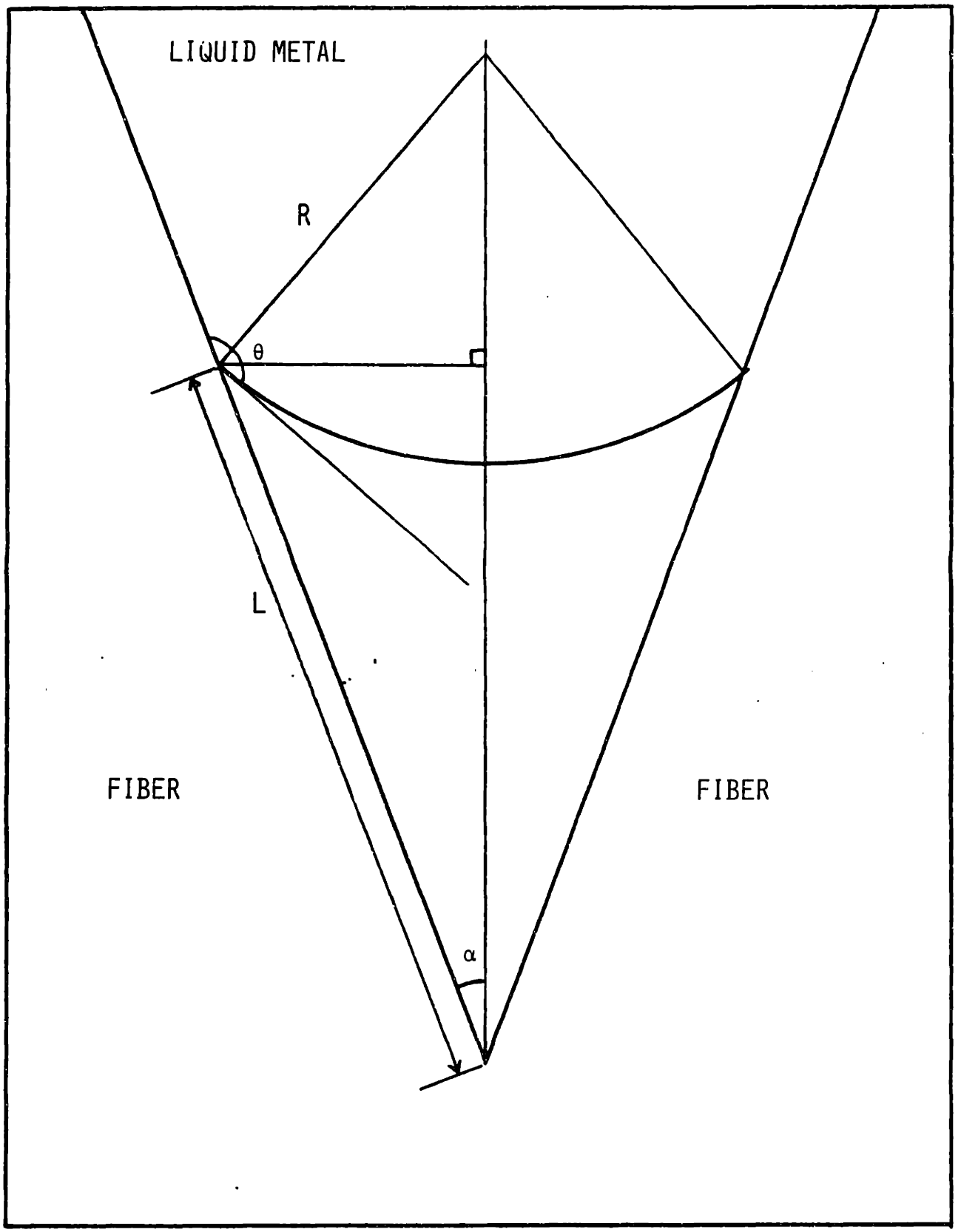

Figure C-1 - Infiltration of a wedge by a non-wetting metal.

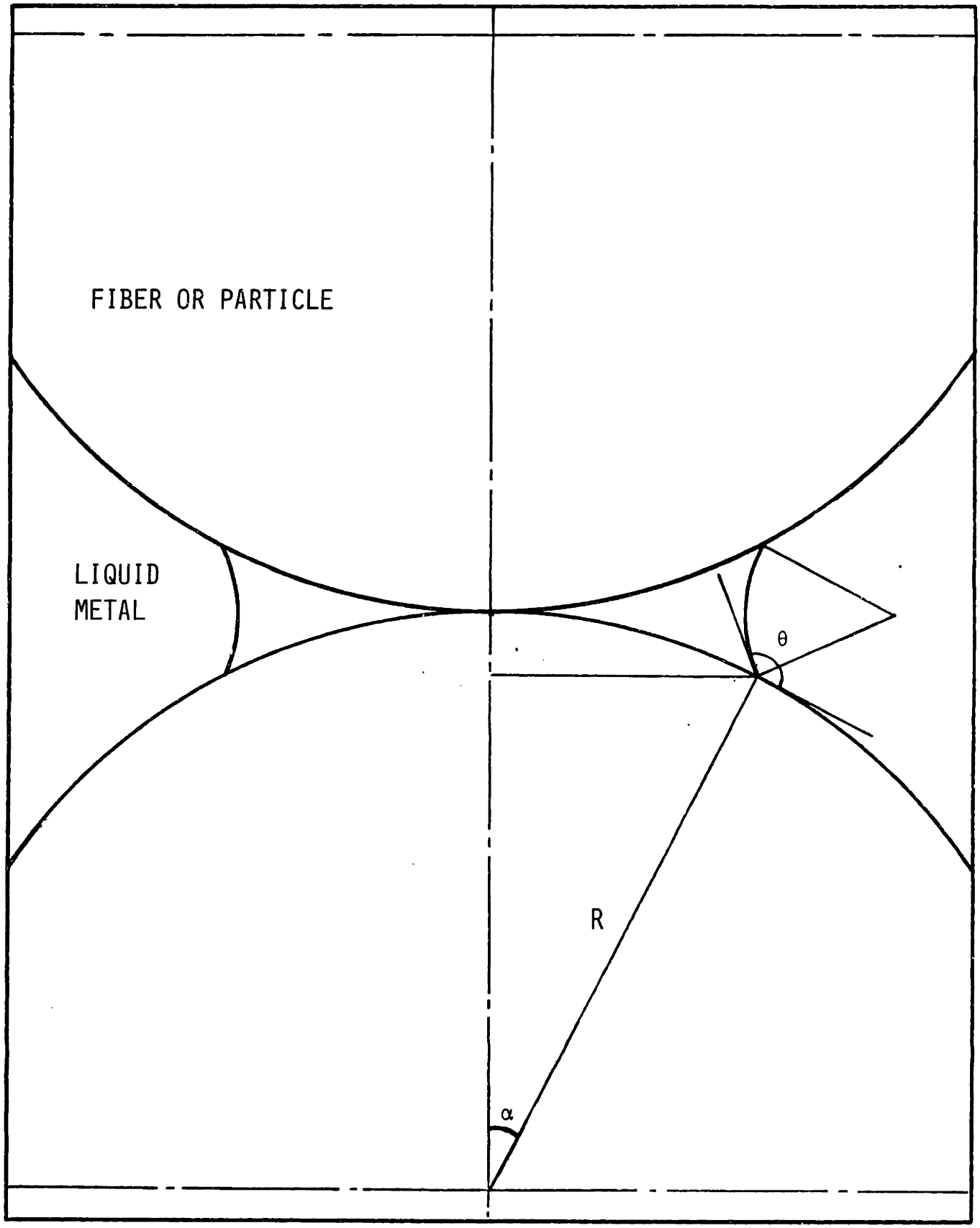

Figure C-2. Infiltration by a non-wetting metal of the contact area between two fibers or spherical particles.

APPENDIX D

TIME FOR COALESCENCE OF RIPENING DENDRITE ARMS

An array of secondary dendrite arms is considered, with neighboring arms separated by a narrow channel of width 2 R . This channel is assumed to gradually fill in by surface tension driven diffusion of matter from the dendrite tips (region B) to the bottom of the trough (region A). The background relevant to the process and fundamental equations are given in the "theory" chapter, section I-a.

The dendritic array is schematically described in figure D. The half width at the bottom of the interdendritic channel is assumed to be approximately given by:

$$n_A \simeq \frac{\lambda_2}{2} f_L$$

where f_L is the volume fraction liquid given by the Scheil equation:

$$f_L = \left(\frac{C_L}{C_0} \right)^{\frac{1}{k-1}} \qquad (D\text{-}1)$$

Secondary dendrite arms are assumed to coarsen by ripening, so λ_2 is an increasing function of time t during solidification. The coarsening law is taken in its most general form :

$$\lambda_2^n = \lambda_{20}^n + Kt \qquad (D\text{-}2)$$

In addition, the cooling rate is assumed to be constant:

$$C_L = C_0 + \frac{GR}{(-m_L)} t \qquad (D\text{-}3)$$

Secondary dendrite arm coalescence is to be sluggish when the volume fraction is below a fixed value f_{Si} which depends on the metal alloy and the dendrite geometry (see "theory" chapter). The equation determining the rate of in-filling of the interdendritic channel is (equation (1) of the " theory" chapter):

$$\frac{1}{S_A}\cdot\frac{dV_A}{dt} = \frac{D_L\,\Gamma\cdot(K_B - K_A)}{(-m_L)\cdot(1-k)\cdot d\cdot C_L} \qquad (D-4)$$

Geometrical simplifications are as before (figure 54):

$$-K_A = \frac{2}{\lambda_2\, f_L}$$

$$K_B << -K_A$$

$$d = l$$

$$\frac{1}{S_A}\,\frac{dV_A}{dt} = -\frac{dl}{dt}$$

Equation (D-4) becomes:

$$-l\,dl = \frac{D_L\,\Gamma}{(-m_L)(1-k)}\,\frac{2}{\lambda_2 f_L}\,\frac{dt}{C_L}$$

and from equations (D-1 - D-3):

$$-l\,dl = \frac{2\,D_L\,\Gamma}{(1-k)GR}\left(\frac{C_L}{C_0}\right)^{\frac{1}{1-k}}\left[\frac{(-m_L)K}{GR}C_L - \frac{(-m_L)K}{GR}C_0 + \lambda_{2_0}^{n}\right]^{-\frac{1}{n}}\frac{dC_L}{C_L}$$

(D-5)

λ_{2_0} is roughly equal to twice the dendrite tip radius [125,129,130,130, 132-137]. λ_{2_0} can therefore be obtained from figure 4 for Al-4.5 wt%Cu or evaluated in general from simple relationships as found in reference [84] page 82.

For Al-4.5wt%Cu, Young and Kirkood's experimental coarsening law [149]:

$$\lambda_2 = 16.1 \cdot 10^{-6}\ t^{0.31} \qquad \text{(S.I. units)}$$

yields $n = \frac{1}{0.31}$ and $B = (16.1 \cdot 10^{-6})$ in SI units.

Provided the initial dendrite arm length ℓ_i is known, the remaining dendrite arm length when the liquid reaches a composition C_L is obtained by integrating equation (D-5):

$$\ell_i^2 - \ell^2 = \frac{4 D_L \Gamma}{(1-k) G R\, C_0^{1/1-k}} \int_{C_{L_i}}^{C_L} \left[\frac{(-m_L) K}{GR} C - \frac{(-m_L) K}{GR} C_0 + \lambda_{2_0}^m \right]^{-\frac{1}{m}} C^{\frac{k}{1-k}} dC \qquad (D\text{-}6)$$

where C_{L_i} is the liquid composition at which $f_s = f_{s_i}$, given by the Scheil equation (D-1). Equation (D-6) can then be integrated numerically to yield ℓ and the time t_c for complete secondary dendrite arm coalescence ($\ell = 0$).

A simplifying assumption is to take:

$$\lambda_{2_0}^m - \frac{(-m_L) K C_0}{GR} \simeq 0 \qquad (D\text{-}7)$$

in which case equation (D-6) takes a simple form:

$$\ell_i^2 - \ell^2 = \frac{4 D_L \Gamma}{(1-k) G R\, C_0^{1/1-k}} \left[\frac{GR}{(-m_L) K} \right]^{\frac{1}{m}} \left[\frac{C_L^{\frac{1}{1-k}-\frac{1}{m}} - C_{L_i}^{\frac{1}{1-k}-\frac{1}{m}}}{\frac{1}{1-k} - \frac{1}{m}} \right] \qquad (D\text{-}8)$$

This assumption will only introduce a significant error in the secondary dendrite arm spacing λ_2 during the early stages of solidification, when $C_L \simeq C_o$. With f_{si} greater than 0.5, the error introduced by neglecting the terms in (D-7) is therefore small.

With $n \to \infty$, equation (D-8) becomes equation (5) of the "Theory" chapter with $\lambda_2 = K^{1/n}$.

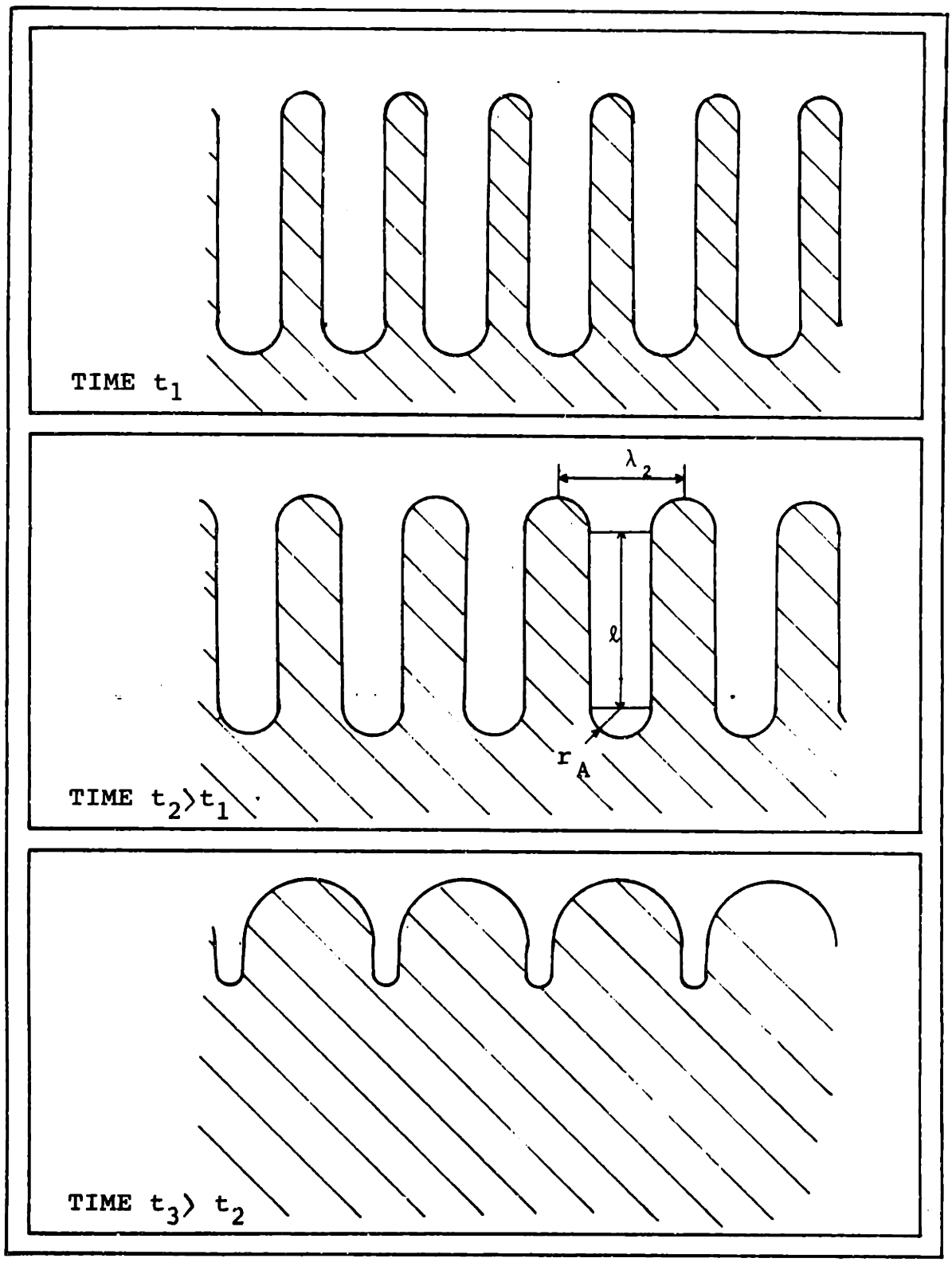

Figure D - Coalescence of ripening dendrite arms.
Schematic description of the model.

APPENDIX E

CALCULATION OF MICROSEGREGATION IN Al-4.5wt%Cu

a - The finite difference solution

The total radius is divided into 100 parts $\Delta\rho = 0.01$, each denoted by the indice i in what follows. The interface is allowed to float between these points, so that

$$\rho^* = i^* \Delta\rho + \delta\rho^*$$

with $\delta\rho^*$ taken between 0,005 and 0.015 for reasons that follow. The following variables are functions of time or, equivalently, the liquid concentration C_{L_j} only:

i^*_j , $\delta\rho^*_j$, D_{s_j} , the indice j denoting the time increment.

By definition, $$\xi = \frac{\Delta C_L}{(\Delta\rho)^2}\left[-\frac{D_s\, m_L}{\ell_o^2\, GR}\right]$$

Concentrations are also rendered dimensionless: $c = C/4.5$.

During each increment Δc_{L_j}, diffusion and growth take place simultaneously. These two processes are decoupled in the model for each Δc_{L_j}, so that:

1 - Diffusion takes place, according to equation (22) in section III of the "theory" chapter, for a fixed interface position and a fixed concentration in the liquid.

2 - Growth takes place "instantaneously", taking into account

the amount of solute incorporated into the solid phase during Δt. Mathematical details and approximations for each step are as follows:

1 - For diffusion, an explicit finite difference scheme is used:

for i = 0: $\quad c_{0,j+1} = c_{0,j} + 4\xi\,(c_{i,j} - c_{0,j})$

for $0 < i < i_j^*$: $c_{i,j+1} = c_{i,j} + \xi\,\dfrac{(2i+1)\,c_{i+1,j} - 4i\,c_{i,j} + (2i-1)\,c_{i-1,j}}{2i}$

for $i = i_j^*$, the equation is slightly more complex, as this point is not equidistant to the two adjoining points. Writing a mass balance over the volume element $[i_j^*\Delta\rho - \frac{\Delta\rho}{2},\ i_j^*\Delta\rho + \frac{\delta\rho_j^*}{2}]$, one gets:

$$c_{i_j^*,j+1} = c_{i_j^*,j} + \xi\left[\frac{kC_{i,j}\left(2i_j^*\frac{\Delta\rho}{\delta\rho_j^*}+1\right) - c_{i_j^*,j}\cdot 2i_j^*\left(1+\frac{\Delta\rho}{\delta\rho_j^*}\right) + c_{i_j^*-1,j}\,(2i_j^*-1)}{i_j^*\left(1+\frac{\Delta\rho}{\delta\rho_j^*}\right) + \frac{\delta\rho_j^{*2}}{4\,\Delta\rho^2} - \frac{1}{4}}\right]$$

As $\delta\rho_j^*$ approaches zero, some terms become very large, and errors will result. It is for this reason that $\delta\rho_j^*$ was chosen in the range]0.005, 0.015] in what precedes.

In an explicit finite difference solution of the diffusion equation, stability is a concern [214,215]. Therefore, ξ remains constant and Δc_i is allowed to vary as D_s decreases. No criterion for stability was found for the equation in cylindrical coordinates. However, by running the program, no instabilities were found with ξ in the range 0.1 to 0.05. Also, results obtained with ξ = 0.1 and 0.05 were similar to a precision of three digits. Therefore, all calculations were performed with ξ = 0.05.

2 - Next, the solid must grow. Rather than using a finite difference form of equation (21) in section III of the "theory" chapter, for better accuracy, the amount of solute incorporated into the solid by diffusion was calculated by integration of the solute profile. Specifically, the equation determining the new position of the interface is:

$$\int_0^{\rho^*} 2\pi\rho\, c_{\rho,j+1}\, d\rho + (1-\rho^{*2})\pi c_{L_{j+1}} = \pi$$

where $c_{\rho,j+1}$ denotes the concentration after diffusion in the solid, and

$$c_{L_{j+1}} = c_{L_j} + \xi\eta \cdot 10^{-4}\left(-m_L D_s\right)^{-1}$$

From $\rho = 0$ to $i_j^* \Delta\rho$, the integral was calculated using Gregory's interpolation formula and conserving only the first correction term [213,214]. Between $i_j^* \Delta\rho$ and ρ_j^* as well as in the liquid, the trapezoidal rule was used. The position of the interface is then obtained by solving a linear equation of the second degree.

If $(\rho_{j+1}^* - i_j^* \Delta\rho)$ becomes larger than 0.015, i^* increases by one and a value must be ascribed to $c_{i_{j+1}^*, j+1}$. This was done with Lagrange's interpolation formula [213] between points at $(i_j^* - 1)\Delta\rho$, $i_j^* \Delta\rho$ and ρ_{j+1}^*.

As for the initial values, $\rho_0^* = 0$ would be impractical, so solidification is assumed to take place according to the Scheil equation in the very first instants of the process. The initial volume fraction was thus taken at 0.0016, and the solute content varied at that point between 0.171 and 0.1711277. Proceeding in

the same manner but assuming equilibrium solidification up to = 0.0016 led to no appreciable change in the results.

b - refinements of the solution.

1 - Once all the liquid has been absorbed, growth ceases. Therefore, a test was incorporated to ascertain that some liquid is present ($\rho^* < 1$). If not, the growth process ceases, and only diffusion takes place with a no-flux boundary condition at $\rho = 1$.

2 - To model solidification experiments that include an isothermal hold at a given temperature T_h, an exit was included to a similar program once T_h is reached. In this new program, the only modification is that T and $\mathcal{L}_L$ are held constant.
Both program listings follow.

c - Computer program.

Listings of the two programs are given in the following pages. The computer language is Basic, and variables are redefined as follows:

CA and CB:	c
LA and LB:	c
DS :	D
TI :	t
RA and RB:	$\delta\rho^*$

IA and IB: i^* .

Other variables are defined in the programs.

The second program allows to hold the sample at a chosen temperature after solidification to that temperature. This temperature is chosen by indicating the corresponding liquid (dimensionless) composition LX.

```
10 DIM CA(100)
20 DIM CB(100)
30 DEFINT I
40 LPRINT "Solid state diffusion during directionnal growth of Al-4.5Cu"
50 INPUT "radius squared =";PR
60 LPRINT "         radius squared = ";PR
70 INPUT "cooling rate = in C/s ";PC
80 LPRINT "         GxR = ";PC;"GxRxR^2 =";PR*PC
90 INPUT "r = ";R
100 LPRINT "         r = ";R
110 INPUT "Print every ... cycles";IC
120 LA=.1713552
130 LB=LA
140 IA=4
150 IB=IA
160 RA=.01
170 RB=RA
180 DA=.29*EXP(-15662/(933-89.47*LA))
190 TI=0
200 DB=DA
210 FOR I=1 TO 4
220 CA(I)=.171/(1-(I-1)^2*.0001)^.829
230 NEXT I
240 FOR I=5 TO 100
250 CA(I)=0
260 NEXT I
270 FOR I=1 TO 100
280 CB(I)=0
290 NEXT I
300 LPRINT "Initial temperature =";660-89.47*LB
310 Z=(IB-1)*.01+RB
320 LPRINT "Interface position = ";Z;",  Fraction solid = ";Z^2
330 FOR I=1 TO 3
340 LPRINT "i=";I;"C=";CA(I),
350 NEXT I
360 LPRINT "and for i=4, C=";CA(4)
370 FOR W=1 TO 10000
380 FOR X=1 TO IC
390 CB(1)=CA(1)+4*R*(CA(2)-CA(1))
400 FOR I=2 TO IA-1
410 CB(I)=CA(I)+R*((2*I-1)*CA(I+1)+(2*I-3)*CA(I-1)-4*(I-1)*CA(I))/(2*(I-1))
420 NEXT I
430 F=LA*((IA-1)*.02/RA+1)+CA(IA-1)*(2*IA-3)-CA(IA)*2*((IA-1)*(1+.01/RA)
440 CB(IA)=CA(IA)+R*F/((IA-1)*(1+.01/RA)+RA^2/.0004-.25)
450 LB=LA
460 IB=IA
470 RB=RA
480 DB=DA
490 PRINT;LA
500 LA=LA+1.117647E-06*PR*PC*R/DB
510 DA=.29*EXP(-15662/(933-89.474*LA))
520 IF LA>1.2555 THEN GOTO 850
530 S=.00005*(IB-1)*CB(IB)
540 FOR I=2 TO IB-1
550 S=S+.0001*(I-1)*CB(I)
560 NEXT I
570 K=(IB-1)*CB(IB)-(IB-2)*CB(IB-1)-CB(2)
580 S=S-8.333E-06*K
590 A=4.84795*LA
600 B=(IB-1)*.01*(LA-CB(IB))
610 C=2*S-(IB-1)^2*.0001*CB(IB)-1+5.84795*LA
620 D=B^2+4*A*C
630 T=(SQR(D)-B)/(2*A)
640 U=T-.01*(IB-1)
650 IF U>.025 THEN GOTO 950
660 IF U>.015 THEN IA=IB+1
670 RA=T-.01*(IA-1)
680 IF T>1 THEN GOTO 970
690 K=CB(IB)*.02*RB/(.01*(.01+RB))+LB*.0002/((.02+RB)*(.01+RB))
```

```
700 IF U>.015 THEN CA(IA)=K-CB(IB-1)*.01*RB/((.02+RB)*.01)
710 FOR I=1 TO IB
720 CA(I)=CB(I)
730 NEXT I
735 TI=TI+R*PR*.0001/DA
740 NEXT X
750 LPRINT "time  =";TI;"   n = ";W
760 LPRINT "Liquid composition =";LB/.171;",     Temperature = ";660-89.47*LB
770 Z=(IA-1)*.01+RA
780 LPRINT "Interface position = ";Z;",  Fraction solid = ";Z^2
790 FOR I=1 TO 99
800 LPRINT "i=";I;"C=";CA(I),
810 NEXT I
820 LPRINT "i=100,C=";CA(100)
830 NEXT W
840 END
850 LPRINT "time  =";TI;"   n = ";W
860 LPRINT "Liquid composition =";LB/.171;",     Temperature = ";660-89.47*LB
870 Z=(IB-1)*.01+RB
880 LPRINT "Interface position = ";Z;",  Fraction solid = ";Z^2
890 FOR I=1 TO 99
900 LPRINT "i=";I;"C=";CB(I),
910 NEXT I
920 LPRINT "i=100,C=";CB(100)
930 LPRINT "That's all folks "
940 END
950 LPRINT "U>.025"
960 END
970 RA=.01
980 KA=LA
990 RB=RA
1000 LPRINT "time  =";TI;",fully solid now "
1010 LPRINT "Liquid composition =";LA/.171;",     Temperature = ";660-89.47*LA
1020 Z=(IA-1)*.01+RA
1030 LPRINT "Interface position = ";Z;",  Fraction solid = ";Z^2
1040 FOR I=1 TO 99
1050 LPRINT "i=";I;"C=";CB(I),
1060 NEXT I
1070 LPRINT "i=100,C=";CB(100)
1080 FOR IZ=1 TO 1000
1090 FOR IK=1 TO IC
1100 CB(1)=CA(1)+4*R*(CA(2)-CA(1))
1110 FOR I=2 TO IA-1
1120 CB(I)=CA(I)+R*((2*I-1)*CA(I+1)+(2*I-3)*CA(I-1)-4*(I-1)*CA(I))/(2*(I-1))
1130 NEXT I
1140 CB(IA)=CA(IA)+R*((2*IA-1)*LA+(2*IA-3)*CA(IA-1)-4*(IA-1)*CA(IA))/(2*(IA-1))
1150 LB=LA+R*(CA(IA)-LA)*2
1160 TI=TI+R*PR*.0001/DA
1170 PRINT LB
1180 LA=LB
1190 FOR I=1 TO 100
1200 CA(I)=CB(I)
1210 NEXT I
1220 KA=KA+1.117647E-06*PR*PC*R/DA
1230 IF KA>1.2555 THEN GOTO 1360
1240 DA=.29*EXP(-15662/(900-89.474*KA))
1250 NEXT IK
1260 LPRINT "time  =";TI;"   n = ";IZ
1270 LPRINT "                    ";",          Temperature = ";660-89.47*KA
1300 FOR I=1 TO 100
1310 LPRINT "i=";I;"C=";CA(I),
1320 NEXT I
1330 LPRINT "i=101,C=";LB
1340 NEXT IZ
1350 END
1360 LPRINT "time  =";TI;"   n = ";IZ
1370 LPRINT "                    ";",          Temperature = ";660-89.47*KA
1380 GOTO 890
```

```
10 DIM CA(100)
20 DIM CB(100)
30 DEFINT I
40 LPRINT "Solid state diffusion during directionnal growth of Al-4.5Cu"
50 INPUT "radius squared =";PR
60 LPRINT "         radius squared = ";PR
70 INPUT "cooling rate = in C/s ";PC
80 LPRINT "         GxR = ";PC;"GxRxRs2 =";PR*PC
90 INPUT  "isothermal hold at C1 = ";LX
100 LPRINT "         Hold at C1 = ";LX
110 INPUT "r = ";R
120 LPRINT "         r = ";R
130 INPUT "Print every ... cycles";IC
135 LPRINT "         print every k cycles, k = ";IC
140 LA=.1713552
150 LB=LA
160 IA=4
170 IB=IA
180 RA=.01
190 RB=RA
200 DA=.29*EXP(-15662/(933-89.47*LA))
210 TI=0
220 FOR I=1 TO 4
230 CA(I)=.171/(1-(I-1)^2*.0001)^.829
240 NEXT I
250 FOR I=5 TO 100
260 CA(I)=0
270 NEXT I
280 FOR I=1 TO 100
290 CB(I)=0
300 NEXT I
310 LPRINT "Initial temperature =";660-89.47*LB
320 Z=(IB-1)*.01+RB
330 LPRINT "Interface position = ";Z;",  Fraction solid = ";Z^2
340 FOR I=1 TO 3
350 LPRINT "i=";I;"C=";CA(I),
360 NEXT I
370 LPRINT "and for i=4, C=";CA(4)
380 FOR W=1 TO 10000
390 FOR X=1 TO IC
400 CB(1)=CA(1)+4*R*(CA(2)-CA(1))
410 FOR I=2 TO IA-1
420 CB(I)=CA(I)+R*((2*I-1)*CA(I+1)+(2*I-3)*CA(I-1)-4*(I-1)*CA(I))/(2*(I-1))
430 NEXT I
440 F=LA*((IA-1)*.02/RA+1)+CA(IA-1)*(2*IA-3)-CA(IA)*2*(IA-1)*(1+.01/RA)
450 CB(IA)=CA(IA)+R*F/((IA-1)*(1+.01/RA)+RA^2/.0004-.25)
460 LB=LA
470 PRINT;LA
480 LA=LA+1.117647E-06*PR*PC*R/DA
490 DA=.29*EXP(-15662/(933-89.474*LA))
500 S=.00005*(IB-1)*CB(IB)
510 FOR I=2 TO IB-1
520 S=S+.0001*(I-1)*CB(I)
530 NEXT I
540 K=(IB-1)*CB(IB)-(IB-2)*CB(IB-1)-CB(2)
550 S=S-8.333E-06*K
560 A=4.84795*LA
570 B=(IB-1)*.01*(LA-CB(IB))
580 C=2*S-(IB-1)^2*.0001*CB(IB)-1+5.84795*LA
590 D=B^2+4*A*C
600 T=(SQR(D)-B)/(2*A)
610 U=T-.01*(IB-1)
620 IF U>.025 THEN GOTO 960
630 IF U>.015 THEN IA=IB+1
640 RA=T-.01*(IA-1)
650 IF T>1 THEN GOTO 860
660 K=CB(IB)*.02*RA/(.01*(.01+RA))+LA*.0002/((.02+RA)*(.01+RA))
670 IF U<.015 THEN CA(IA)=K-CB(IB-1)*.01*RA/((.02+RA)*.01)
680 FOR I=1 TO IB
690 CA(I)=CB(I)
```

```
700 NEXT I
710 IB=IA
720 RB=RA
730 TI=TI+R*PR*.0001/DA
740 IF LA=>LX THEN GOTO 980
750 NEXT X
760 LPRINT "time  =";TI;"   n = ";W
770 LPRINT "Liquid composition =";LB/.171;",      Temperature = ";660-89.47*LB
780 Z=(IB-1)*.01+RB
790 LPRINT "Interface position = ";Z;",  Fraction solid = ";Z^2
800 FOR I=1 TO 99
810 LPRINT "i=";I;"C=";CA(I),
820 NEXT I
830 LPRINT "i=100,C=";CA(100)
840 NEXT W
850 END
860 LPRINT "time  =";TI;"   n = ";W
870 LPRINT "Liquid composition =";LB/.171;",      Temperature = ";660-89.47*LB
880 Z=(IB-1)*.01+RB
890 LPRINT "Interface position = ";Z;",  Fraction solid = ";Z^2
900 FOR I=1 TO 99
910 LPRINT "i=";I;"C=";CB(I),
920 NEXT I
930 LPRINT "i=100,C=";CB(100)
940 LPRINT "That's all folks "
950 END
960 LPRINT "U>.025"
970 END
980 LA=LX
990 LPRINT "time  =";TI;", the isothermal hold starts "
1000 LPRINT "Liquid composition =";LB/.171;",      Temperature = ";660-89.47*LB
1010 Z=(IB-1)*.01+RB
1020 LPRINT "Interface position = ";Z;",  Fraction solid = ";Z^2
1030 FOR I=1 TO 99
1040 LPRINT "i=";I;"C=";CA(I),
1050 NEXT I
1060 LPRINT "i=100,C=";CA(100)
1070 FOR ID=1 TO 10000
1080 FOR IE=1 TO IC
1090 CB(1)=CA(1)+4*R*(CA(2)-CA(1))
1100 FOR I=2 TO IA-1
1110 CB(I)=CA(I)+R*((2*I-1)*CA(I+1)+(2*I-3)*CA(I-1)-4*(I-1)*CA(I))/(2*(I-1))
1120 NEXT I
1130 F=LA*((IA-1)*.02/RA+1)+CA(IA-1)*(2*(A-3)-CA(IA)*2*(IA-1)*(1+.01/RA)
1140 CB(IA)=CA(IA)+R*F/((IA-1)*(1+.01/RA)+RA^2/.0004-.25)
1150 IB=IA
1160 RB=RA
1170 PRINT LA
1180 S=.00005*(IB-1)*CB(IB)
1190 FOR I=2 TO IB-1
1200 S=S+.0001*(I-1)*CB(I)
1210 NEXT I
1220 K=(IB-1)*CB(IB)-(IB-2)*CB(IB-1)-CB(2)
1230 S=S-8.333E-06*K
1240 A=4.84795*LA
1250 B=(IB-1)*.01*(LA-CB(IB))
1260 C=2*S-(IB-1)^2*.0001*CB(IB)-1+5.84795*LA
1270 D=B^2+4*A*C
1280 T=(SQR(D)-B)/(2*A)
1290 U=T-.01*(IB-1)
1300 IF U>.025 THEN GOTO 960
1310 IF U>.015 THEN IA=IB+1
1320 RA=T-.01*(IA-1)
1330 K=CB(IB)*.02*RA/(.01*(.01+RA))+LA*.0002/((.02+RA)*(.01+RA))
1340 IF U>.015 THEN CA(IA)=K-CB(IB-1)*.01*RA/((.02+RA)*.01)
1350 FOR I=1 TO IB
1360 CA(I)=CB(I)
1370 NEXT I
1380 TI=TI+R*PR*.0001/DA
1390 IF T>1 THEN GOTO 1510
```

APPENDIX F

APPROXIMATE SOLUTE REDISTRIBUTION EQUATION FOR SIMULTANEOUS RIPENING AND SOLID STATE DIFFUSION

Proceeding as in the "theory" chapter, equations (14), (15) and (20):

$$r_T = B\, t^{1/n} \qquad (F\text{-}1)$$

$$C_L = C_o + At \qquad \text{where} \quad A = -\frac{GR}{m_L}\, t \qquad (F\text{-}2)$$

$$(C_o + At)(1-k)\, 2\, r^* \frac{dr^*}{dt} + A r^{*2} = \left(1 + \frac{2}{n}\right) AB^2\, t^{2/n} + 2\, D_s\, r^* \left(\frac{\partial C_s}{\partial r}\right)_{r^*} \qquad (F\text{-}3)$$

define the problem if an approximate value is given for the concentration gradient $\left(\frac{\partial C_s}{\partial r}\right)_{r^*}$ at the interface. Using an approach similar to that of Brody and Flemings [83,164], the following assumptions are made:

Diffusion in the solid is small so that the solute concentration gradient is not changed appreciably by diffusion:

$$\left(\frac{\partial C_s}{\partial r}\right)_{r^*} = \frac{dC_s^*}{dr^*}$$

With this assumption, the problem is completely defined by the four preceding equations. The resulting differential equation is, however, quite involved, so an additional assumption is made, again using an approach similar to that of Brody et al.: the term $\frac{dt}{dr^*}$ is approximated by its average over time t:

$$\frac{dt}{dr^*} \simeq \frac{t}{r^*}$$

Equation (F-3) now becomes:

$$(C_0 + At)(1-k)\, 2 r^* \frac{dr^*}{dt} + A r^{*2} = \left(1+\frac{2}{n}\right) AB^2 t^{2/n} + 2 D_s k A t$$

and the result, derived as in section II of the "theory" chapter for a constant diffusion coefficient D_s is:

$$r^{*2} = \left(1+\frac{2}{n}\right) \frac{AB^2}{1-k} (C_0+At)^{\frac{1}{k-1}} \int_0^t (C_0+At)^{\frac{k}{1-k}}\, t^{2/n}\, dt$$

or:

$$+ \frac{2 D_s k}{A} \left[\frac{C_L}{2-k} + \frac{1-k}{2-k} C_0^{\frac{2-k}{1-k}} C_L^{\frac{1}{k-1}} - C_0 \right]$$

$$\beta_s = \left(\frac{r^*}{r_T}\right)^2 = \frac{1+2/n}{1-k} \frac{C_L^{\frac{1}{k-1}}}{(C_L-C_0)^{2/n}} \int_{C_0}^{C_L} C^{\frac{k}{1-k}} (C-C_0)^{2/n}\, dC$$

$$+ \frac{2 D_s k}{B^2 A^{(1-\frac{2}{n})}} \frac{1}{(C_L-C_0)^{2/n}} \left[\frac{C_L}{2-k} + \frac{1-k}{2-k} C_0^{\frac{2-k}{1-k}} C_L^{\frac{1}{k-1}} C_0 \right]$$

It is seen that the added effect of solid state diffusion translates into an additional term in the right hand side of equation (17) of the "theory" chapter for coarsening with no solid state diffusion. This term is dependent on the cooling rate and the coarsening law constants by means of one parameter:

$$\frac{D_s}{A\, r_T^2} = \frac{(-m_L)}{\Delta T}\,\frac{D_s\, t_f}{r_T^2}$$

The effect of a small amount of solid state diffusion is thus to add a small amount to the solid formed at C_L . In particular, the amount of eutectic f_E formed with coarsening but no solid state diffusion is slightly reduced to become:

$$f_E^{\,d} = f_E - \frac{2\, D_s\, k}{B^2\, A^{(1-\frac{2}{m})}}\,\frac{1}{(C_E - C_o)^{2/m}}\left[\frac{C_E}{2-k} + \frac{1-k}{2-k}\, C_o^{\frac{2-k}{1-k}}\, C_E^{\frac{1}{1-k}} - C_o\right]$$

REFERENCES

1- J.E Shoutens and K.Tempo, "Introduction to Metal Matrix Composites" MMCIAC Tutorial Series MMC n.272.

2- H.Fukunaga and T.Ohde, "Progress in Science and Eng. of Composites", Hayashi et al. ed., ICCM IV Tokyo 1982 p. 1443.

3- H.Fukunaga and M. Kuriyama, Bull. of the Jap. Soc. of Mech. Eng., 25 (203) p.842 May 1982.

4- W.H.Sutton, "Whisker Technology", A.P.Levitt ed., Wiley Interscience 1970 p.273.

5- T.W.Clyne, M.G.Bader, G.R.Cappleman and P.A.Hubert, J. of Materials Science, 20 p.85, 1985.

6- T.W.Clyne and M G.Bader, Proc. of the fifth Int. Conf. on Composite Materials ICCM V, San Diego, 1985, Harrigan et al. ed. p.755.

7- P.K.Rohatgi, R.Asthana and S.Das, "Solidification Processing of Metal-Ceramic Particle Composites", Monograph, Regional Research Laboratory, Council of Scientific and Industrial Research, Hoshangabad Road, Bhopal 462026 (M.P.).

8- H.Fukunaga and K.Goda, J. of the Jap. Institute of Metals, 49 (1) p.78, 1985.

9- G.H.Geiger and D.R.Poirier, Transport Phenomena in Metallurgy, Addison-Wesley, 1973.

10- H.Fukunaga and K.Goda, Bull. of the Jap. Soc. of Mech. Eng., 27 (228) p.1245 June 1984.

11- S.Nagata and K.Matsuda, IMONO (J. of the Jap. Foundrymen's Soc.) 53 (6) p.300, 1981.

12- S.Nagata and K.Matsuda, Trans. of the Japan Foundrymen's Society 2, 1983, p.46.

13- S.Nagata and K.Matsuda, Trans. of the Japan Foundrymen's Soc., 3 p.35, 1984.

14- H.Fukunaga and K.Goda, Bull. of the Jap. Soc. of Mech. Eng., 28 (235) p.1 Jan. 1985.

15- H.Fukunaga, S.Komatsu and Y.Kanoh, Bull. of the Jap. Soc. of Mech. Eng., 26 (220) p.1814 Oct. 1983.

16- P.R.Beeley, Foundry Technology, Butterworths, 19 .

17- C.Williams and K.M.Fisher, "Solidification Technology in the Foundry and Casthouse", the Metals Soc., 1983, p.137.

18- L.Ackermann, J.Charbonnier, G.Desplanches and H.Koslowski, Proc. of the Fifth Int. Conf. on Composite Materials ICCMV, San Diego 1985, Harrigan et al. ed. p. 687.

19- Y.Sawada and M.G.Bader. idem ICCM V p.785.

20- E.Nakata, Y.Kagawa and H.Terao, Report of the Castings Research Laboratory, Waseda University, n.34 1983 p.27.

21- Y.Abe, S.Kohiri, K.Fujiyama and E.Ichihi, "Progress in Science and Eng. of Composite Materials" ICCM IV, Hayashi et al. ed., Tokyo 1982, p.1427.

22- J.G.Banker, SAMPE Quartely, Jan.1974 p.39.

23- J.Maire et al., "carbon fibres: their composites and application", Int.Carbon Fibres Conf., London, 1971 p.107.

24- A.R.Champion, W.H.Krueger, H.S.Hartmann and A.K.Dhingra, Proc. of the 1978 Int. Conf. on Composite Materials, AIME, ICCM 2 p.883.

25- I.Ahmad and J.Barranco, "Advanced Fibers and Composites for Elevated Temperatures", Ahmad and Noton ed., 1979, TMS of AIME,p.183.

26- R.C.Helminh and T.S.Piwonka, idem, p.205.

27- R.Mehrabian, R.G.Riek and M.C.Flemings, Metall. Trans. 5 aug.1974 p.1899.

28- M.C.Flemings and R.Mehrabian, Trans. Int. Foundry Congress, Moscow 1973, Am. Foundrymen's Soc. Trans. Vol.81, p.81.

29- C.G.Levi, G.J.Abashian and R.Mehrabian, "Failure Modes in Composites IV", J.A.Cornie and Crossman ed., AIME, 1977.

30- W.Meyerer et al., Proc. of the 1978 Int. Conf. on Composite Materials ICCM 2, AIME, p.141.

31- W.C.Harrigan and R.H.Flowers, "failure Modes in Composites IV, Cornie and Crossmann Ed., AIME, 1977, p.319.

32- A.Kohyama et al., Proc. of the Fifth Int. Conf. on Composite Materials, San Diego 1985, AIME, Harrigan et al. ed., p.609.

33- R.T.Pepper and R.A.Penty, J. of Composite Materials, 8 p.29 Jan. 1974.

34- E.G.Kendall, "Composite Materials Vol.4, Metallic Matrix Composites", K.G.Kreider ed., Acad. Press, 1974.

35- S.Yajima et al., "Composite Materials", Kawata et al. ed., Proc. US-Japan Conf. Tokyo 1981, p.232.

36- Tanaka et al., "progress in Science and Eng. of Composites", ICCM IV, Hayashi et al. ed., Tokyo 1982, p.1407.

37- A.W.H.Morris, "Carbon fibres, their Composites and Applications", Int. Carbon Fibre Conf., London,1971, p. .

38- W.C.Harrigan and D.M.Goddard, Proc. of the 1975 Int. Conf. on Composite Materials ICCM 1, Scala et al. ed., TMS of AIME, p.849.

39- B.Toloui, Proc. of the Fifth Int. Conf. on Composite Materials, San Diego 1985, ICCM V, Harrigan et al. ed., p.773.

40- S.Kohara and N.Muto, idem ICCM V, p.747.

41- S.Takahashi, idem ICCM V, p.747.

42- S.Yajima et al., J. of Materials Sc. 15, 1980 letters p.2131.

43- S.R.Nutt and F.E.Wawner, J.of Materials Science 20, 1985, p.1953.

44- J.A.Cornie, private communication.

45- S.R.Nutt and F.E.Wagner, " Metal Matrix Composites II ", J.D.Buckley ed., Proc. of a joint NASA / DOD Conf., Florida 1982, NASA Conf. Publ. 2252, p.27.

46- J.A.Cornie, R.J.Suplinskas and H.Debolt, "Surface enhancement for Metal Matrix Composites", O.N.R. Contract NOO14-79-C-0691, Final Report.

47- J.A.Cornie, R.J.Suplinskas and A.W.Hauze, Proc. of the fourth annual conf. on Composite nd Advanced Materials, the Am. Cer. Soc., 1980, p.728.

48- M.K.Shorshorov, T.A.Chernyshova and L.I.Kobeleva, "Progress in Science and Eng. of Composites", ICCM IV, Hayashi et al. ed., Tokyo 1982, p.1273.

49- K.Motoki and A.Okura, idem ICCM IV, p.1281.

50- X.Li, H.Zhang and R.Wu, Proc. of the Fifth Int. Conf. on Composite Materials ICCM V, San Diego 1985, Harrigan et al. ed., p.623.

51- Kohara and Muto, idem ICCM V, p.631.

52- Y.Sawada and M.G.Bader, idem ICCM V, p.785.

53- R.G.Dixon, M.Sc. Thesis, MIT, Dept of Mat. Sc. and Eng., 1985.

54- I.H.Khan. Met. Trans 7A, Sept. 1976, p.1281.

55- K.I.Portnoi et al., Soviet Powder Met. and Metal Ceramics 20 (2) 1981 p.116.

56- Y.Kimura, Y.Mishima, S.Umekawa and T.Suzuki, J.Mater.Sc. 19, 1984 p.3107.

57- M.G.Nicholas and D.Mortimer, in "Carbon Fibres: their Composites and Applications", Int. Carbon Fibre Con., London, 1971, p.129.

58- Y.V.Naidich and G.A.Kolesnichenko, Soviet Powder Met. and Metal Cer., 1 (19) Jan.-Feb. 1964, p.191.

59- C.H.Anderson and R.Warren, Composites. 15 (1) Jan.1984 p.16, Parts 1 and 2.

60- A.R.Kieffer, W.H.Kruss, A.F.Vendl and R.M.Hubatschek, "Silicon Carbide", Marshall et al. ed., Univ. of S.Carolina Press, 1973, p.375.

61- T.Iseki, T.Kameda and T.Maruyama, J. of Mater. Sc., 19 (1984) p.1692.

62- S.Kohara, "Composite Materials", Kawata and Akesaha ed., Proc. US-Japan Conf., Tokyo, 1981, p.224.

63- S.Towata and S.Yamada, J.Jap. Inst. of Metals 47 (2) 1983 p.159.

64- S.Towata and S.Yamada, J.Jap. Inst. of Metals 48 (12) 1984 p. 1192.

65- V.M.Bermudez, Appl.Phys. Letters 42 (1) 1983 p.70.

66- J.A.Cornie, A.Mortensen, M.N.Gungor and M.C.Flemings, Proc. of the Fifth Int. Conf. on Composite Materials ICCM V, San Diego 1985, Harrigan et al. ed., p.809.

67- B.P.Krishnan and P.K.Rohatgi, Metals Tech. 11 Feb. 1984, p.41.

68- G.R.Capplemann, J.F.Watts and T.W.Clyne, J. of Mater. Sc. 20, 1985 p. 2159.

69- R.G.Page and G.R.Leverant, Proc. of the Fifth Int. Conf. on Composite Materials ICCM V, San Diego 1985, Harrigan et al. ed., p.867.

70- W.C.Harrigan Jr, Met. Trans. 9A, April 1978, p.503.

71- Nunes et al., idem ICCM V, p.723.

72- L.F.Mondolfo, Aluminum Alloys, Stucture and Properties, Butterworths 1976, p.513.

73- R.J.Arsenault and R.M.Fisher, Scripta Met. 17, 1983 p.67.

74- T.G.Nieh and R.F.Karlak, Scripta Met. 18, 1984 p.25.

75- H.L.Marcus, D.L.Hull and M.F.Amateau, "Failure Modes in Composites IV", Cornie and Crossman ed., AIME, 1977, p.308.

76- S.D.Tsai, M.Schmerling and H.L.Marcus, Ceramic Sc. and Eng. 2 (7-8) 1981, p.798, 5th Annual Conf. on Composites and Advanced Ceramic Materials.

77- G.Blankenburgs, J. of the Australian Institute of Metals 14 (4), 1969, p.236.

78- Metals Handbook, 8th edition, American Society for Metals.

79- Smithells Metals Reference Book, Butterworth, Brandes ed., 6th edition.

80- R.M.Brick, A.W.Pense and R.B.Gordon, Structure and Properties of Engineering Materials, McGraw-Hill, 4th edition, 1977.

81- T.F.Bower, D.Sc. Thesis, Dept. of Materials Sc and Eng. MIT, 1965.

82- T.F.Bower, H.D.Brody and M.C.Flemings, Trans. TMS/AIME 236, 1966, p.624.

83- M.C.Flemings, Solidification Processing, McGraw-Hill, 1974.

84- W.Kurz and P.J.Fisher, Fundamentals of Solidification, Trans Tech Publications, 1984.

85- G.J.Davies, Solidification and Casting, Halsted Press, John Wiley and Sons, 1973.

86- R.Morando, H.Biloni, G.S.Cole and G.F.Bolling, Metallurgical Transactions 1, 1970 p.1407.

87- T.F.Bower and M.C.Flemings, Trans. TMS?AIME 239, 1967, p.216.

88- H.Biloni and R.Morando, Trans. TMS/AIME 242, 1968, p.1121.

89- K.A.Jackson, J.D.Hunt, D.R.Uhlmann and T.P.Sewart, Trans. TMS/AIME 236, 1966, p.149.

90- R.J.Schaeffer and M.E.Glicksman, Trans. TMS/AIME 239, 1967, p.257. Also in "the Solidification of Metals", ISI Publication 110, London 1967 p.43.

91- S.Wojciechowski and B.Chalmers, Trans. TMS/AIME, 242, 1968

p.690.

92- G.S.Cole and G.F.Bolling, Trans. TMS/AIME 239, 1967, p.1824. Also, idem 233, 1965, p.1568. Also, "the Solidification of Metals", ISI Publication 110, London 1967, p.323.

93- J.A.Spittle, G.W.Dellemare and R.W.Smith, "the Solidification of Metals", ISI Publication 110, London 1967, p.318.

94- R.T.Southin, Trans. TMS/AIME 239, 1967, p.220.

95- B.Chalmers, Principles of Solidification, Krieger 1964 (first publisher Wiley)

96- W.A.Tiller,K.A.Jackson,R.W.Rutter and B.Chalmers, Acta Metallurgica 1, 1953, p.428.

97- W.W.Mulins and R.F.Sekerka, J. of Applied Physics, 35 (2) 1964, p.444.

98- R.F.Sekerka, J. of Applied Physics 36 (1), 1965, p.264.

99- R.F.Sekerka, J. of Crystal Growth, 3,4, 1968, p.71.

100-V.V.Voronkov, Soviet Physics-Solid State, 6 (10), 1965, p.2378.

101-J.S.Langer, Rev. of Modern Physics, 52 (1), 1980, p.1.

102-R.T.Delves, in "Crystal Growth", B.R,Pamplin ed., Pergamon 1975, first edition, p.40.

103-L.J.Masur, M.Sc. Thesis, Dept. of Materials Sc. and Eng., MIT 1981.

104-M.C.Flemings,in "Metallurgical Treatises", Tien and Elliott ed., p.291, 1981, TMS/AIME.

105-G.Dee and R.Mathur, Physical Review B 27 (12) 1983 p.7073.

106-R.Doherty, in "Crystal Growth", Pamplin ed., Pergamon 1975, first edition, p.576.

107-M.H.Burden and J.D.Hunt, J. of Crystal Growth, 22,1974, p.99 and p.109. (Note: see comments by Laxmanan in Acta Metallurgica 33 (6), 1985, p.1023.)

108-W.Kurz and D.J.Fisher, Acta Metallurgica 29, 1981, p.11.

109-G.P.Ivantsov,"Growth of Crystals" Vol.1, Shubnikov and Sheftal' ed., Consultants Bureau, 1959. (the original russian articles are Dokl. Akad. Nauk. SSSR 58, 1947, p.567 and 83, 1952, p.573.)

110-G.Horvay and J.W.Cahn, Acta Metallurgica 9, 1961, p.695.

111-G.F.Bolling and W.A.Tiller, J. of Applied Physics 32 (12), 1961, p.2587.

112-D.E.Temkin, Soviet Physics Doklady, Technical Physics, 5, 1960, p.609.

113-M.E.Glicksman, R.J.Shaeffer and J.D.Ayers, Metallurgical Transactions 7A, 1976, p.1747.

114-G.Lesoult, Ecole des Mines de Paris, personal communication.

115-G.R.Kotler and L.A.Tarshis, J. of Crystal Growth, 3,4, 1968, p.603.

116-idem, 5, 1969, p.90.

117-R.Trivedi, Acta Metallurgica, 18, 1970, p.287.

118-E.G.Holzmann, J. of Applied Physics, 41 (4), 1970, p.1460.

119-I.Jin and G.R.Purdy, J. of Crystal Growth, 23, 1974, p.29 and p.37.

120-G.E.Nash and M.E.Glicksman, Acta Metallurgica 22, 1974, p.1283 and p.1291.

121-W.Oldfield, G.T.Geering and W.A.Tiller, Materials Sc. and Eng. 2, 1967, p.91. Also : W.Oldfield, "The Solidification of Metals", ISI Publication 110, London 1967, p.70.

122-W.Oldfield, Materials Sc. and Eng. 11, 1973, p.211.

123-D.G.Mc Cartney and J.D.Hunt, Metallurgical Transactions 15A, 1984, p.983.

124-R.D.Doherty, B.Cantor and J.M.Fairs, Metallurgical Transactions 9A, 1978, p.621.

125-J.S.Langer and H.Muller-Krumbhaar, Acta Metallurgica 26, 1978, p.1681,1689 and 1697.

126-J.S.Langer and H.Muller-Krumbhaar, J. of Crystal Growth 42, 1977, p.11.

127-J.S.Langer, R.F.Sekerka and T.Fujioka, J. of Crystal Growth 44, 1978, p.414.

128-R.Trivedi, J. of Crystal Growth 49, 1980, p.219.

129-S.C,Huang and M.E.Glicksman, Acta Metallurgica 29, 1981, p.701 and 717.

130-M.E.Glicksman, Materials Sc. and Eng. 65, 1984, p.45.

131-H.Esaka and W.Kurz, J. of Crystal Growth, 69, 1984, p.362.

132-Y.Miyata, T.Suzuki and J.I.Uno, Metallurgical Transactions 16A, 1985, p.1799 and 1807.

133-K.Somboonsuk, J.T.Mason and R.Trivedi, Metallurgical Transactions 15A, 1984, p. 967 and 977.

134-R.Trivedi and K.Somboonsuk, Materials Sc. and Eng. 65 (1984) p.65.

135-H.Esaka and W.Kurz, J. of Crystal Growth 72, 1985, p.578.

136-R.Trivedi and K.Somboonsuk, Acta Metallurgica 33 (6), 1985, p.1061.

137-K.Somboonsuk and R.Trivedi, Scripta Met. 18, 1984,p.1285.

138-R.M.Sharp and A.Hellawell, J. of Crystal Growth 6, 1970, p.253 and 334.

139-G.F.Bolling and D.Fainstein-Pedraza, Acta Metallurgica 22, 1974 p.1033.

140-J.D.Hunt in "Solidification and Casting of Metals", The Metals Society Book 192, London 1979, p.3.

141-R.A.Wasson, PhD Thesis, Dept. of Materials Sc. and Eng., MIT, 1978.

142-B.P.Bardes and M.C.Flemings, Trans. AFS 74, 1966, p.406.

143-T.Z.Kattamis, J.C.Coughlin and M.C.Flemings, Trans. TMS/AIME 239, 1967, p.1504.

144-T.Z.Kattamis, U.T.Holmberg and M.C.Flemings, J. of the Institute of Metals, 95, 1967, p.343.

145-M.Kahlweit, Scripta Met. 2, 1968, p.251.

146-K.Kusabiraki and K.Imai, J. of the Japan Institute of Metals 47, 1983, p.450.

147-K.H.Chien and T.Z.Kattamis, Zeitschrift fur Metallkunde 61, 1970, p.475.

148-R.M.Sharp and A.Hellawell, J. of Crystal Growth 11, 1971, p.77.

149-K.P.Young and D.H.Kirkwood, Metallurgical Trans. 6A, 1975, p.197.

150-P.C.Dann, L.M.Hogan and J.A.Eady, Metals Forum 2 (4), 1979, p.213.

151-M.E.Glicksman and P.W.voorhees, Metallurgical Tran. 15A, 1984, p.995 and 1081.

152-P.W.Voorhees and M.E.Glicksman, Acta Metallurgica 32 (11), 1984, p.2001 and 2013.

153-P.W.Voorhees and M.E.Glicksman, "Chemistry and Physics of Rapidly Solidified Materials", Berkowitz and Scattergood ed., Proc. Conf. AIME, 1983, p.63.

154-G.W.Greenwood, Acta Metallurgica 4, 1956, p.242.

155-I.M.Lifschitz and V.V.Slyozov, J. Phys. Chem. Solids 19 (1-2), 1961, p.35.

156-C.Wagner, Zeitschrift fur Elektrochemie 65, 1961, p.581.

157-J.A.Marqusee and J.Ross, J. Chem. Phys. 79 (1), 1983 p.373.

158-N.J.Whistler and T.Z.Kattamis, J. of Crystal Growth 15, 1972, p.20.

159-D.J.Allen and J.D.Hunt, Metallurgical Trans. 7A, 1976, p.767.

160-D.J.Allen and J.D.Hunt, "Solidification and Casting of Metals", the Metals Society 1979, p.39.

161-P.C.Dann, J.A.Eady and L.M.Hogan, J. of the Australian Institute of Metals 19 (2), 1974, p.140.

162-H.M.Tensi and H.Fuchs, Zeitschrift fur Metallkunde 74 (6), 1983, p.351.

163-M.Taha, Metal Science, 13, 1979, p.9.

164-H.D.Brody and M.C.Flemings, Trans. TMS/AIME 236, 1966, p.615.

165-T.W.Clyne and W.Kurz, Metallurgical Trans. 12A, 1981, p.965.

166-M.Solari and H.Biloni, J. of Crystal Growth, 49, 1980, p.451.

167-D.J.Allen and J.D.Hunt, Metallurgical Trans. 10A, 1979, p.1389.

168-M.C.Flemings, B.D.Poirier, R.V.Barone and H.D.Brody, J. of the Iron and Steel Institute 208, 1970 p.371.

169-A.Roosz, Z.Gacsi and E.G.Fuchs, Acta Metallurgica 32, (1984), p.1745.

170-D.H.Kirkwood and D.J.Evans, "the Solidification of Metals,

Proc. Conf. London 1967, ISI Publication 110, 1967, p.108.

171-D.H.Kirkwood, Materials Sc. and Eng. 65, 1984, p.101.

172-M.Basaran, Metallurgical Trans. 12A, 1981, p.1235.

173-B.A.Rickinson and D.H.Kirkwood, "Solidification and Casting of Metals", The Metals Society 1979, p.44.

174-D.A.Bennett and D.H.Kirkwood, Metal Science 18, 1984, p.17.

175-J.B.Murphy, Acta Metallurgica 9, 1961, p.563.

176-J.R.Cahoon, Metallurgical Trans. 3, 1972, p.1324.

177-M.S.Anand, S.P.Murarka and R.P.Garwala, J. of Applied Physics 36 (12), 1965, p.3860.

178-Fujiwaka and Hirano, as cited in Diffusion Data Vol.5, 1971, p.11.(Keikinzoku 20 (6) 1970, p.267.

179-Ceresara, Phys. Stat. Solidi 27 (2), 1968, p.517.

180-M.G.Hall and C.W.Haworth, Acta Metallurgica 18, 1970, p.33.

181-Peterson and Rothman, as cited in Diffusion Data Vol.4, 1970, p.300. (Phys. Rev. B 1 (8), 1970, p.3264.)

182-Alexander and Sifkin, as cited in Diffusion Data Vol.4, 1970, p.301. (Phys. Rev. B 1 (8), 1970 p.3274.)

184-Beyeler, Maurice and Seguin, as cited in Diffusion Data Vol.4, 1970, p.412. (Memoires Scientifiques de la Revue de Metallurgie 67 (4), 1970, p.295.)

185-N.L.Petersen and S.J.Rothman, as cited in Diffusion and Defect Data Vol.18-19, 1979, Trans. Tech p.13. (Phys. Rev. B 17 (12), 1978, p.4666.)

186-M.P.Watson and J.D.Hunt, Metallurgical Tran. 8A, 1977, p.1793.

187-M.Gunduz and J.D.Hunt, Acta Metallurgica 33 (9) 1985, p.1651.

188-L.F.Mondolfo, Aluminum Alloys, Structure and Properties, Butterworths, London 1976.

189-J.Xing, T.Motegi and A.Ohno, Trans. of the Japan Institute of Metals, 26 (2), 1985, p.144.

190-D.R.Uhlmann, T.P.Seward III and B.Chalmers, Trans. TMS/AIME 236, 1966, p.527.

191-R.E.Jesse, J. of Crystal Growth, 5, 1969, p.132.

192-S.Towata, S.Yamada and T.Ohwaki, Trans. of the Japan Institute of Metals 26 (8), 1985, p.563.

193-R.J.Arsenault and C.S.Pande, Scripta Metallurgica 18, p.1131, 1984.

194-N.J.Whisler and T.Z.Kattamis, J. of Materials Science 7, 1972, p.888.

195-H.Esaka and W.Kurz, Z. fur Metallkunde 76 (2), 1985, p.127.

196-M.Taha, J. of Materials Sc. Letters 3, 1984, p.194.a

197-M.H.Burden and J.D.Hunt, Metal Science 10, 1976, p.156.

198-D.G.McCartney and J.D.Hunt, Acta Metallurgica 29, 1981, p.1851.

199-R.M.Sharp and A.Hellawell, J. of Crystal Growth, 12, 1972, p.339.

200-G.F.Vander Voort, Metallography, Principles and Practice, McGraw-Hill, 1984.

201-F.Erdmann-Jesnitzer and W.Bernhardt, Metall, 11 (12), 1957, p.1032.

202-C.Buckle, C.Changarnier and J.Calvet, Comptes Rendus de l'Academie des Sciences, 235, 1952, p.1040.

203-F.Mollard, PhD Thesis, Department of Materials Science, MIT.

204-M.Gungor, PhD Thesis, Department of Materials Science, MIT, 1986, in preparation.

205-R.C.Brower, D.A.Kessler, J.Koplik and H.Levine, Scripta Metallurgica 18, 1984, p.463.

206-T.H.Courtney, Metallurgical Trans. 8A, 1977, p.671, p.679 and p.685.

207-C.H.K.L.Davies, P.Nash and R.N.Stevens, Acta Metallurgica 28, 1980, p.179.

208-S.Takajo, W.A.Kaysser and G.Petzow, Acta Metalurgica 32 (1), 1984, p.107 and 115.

209-W.A.Kaysser, S.Takajo and G.Petzow, "Sintering-Theory and Practice", Kolar et al. ed., Materals Sc. Monographs Vol.14, p.321, 1982.

210-R.Watanabe and Y.Masuda, Materials Sc. Research Vol.10, "Sintering and Catalysis", Kuczinski ed., Plenum Press N.Y. 1975, p.389.

211-A.N.Niemi and T.H.Courtney, J.of Materials Science 16, 1981, p.226.

212-S.S.Kim and D.Y.Noon, Acta Metallurgica 31 (8), 1983, p.1151.

213-Korn and Korn, Mathematical Handbook, 2nd ed., Mc Graw-Hill.

214-Jeffreys and Jeffreys, Methods of Mathematical Physics, 3rd ed., Cambridge University Press.

215-J.Crank, The Mathematics of Diffusion, 2nd ed., Oxford.

216-J.C.Coughlin, M.Sc. thesis, MIT, Department of Materials Science and Engineering, 1967.

217-D.H.Kirkwood, Materials Science and Engineering 73, 1985, pp L1-L4.

218- N.K.Adam, The Physics and Chemistry of Surfaces, Dover.